Dissertation

submitted to the

Combined Faculties of the Natural Sciences and Mathematics
of the Ruperto-Carola University of Heidelberg, Germany

for the degree of

Doctor of Natural Sciences

Put forward by

Youness Ayaita

born in Paris, France

Oral examination: June 19, 2013

Cosmology with strongly coupled quintessence

Referees: Prof. Dr. Christof Wetterich
Prof. Dr. Matthias Bartelmann

Kosmologie mit stark gekoppelter Quintessenz

Das Problem der kosmologischen Konstante motiviert alternative Ansätze zur Erklärung der beobachteten beschleunigten Expansion des Universums. Quintessenz-Modelle beschreiben eine dynamische dunkle Energie mittels eines Skalarfelds, des Kosmons; im Gegensatz zum Szenario einer kosmologischen Konstante ist die erwartete gegenwärtige Menge dunkler Energie vergleichbar mit der Energiedichte der Materie. Den einfachsten Modellen fehlt jedoch eine natürliche Erklärung dafür, daß die dunkle Energie gerade in der gegenwärtigen Epoche begonnen hat, die Energiedichte des Universums zu dominieren. Eine Kopplung zwischen Kosmon und Neutrinos stellt eine mögliche Lösung dieses Koinzidenzproblems dar. Auf der Ebene von Störungen in den Energiedichten vermittelt diese Kopplung eine anziehende Kraft zwischen Neutrinos, deren Stärke diejenige der Gravitation übersteigt. Das impliziert drastische Konsequenzen für jedwede quantitative Untersuchung des Modells. Das methodische Standardrepertoire, namentlich lineare Störungstheorie und Newtonsche N-Körper-Simulationen, schlägt fehlt. Selbst die Expansion des Friedmann-Lemaître-Robertson-Walker-Hingergrunds hängt aufgrund eines Rückkopplungseffekts von nichtlinearen Störungen ab. Wir präsentieren eine umfassende Methode, begleitet von einem vertieften physikalischen Verständnis, zur quantitativen Beschreibung des Modells und eröffnen die Möglichkeit, den Parameterraum des Modells systematisch zu untersuchen und einen Vergleich mit Beobachtungen herzustellen.

Cosmology with strongly coupled quintessence

The cosmological constant problem motivates alternative approaches for explaining the observed accelerated expansion of the Universe. Quintessence models describe a dynamical dark energy component in terms of a scalar field, the cosmon; in contrast to the cosmological constant scenario, the predicted amount of present dark energy is, generically, comparable to that of matter. The simplest models lack, however, a natural explanation why the dark energy has started to dominate the energy budget of the Universe just around the present cosmic epoch. Growing neutrino quintessence, proposing a coupling between the cosmon and the neutrinos, is a potential solution to this coincidence problem. At the level of perturbations in the energy densities, this coupling mediates an attractive force between the neutrinos stronger than gravity. This has drastic consequences for quantitative analyses of the model. The standard technical repertoire of linear perturbation theory and Newtonian N-body simulations fails. Even the evolution of the Friedmann-Lemaître-Robertson-Walker background depends on the nonlinear perturbations by virtue of a backreaction effect. We present a comprehensive method, accompanied with an improved physical understanding, for a quantitatively reliable investigation of the model and open the door to a systematic exploration of its parameter space and a confrontation with observational constraints.

Preface

If I were to describe the spirit of this thesis, I would adopt a slogan that served as the title for a 2012 workshop at Ringberg Castle: "The Dark Energy quest: when theory meets simulations." We are more used to theory meeting *observations*. However, as will be illustrated throughout this thesis, simulations can play the role of a laboratory testing and inspiring new theoretical concepts and ideas. The fruitful interplay between numerical approaches, analytical progress, and physical insights characterizes the intellectual journey summarized in this thesis.

The research carried out for this thesis took place in exciting times for the science of cosmology. In May 2009, I followed, among scientists and students in the lecture hall of Heidelberg's *Physikalisches Institut*, the launch of ESA's Planck mission that would provide measurements of the anisotropies in the cosmic microwave background radiation — a key observable for cosmology — with unprecedented accuracy. Shortly before the submission of this thesis, I had the pleasure to witness the presentation of the mission's long-awaited results, which spectacularly confirm our scientific understanding. In October 2011, during a talk at "The Dark Universe Conference" in Heidelberg, we were all surprised and pleased by the announcement that the 2011 Nobel Prize in physics was awarded to Saul Perlmutter, Brian P. Schmidt, and Adam G. Riess for their 1998 discovery of the accelerated expansion of the Universe. One of the potential explanations for this observation, dynamical dark energy, is the starting point for this thesis. Apart from this, our understanding of many cosmological and astrophysical observations relies on the assumption of dark matter, which does not interact with light. During the last years, cosmologists hoped for possible hints for its detection at CERN's Large Hadron Collider (LHC). Although LHC data confirmed, as became public in July 2012, the existence of a new particle, presumably the Standard Model Higgs boson, hints for dark matter have not yet been found. In addition to the remarkable efforts in observational cosmology undertaken in recent years, many new projects are planned today. For example, the Euclid space telescope, with the largest astronomical collaboration so far, is expected to provide, during the next decade, precision information about the large-scale structure in the Universe thereby scrutinizing the idea of a hypothetical dynamical dark energy component.

Fortunately, working on this thesis has not been a solitary effort. I am indebted to many people who have accompanied and supported me in different ways. First of all, I am grateful to Christof Wetterich for giving me the opportunity to work in his group and for his constant support and encouragements. With his admirable optimism and unconventional ideas, he has a large share of the success of this thesis. My grateful thanks are also extended to Matthias Bartelmann who agreed to be the second referee. I immensely enjoyed the innumerable fruitful discussions with my collaborators, namely Maik Weber, Björn Malte Schäfer, Marco Baldi, and Ewald Puchwein. David Fonseca Mota kindly provided his numerical implementation of linear perturbation theory for the growing neutrino quintessence model, which I wish to acknowledge. Special thanks should also be given to Rocky Kolb, who motivated the investigation

whether the neutrino detections from SN1987A constrain growing neutrino quintessence. I am also thankful for discussions with Luca Amendola, Nico Wintergerst, Valeria Pettorino, Joschka Beyer, Lily Schrempp, Wessel Valkenburg, Ignacy Sawicki, Valerio Marra, Nelson Nunes, Andy Taylor, Nicolai Christiansen, and Igor Böttcher. Like every member of the institute, I very much appreciate the excellent administrative work of Eduard Thommes and the reliable technical support by Elmar Bittner. Finally, I wish to express my gratitude to the Deutsche Forschungsgemeinschaft and the Transregional Collaborative Research Centre "The Dark Universe" both for the financial support and for providing an excellent research environment.

The results presented in this thesis base largely on three published works: Ayaita et al. (2012b): "Structure formation and backreaction in growing neutrino quintessence"; Ayaita et al. (2013): "Neutrino lump fluid in growing neutrino quintessence"; Ayaita et al. (2012a): "Investigating clustering dark energy with 3d weak cosmic shear". There is, consequently, an overlap between this thesis and the papers as regards the derivations and the figures showing quantitative results. For each corresponding figure individually, I refer to the publication from which it is taken. Similarly, I indicate whenever a section follows the presentation of one of the papers. Since these are collaborative works, credit is shared among the authors. My contributions focus mainly on the overall cosmological evolution of growing neutrino quintessence (in particular on the backreaction effect on the expansion dynamics), the modeling and the dynamics of the cosmon perturbation, the physics and the cosmological evolution of the cosmon-neutrino lump fluid, the analytical understanding of the pressure cancellation within lumps and of the role of the total angular momentum in stabilizing the lumps, and numerical techniques allowing for an efficient calculation of the 3d weak lensing Fisher matrix. So far unpublished results of this thesis include the overcoming of the technical difficulties in evolving the simulations beyond the cosmological redshift $z = 1$, the discussion of the subsequent cosmological evolution, the investigation of the varying coupling model at the nonlinear level, and an analysis of the idea whether the model can be constrained by the detection of high-energy neutrinos emitted, e. g., by supernovae.

Contents

1 Introduction

1.1 The accelerating Universe

The discovery of an accelerated expansion of the Universe (Perlmutter et al., 1999; Riess et al., 1998) is at odds with our basic intuition of gravity described by Newton's law. How can distant galaxies appear to be receding from us at an increasing velocity if all matter attracts all other matter? According to Newton's law of gravitation, the relative velocity of two initially receding bodies decreases by virtue of their mutual attraction. Nonetheless, the original discovery of the accelerated expansion, based on the observation that distant type Ia supernovae appear dimmer than expected, has been spectacularly confirmed and complemented by various subsequent studies. Not only more recent supernova surveys (Astier et al., 2006; Wood-Vasey et al., 2007; Riess et al., 2007; Kowalski et al., 2008), also precision measurements of fluctuations in the cosmic microwave background radiation (Spergel et al., 2003; Ade et al., 2013c), large-scale structure (Tegmark et al., 2004b), baryon acoustic oscillations (Eisenstein et al., 2005; Percival et al., 2010), and limits on the age of the Universe (Krauss and Chaboyer, 2003) all fit into this new picture.

Einstein's theory of general relativity (Einstein, 1915a,b) replaces Newton's law as the fundamental theory of (classical) gravity, and it first made possible to describe the Universe as a whole (Einstein, 1917). Its equations allow for an accelerated expansion in two ways. First, a *cosmological constant* Λ can be introduced to the theory without violating its symmetries. This proposal goes back to Einstein himself when he vainly argued for a static universe in which the cosmological constant would balance the gravitational attraction of matter. Second, an exotic form of energy, called *dark energy*, could fill the Universe that violates the so-called strong energy condition; it would have a substantial negative pressure. This possibility is used in models of dynamical dark energy such as *quintessence* models where the dark energy component is described by a scalar field (Wetterich, 1988; Ratra and Peebles, 1988). As a third option, one might consider modifications to Einstein's theory of general relativity that account for the accelerated expansion. This route is taken in *modified gravity* models (cf., e. g., Nojiri and Odintsov, 2006a, and references therein). The second idea, i. e. dynamical dark energy, in the form of quintessence, is the main topic of this thesis.

It is not the first time that cosmology and astrophysics reveal a gap in our physical understanding. By a comparison between the observed velocity dispersion of galaxies in the Coma cluster with the expectation based on the virial theorem, Zwicky (1933) found a strong discrepancy between the total mass and the luminous mass. The idea of *dark matter*, accounting for the missing mass, was born. Subsequently, a large number

of observations strengthened the hypothesis of an approximately collisionless nonrelativistic matter component not interacting with light (D'Amico et al., 2009), called *cold dark matter*. Today, it constitutes a main pillar of almost all cosmological models, and its mass density in the Universe is assumed to exceed that of ordinary matter by a factor of about five to six (Bennett et al., 2012; Ade et al., 2013c). Cold dark matter may serve as an example how a new idea is attacked from different sides and thereby combines efforts from different fields of physics. As the Standard Model of particle physics does not include a cold dark matter particle, cosmology and astrophysics have provided clear evidence of physics beyond the Standard Model. The detection of cold dark matter particles, e. g. in particle accelerators, is a central goal of particle physics today; and this search is complemented by many theoretical efforts to propose and study dark matter candidates in extensions of the Standard Model (Bertone et al., 2005; Feng, 2010; Rajaraman et al., 2011). At the same time, cosmologists and astrophysicists scrutinize the properties of cold dark matter from the observational side (cf., e. g., Viel et al., 2005; Abdo et al., 2010).

Similarly, investigating the reasons of the Universe's accelerated expansion brings theorists and observers together. While observers provide much-needed information and constraints about the properties of a hypothetical dark energy or a modification of gravity, theorists refine their models, motivate new ideas from fundamental considerations, make quantitative predictions, and thereby tell the observers where to look for possible signatures. In the same spirit, this thesis considers a theoretically well-motivated model of coupled dynamical dark energy, *growing neutrino quintessence* (Amendola et al., 2008a; Wetterich, 2007), and presents the techniques necessary for a confrontation with observations. Before we describe this task more concretely, we turn to the current status of our understanding of the accelerated expansion.

From the three prominent approaches to explain the accelerated expansion, the cosmological constant Λ has clearly emerged as the standard working hypothesis. Together with the assumption of cold dark matter (CDM), general relativity, well-known particle physics (the Standard Model), large-scale spatial homogeneity, isotropy, and flatness, and a nearly scale-invariant spectrum of primordial perturbations, it forms the *cosmological concordance model* 'ΛCDM' of the (post-inflationary) Universe. With only very few parameters like the value of the cosmological constant Λ, the energy densities of the different components, and the amplitude of initial perturbations, this simple model fits a huge wealth of observational data, among them all the major observational probes listed in the beginning of this chapter. It increasingly plays the role of a *de facto standard model* of cosmology. A more basic use of the term 'standard cosmological model' is due to Peebles (1980, 1993, 1998) referring to three key observations whose explanations form building blocks of *Big Bang* cosmology: the *Hubble diagram* demonstrating the expansion of the Universe (Hubble, 1929), the abundances of light elements in accordance with the predictions of *Big Bang nucleosynthesis* (Alpher et al., 1948; Gamow, 1948), and the *cosmic microwave background* radiation (Penzias and Wilson, 1965) emitted when the energy density of the Universe had fallen enough to allow for the formation of neutral, and hence transparent, hydrogen. The considerable evolu-

tion of what we may call *standard* in cosmology, from basic pillars only a few decades ago to a detailed and matured picture today, documents the impressive progress the science of cosmology has experienced in recent times.

We may interpret the role of the cosmological constant in the current standard paradigm of cosmology in two ways. First, we may regard it as a mere parametrization of the unknown without, necessarily, assuming that the accelerated expansion is *really* due to a cosmological constant. Even if falsified one day, the cosmological constant might survive in this way as a useful approximation due to its technical simplicity. If we assume general relativity to hold, a cosmic fluid — coupled to other matter only via gravity — is generically described by two parameters, its *equation of state* w and its *sound speed* c_s^2. The equation of state may be a function of time and completely describes the effect of the fluid on the expansion dynamics of the Universe. The sound speed can be a function of time and scale, and it is needed to describe the fluid's clustering in linear approximation. The fluid is equivalent to a cosmological constant if $w = -1$. A natural way to allow for alternatives is to relax this restriction on w and to, possibly, also consider nontrivial sound speeds c_s^2. This reasoning motivates the introduction of the so-called wCDM parametrization of dark energy. Usually, the possible clustering due to the sound speed is neglected, and the equation of state w is assumed to be constant or to linearly depend on some time coordinate (typically the cosmic scale factor a). This parametrization has become an extremely common choice for cosmological parameter estimations (cf., e. g., Bennett et al., 2012; Ade et al., 2013c). Yet, the drawbacks are obvious. Not only does the wCDM parametrization exclude possible couplings between the parametrized dark energy fluid and other components. The simplistic time evolution of the equation of state parameter w will not resemble concrete theories of dynamical dark energy such as standard quintessence models. In these models, one expects a nonnegligible fraction of *early dark energy*, which the wCDM parametrization ignores. The approach of merely parametrizing dark energy as a generic fluid, although convenient, is clearly limited. There is a pressing need to consider dynamical, theoretically motivated theories of dark energy.

Second, we can take the cosmological constant seriously in the sense that we suspect it to be the true reason for the accelerated expansion of the Universe. Just as particle physicists will need to account for cold dark matter in their models, we will then have to search for explanations of the cosmological constant within our fundamental theories. Here lies the problem. The value of the cosmological constant is ridiculously small as compared to all fundamental energy scales we know. This is called the *cosmological constant problem* (Weinberg, 1989). Let us become more precise. Often, the cosmological constant is either seen as a free parameter in Einstein's theory of general relativity or as an energy density of the vacuum, in particular of the quantum vacuum. Although equivalent at the level of Einstein's field equations, these two views are fundamentally different. Still, both have their justification, and we argue here that, in general, we should consider several contributions to the effective, observable cosmological constant. If the classical theory of general relativity emerges from some more fundamental theory, we might speculate, in the spirit of effective field theory, that

all terms compatible with the symmetry of the theory should appear. Among them would be, in the effective theory of gravity, a nonzero cosmological constant Λ_G. In addition to this, we expect zero-point energies in quantum field theories. The natural energy scale of the resulting cosmological constant contribution Λ_{QFT} would be, in a naive estimate, given by the cutoff scale up to which we trust our theory. If we assume the (reduced) Planck scale M_P here, this energy scale is $M_P \sim 10^{18}$ GeV. Even if we mistrust this naive quantum field theory estimate or if we hope to get away with this contribution, e. g. due to normal ordering prescriptions, there is yet another expected contribution to the cosmological constant to cope with. During phase transitions in the very early Universe, the vacuum energy is believed to have changed quite substantially (cf. Carroll, 2001). For example, electroweak symmetry breaking induces a change in the vacuum energy with the energy scale $M_{\mathrm{EW}} \approx 200$ GeV and, correspondingly, a contribution Λ_{EW} to the cosmological constant. Similar statements can be made about the quantum chromodynamics phase transition at $M_{\mathrm{QCD}} \approx 0.2$ GeV and other possible phase transitions. Hence, all these fundamental energy scales should enter the value of the effective cosmological constant. In stark contrast to this expectation, the observationally inferred value of the cosmological constant corresponds to a tiny energy scale $\rho_\Lambda^{1/4} \sim 10^{-12}$ GeV. The comparison between this scale and the fundamental energy scales reveals an enormous amount of fine-tuning.

Worse still, the energy scale of the cosmological constant is not only puzzling in itself. It is just comparable to the energy density of matter in the *present* Universe, whereas it was completely negligible in the early Universe and will dominate in the future. This puzzling coincidence is a strong motivation for the investigation of dynamical dark energy models. In quintessence models (Wetterich, 1988; Ratra and Peebles, 1988), the energy density of the dark energy scalar field, the cosmon φ, decays during most of the cosmological evolution just like radiation and matter. The smallness of its present energy density is then a direct consequence of the large age of the Universe. If these models are assumed, the cosmological constant problem is reformulated. Rather than explaining a fine-tuned tiny, but nonzero value of Λ, one now has to argue why the cosmological constant vanishes. This task is more subtle than it might seem at first sight since, even if the cosmological constant was zero in some high-energy limit, phase transitions in the early Universe would be expected to change its value and to induce a large cosmological constant for the subsequent evolution of the Universe. A comprehensive solution to this problem has been proposed, in which the dark energy scalar field, the cosmon φ, naturally occurs as the pseudo-Goldstone boson of a spontaneously broken dilatation symmetry (Wetterich, 2008). So, quintessence models address the cosmological constant problem in two steps. First, it is argued that the cosmological constant vanishes; second, the dynamical evolution of dark energy naturally accounts for a nonvanishing amount of dark energy, roughly comparable to the matter energy density in the present Universe.

Despite of the severe cosmological constant problem, the situation of the cosmological constant is not entirely hopeless from the theoretical side. A tentative explanation of its tiny value that has gained in popularity is an argument based on the *anthropic*

principle. According to Carter (1974), "what we can expect to observe must be restricted by the conditions necessary for our existence as observers." Weinberg (1987) illustrated with the help of a rough estimation that a positive cosmological constant with an energy density three orders of magnitude above the observationally inferred value or larger would exclude our existence. The accelerated expansion induced by such a large cosmological constant would have started so early that no nonlinear structures and hence no galaxies, stars, and planets would have formed. The anthropic principle has, subsequently, been refined; it is not only limited to the investigation of strict bounds for our existence. Instead, the *principle of mediocrity* (Vilenkin, 1995) and the *self-sampling assumption* (Bostrom, 2002) express anthropic reasoning in terms of probability theory. In essence, these approaches base upon the idea that we should think of ourselves as randomly selected from all observers that have ever existed or will ever exist anywhere. In order to apply this to the value of the cosmological constant, we need a theory predicting a distribution of values for Λ such that there will be observers inferring different values for the cosmological constant depending on their location.

Eternal inflation (Vilenkin, 1983) is a candidate for such a theory. It builds upon *inflationary theory* describing a phase of rapid, exponential expansion in the very early Universe and naturally explaining the observed flatness and isotropy of the Universe on very large scales (Guth, 1981) and the basic properties of the primordial perturbations that grew to become the inhomogeneities like the galaxy clusters, galaxies, and stars surrounding us today (Chibisov and Mukhanov, 1982; Lukash and Novikov, 1982). Although typically assumed to happen around the scale of grand unification $M_{\mathrm{GUT}} \sim 10^{16}$ GeV and thereby far beyond energy scales probed in particle accelerators, the success of this theory has consolidated its place in the standard paradigm of cosmology (cf., e. g., Mukhanov, 2005; Weinberg, 2008; Lyth and Liddle, 2009). In many inflationary models, the phase of inflation never ends globally (inflation is *eternal*), but different, essentially disconnected regions stop inflating at different times (cf. Winitzki, 2009). Each of these regions (so-called *pocket* universes) then undergoes a post-inflationary expansion with potentially different cosmological parameters and, in particular, different values for the cosmological constant. With the help of this idea and the prescription of obtaining probabilities going back to the principle of mediocrity or the self-sampling assumption, Tegmark et al. (2006a) motivate anthropic bounds on the value of the cosmological constant that come close to the observationally inferred value.

This line of thought is less complete than it seems. A severe conceptual complication is the *measure problem* of eternal inflation (Winitzki, 2009). It is related to the fact that the number of observers or civilizations expected from eternal inflation is countably infinite. There is no uniform probability distribution on countable sets, and, consequently, the principle of mediocrity and the self-sampling assumption (based upon regarding us a random sample from such a set) are inherently ill-defined. Moreover, anthropic constraints on Λ rely on assumptions about a prior probability distribution of Λ on the pocket universes generated during eternal inflation. Here, it is typically

assumed that the prior is flat in the relevant range of values (using an argument by Weinberg, 1987). This ignores the possibility that the 'theory space' populated during eternal inflation is large enough to also include models with a fundamental cancellation mechanism of the cosmological constant and a dynamical dark energy component (like the one described by Wetterich, 2008).

1.2 Quintessence

The open issues of the cosmological constant scenario motivate the investigation of alternative models capable of describing the accelerated expansion of the Universe. In order to provide conceptual advantages, these models should alleviate the amount of fine-tuning associated to the cosmological constant problem. Still, the models will rely on the assumption of a fundamental cancellation mechanism leading to a vanishing of the cosmological constant (Wetterich, 2008). Whereas the energy density of a cosmological constant has hardened in the very early Universe, the energy density of dynamical dark energy evolves with time. This opens the possibility to explain physically why the energy density of dark energy is comparable to that of matter in the present Universe. Rather than being fine-tuned, it decays dynamically — just as the energy densities of radiation and matter — and naturally assumes a small value today.

A quantity that depends on time has to also depend on space since general relativity treats time and space on an equal footing. A simple and straightforward example of such a quantity is a scalar field $\varphi(x)$. Describing dark energy by a canonical scalar field, the *cosmon*, is the starting point of *quintessence* models (Wetterich, 1988; Ratra and Peebles, 1988). The name 'quintessence' alludes to its role as the 'fifth element' next to the other four basic components of the Universe, namely cold dark matter, baryonic (i. e. ordinary) matter, photons, and neutrinos. Describing a phase of accelerated expansion with the help of a scalar field is not new to cosmology; the simplest inflationary models similarly base upon a scalar field, the *inflaton* (Guth, 1981; Linde, 1982). A mechanism that worked in the very early Universe might also describe the accelerated expansion in the late Universe (for a recent example of a unified picture, cf. Wetterich, 2013).

The dynamics of the cosmon φ is governed by its potential $V(\varphi)$. For a large class of potentials, there exist *tracker solutions* for the evolution of the cosmon. These solutions are approached for a wide range of initial conditions (Wetterich, 1988; Ratra and Peebles, 1988; Steinhardt et al., 1999; Zlatev et al., 1999). The evolution of the cosmon is, accordingly, insensitive to its initial value and its initial time derivative but rather completely characterized by the parameters of the potential $V(\varphi)$. Common choices are an exponential potential (Wetterich, 1988) and a power-law potential (Ratra and Peebles, 1988). In the case of the exponential potential, the tracker solution exactly follows the dominant component. During radiation domination in the early Universe, the energy density of the cosmon decays proportionally to the energy density in radiation; and after the crossover to matter domination, dark energy decays just as matter. As a consequence, the order of magnitude of the present-day energy fraction of dark

energy is, automatically, roughly comparable to that of matter.

Although naturally accounting, in contrast to the cosmological constant, for a sufficiently small amount of present dark energy, quintessence models suffer from a different fine-tuning problem. Why has the dark energy stopped so recently in cosmic history to decay as matter and started to dominate the energy budget of the Universe, thereby initiating a phase of accelerated expansion? This is the *coincidence* or *why now* problem of dark energy. It similarly applies to the cosmological constant, which is not only unnaturally small (cosmological constant problem) but just large enough to surpass the energy density of matter around the present cosmic time. If a quintessence model with a power-law potential is assumed, the onset of dark energy domination has to be fine-tuned. For an exactly exponential potential and a canonical kinetic term, the cosmon continuously rolls down the potential, its energy density follows the dominant component forever, and no accelerated expansion will occur.

The *growing neutrino quintessence* model has been proposed as a possible solution to the coincidence problem (Amendola et al., 2008a; Wetterich, 2007). A coupling between the cosmon and the neutrinos acts as an effective potential barrier that stops the evolution of the cosmon. The approximately constant potential energy then serves as an effective cosmological constant initiating a phase of accelerated expansion. The resulting homogeneous evolution of the model is very similar to the cosmological constant scenario. The model belongs to the class of coupled quintessence models (Wetterich, 1995; Amendola, 2000). At the particle physics level, the cosmon-neutrino coupling is expressed by a dependence of the neutrino masses on the cosmon field φ (Wetterich, 2007). As the cosmon rolls down its potential $V(\varphi)$, the neutrino masses increase. Consequently, once the neutrinos have become nonrelativistic, their energy density grows as compared to matter and to the cosmon following its tracker solution. This ensures that the neutrinos will have eventually, by virtue of the coupling, a significant effect on the evolution of the cosmon. The moment when the neutrinos become nonrelativistic serves as a trigger for the onset of dark energy domination. This mechanism naturally leads to an accelerated expansion roughly at the present cosmic epoch.

Analyzing the homogeneous evolution constitutes the first of three well-established steps in the study of cosmological models. It is assumed to accurately describe the expansion of the Universe and hence the cosmological evolution on the largest scales. The second step is to allow for small, i. e. linear perturbations around this homogeneous solution. Linear cosmological perturbation theory provides the technical framework for this task (Kodama and Sasaki, 1984; Mukhanov et al., 1992) and it is generally expected to provide a reliable estimate for the growth of inhomogeneities on large scales. On small scales, nonlinearities are important, and their study typically relies on Newtonian N-body simulations as the third step (Bertschinger, 1998). Taken together, this scheme provides a complete picture of the cosmological evolution.

The application of this scheme to the growing neutrino quintessence model revealed tremendous technical difficulties. They are due to the cosmon-neutrino coupling being, in realistic cosmologies, substantially stronger than gravity. In the neutrino per-

turbations, the coupling is reflected as an additional, attractive force. When linear perturbation theory was applied to the model, neutrino overdensities were found to grow quickly and to become nonlinear even on very large scales rendering linear theory essentially useless for obtaining quantitative results (Mota et al., 2008). In Newtonian N-body simulations, the effective neutrino particles were quickly accelerated to the speed of light and hence left the Newtonian limit (Baldi et al., 2011). The calculations indicated the formation of large, nonlinear neutrino lumps. Tentative studies suggested that, within these lumps, the local cosmon field could decouple from the outside field (Nunes et al., 2011), and the resulting mass differences for neutrinos within lumps as compared to the background value could exert a substantial *backreaction effect* (Pettorino et al., 2010). The homogeneous evolution would sensitively depend on the evolution of nonlinear perturbations. The three steps of the standard technical repertoire all failed.

This situation has motivated the development of a comprehensive approach, designed from scratch to include all the relevant effects of the growing neutrino quintessence model. These effects include relativistic neutrino velocities, locally varying neutrino masses, strongly nonlinear structure formation, and the backreaction effect of the nonlinear perturbations on the homogeneous evolution. This has been achieved by Ayaita et al. (2012b), and the presentation of the approach and its quantitative results is a central part of this thesis. Whereas the first results were limited to cosmic scale factors $a \lesssim 0.5$ (Ayaita et al., 2012b), i. e. cosmological redshifts $z \gtrsim 1$, we will explain in this thesis how to overcome this barrier with the help of adequate numerical techniques. The completion of the method opens the door for an exploration of the parameter space of growing neutrino quintessence and, eventually, for a confrontation with observational constraints. We take the first steps in this road by identifying two extreme cases of the cosmological evolution marking two qualitatively very different regimes. In one of them, large and stable cosmon-neutrino lumps form with a substantial backreaction effect on the homogeneous evolution; in the opposing regime, strong oscillations in the cosmon-neutrino coupling parameter prohibit the formation of stable structures, and the cosmological evolution becomes similar to the ΛCDM scenario even at the level of perturbations.

The comprehensive simulation method has served as an inspiration and as a 'laboratory' for analyzing the physics behind the numerics. This strategy has culminated in a detailed understanding of the physics of cosmon-neutrino lumps, their mutual interactions, and of their influence on the cosmological evolution (Ayaita et al., 2013). The collection of cosmon-neutrino lumps behaves as a fluid of nonrelativistic particles, interacting with a coupling mediated by the cosmon field between the lumps, which is substantially reduced as compared to the fundamental cosmon-neutrino coupling parameter. The discussion of this *cosmon-neutrino lump fluid* constitutes a second main pillar of this thesis.

1.3 Outline

In Chapter 2, we take the time to recall the fundamentals of cosmology to which we will refer again and again throughout this thesis. The experienced reader may safely skip this chapter or skim through it to catch the main conventions and notations that will be used in subsequent chapters. The journey starts with the homogeneous approximation (Sec. 2.1), i. e. the Friedmann equations describing the expansion of the Universe in the presence of different components of the cosmic fluid. We then account for inhomogeneities (Sec. 2.2) by first reviewing the basics of cosmological linear perturbation theory and then discussing the nonlinear regime. In particular, we already explain the backreaction effect and the N-body simulation technique in the standard framework of purely gravitational structure formation. In later chapters, we will build upon this well-established knowledge and adapt it to the needs of the growing neutrino quintessence model.

The main theoretical motivation of this thesis are the problems related to the cosmological constant scenario. Rather than dismissing the idea of a cosmological constant out of hand, just referring to its unnaturally small value, we discuss the cosmological constant in quite some detail in Chapter 3. We take the attitude that the increasing popularity of the cosmological constant as the standard explanation for the Universe's accelerated expansion together with its remarkable consistency with observational constraints motivate an intellectually honest discussion of its pros and cons. Therefore, we describe the different facets of the cosmological constant problem (Sec. 3.1) and explain the cornerstones of the proposed anthropic solution (Sec. 3.2), including the relevant concepts from eternal inflation. This will show that, although considerable progress has been made, important open issues persist. In Sec. 3.3, alternatives to the cosmological constant scenario are reviewed; most importantly, we introduce the main ideas behind quintessence (Sec. 3.3.1).

We go a step back in Chapter 4, where we regard dark energy as a generic fluid and investigate the potential of the 3d weak lensing method to constrain this fluid. The wCDM parametrization of dark energy, including a nontrivial sound speed parameter c_s^2, is critically introduced in Sec. 4.1, where we will also quantify the clustering of the parametrized dark energy component. 3d weak gravitational lensing is then explained as a proposed method to take advantage of the full three-dimensional information stored in the cosmic shear in order to infer properties of the large-scale gravitational potentials and the distribution of matter (Sec. 4.2). Forecasts on parameter constraints that will be possible with data from the Euclid mission are obtained in a Fisher information matrix approach with suitable numerical techniques for 3d weak lensing (Secs. 4.3 and 4.4). The presentation follows Ayaita et al. (2012a).

The growing neutrino quintessence model is the topic of Chapter 5. We explain its basic ideas and equations in Sec. 5.1, where we also quantify and discuss the homogeneous evolution of the model. A review of early studies of the model (Sec. 5.2) clarifies the technically and theoretically challenging aspects of the model. Based on this experience, we develop the key points of the comprehensive simulation method in Sec. 5.3.

We postpone the technical details to the next chapter in order to first provide for a firm physical understanding of the cosmological evolution. This will equip us with the necessary concepts and insights to later understand in depth what happens in the numerical simulations. We will describe cosmon-neutrino lumps as particles forming a fluid, and we will show how the properties of the lumps and their mutual interactions dictate the cosmological evolution (Sec. 5.4) following Ayaita et al. (2013). Although no definite comparison of the model with observational constraints can be made at this point, we briefly discuss possible observational signatures of growing neutrino quintessence in Sec. 5.5.

We then turn to the details and to the results of the comprehensive simulation method of growing neutrino quintessence in Chapter 6, as developed by Ayaita et al. (2012b). The chapter starts with recalling why and how the simulation method differs from standard cosmological simulations. A brief technical overview is given in Sec. 6.1. We then explain the main ingredients of the simulation separately. The procedure of obtaining initial conditions based on linear theory is the topic of Sec. 6.2. The modeling and the motion of potentially relativistic effective neutrino particles under the influence of gravity and the cosmon-mediated attractive force is explained in Sec. 6.3. The equations of motion rely on the knowledge of fields, namely the cosmon and the gravitational potentials. We describe how they are evaluated in Sec. 6.4, where we also account for the backreaction effect at the technical level. Quantitative results until the cosmic scale factor $a = 0.5$ (Ayaita et al., 2012b) are presented in Sec. 6.5. We next describe how the numerical issues related to the limitation of $a \lesssim 0.5$ can be solved (Sec. 6.6). Finally, following the cosmological evolution until the present cosmic time $a = 1$ (and beyond) becomes possible. We show preliminary results and make first steps towards an investigation of the parameter space.

An overview of what has been achieved and of what will be the next steps in the analysis of the growing neutrino quintessence model, in particular in the light of observational constraints, concludes this thesis in Chapter 7.

2 Cosmology

The study of the Universe in its totality has developed, within about a century, a wealth of well-established and fundamental concepts, theoretical techniques, and physical results. In the course of this thesis, we will encounter and use these fundamentals again and again. The repertoire of these terms and concepts forms a 'language' in which we shall express our ideas and findings. This concerns the dynamics of expansion, the evolution of perturbations (in the linear and nonlinear regimes), the properties of different components of the cosmic fluid, and finally the discussion of observations linked to events like recombination, i. e. the cosmic microwave background radiation.

Although the contents presented in this chapter have reached the maturity of textbook material and, indeed, can be found in many textbooks, an overview for introducing all terms used later and for fixing conventions is in order. The experienced reader may skip this chapter.

The chapter is divided into two main sections. First, we restrict ourselves to the homogeneous approximation, Sec. 2.1. This allows to study the dynamics of expansion, to introduce the different species relevant in cosmology, and to give a brief account of the most important epochs and events in the cosmic history of the Universe. Second, we turn to the technically more challenging, yet for this thesis equally fundamental aspect of perturbations, Sec. 2.2. We will discuss their origin, their linear and nonlinear evolution, standard techniques of treating them (in N-body codes), and finally their influence, i. e. their *backreaction*, on the homogeneous evolution.

2.1 Homogeneous approximation

The study of celestial objects such as galaxies defines astronomy but not cosmology. The step from the study of individual objects to the study of the Universe as a whole requires to make assumptions about the distribution of celestial objects throughout the Universe. If there was no regularity in the distribution of, e. g., galaxies in space, it would be hard to think of a successful cosmological theory. Cosmology relies on the presence of regularities, preferably symmetries, of the distribution of matter, radiation, etc. in the Universe. A natural starting point is the drastic assumption of complete homogeneity and isotropy. This is the approximation used throughout this section. More precisely, it states that there are observers, i. e., there is a suitable coordinate system such that all quantities describing the Universe do not depend on space but only on time. It comes as no surprise that this approximation, due to its technical simplicity, was used by Friedmann to derive the first equations quantifying the expansion dynamics of the Universe, cf. Sec. 2.1.1. Often, the working hypothesis of

homogeneity is even promoted to a fundamental principle, the so-called *Cosmological Principle* stating that the Universe should look the same for all observers within it, regardless of their spatial location.

Of course, in a strict sense, the Universe is clearly not homogeneous. It is important to distinguish between length scales where the Universe looks very different. On Earth, but also in our astronomical environment (Solar System, Milky Way, Local Group, ...), the Universe is all but homogeneous. This picture remains valid until length scales of about 100 Mpc (corresponding to $\approx 3\times10^8$ light years or $\approx 3\times10^{26}$ cm) (Sarkar et al., 2009). If we wash out all inhomogeneities on scales below $\approx$ 100 Mpc, the assumption of a homogeneous Universe seems to be compatible with present-day observations. Several remarks, however, are in order. First, observations are restricted to the observable part of the Universe, which has a size of only several thousand Megaparsecs. They do not tell us how the Universe looks on larger scales. Second, the question how well the assumption of homogeneity fits observational data is still under dispute. This concerns the analysis of the distribution of galaxies in galaxy surveys (Labini et al., 2009a,b) but also the large-scale anisotropies in the cosmic microwave background radiation (Hansen et al., 2009; Hoftuft et al., 2009; Copi et al., 2009; Ayaita et al., 2010). Third, interpreting observations as supporting the assumption of homogeneity faces several loopholes. For example, we might happen to be located in the center of a large-scale spherically symmetric inhomogeneity. Galaxy distributions etc. would then still look isotropic, and assuming a wrong expansion history could give the impression of them also being homogeneous (cf., e. g., Enqvist, 2008).

Bearing these points in mind, it is still fair to say that the assumption of a homogeneous Universe on large scales is, nowadays, more than a mere working hypothesis. It is the by far simplest assumption compatible with major observational probes. On theoretical grounds, however, it is to be expected that the Universe is highly inhomogeneous on scales much larger than its observationally accessible part. This is a consequence of the theory of inflation (cf. Sec. 3.2.2). At first sight, this might seem irrelevant as science is concerned with predictions that are accessible to experiments. Looking at inflationary theory more closely, however, reveals that the 'global' structure of the Universe, although not observable directly, leads to many statistical predictions that, indeed, can be tested by observations. Since this kind of reasoning is often employed to sketch possible solutions to the cosmological constant problem, we will not completely neglect this aspect.

Another drawback of the homogeneous approximation is of high relevance for this thesis: the backreaction of inhomogeneities on the expansion of the homogeneous background. Even if the Universe looks homogeneous on scales larger than 100 Mpc, this does not imply that all calculations for the evolution of the large-scale Universe can be performed by assuming homogeneity. Washing out small-scale inhomogeneities technically corresponds to applying a window function $W_\lambda(\boldsymbol{x})$, flat on scales $|\boldsymbol{x}| < \lambda$ and falling off quickly for $|\boldsymbol{x}| \gg \lambda$. If the equations governing the expansion of the Universe were linear, the processes of applying the window function and evolving the equations would commute. In that case, calculations could be performed assuming

a homogeneous Universe. Yet, Einstein's equations describing the evolution of the Universe are not linear. Applying the window function first and then evolving the equations does not give the same result as first applying the equations on the full Universe including inhomogeneities and applying the window function thereafter. We will consider this *backreaction effect* in Sec. 2.2.2. Although it gives only minor corrections in most cosmological models, the effect turns out to be important, decisive even, for the calculations performed in this thesis.

This section is structured as follows. We will recall some basic concepts of the theory of general relativity, Friedmann's equations governing the expansion of the homogeneous Universe, and some related fundamental concepts in Sec. 2.1.1. The cosmologically relevant forms of matter or *components* of the cosmic fluid are presented in Sec. 2.1.2. We are then capable of describing the different epochs and events in the evolution of the Universe in Sec. 2.1.3. This textbook material can be found in many textbooks on modern cosmology (Weinberg, 2008, 1972; Mukhanov, 2005; Dodelson, 2003; Hobson et al., 2006). We also follow partly Ayaita (2009, Diploma thesis).

2.1.1 Dynamics of expansion

General relativity

In general relativity, we think of spacetime not as a fixed background on which physics happens, but as a dynamical entity which itself is subject to laws of physics (Einstein, 1915a,b, 1917). In this way, the 'expansion' of the Universe really refers to the geometry of spacetime.

In the (almost complete) absence of experimental data, the development of general relativity relied on guiding principles motivated by theoretical considerations. First, of course, in a suitable limit, general relativity must reduce to Newtonian gravity where the gravitational field equation is the Poisson equation for the Newtonian gravitational potential Φ,

$$\Delta\Phi = \frac{\rho}{2}, \tag{2.1}$$

with the energy density ρ, which, already in special relativity, is related to the 0-0 component of the *energy-momentum tensor* $T^{\mu\nu}$: $\rho = -T^0{}_0$. For convenience, we have set the reduced Planck mass to unity, $1 = M_P = \sqrt{\hbar c}/\sqrt{8\pi G} \approx 2.4 \times 10^{18}\,\mathrm{GeV}/c^2 \approx 4 \times 10^{-6}$ g. Here and in the following, we use units where also $\hbar = c = k_B = 1$.

Second, the theory must be *generally covariant* under coordinate changes. This notion is physically motivated by the so-called *Equivalence Principle* stating that, at every location, there is a coordinate system in which the effects of gravity vanish in the limit of a very small environment around that location.

General relativity then describes spacetime as a four-dimensional Lorentzian manifold. The effects of gravity are encoded in the geometry of the manifold. The Newtonian gravitational potential, e. g., is linked to geometric quantities. The gravitational Poisson equation (2.1), tells us that the geometry must be linked to the energy content of spacetime.

Restricting oneself to partial differential equations of second order (motivated by, e. g., the Poisson equation), the only generally covariant equations satisfying the correct Newtonian limit (2.1) are

$$R_{\mu\nu} - \frac{1}{2} R\, g_{\mu\nu} = T_{\mu\nu}, \tag{2.2}$$

Einstein's field equations. Here, $g_{\mu\nu}$ is a Lorentzian metric tensor with the signature $(-,+,+,+)$. It defines the Levi-Civita connection with the following connection coefficients, the Christoffel symbols:

$$\Gamma^{\mu}_{\alpha\beta} = \frac{1}{2} g^{\mu\lambda} \left(\partial_\beta g_{\lambda\alpha} + \partial_\alpha g_{\lambda\beta} - \partial_\lambda g_{\alpha\beta} \right), \tag{2.3}$$

where we abbreviate the partial derivatives according to $\partial / \partial x^\mu \equiv \partial_\mu$. They can be used to write the covariant derivative of a vector v^α as

$$\nabla_\alpha v^\mu \equiv v^\mu{}_{;\alpha} \equiv \partial_\alpha v^\mu + \Gamma^{\mu}_{\alpha\beta} v^\beta. \tag{2.4}$$

The Ricci-tensor $R_{\mu\nu}$ and the Ricci scalar R in Einstein's field equations are contractions of the Riemann (curvature) tensor $R^\mu{}_{\nu\alpha\beta}$. The curvature tensor of a manifold can be expressed as the change in a vector after parallel transport along an infinitesimal closed loop,

$$R^\mu{}_{\nu\alpha\beta} v_\mu = \nabla_\beta \nabla_\alpha v_\nu - \nabla_\alpha \nabla_\beta v_\nu, \tag{2.5}$$

or directly with the Christoffel symbols

$$R^\mu{}_{\nu\alpha\beta} = \partial_\alpha \Gamma^{\mu}_{\nu\beta} - \partial_\beta \Gamma^{\mu}_{\nu\alpha} + \Gamma^{\lambda}_{\nu\beta} \Gamma^{\mu}_{\lambda\alpha} - \Gamma^{\lambda}_{\nu\alpha} \Gamma^{\mu}_{\lambda\beta}. \tag{2.6}$$

The Ricci tensor and Ricci scalar are then

$$R_{\mu\nu} = R^\lambda{}_{\mu\lambda\nu}, \quad R = R^\lambda{}_\lambda. \tag{2.7}$$

It is often useful to work with an action principle instead of the field equations that follow from it. This is particularly convenient if not only gravity is considered, but if we want to add the action for some matter field. Einstein's field equations indeed follow from an action principle if we define the Lagrangian density $\mathscr{L}_G = R/2$ and thereby the Einstein-Hilbert action for gravity,

$$S_G = \frac{1}{2} \int d^4x \, \sqrt{-g(x)} R(x), \tag{2.8}$$

with the determinant of the metric $g \equiv \det(g_{\mu\nu})$.

The 'coupled' system of gravity and some matter content is then described by the action $S = S_G + S_m$. The translation back to Einstein's equations is given by the definition of the energy-momentum tensor as a variation of the Lagrangian density $\mathscr{L}_m$ for matter,

$$T_{\mu\nu} = \frac{-2}{\sqrt{-g}} \frac{\delta \left(\sqrt{-g} \mathscr{L}_m \right)}{\delta g^{\mu\nu}}, \tag{2.9}$$

and the equations of motion for matter are then encoded in the energy-momentum conservation equation

$$\nabla_\nu T^{\mu\nu} = 0. \tag{2.10}$$

Note that this equation, in general, does not give rise to a conserved charge. There is no globally conserved energy.

In later chapters, we will need to evolve point particles on a given spacetime. In the simplest case, where a particle of mass m and with proper time η moves only under the influence of gravity, the equation of motion can be derived from the action

$$S = -m \int d\eta, \tag{2.11}$$

whose variation leads to the geodesic equation

$$\frac{d^2 x^\mu}{d\eta^2} + \Gamma^\mu_{\alpha\beta} \frac{dx^\alpha}{d\eta} \frac{dx^\beta}{d\eta} = 0. \tag{2.12}$$

Friedmann equations

Under the assumptions of homogeneity and isotropy everywhere, Einstein's equations specialize to the Friedmann equations. Whether spacetime looks homogeneous and isotropic depends on the observer, i. e. on the chosen coordinate system. Those observers that see a (large-scale) homogeneous Universe are called *comoving observers*.

In general, we say that a spacetime is homogeneous if there is a suitable time coordinate t (corresponding to a foliation of spacetime by spatial hypersurfaces Σ_t) such that for constant time, every point p can be mapped on any other point q by a diffeomorphism. We speak of isotropy around a point p if there is a four-velocity u such that an observer located at p and moving with u cannot single out any preferred direction. We shall see that this velocity coincides with the velocity of the cosmic fluid, hence the name *comoving*.

It can be shown that for a (spatially) homogeneous and isotropic spacetime, the Riemann tensor of the three-dimensional hypersurfaces Σ_t is

$${}^{(3)}R_{ijkl} = K \left({}^{(3)}g_{ik} {}^{(3)}g_{jl} - {}^{(3)}g_{il} {}^{(3)}g_{jk} \right), \tag{2.13}$$

where K quantifies the curvature and is related to the Ricci scalar by ${}^{(3)}R = 6K$. One can write the metric in the form

$$ds^2 = g_{\mu\nu} dx^\mu dx^\nu = -dt^2 + a(t)^2 \left[\frac{dr^2}{1-kr^2} + r^2 \left(d\theta^2 + \sin^2\theta \, d\varphi^2 \right) \right], \tag{2.14}$$

in suitable (comoving) coordinates $(x^\mu) = (t, r, \theta, \varphi)$. This is the Friedmann-Lemaître-Robertson-Walker (FLRW) metric. k denotes the sign of K (and $k = 0$ for $K = 0$), $a(t)$ is the so-called *scale factor* describing the expansion of spacetime, r is the *comoving*

distance from the origin (the *physical distance* of a point from the center measured by a ruler would evolve as $r_{\mathrm{ph}}(t) \propto a(t)\, r$). For convenience, we normalize the scale factor at the present cosmic time t_0 to unity, $a(t_0) = 1$. The Levi-Civita connection of the metric is given by

$$\Gamma^0_{ij} = \dot{a} a^{(3)} g_{ij}, \quad \Gamma^i_{0j} = \frac{\dot{a}}{a} \delta^i_j, \quad \Gamma^i_{jk} = {}^{(3)}\Gamma^i_{jk}. \tag{2.15}$$

The Hubble parameter $H = \dot{a}/a$ quantifies the increase of the scale factor. The Universe is said to expand for $\dot{a} > 0$, to contract for $\dot{a} < 0$. The expansion is said to accelerate for $\ddot{a} > 0$ and to decelerate for $\ddot{a} < 0$. The acceleration or deceleration is often quantified in terms of the *deceleration parameter* q,

$$q = -\frac{\ddot{a}\, a}{\dot{a}^2} = -\left(1 + \frac{\dot{H}}{H^2}\right). \tag{2.16}$$

An artefact of the times where the Hubble parameter was not known to high accuracy is the parameterization of the present Hubble parameter H_0 as

$$H_0 = 100 h \, \frac{\mathrm{km}}{\mathrm{s}} \, \mathrm{Mpc}^{-1}, \tag{2.17}$$

where the uncertainty is shifted to the dimensionless parameter h, which is of order one. Instead of keeping the uncertainty in H_0, one often shifts it to the distance unit for which one then uses $h^{-1}\mathrm{Mpc}$.

Instead of the cosmological time coordinate t, we will often use the scale factor a, the *redshift* $z = 1/a - 1$, or the *conformal time* τ given by $d\tau = dt/a(t)$.

After having collected all the ingredients for the left-hand side of Einstein's equations, we now turn to the right-hand side. The exact form of the energy-momentum tensor $T_{\mu\nu}$ will depend on the energy-matter content of spacetime. Since the geometry of spacetime, however, is directly related to its energy-matter content, $T_{\mu\nu}$ is constrained by symmetries. Homogeneity everywhere means that the coefficients of $T_{\mu\nu}$ can only depend on time. Together with the isotropy assumption, it is clear that $T^\mu{}_\nu = \mathrm{diag}(-\rho, p, p, p)$ in comoving coordinates. The two remaining parameters are the energy density ρ and the pressure p. The energy-momentum tensor has the form of a perfect fluid,

$$T^{\mu\nu} = (\rho + p) u^\mu u^\nu + p\, g^{\mu\nu}, \tag{2.18}$$

at rest, i. e. $(u^\mu) = (1, 0, 0, 0)$.

Put together, we eventually obtain the Friedmann equations

$$\frac{\ddot{a}}{a} = \dot{H} + H^2 = -\frac{1}{6}(\rho + 3p), \tag{2.19}$$

$$\left(\frac{\dot{a}}{a}\right)^2 = H^2 = \frac{\rho}{3} - \frac{k}{a^2}. \tag{2.20}$$

A useful additional relation, although contained in the Friedmann equations, is given by $\nabla_\lambda T^{0\lambda} = 0$:

$$\dot{\rho} + 3H(\rho + p) = 0. \tag{2.21}$$

Throughout this work, we make the assumption that the Universe is flat, which is consistent with present-day observational data (Hinshaw et al., 2012; Bennett et al., 2012; Ade et al., 2013c,e) and expected by inflationary theory. We shall thus work with $k = 0$.

Propagation of light

Light and its motion in the homogeneous Universe give rise to several often-used concepts. The *redshift* z will be used as both a time and a distance coordinate. The propagation of light also defines horizons.

A lightlike geodesic $ds^2 = 0$ in a flat FLRW metric is described by

$$dt = \pm a(t)dr. \tag{2.22}$$

Let the source S be located at $r > 0$, emitting signals in infinitesimal intervals dt_S. These signals are observed at $r = 0$ by an observer in intervals dt_O. According to the equation above, we have $dt_S/a_S = dt_O/a_O$. The redshift z, quantifying the change of frequency, is then given by $1 + z = a_O/a_S$.

We normalize $a_O = 1$ and relate scale factor a, cosmic time t, and comoving distance r to a *cosmological redshift* in the following ways:

$$a = \frac{1}{1+z}, \quad t = \int_z^\infty \frac{dz'}{H(z')(1+z')}, \quad r = \int_0^z \frac{dz'}{H(z')}. \tag{2.23}$$

This cosmological redshift is not identical to the observed redshift of lines in the spectra of galaxies. The redshift is changed due to the rotation of the galaxy, perturbations along the light path, and, most importantly, by the so-called *peculiar motion* of the galaxy with respect to the comoving frame.

The questions of what can be observed today and of what can, in principle, be observed in the future, are closely related to the propagation of light. We speak of a *particle horizon* and an *event horizon*, concepts introduced by Rindler (1956).

The maximum comoving distance from which light can reach an observer at time t is the particle horizon

$$r_{PH}(t) = \int_0^t \frac{dt'}{a(t')}, \tag{2.24}$$

where we have identified the beginning of the Universe with $t = 0$. If $a(t)$ was constant, the particle horizon would correspond to the age of the Universe as expected in special relativity. The expanding Universe satisfies $\dot{a} > 0$ at all times, most drastically during the inflationary epoch. Consequently, r_{PH} is very large, in principle. However,

the Universe was opaque to photons before *recombination* such that the *optical* particle horizon relevant for most observations is

$$r_{PH,\text{optical}}(t) \approx \int_{t_{\text{rec}}}^{t} \frac{dt'}{a(t')} \ll r_{PH}(t). \tag{2.25}$$

This restriction does not apply to gravitational wave astronomy.

The event horizon $r_{EH}(t)$ encloses the region which will ultimately be reached by light emitted at the origin at time t,

$$r_{EH}(t) = \int_{t}^{\infty} \frac{dt'}{a(t')}, \tag{2.26}$$

assuming that the Universe reaches infinite age.

The Hubble scale $1/H$ is also often called *horizon*, usually *Hubble horizon* but sometimes confounded with the particle horizon. This has historical reasons because the Hubble scale and the particle horizon are of similar order if the expansion of the Universe is dominated by radiation or matter at all times. The Hubble scale describes at which distances the effects of the cosmic expansion become important. It is crucial for classifying perturbations. Perturbations on physical scales $\lambda \ll H^{-1}$, so-called *subhorizon* perturbations, will experience growth due to gravitational attraction. On *superhorizon* scales, $\lambda \gg H^{-1}$, this mechanism does not work.

2.1.2 Cosmic inventory

The two free parameters describing the energy content of the Universe are the energy density ρ and the pressure p. It is useful to decompose the cosmic fluid into different species that have particularly simple properties. We write

$$T^{\mu\nu} = \sum_i T_i^{\mu\nu} = \sum_i \left[(\rho_i + p_i)u^\mu u^\nu + p_i g^{\mu\nu}\right]. \tag{2.27}$$

The total energy density and pressure are thus sums over ρ_i and p_i respectively.

We will see that the energy densities of different species depend differently on the scale factor a. Not surprisingly, there are epochs during which the energy density of one single species greatly exceeds those of the other species. For example, the Universe was dominated by radiation at early times, later by nonrelativistic matter, and will finally be dominated by dark energy or a cosmological constant. During each of these epochs, the other species may be neglected for the calculation of the expansion.

The energy fraction of a species i is quantified by

$$\Omega_i \equiv \frac{\rho_i}{\sum_j \rho_j} = \frac{\rho_i}{3H^2}, \tag{2.28}$$

where we used the second Friedmann equation for $k = 0$ in the last step. The dynamics of expansion is particularly simple if the dominating species has a constant equation of

state $w \equiv p/\rho$. In this case, the Friedmann equations can be integrated to give

$$\rho \propto a^{-3(1+w)}, \quad a(t) \propto t^{\frac{2}{3(1+w)}}, \tag{2.29}$$

where the latter equation holds for $w > -1$. In the case $w = -1$, we have $a(t) \propto \exp(Ht)$ with a constant Hubble parameter H.

From Eq. (2.29) above or from the second Friedmann equation, we deduce that the expansion of the Universe can only accelerate if $\rho + 3p < 0$, i. e., if $w < -1/3$. This is a violation of the so-called strong energy condition but indeed occurs in the case of dark energy or a cosmological constant.

Photons and neutrinos

Although both, photons and neutrinos, are produced in stars, their dominant cosmological contribution is an approximately homogeneous and isotropic background distribution left over from the early Universe. For photons, this is directly observable as the ≈ 3K cosmic microwave background radiation (CMB) we will discuss later. The neutrino background has not been observed due to the very small neutrino energies and, therefore, tiny reaction cross sections. In the course of this thesis, we will even make the assumption that the neutrinos, in recent cosmic history, behave much different.

It is very useful to establish a connection between the phase-space distribution function $f(x, p)$ and the energy-momentum tensor,

$$T^{\mu}{}_{\nu} = g \int d^3p \, \frac{1}{\sqrt{-g}} \, \frac{p^{\mu} p_{\nu}}{|p_0|} f(x, p), \tag{2.30}$$

with a degeneracy g. If the species under consideration is in thermal equilibrium everywhere, $f(x, p)$ is a Fermi-Dirac or Bose-Einstein distribution for fermions and bosons, respectively. Under the assumption of homogeneity, neither the temperature T nor the chemical potential μ can depend on space:

$$f(x, p) = f(|\boldsymbol{p}|) = \frac{1}{e^{\frac{E-\mu}{T}} \pm 1}, \tag{2.31}$$

with $E = p^0 = \sqrt{\boldsymbol{p}^2 + m^2}$.

From here, the two parameters, energy density ρ and pressure p, can be calculated,

$$\rho = -T^0{}_0 = g \int d^3p \, \frac{1}{\sqrt{-g}} \, E f(x, p), \tag{2.32}$$

$$p = \frac{1}{3} T^i{}_i = g \int d^3p \, \frac{1}{\sqrt{-g}} \, \frac{p^i p_i / 3}{|p_0|} f(x, p). \tag{2.33}$$

In the massless (or highly relativistic) limit $m = 0$ and for vanishing chemical potential $\mu = 0$ (which holds if particle number is not conserved), the expressions can be evaluated (Amendola and Tsujikawa, 2010, p. 14) to yield

$$\rho = \begin{cases} g\,\frac{\pi^2}{30}\,T^4 & \text{for bosons} \\ g\,\frac{7}{8}\,\frac{\pi^2}{30}\,T^4 & \text{for fermions} \end{cases}, \qquad p = \frac{\rho}{3}. \tag{2.34}$$

We have just established $w = 1/3$ for relativistic species. We deduce $\rho \propto a^{-4}$ and $a(t) \propto t^{1/2}$.

Let us have a closer look at the photons. Since photons are essentially free-streaming today, why did we consider an equilibrium distribution? In the early Universe, prior to recombination, they interacted with baryonic matter via

$$\gamma + H \longleftrightarrow p + e^-, \tag{2.35}$$

which requires a photon energy $E_\gamma \geq 13.6$ eV. When the temperature of the plasma fell much below 13.6 eV due to the expansion of the Universe, almost no photons had enough energy for the above reaction.

The photons, however, kept their distribution function; it has $\mu = 0$ because photon number was not conserved during equilibrium. By $\rho_\gamma = 2(\pi^2/30)T_\gamma^4$ and $\rho_\gamma \propto a^{-4}$, we find that the temperature parameter decreases as $T_\gamma \propto a^{-1}$.

In accordance with theoretical expectations, the Cosmic Background Explorer satellite (COBE) confirmed the shape of the distribution function and measured $T_\gamma = (2.725 \pm 0.002)$ K (Fixsen et al., 1996). This corresponds to a present energy fraction

$$\Omega_{\gamma,0} = \frac{2\,\frac{\pi^2}{30}\,T_{\gamma,0}^4}{3H_0^2} \approx 5 \times 10^{-5}. \tag{2.36}$$

The neutrinos left thermal equilibrium much earlier. In the very early Universe, they interacted via processes like

$$\nu_e + \bar{\nu}_e \longleftrightarrow e^- + e^+. \tag{2.37}$$

The interaction rate $\Gamma = n\,\langle\sigma v\rangle$ decreases due to the 'thinning' $n \propto a^{-3}$ of the number density and $\langle\sigma v\rangle \propto G_F^2 T^2$ with Fermi's constant G_F,

$$\Gamma \propto G_F^2 T^5 \propto G_F^2 a^{-5}. \tag{2.38}$$

The competing effect is the expansion rate. Once $H \gg \Gamma$, the reaction is very unlikely to happen. Evaluating H for a radiation-dominated Universe and comparing with Γ yields a critical temperature of order $T \sim 1$ MeV.

The relation between T_ν and T_γ is $T_\nu = (4/11)^{1/3} T_\gamma$. For massless neutrinos, one would have $\Omega_\nu \approx 0.68\Omega_\gamma$. Yet, neutrinos are known to be not massless. The flavor

eigenstates $|\nu_a\rangle$, $a = e, \mu, \tau$, are related to the mass eigenstates $|\nu_i\rangle$ by the Pontecorvo-Maki-Nakagawa-Sakata (MNS) matrix U_{ai},

$$|\nu_a\rangle = \sum_i U_{ai} |\nu_i\rangle. \tag{2.39}$$

In the presence of non-vanishing mass differences, *neutrino oscillations* can be observed. An initial neutrino of flavor a can eventually be detected after time t as a neutrino of flavor b (Akhmedov, 1999) with probability

$$P_{a\to b} = \left| \sum_j U_{bj} e^{-iE_j t} U^*_{aj} \right|^2 . \tag{2.40}$$

These oscillations have been observed in the solar neutrino flux (Fukuda et al., 1998). The corresponding squared mass differences (Fukuda et al., 1998; Araki et al., 2005) indicate that at least one mass eigenstate is above $m_i \gtrsim 0.04$ eV (Beringer et al., 2012).

Assuming that the neutrino mass is constant throughout cosmic history and that the cosmological concordance model is correct, a limit of $\sum_i m_i < 0.2$-0.4 eV can be inferred from cosmological observations (Goobar et al., 2006). In laboratory experiments, the most stringent bounds come from the measurement of β-decays providing an upper limit of about 2 eV (Beringer et al., 2012).

Since the exact mechanism by which neutrinos gather mass is still unknown (they are massless in the Standard Model of particle physics), this mechanism is a possible place for new and unexpected physics. We will come back to this point in later chapters.

Dark matter and baryons

If we sample the phase-space distribution with point particles of masses m_p, trajectories $x^\mu_p(\eta)$ with proper time η, and four-velocities $u^\mu_p = dx^\mu_p/d\eta$, the energy-momentum tensor can be written as

$$T^\mu{}_\nu = \frac{1}{\sqrt{-g}} \sum_p \int d\eta_p \, m_p \, u^\mu_p \, u_{p,\nu} \delta^4(x - x_p(\eta_p)). \tag{2.41}$$

Here, we see that the pressure contribution is proportional to $T^i{}_i \propto m_p \boldsymbol{u}_p^2$; for non-relativistic particles, this is negligible compared to the energy density whence $w = 0$. We conclude $\rho \propto a^{-3}$ and $a(t) \propto t^{2/3}$ in a matter-dominated universe.

The dominant non-relativistic component is dark matter, whose discovery goes back to Zwicky (1933) observing the velocity dispersion in the Coma cluster, confirmed also in the Virgo cluster (Smith, 1936). The term 'dark' matter refers to the lack of interactions with light (Bond et al., 1984) whereby dark matter can only be observed indirectly by its gravitational effects.

Dark matter does not only account for a large fraction of the mass in the intergalactic space in clusters; it is also essential within galaxies as was understood by analyzing galactic rotation curves, first in the Andromeda nebula (Babcock, 1939). Today, a large number of observations in astronomy and cosmology solidify the presence of a cold, i. e. non-relativistic, approximately collisionless dark matter component (D'Amico et al., 2009). Its energy fraction today is about $\Omega_{c,0} \approx 1/5$ (Bennett et al., 2012; Ade et al., 2013c).

Baryonic matter refers to matter that interacts with light. In particular, in contrast to the convention in other branches of physics, baryonic matter includes electrons. Unlike dark matter, baryons do not only interact gravitationally. Instead, their dynamics includes very complicated physics, e. g., star formation, supernovae, and hydrodynamics. The correct modeling of baryonic physics starts to be a crucial caveat for high precision calculations that will be needed to fully exploit the cosmological information of upcoming observational data (see, e. g., Zentner et al., 2012; Gnedin et al., 2004; Gustafsson et al., 2006). In this thesis, however, we will not be concerned much with these details. Instead, most of the time, it will be sufficient for us to treat baryons like dark matter, i. e., to reduce them to their gravitational effects.

In groups and clusters of galaxies, most of the baryons are located in the intergalactic space. Their abundance can be estimated from the absorption of light (originating from distant quasars) by hydrogen (Tytler et al., 2004), and it can be compared with the estimated density of dark matter (White et al., 1993). Another approach is to use the CMB radiation in combination with other cosmological probes, which gives a ratio of baryons to cold dark matter of roughly $\Omega_b/\Omega_m \approx 1/6$ (Bennett et al., 2012; Ade et al., 2013c).

The cosmological constant

The cosmological constant Λ, introduced to general relativity by Einstein (1917), is mathematically particularly simple but conceptually involved. It describes a contribution to the energy-momentum tensor of the form $T_{\mu\nu} = -\rho_\Lambda g_{\mu\nu}$ proportional to the metric with $\rho_\Lambda = \Lambda M_P^2$. In this way, it may be interpreted as the energy density of empty space. Often, the cosmological constant is instead interpreted as a free parameter in general relativity, modifying its basic equations, the Einstein-Hilbert action and Einstein's field equations to (setting $M_P = 1$)

$$S = \frac{1}{2}\int d^4x\,\sqrt{-g}\,(R - 2\Lambda) + S_m, \tag{2.42}$$

$$R_{\mu\nu} - \frac{1}{2}R g_{\mu\nu} + \Lambda g_{\mu\nu} = T_{\mu\nu}. \tag{2.43}$$

In fact, both interpretations are conceptually problematic. If we assume a free parameter Λ_G in general relativity, it would not be identical to the observable cosmological constant Λ. Instead, the observable, *effective* cosmological constant Λ would also include the vacuum energy,

$$\Lambda = \Lambda_G + \rho_{\text{vac}} M_P^{-2}. \tag{2.44}$$

Whereas Λ_G would be a 'true' cosmological constant not depending on space and time, ρ_{vac} is expected to depend on time. This is because it is expected to change its value during phase transitions in the early Universe.

One may argue that Λ_G is somewhat inelegant as it introduces a fundamental length scale into the otherwise scale-free theory of general relativity. On the other hand, in the spirit of effective field theory, Λ_G should be included as it is compatible with the symmetries of general relativity and might find its explanation in a fundamental theory of gravity. The vacuum energy ρ_{vac} is fixed after the phase transitions in the early Universe and can then be treated as a contribution to the cosmological constant. We will discuss this in much more detail in Sec. 3.1.

The equation of state of a cosmological constant is $w_\Lambda = p_\Lambda/\rho_\Lambda = -1$. Unlike the previously discussed components of the cosmic fluid, the cosmological constant can lead to accelerated expansion $\ddot{a} > 0$. The discovery of the Universe's accelerated expansion (Riess et al., 1998; Perlmutter et al., 1999) has lead to a revival of the idea that the cosmological constant may play a crucial role in the expansion dynamics of the Universe. The observational data can be fitted by a present energy fraction $\Omega_{\Lambda,0} \approx 3/4$ in a cosmological constant (Astier et al., 2006; Riess et al., 2007; Wood-Vasey et al., 2007; Kowalski et al., 2008).

The so-called *cosmological concordance model* ΛCDM (CDM abbreviates Cold Dark Matter) describes the Universe with all the components we have just introduced. It increasingly plays the role of a standard model so far consistent with all major observational probes (Bartelmann, 2010b). Its theoretical flaws will be the subject of Chapter 3. With $\Omega_{\Lambda,0} \approx 2/3$, the energy density is of order $\rho_{\Lambda,0} = 3H_0^2\,\Omega_{\Lambda,0} \sim 10^{-47}\ \mathrm{GeV}^4$, ridiculously far away from all fundamental physics scales that could enter ρ_{vac}. This is the *cosmological constant problem*.

Scalar fields

In the standard picture, the inflationary epoch is dominated by a scalar field, the *inflaton* ϕ. It accounts, similarly to a cosmological constant, for a phase of exponential expansion. With its quantum fluctuations, it is the presumed origin of primordial inhomogeneities. An accelerated expansion driven by a scalar field can also work in the late Universe and thus replace the cosmological constant. Such a scalar field is called the *cosmon* φ, introduced in Sec. 3.3.1.

Let us consider a scalar field χ with a canonical action

$$S_\chi = \int d^4x\,\sqrt{-g}\left[-\frac{1}{2}\partial^\lambda\chi\,\partial_\lambda\chi - V(\chi)\right] \tag{2.45}$$

and a self-interaction potential $V(\chi)$. Its energy-momentum tensor then is

$$T_{\mu\nu} = \partial_\mu\chi\,\partial_\nu\chi + g_{\mu\nu}\mathscr{L}_\chi. \tag{2.46}$$

In a homogeneous universe, all spatial derivatives vanish, and we are left with

$$\rho = -T^0{}_0 = \frac{1}{2}\dot{\chi}^2 + V(\chi), \tag{2.47}$$

$$p = \frac{1}{3}T^i{}_i = \frac{1}{2}\dot{\chi}^2 - V(\chi). \tag{2.48}$$

The equation of state $w = p/\rho$ can, if the potential is positive, take any value between -1 (if the potential energy dominates over the kinetic term $\propto \dot{\chi}^2$) and $+1$ (if the kinetic energy dominates).

2.1.3 Chronology of the Universe

We conclude the section on the homogeneous approximation by a brief presentation of the chronology of the Universe. First, we evaluate the energy densities according to the dynamics of expansion explained in Sec. 2.1.1 for a ΛCDM universe. The result is shown in Fig. 2.1. At early times ($a \lesssim 10^{-4}$), the Universe was dominated by

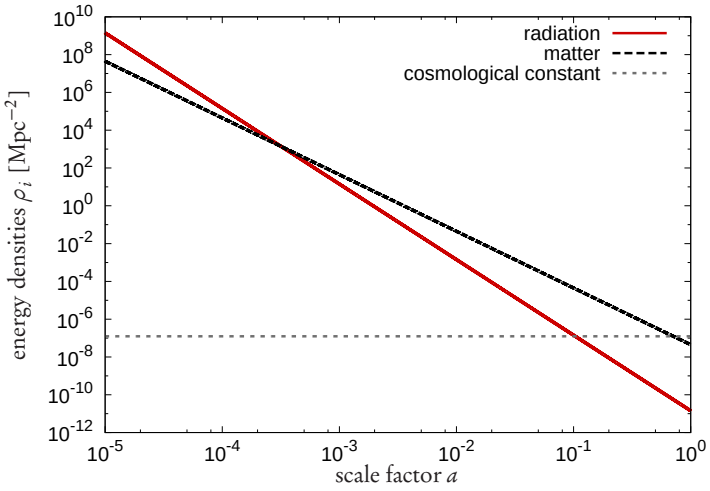

Figure 2.1: Energy densities of radiation, matter, and the cosmological constant as functions of the scale factor a with the parameters of Bennett et al. (2012).

radiation. The energy density of radiation decayed more quickly than that of matter, leading to a phase of matter domination. Eventually, the constant energy density of the cosmological constant surpasses matter in very recent cosmic history.

In this thesis, we will be concerned with the late-time expansion history where the onset of dark energy / cosmological constant domination takes place. The ΛCDM model, which fits the observational data, serves as a fiducial model with which alternative models can be compared. For later reference, we show the evolution of the fractional energy densities Ω_i on a linear scale in a in Fig. 2.2.

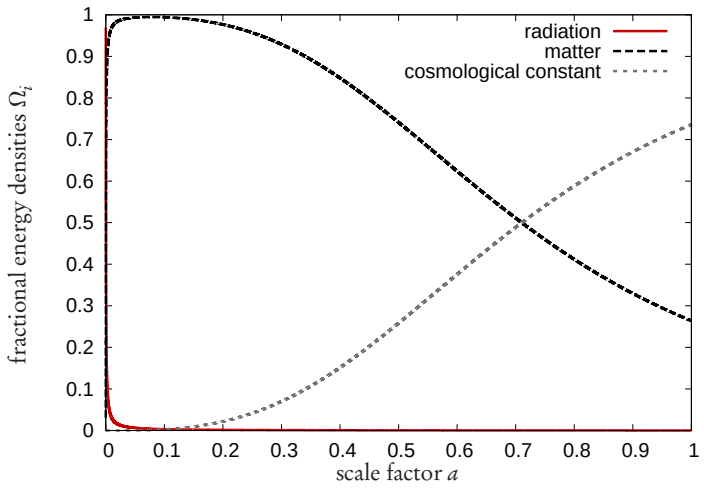

Figure 2.2: Late-time evolution of the fractional energy densities Ω_r, Ω_m, Ω_Λ.

Let us now turn to the thermal history where we mainly follow the presentation given by Mukhanov (2005, p. 72 et seqq.).

Planck epoch

When the temperature of the cosmic fluid was at $T \sim 10^{19}$ GeV, comparable to the Planck mass, the theory of general relativity is expected to break down. In particular, the classical notions of space and time become conceptually unclear. An extrapolation of the expansion from the radiation-dominated epoch would locate the Planck epoch at $t \sim 10^{-43}$ sec after the classical singularity. A detailed understanding would require a full quantum theory of gravity.

Grand Unification and electroweak epochs

$t \sim 10^{-43}$-10^{-10} sec, $T \sim 10^{2}$-10^{19} GeV. We may expect that the classical theory of general relativity works well. One often assumes grand unification of the strong and electroweak forces at energies around 10^{16} GeV, the *GUT scale*.

Near this scale, ending typically around $t \sim 10^{-32}$ sec, one expects the inflationary epoch. During this epoch, the hypothetical inflaton ϕ caused a rapid expansion of the Universe, accounting for its observed flatness and homogeneity, the dilution of possible relics of high-energy physics (such as magnetic monopoles), an increase of the particle horizon, and the seed of primordial perturbations. At the end of inflation, in a process called *reheating*, the energy density of the inflaton was transformed into Standard Model particles.

Until $T \sim 100$ GeV, the electroweak symmetry was restored, the W and Z gauge bosons were massless. Then, the electroweak phase transition took place breaking the

$SU(2) \times U(1)$ symmetry of the electroweak field.

Hadron epoch

$t \sim 10^{-6}$-1 sec, $T \sim$ 500-0.5 MeV. At around $T \approx 200$ MeV, the quark-gluon transition took place. Neutrinos leave thermal equilibrium at $T \sim$ 1-2 MeV; the primordial neutrinos decouple.

Nucleosynthesis

$t \sim$ 200-300 sec, $T \sim 0.05$ MeV. Light elements form from neutrinos and protons. The theory of big bang nucleosynthesis (BBN) predicts precise values for the abundances of light elements, which are confirmed by observations.

Recombination and last scattering

$t \sim 10^{12}$-10^{13} sec $\sim 300{,}000$ years, $T \sim 0.3$ eV, redshift $z \sim 1100$. Neutral hydrogen has formed from electrons and protons of the primordial plasma (*recombination*). The Universe became transparent, photons could travel freely and decoupled (*last scattering*). They form the cosmic microwave background radiation.

Structure formation

While the baryons were still tightly coupled to photons, cold dark matter already started to form increasing overdensities under the influence of gravity. After recombination, the baryons quickly fell into these potential wells. The overdensities eventually became the large-scale structure, galaxy clusters, and galaxies observable today.

2.2 Inhomogeneities

The expansion history is mainly, and most directly, probed by the observation of Type Ia supernovae (Riess et al., 1998; Perlmutter et al., 1999). This, however, constitutes only a very small fraction of the observationally accessible data. The most important probes are related to *inhomogeneities*, i. e. deviations from the homogeneous approximation of Sec. 2.1.

The observation of small temperature fluctuations $\Delta T/T \sim 10^{-5}$ in the cosmic microwave background radiation in satellite missions (Fixsen et al., 1996; Bennett et al., 2003; Hinshaw et al., 2003; Ade et al., 2013a) and balloon-based experiments (Netterfield et al., 2002; Jaffe et al., 2001) is extremely powerful in constraining cosmological models. The temperature fluctuations are mainly due to density perturbations in the primordial plasma. The observations, consequently, mainly probe cosmology at the time of recombination. After last scattering, the light propagated through the expanding Universe with its metric fluctuations and hence also carries information about the geometry, expansion history, and structure formation at later times (Durrer, 2008).

Galaxy surveys record the distribution of galaxies in the observationally accessible regions of the night sky (Colless et al., 2001; Cole et al., 2005; Tegmark et al., 2004a, 2006b). The galaxies' redshifts serve as a distance measure allowing to infer the three-dimensional distribution. The distribution of galaxies is expected to trace the inhomogeneities of baryons and thus ultimately of dark matter. The details of this relation depend on the complicated process of galaxy formation and are accounted for by *bias* models (Kauffmann et al., 1997; Peacock and Smith, 2000; Gao and White, 2007). A cleaner way to measure inhomogeneities is via *weak gravitational lensing* (Bartelmann and Schneider, 2001; Munshi et al., 2008). This method can, in principle, also be used to reconstruct the three-dimensional distribution of perturbations, either incompletely (Hu, 1999) or in a comprehensive approach (Heavens, 2003).

Regarding these powerful observations, it is far from sufficient for a cosmological model to produce the correct expansion history; it must pass observational constraints linked to inhomogeneities. The modeling and calculation of inhomogeneities will consequently occupy a large fraction of this thesis. In growing neutrino quintessence, the situation is even more involved. The expansion history is not decoupled from the evolution of perturbations. There is a decisive backreaction, which needs to be taken into account.

In this section, we will recall all necessary theoretical concepts and techniques that will be used in subsequent chapters. In the early Universe, in particular for understanding the CMB, one is in the lucky position that perturbations can be treated linearly, Sec. 2.2.1. Once, under the influence of the gravitational attraction or extra forces, the linear approximation breaks down, a switch to a nonlinear treatment is in order, Sec. 2.2.2. In our case, the backreaction of the inhomogeneities is essential. Finally, we present the well-established N-body technique to actually calculate the nonlinear growth of inhomogeneities in Sec. 2.2.3. This technique will be used, adapted, and enhanced in later chapters.

2.2.1 Linear perturbations

In linear perturbation theory, quantities A (e. g. energy densities) are decomposed into an average *background* value $\bar{A}(\tau)$ only depending on time and a perturbation $\delta A(x)$ depending on space and time. One assumes $\delta A(x) \ll 1$ such that expressions in δA can be linearized, neglecting all higher orders. Before we go into the details, we note three immediate technical advantages of this approach:

1. When averaging a linear expression $f(A) \approx f(\bar{A}) + f'(\bar{A})\,\delta A$, the perturbation term drops out because δA vanishes on average. In particular, if applied on Einstein's field equations, the averaged field equations will again give the simple Friedmann equations. Stated differently, their is a *background evolution* independent of perturbations; there is no backreaction effect. One can study the evolution of perturbations δA on a known background.

2. Spatial derivatives $\boldsymbol{\nabla}\delta A(\boldsymbol{x})$ are related to mere multiplications $i\boldsymbol{k}\delta A(\boldsymbol{k})$ in Fourier space. In linear equations, different modes $\boldsymbol{k}$, $\boldsymbol{k}'$ do not couple. We move

from differential equations to algebraic equations.

3. By the assumption of (statistical) isotropy, the evolution equations for the perturbations will not depend on the direction of the mode $\boldsymbol{k}$ but only on the absolute value $|\boldsymbol{k}|$. Consequently, the four-dimensional problem in $(\tau, \boldsymbol{x})$ is reduced to a two-dimensional problem in $(\tau, |\boldsymbol{k}|)$.

Linear perturbation theory on the expanding spacetime was developed by Lifschitz (1946) who already introduced the so-called *synchronous gauge* still widely used today. Important progress was made by a clear understanding of *gauging* and the introduction of a gauge-invariant formalism (Bardeen, 1980). A comprehensive and influential review article is due to Kodama and Sasaki (1984). We will, instead, mainly stick to the notations and the presentation of Mukhanov et al. (1992), a later review with an emphasis also on quantum perturbations (Mukhanov and Chibisov, 1981). For a pedagogical introduction, see Bertschinger (2001), for a comprehensive collection of main formulae, we refer to Ma and Bertschinger (1995).

Scalar metric perturbations

We start by considering the metric tensor $g_{\mu\nu}$ in linear perturbation theory,

$$g_{\mu\nu} = \bar{g}_{\mu\nu} + \delta g_{\mu\nu}. \tag{2.49}$$

We wish to consider perturbations as functions on the background spacetime, which is given by $\bar{g}_{\mu\nu}$. We will thus use the background metric $\bar{g}_{\mu\nu}$ for lowering and raising indices and for the definition of covariant derivatives.

Rather than keeping $\delta g_{\mu\nu}$ as ten independent functions (due to symmetry $\delta g_{\mu\nu} = \delta g_{\nu\mu}$), it is useful to start by classifying different sorts of metric perturbations. It is straightforward to collect the possibilities in which scalar, vector, and tensor quantities can enter into $\delta g_{\mu\nu}$. Four scalars ϕ, ψ, B, and E can be part of $\delta g_{\mu\nu}$. A general scalar metric perturbation (Mukhanov et al., 1992) then is

$$\delta g_{00} = -2a^2\psi, \quad \delta g_{0i} = \delta g_{i0} = -a^2 B_{,i}, \quad \delta g_{ij} = -2a^2\left(\phi\delta_{ij} - E_{,ij}\right) \tag{2.50}$$

equivalent to the line element

$$ds^2 = a^2\left[-(1+2\psi)d\tau^2 - 2B_{,i}\,d\tau\,dx^i + \left((1-2\phi)\delta_{ij} + 2E_{,ij}\right)dx^i dx^j\right]. \tag{2.51}$$

From the evolution equations of linear perturbations, it can be shown that only scalar metric perturbations lead to the growth of cosmic structure. Tensor perturbations decouple as gravitational waves and vector perturbations decay (Mukhanov et al., 1992). Hence, it is sufficient for us to only consider scalar perturbations.

Gauges

So far, we pretended that the split between background and perturbations was unproblematic. Yet, on a perturbed spacetime, there is no canonical way to define a background. Instead, many ways of *splitting* the spacetime into background and perturbations work equally well. They are related to each other by *gauge transformations*. Mathematically, these transformations correspond to infinitesimal changes in the (background) coordinates used to label points on the spacetime manifold,

$$x^\mu \mapsto \tilde{x}^\mu = x^\mu + \xi^\mu. \tag{2.52}$$

Even an unperturbed scalar quantity $A = \bar{A}$ would gather a perturbation after such a transformation, $A(x+\xi) = A(x) + \xi^\lambda \partial_\lambda A(x)$. In the same way, a perturbation could be gauged away by an appropriate opposite coordinate transformation. This is a possible area of confusion, which is resolved by formalizing the concept of gauges and by introducing gauge-invariant quantities.

Under a gauge transformation (2.52), the metric tensor transforms as

$$g_{\mu\nu} \mapsto \tilde{g}_{\mu\nu} = \frac{\partial x^\alpha}{\partial \tilde{x}^\mu} \frac{\partial x^\beta}{\partial \tilde{x}^\nu} g_{\alpha\beta}, \tag{2.53}$$

which can be linearized in ξ^μ and be rewritten for the perturbations (Mukhanov et al., 1992):

$$\delta g_{\mu\nu} \mapsto \widetilde{\delta g}_{\mu\nu} = \delta g_{\mu\nu} - \xi^\lambda \partial_\lambda \bar{g}_{\mu\nu} - \bar{g}_{\lambda\nu} \partial_\mu \xi^\lambda - \bar{g}_{\mu\lambda} \partial_\nu \xi^\lambda. \tag{2.54}$$

Decomposing the spatial components $\xi^i = \eta^i + \delta^{ij}\partial_j \zeta$ into a divergence free part, $\partial_i \eta^i = 0$, and the derivative of a scalar valued function ζ, we can ultimately rewrite Eq. (2.54) for the scalar metric perturbations (Mukhanov et al., 1992):

$$\tilde{\phi} = \phi + \frac{a'}{a}\xi^0, \quad \tilde{\psi} = \psi - \frac{a'}{a}\xi^0 - \xi^{0\prime}, \quad \tilde{B} = B + \xi^0 + \zeta', \quad \tilde{E} = E + \zeta, \tag{2.55}$$

where primes denote partial derivatives with respect to conformal time τ. The *Bardeen potentials* Ψ and Φ are combinations of the scalar metric perturbations, which are gauge-invariant,

$$\Psi \equiv \psi + \frac{1}{a}\left[a(B - E')\right]', \quad \Phi \equiv \phi - \frac{a'}{a}(B - E'). \tag{2.56}$$

For practical calculations, apart from conceptual studies, the gauge-invariant formulation of cosmological perturbation theory has never become the standard. The *synchronous* gauge, for historical reasons due to its early invention (Lifschitz, 1946) and due to minor numerical advantages, is still the most widely used gauge in so-called Boltzmann codes for calculating linear perturbations and CMB anisotropies, namely in CMBFAST and CAMB (Seljak and Zaldarriaga, 1996; Zaldarriaga et al., 1998; Lewis et al., 2000; Lewis and Bridle, 2002), although some codes provide facilities for other gauges

(Doran, 2005; Doran and Müller, 2004; Lesgourgues, 2011a,b). It sets $\psi = B = 0$. In this way, $\delta g_{00} = \delta g_{0i} = \delta g_{i0} = 0$, hence the name 'synchronous' — the time components of the metric are unperturbed. This does not entirely fix the gauge freedom. In CAMB, a specific synchronous gauge is chosen, namely such that the velocity perturbation of cold dark matter vanishes.

The second very frequently used gauge is the *conformal Newtonian* or *longitudinal* gauge setting $B = E = 0$. This does not only completely fix the gauge freedom, it has several important advantages. First, the remaining scalar metric fluctuations ϕ and ψ are then identical to the gauge-invariant Bardeen potentials Φ and Ψ. Second, in the Newtonian limit, Φ and Ψ both reduce to Newton's gravitational potential. This is very useful when mixing general-relativistic perturbation theory with Newtonian physics, e. g. when linear perturbation theory is matched to a Newtonian N-body calculation. In general, we will prefer the conformal Newtonian gauge and use its line element

$$ds^2 = a^2\left[-(1+2\Psi)d\tau^2 + (1-2\Phi)dx^2\right]. \tag{2.57}$$

For later reference, we collect the resulting Christoffel symbols

$$\Gamma^0_{00} = \frac{a'}{a} + \Psi', \quad \Gamma^0_{0i} = \Gamma^0_{i0} = \partial_i\Psi, \quad \Gamma^0_{ij} = \left[\frac{a'}{a}(1-2(\Psi+\Phi)) + \Phi'\right]\delta_{ij}, \tag{2.58}$$

$$\Gamma^i_{00} = \partial_i\Psi, \quad \Gamma^i_{0j} = \frac{a'}{a}\delta^i_j - \Phi'\delta^i_j, \quad \Gamma^i_{jk} = -\left(\partial_k\Phi\delta^i_j + \partial_j\Phi\delta^i_k\right) + \partial_i\Phi\delta_{jk}. \tag{2.59}$$

Evolution of linear perturbations

If we define the left-hand side of Einstein's equations as the Einstein tensor $G_{\mu\nu} \equiv R_{\mu\nu} - Rg_{\mu\nu}/2$, the linearly perturbed equations may be written as

$$\bar{G^\mu}_\nu = \bar{T^\mu}_\nu \quad \text{and} \quad \delta G^\mu{}_\nu = \delta T^\mu{}_\nu, \tag{2.60}$$

where the first equations are the usual Friedmann equations. For the perturbations (Mukhanov et al., 1992), we choose the conformal Newtonian gauge, which simplifies the general expressions, and find

$$\delta G^0{}_0 = \frac{2}{a^2}\left[-\Delta\Phi - 3\frac{a'}{a}\left(\Phi' + \frac{a'}{a}\Psi\right)\right], \tag{2.61}$$

$$\delta G^0{}_i = \frac{2}{a^2}\partial_i\left(\Phi' + \frac{a'}{a}\Psi\right), \tag{2.62}$$

$$\delta G^i{}_j = \frac{2}{a^2}\left[\left(2\left(\frac{a'}{a}\right)' + \left(\frac{a'}{a}\right)^2\right)\Psi + \frac{a'}{a}\Psi' + \Phi'' + 2\frac{a'}{a}\Phi' - \frac{1}{2}\Delta(\Phi-\Psi)\right]\times \delta^i_j + \frac{1}{a^2}\partial_i\partial_j(\Phi-\Psi). \tag{2.63}$$

The (scalar) perturbations of the energy-momentum tensor (Mukhanov et al., 1992) are written as

$$\delta T^0{}_0 = -\delta\rho, \tag{2.64}$$

$$\delta T^0{}_i = (\bar{\rho}+\bar{p})\, v_i, \tag{2.65}$$

$$\delta T^i{}_j = \delta p\, \delta^i_j + \Sigma^i{}_j, \tag{2.66}$$

with the density perturbation $\delta\rho$ (we will often use the density contrast $\delta \equiv \delta\rho/\rho$ instead), the peculiar velocity v_i, the pressure perturbation δp, and the anisotropic shear $\Sigma^i{}_j$, $\Sigma^i{}_i = 0$. If we work with the linearized Einstein's equations, we will transform them into Fourier space (Ma and Bertschinger, 1995) where they read

$$k^2\Phi_k + 3\frac{a'}{a}\left(\Phi_k' + \frac{a'}{a}\Psi_k\right) = -\frac{a^2}{2}\delta\rho_k, \tag{2.67}$$

$$k^2\left(\Phi_k' + \frac{a'}{a}\Psi_k\right) = \frac{a^2}{2}(\bar{\rho}+\bar{p})\, i\boldsymbol{k}\cdot\boldsymbol{v}_k, \tag{2.68}$$

$$\Phi_k'' + \frac{a'}{a}(\Psi_k' + 2\Phi_k') + \left(2\frac{a''}{a} - \frac{a'^2}{a^2}\right)\Psi_k + \frac{k^2}{3}(\Phi_k - \Psi_k) = \frac{a^2}{2}\,\delta p_k, \tag{2.69}$$

$$k^2(\Phi_k - \Psi_k) = \frac{3a^2}{2}(\bar{\rho}+\bar{p})\sigma_k, \tag{2.70}$$

with the scalar anisotropic shear perturbation σ_k defined by

$$(\bar{\rho}+\bar{p})\,\sigma_k \equiv -\left(\frac{k_i k_j}{k^2} - \frac{1}{3}\delta_{ij}\right)\Sigma^i_{kj}. \tag{2.71}$$

The expression $i\boldsymbol{k}\cdot\boldsymbol{v}_k$ might give the wrong impression of the above equations depending on the direction of $\boldsymbol{k}$. One can, however, express the peculiar velocity in terms of a scalar velocity perturbation, $kv_k \equiv i\boldsymbol{k}\cdot\boldsymbol{v}_k$.

Although the perturbed part of Einstein's equations completely determines the evolution of perturbations, it will prove useful to explicitly use the automatically satisfied energy-momentum conservation equation $\nabla_\nu T^{\mu\nu} = 0$. We introduce the short-hands $w \equiv \bar{p}/\bar{\rho}$ (the equation of state already known from the dynamics of expansion) and the *sound speed* $c_s^2 \equiv \delta p_k/\delta\rho_k$ (Ma and Bertschinger, 1995) and get

$$\delta_k' = -(1+w)\left(kv_k - 3\Phi_k'\right) - 3\frac{a'}{a}\left(c_s^2 - w\right)\delta_k, \tag{2.72}$$

$$v_k' = -\frac{a'}{a}(1-3w)v_k - \frac{w'}{1+w}v_k + \frac{c_s^2}{1+w}k\delta_k - k\sigma_k + k\Psi_k. \tag{2.73}$$

The last term in the second equation is the Newtonian gravitational attraction $\propto \boldsymbol{\nabla}\Psi$. Note that these equations refer to the density and velocity perturbation of the full

energy-momentum tensor of the cosmic fluid. In practice, one will instead decompose the cosmic fluid into its different components with special properties (such as known equation of state and sound speed). If the components are only coupled to each other via gravity, then they individually satisfy the energy-momentum conservation equation and, accordingly, also Eqs. (2.72) and (2.73) above. If there is an additional coupling, the energy-momentum conservation equation and thereby the perturbation equations are modified.

Spectra and random fields

Given initial perturbations at some conformal time τ_1 at all positions in space, the evolution equations for linear perturbations allow the propagation of these perturbations to any other conformal time τ_2. In practice, it is more convenient to look at this from another perspective. First, the evolution equations are independent of the direction of the Fourier mode $\boldsymbol{k}$, so it seems more appropriate to only evolve the equations for varying absolute value $k = |\boldsymbol{k}|$. Second, since the equations are linear, the evolution will not depend on the amplitude of the initial perturbations. We shall now see how to exploit these thoughts.

Formally, defining a vector $y^a_{\boldsymbol{k}}$ whose components a are all the scalar perturbation variables introduced above, the evolution equations may be written in the form

$$\frac{dy^a_{\boldsymbol{k}}}{d\tau} = M^{ab}_k(\tau) y^b_{\boldsymbol{k}}(\tau) \tag{2.74}$$

with a matrix $M^{ab}_k(\tau)$ depending on time and the absolute value $k = |\boldsymbol{k}|$. Note that different modes do not couple, the matrix product is only taken over the different perturbation variables. This differential equation is formally solved by applying a time evolution operator

$$F^{ab}_k(\tau_1 \to \tau_2) = \mathcal{T} \exp \int_{\tau_1}^{\tau_2} d\tau \, M^{cd}_k(\tau) \tag{2.75}$$

with the time ordering operator $\mathcal{T}$. If this matrix is known for all k, any initial perturbation at τ_1 can be evolved to τ_2 simply by applying this operator on $y^a_{\boldsymbol{k}}(\tau_1)$.

The Boltzmann codes typically used to evolve the linear equations, however, do not calculate the full matrix $F^{ab}_k(\tau_1 \to \tau_2)$. Rather, they reduce the necessary information to a vector by reducing the freedom we have in the initial perturbations $y^a_{\boldsymbol{k}}(\tau_1)$. Typically, we choose *adiabatic* conditions where the entropy perturbation between any two components vanishes. A choice of the type of initial conditions means to write

$$y^a_{\boldsymbol{k}}(\tau_1) = \eta^a \, \alpha_{\boldsymbol{k}}(\tau_1), \tag{2.76}$$

where $\alpha_{\boldsymbol{k}}(\tau_1)$ is scalar valued, and η^a contains the information relating different components to each other. From a linear code, one thus typically obtains solutions equivalent to the vector $F^{ab}_k(\tau_1 \to \tau_2)\eta^b$. Multiplying them with the initial scalar valued field $\alpha_{\boldsymbol{k}}(\tau_1)$ eventually yields the final perturbation variables $y^a_{\boldsymbol{k}}(\tau_2)$ at τ_2.

Cosmological models are not only applicable to a particular realization of primordial perturbations encoded in $\alpha_{\boldsymbol{k}}(\tau_1)$. Such a concrete realization cannot be theoretically predicted. Rather, the inflationary theory predicts statistical properties of these primordial perturbations, namely their two-point correlation

$$\left\langle \alpha_{\boldsymbol{k}} \alpha^*_{\boldsymbol{k}'} \right\rangle = (2\pi)^3 P_{\text{prim}}(k)\, \delta^3(\boldsymbol{k} - \boldsymbol{k}'). \tag{2.77}$$

Although the perturbed Universe is no longer homogeneous and isotropic, what we have assumed here is *statistical* isotropy (statistical averages cannot depend on direction). In this sense, the notions of homogeneity and isotropy also apply to the, strictly speaking, inhomogeneous Universe. We call $P_{\text{prim}}(k)$ the *power spectrum* of primordial perturbations.

The two-point correlation contains *all* the statistical information if the field α is a Gaussian random field. This is suggested to be a very good approximation according to observations (Bennett et al., 2012; Ade et al., 2013d); there are no clear observational hints for primordial *non-Gaussianity*. The condition for a random field $f_{\boldsymbol{k}}$ to be Gaussian are given by

$$\left\langle f_{\boldsymbol{k}_1} \cdots f_{\boldsymbol{k}_{2n}} \right\rangle = \sum_{\text{pairings}} \prod_{\text{pairs } i,j} \left\langle f_{\boldsymbol{k}_i} f_{\boldsymbol{k}_j} \right\rangle, \tag{2.78}$$

$$\left\langle f_{\boldsymbol{k}_1} \cdots f_{\boldsymbol{k}_{2n+1}} \right\rangle = 0. \tag{2.79}$$

All averages with an odd number of points vanish, and all averages with an even number of points reduce to two-point correlators (Weinberg, 2008). Since all cumulants above the first two vanish, the probability distribution for the real and complex parts of every $f_{\boldsymbol{k}}$ is indeed a Gaussian probability distribution. Stated differently, the absolute value $|f_{\boldsymbol{k}}|$ is Gaussian and its phase is (uniformly) random,

$$p(|f_{\boldsymbol{k}}|) = \frac{1}{\sqrt{2\pi \left\langle |f_{\boldsymbol{k}}|^2 \right\rangle}} \exp\left(-\frac{|f_{\boldsymbol{k}}|^2}{2 \left\langle |f_{\boldsymbol{k}}|^2 \right\rangle} \right). \tag{2.80}$$

We shall use this later to generate initial conditions for $\alpha_{\boldsymbol{k}}$. Of course, the above expression for the probability distribution p becomes ill-defined in the limit where the two-point correlator is a Dirac delta. In practice, we will discretize the fields moving from a Dirac delta to a Kronecker delta.

In addition to their role for initial conditions, two-point correlators are an essential tool to confront cosmological models with observational data, but also to analyze and to understand the evolution of cosmological perturbations. For perturbation variables $\delta A_{\boldsymbol{k}}$ and $\delta B_{\boldsymbol{k}}$, we generally define the power spectrum

$$\left\langle \delta A_{\boldsymbol{k}}\, \delta B^*_{\boldsymbol{k}'} \right\rangle = (2\pi)^3 P_{\delta A\, \delta B}(k)\, \delta^3(\boldsymbol{k} - \boldsymbol{k}'). \tag{2.81}$$

If $\delta A_{\boldsymbol{k}}$ and $\delta B_{\boldsymbol{k}}$ denote the same perturbation variable, $P_{\delta A\, \delta B}$ is the (auto-correlation) power spectrum, otherwise it is called the *cross-correlation* power spectrum. Let us

consider for now the auto-correlation spectrum and thus omit the index $\delta A\,\delta B$. Since the Dirac delta carries the unit of volume, the power spectrum is not dimensionless. It is often useful to define a dimensionless spectrum by

$$\Delta^2(k) = \frac{2\pi^2}{k^3} P(k). \tag{2.82}$$

This quantity allows for an intuitive interpretation. If we roughly relate the Fourier mode to a real scale R, $k \mapsto R \sim 1/k$, the dimensionless spectrum $\Delta^2(k)$ is typically comparable to the variance σ_R^2 of the perturbation variable averaged in a sphere of radius R,

$$\sigma_R^2 = \left\langle \left(\int d^3y\, W_R(\boldsymbol{x}-\boldsymbol{y}) \delta A(\boldsymbol{y}) \right)^2 \right\rangle, \tag{2.83}$$

where W_R is chosen to be a top hat spherical window function of radius R. Note that, due to statistical homogeneity, this definition is independent of the point $\boldsymbol{x}$.

2.2.2 Nonlinear regime

Once one of the dimensionless spectra — this will be the cold dark matter density perturbation (auto-correlation) spectrum $\Delta_c^2(k)$ — has grown to order unity, linear perturbation theory becomes problematic. Beyond linear theory, the evolution equations for different modes k will couple such that once $\Delta_c^2(k)$ has become large for one (typically large) k, this will have an effect on other scales as well. In the case of cold dark matter, this is of importance for precision calculations but not essential for understanding large-scale perturbations. In growing neutrino quintessence, however, the spectrum $\Delta_\nu^2(k)$ of neutrino density perturbations becomes large even on very large scales. Linear perturbation theory breaks down completely.

Hence, we have to go beyond the linear approximation. A fully nonlinear treatment of general relativity, as needed, e. g., for the collisions of black holes, can fortunately be avoided. The metric perturbations Φ and Ψ will remain small, and we will still be able to work with the linearly perturbed line element (2.57). The nonlinear treatment will thus focus on an appropriate description of the energy-momentum tensor. In this section, we will content ourselves with the introduction of a few basic concepts mainly following the presentation of (Bernardeau et al., 2002). The main task will in the end be numerical.

For the understanding of nonlinear cold dark matter clustering, it is sufficient to go to the Newtonian limit: slowly varying gravitational potentials (i. e. $|\Phi'| \ll |\boldsymbol{\nabla}\Phi|$), *subhorizon* scales (distances are assumed to be small against the Hubble scale), nonrelativistic particles (thereby no anisotropic shear perturbation and $\Phi = \Psi$). Furthermore, we will assume that the backreaction of the perturbations on the background is negligible. All these simplifications will become problematic or even invalid in growing neutrino quintessence.

Phase space and Eulerian dynamics

The hydrodynamical perturbation variables, i. e. the density perturbation $\delta\rho(\boldsymbol{x})$ and the peculiar velocity $\boldsymbol{v}(\boldsymbol{x})$, do not carry the full information of the cold dark matter distribution. Instead, they have already averaged out the 'microscopic' motion of the particles. A full description of cold dark matter particles requires the phase-space distribution function $f(x,p)=f(\tau,x^i,p_j)$, where we use $p^0=\sqrt{\boldsymbol{p}^2+m^2}$. Its evolution can be calculated from the continuity equation in phase space, which follows from particle conservation,

$$\frac{df}{d\tau}=\frac{\partial f}{\partial\tau}+\frac{\partial(f\,x'^i)}{\partial x^i}+\frac{\partial(f\,p_j')}{\partial p_j}=0. \tag{2.84}$$

The canonical momentum variable in the expanding Universe is given by $p_j=amv_j$, and its time derivative is given by the Newtonian equation of motion

$$\boldsymbol{p}'=-am\boldsymbol{\nabla}_x\Psi, \tag{2.85}$$

whereby we can rewrite the continuity equation to

$$\frac{\partial f}{\partial\tau}+\frac{\boldsymbol{p}}{am}\cdot\boldsymbol{\nabla}_x f-am\boldsymbol{\nabla}_x\Psi\cdot\boldsymbol{\nabla}_p f=0, \tag{2.86}$$

which is often called the Vlasov equation (Bernardeau et al., 2002) after a similar approach in plasma physics. The function f depends on time and the six coordinates of phase space. A direct numerical solution is therefore inappropriate. The N-body simulation method samples the phase-space distribution f with a finite number of particles and evolves them directly according to the equation of motion. The advantage compared to a six-dimensional grid is that the method automatically focusses on regions where many particles are located, i. e., where the density is high.

The transition to the language of Eulerian hydrodynamics is achieved by averaging out the microscopic motion of the particles. The energy density ρ, the peculiar velocity $\boldsymbol{v}$, and the stress tensor σ_{ij} appear as moments of the phase-space distribution,

$$\int d^3p\,f(\tau,\boldsymbol{x},\boldsymbol{p})=\rho, \tag{2.87}$$

$$\int d^3p\,\frac{p_j}{am}f(\tau,\boldsymbol{x},\boldsymbol{p})=\rho\,v_j, \tag{2.88}$$

$$\int d^3p\,\frac{p_i\,p_j}{(am)^2}f(\tau,\boldsymbol{x},\boldsymbol{p})=\rho\,v_i\,v_j+\sigma_{ij}. \tag{2.89}$$

We stop here with the second moment of f. This relies on the hope that there will be some hierarchy predicting that the additional higher-order tensors of higher moments are small compared to the first moments and can be set to zero or parameterized effectively. Taking the zeroth and first moments of the continuity equation (2.86) yields

the real-space continuity equation for the energy density and the Euler equation for the peculiar velocity,

$$\rho' = -\boldsymbol{\nabla}\cdot(\rho\boldsymbol{v}), \tag{2.90}$$

$$\boldsymbol{v}' = -\frac{a'}{a}\boldsymbol{v} - \boldsymbol{v}\cdot\boldsymbol{\nabla}\boldsymbol{v} - \boldsymbol{\nabla}\Psi - \frac{1}{\rho}\partial_j(\rho\sigma_{ij}). \tag{2.91}$$

In order to close these equations, a parameterization for σ_{ij} is needed. One may introduce pressure and viscosity coefficients (Bernardeau et al., 2002). Recalling the definition of σ_{ij}, we see that it is a measure of the variance of the microscopic velocities. Denoting the average momentum of the particles located at the same position $\boldsymbol{x}$ by $\bar{p}_j$, we get from Eq. (2.89):

$$\sigma_{ij} = \int d^3p \frac{(p_i - \bar{p}_i)(p_j - \bar{p}_j)}{a^2m^2} f(\tau, \boldsymbol{x}, \boldsymbol{p}) = \rho \left\langle v_{\mathrm{micro},i}(\boldsymbol{x}) v_{\mathrm{micro},j}(\boldsymbol{x}) \right\rangle_f, \tag{2.92}$$

defining the microscopic velocity $\boldsymbol{v}_{\mathrm{micro}}$ as the difference between the total and the peculiar velocity of the particle. We shall later see that the stabilization of nonlinear structures is linked to a balance between this microscopic velocity dispersion and attractive forces. An ad-hoc ansatz for σ_{ij} will thus not be appropriate for studying nonlinear structure formation until the stabilization of structures. In growing neutrino quintessence, a detailed treatment of stable neutrino structures will be crucial for the understanding of the model's cosmological evolution. For this reason, we will not go into the details of semi-analytical methods for nonlinear structure formation or perturbation theory. Many approaches can be found in the recent literature (cf., e. g., Crocce and Scoccimarro, 2006; McDonald, 2007; Jeong and Komatsu, 2006; Matarrese and Pietroni, 2007; Pietroni, 2008). Since they include approximations whose errors can hardly be estimated analytically, their accuracy is investigated by a comparison with numerical N-body simulations (Carlson et al., 2009).

Backreaction

Cosmological *backreaction* is the influence of perturbations on the expansion of the background. So far, we have assumed the Friedmann equations to be valid for the background on which perturbations evolve. Formally, this means that we have used the FLRW metric to define the background Einstein tensor on the left-hand side of Einstein's equations. We now formalize this by means of volume averages. Let $\langle A\rangle$ denote the average of a scalar quantity A in a very large cosmological domain D,

$$\langle A\rangle \equiv \frac{\int_D d^3x\,\sqrt{-g}\,A(x)}{\int_D d^3x\,\sqrt{-g}}. \tag{2.93}$$

We expect this expression to converge for very large D such that the concrete domain will not matter. For vectors and tensors, one would, in principle, need to be more careful to preserve their transformation properties. We shall neglect this subtlety for

our discussion. The FLRW metric then is the average $\langle g_{\mu\nu}\rangle$ of the perturbed metric. Our approach to evaluate the background evolution may be stated as the ansatz

$$G_{\mu\nu}(\langle g_{\alpha\beta}\rangle) = \langle T_{\mu\nu}\rangle. \tag{2.94}$$

Formally averaging over Einstein's field equations, however, would have given the average $\langle G_{\mu\nu}(g_{\alpha\beta})\rangle$. Obviously, the two ways of averaging are identical if perturbations are treated linearly. If nonlinear perturbations are present, we have

$$G_{\mu\nu}(\langle g_{\alpha\beta}\rangle) \neq \langle G_{\mu\nu}(g_{\alpha\beta})\rangle. \tag{2.95}$$

The correct way of obtaining the evolution of the averaged background quantities would be to first evolve the full equations and to average in the end. The simplified method widely used consists in first averaging and then evolving. These processes are visualized in Fig. 2.3. The study of the cosmological backreaction effect is motivated

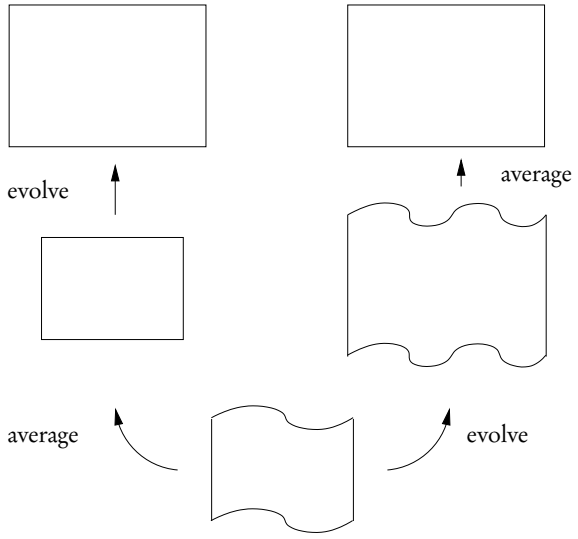

Figure 2.3: Schematic, expanding cosmological domain with metric perturbations.

by the question up to which precision averaging and time evolution commute.

Until today, one of the main motivations to investigate cosmological backreaction is the idea that nonlinear structure formation significantly modifies the observed expansion of the Universe, perhaps even removing the need for a cosmological constant, dark energy, or a modification of gravity (Rasanen, 2010; Marra, 2008; Buchert and Rasanen, 2012; Ellis, 2011). There are even claims that the backreaction effect could not only account for the accelerated expansion but replace even dark matter and the inflaton (Buchert, 2010). These ideas seem very optimistic if not implausible since the inhomogeneity of spacetime is expressed by the scalar potentials Φ and Ψ, which are, even during nonlinear structure formation, small. One would naively expect only

small corrections to averaged quantities if the backreaction is properly taken into account. This is also supported by careful estimates (Wetterich, 2003; Behrend et al., 2008).

We will in few words review the standard approach of treating cosmological backreaction, namely Buchert's equations (Buchert, 2000; Rasanen, 2006). Defining a local expansion rate H_{loc} quantifying the expansion of a small, local volume, Buchert (2000) derives a local version of the Friedmann equations (2.19) and (2.20) for a universe filled with dust, i. e. $p = 0$,

$$H_{\mathrm{loc}}^2 + \dot{H}_{\mathrm{loc}} = -\frac{\rho}{6} - \frac{\Sigma^2}{3}, \tag{2.96}$$

$$H_{\mathrm{loc}}^2 = \frac{\rho}{3} - \frac{{}^{(3)}R}{6} + \frac{\Sigma^2}{3}, \tag{2.97}$$

together with the energy-momentum conservation equation

$$\dot{\rho} + 3H_{\mathrm{loc}}\rho = 0. \tag{2.98}$$

The quantity Σ^2 originates from the fact that the local expansion is, in general, anisotropic and described by an expansion tensor Θ_{ij}, which is decomposed into an average expansion H_{loc} and a traceless part Σ_{ij}, namely $\Theta_{ij} = H_{\mathrm{loc}} g_{ij} + \Sigma_{ij}$. Buchert (2000) then defines the scalar $\Sigma^2 \equiv \Sigma^i{}_j \, \Sigma^j{}_i / 2$. Performing the spatial averaging, Eq. (2.93), yields Buchert's equations describing the evolution of the background in the presence of inhomogeneities,

$$\frac{\ddot{a}}{a} = \frac{d\langle H_{\mathrm{loc}}\rangle}{dt} + \langle H_{\mathrm{loc}}\rangle^2 = -\frac{\langle\rho\rangle}{6} + \frac{\mathcal{Q}}{3}, \tag{2.99}$$

$$\left(\frac{\dot{a}}{a}\right)^2 = \langle H_{\mathrm{loc}}\rangle^2 = \frac{\langle\rho\rangle}{3} - \frac{\langle{}^{(3)}R\rangle}{6} - \frac{\mathcal{Q}}{6}, \tag{2.100}$$

$$\frac{d\langle\rho\rangle}{dt} = -3\frac{\dot{a}}{a}\langle\rho\rangle, \tag{2.101}$$

$$\mathcal{Q} = 6\left(\langle H_{\mathrm{loc}}^2\rangle - \langle H_{\mathrm{loc}}\rangle^2\right) - 2\langle\Sigma^2\rangle, \tag{2.102}$$

which specialize to the usual Friedmann equations for $\mathcal{Q} = 0$.

Although we do not adopt the assumption that the correction terms to the Friedmann equations are quantitatively important, we do recognize the conceptual insights provided by a careful averaging procedure. Buchert's equations show that, in principle, the expansion can be modified due to inhomogeneities. In growing neutrino quintessence, this effect will be very important. It will, however, not be due to metric perturbations but rather visible in the coupling term between the dark energy scalar field and the cosmic neutrinos.

2.2.3 The N-body technique

In the presence of nonlinear clustering, the only comprehensive, established, and reliable method is an N-body based evolution of the Vlasov equation (2.86) by numerical

algorithms. In the cosmological concordance model, this is required only for understanding small scales whereas large scales are still reasonably well described by linear perturbation theory or mild nonlinear corrections (Bernardeau et al., 2002). Stable, virialized, highly nonlinear structures are not well understood (semi-)analytically although they are accurately described by computer simulations. For instance, computer simulations show an approximately universal dark matter halo profile, the Navarro-Frenk-White (NFW) profile due to Navarro et al. (1996) of the form

$$\rho(r) = \frac{\rho_0}{\frac{r}{R}\left(1+\frac{r}{R}\right)^2}. \tag{2.103}$$

So far, no generally accepted analytical argument has been given that predicts this universal profile.

In growing neutrino quintessence, we will see that the cosmological evolution, even if we consider only the expansion history or large-scale perturbations, will crucially depend on the properties of virialized neutrino structures. Due to relativistic neutrino velocities, the physics of these structures is even more involved than for cold dark matter halos. If even the latter are not well understood analytically, we may not expect to quantitatively describe the cosmological evolution of growing neutrino quintessence without numerical simulations.

The N-body simulation method for nonlinear clustering consists in sampling the phase-space distribution function $f(\tau, \boldsymbol{x}, \boldsymbol{p})$ with a finite number N_p of effective particles. Rather than evolving the Vlasov equation (2.86) explicitly, one evolves the equations of motion (2.85) for each effective particle together with the gravitational potential Ψ. Here, we will briefly review the N-body method for the simulation of cold dark matter. We will later extend the concept to also simulate neutrino clustering in growing neutrino quintessence.

The basic principles of N-body simulations are known to astronomers since a long time, and the main techniques still in use today have matured in the 1990s and are summarized by Bertschinger (1998). In terms of numerical performance and accuracy, considerable progress has been made since then until today's state-of-the art simulations (Kuhlen et al., 2012) like GADGET (Springel, 2005). Our presentation will follow Bertschinger (1998); Knebe (2004); Klypin (2000); Trenti and Hut (2008). Examples of N-body simulations including extra forces that have some similarities with the simulation methods developed for growing neutrino quintessence include Zhao et al. (2010); Li and Barrow (2011). The question whether the N-body method really converges to a full solution of the Vlasov equation in the limit of a very large number of particles is not entirely settled (Marcos, 2008) but will be assumed in this thesis.

For N_p nonrelativistic particles, the energy-momentum tensor (2.41) vanishes except for the 0-0 component

$$\rho(\boldsymbol{x}) = -T^0{}_0 = \sum_{p=1}^{N_p} m_p\, \delta^3(\boldsymbol{x} - \boldsymbol{x}_p). \tag{2.104}$$

This density field sources the Newtonian gravitational potential, which is, in the Newtonian limit, given by Poisson's equation

$$\Delta\Psi(\boldsymbol{x}) = \frac{a^2}{2}\,\rho(\boldsymbol{x}). \tag{2.105}$$

The so-called *particle-mesh* (PM) method solves this equation on a grid $\{\boldsymbol{x}_i\}$ of N_c (comoving) cells. The obvious alternative is to calculate the force on particle p directly as a sum over two-body forces,

$$\boldsymbol{F}_p = -\frac{1}{8\pi}\sum_{p\neq q}\frac{m_p\, m_q}{a^2\,|\boldsymbol{x}_p - \boldsymbol{x}_q|^3}(\boldsymbol{x}_p - \boldsymbol{x}_q), \tag{2.106}$$

called the *particle-particle* (PP) method. At first sight, this method seems very inelegant from a numerical perspective. Solving Poisson's equation after a Fast Fourier Transform (FFT), $-k^2\Psi_{\boldsymbol{k}} = a^2\rho_{\boldsymbol{k}}/2$, requires only $\mathcal{O}(N_c\,\log N_c)$ numerical operations. Moreover, the gradients are obtained essentially for free in Fourier space since they are given by a mere multiplication with $i\boldsymbol{k}$. The direct two-body force summation instead will require $\mathcal{O}(N_p^2)$ operations. Still, the immediate advantage of the PP method is that the force resolution is not limited by the grid resolution. The method automatically focusses on regions where more particles are located, providing numerical precision where it is needed.

The combination of both methods can provide both numerical performance and a high force resolution. These hybrid methods are called particle-particle particle-mesh (P^3M) techniques. The large-scale forces are calculated on a grid whereas short-range forces are obtained from a particle summation. The sophistication then lies in the matching between these two regimes. Another option to boost the PP method is to group particles together thereby reducing the number of summations.

In a pure PM method, the particles effectively have the size of a grid cell since smaller scales are left unresolved. In a PP method, the particles are, in principle, point-sized, which leads to possible divergences in the force law. One thus has to introduce a physical smoothing scale Δr again fixing some effective particle size.

The grid resolution in the PM method can be improved dramatically by switching from a fixed grid to an adaptive mesh. Thereby, the resolution can be refined where needed. The disadvantage is that the FFT is restricted to a Cartesian grid. One has to move to more complicated and numerically more expensive methods for solving Poisson's equation.

A simpler method to at least moderately increase the effective resolution is a subgrid interpolation. A particle is then not assigned to the closest grid point. Instead, its mass is distributed to the eight surrounding grid points in a linear manner (*cloud in cell*, CIC, method). Analogously, the gravitational force is trilinearly interpolated from the eight surrounding grid points to the precise location of the particle.

We now turn to the evolution equations for the particles, which read

$$\boldsymbol{x}_p' = \boldsymbol{v}_p, \quad \boldsymbol{v}_p' = -\nabla\Psi(\boldsymbol{x}_p) \tag{2.107}$$

where primes again denote derivatives with respect to conformal time τ and Ψ is a function of all particle positions and masses $\{\boldsymbol{x}_p, m_p\}$. In principle, one could solve these differential equations for all particles by standard techniques like Runge-Kutta rules. These, however, require several evaluations in each step such that particle positions and velocities must be saved several times. Given the large amount of data, it is much more convenient to employ an integration scheme where the positions and velocities need only be known once. A standard technique is the *leapfrog integration scheme* which iterates

$$\boldsymbol{x}_p(\tau + \Delta\tau/2) = \boldsymbol{x}_p(\tau) + \boldsymbol{v}_p(\tau)\frac{\Delta\tau}{2}, \tag{2.108}$$

$$\boldsymbol{v}_p(\tau + \Delta\tau) = \boldsymbol{v}_p(\tau) - \boldsymbol{\nabla}\Psi(\boldsymbol{x}_p(\tau + \Delta\tau/2))\Delta\tau, \tag{2.109}$$

$$\boldsymbol{x}_p(\tau + \Delta\tau) = \boldsymbol{x}(\tau + \Delta\tau/2) + \boldsymbol{v}_p(t + \Delta\tau)\frac{\Delta\tau}{2}. \tag{2.110}$$

This simple scheme is a second-order symplectic integrator and thus very well adapted to the needs of a cosmological N-body simulation.

3 The cosmological constant problem

A positive cosmological constant starting to dominate the energy budget of the Universe today,

$$\rho_\Lambda = 3H_0^2\Omega_\Lambda, \quad \Omega_\Lambda \approx 2/3, \tag{3.1}$$

is compatible with all major observational probes (Bennett et al., 2012; Tegmark et al., 2006b; Percival et al., 2010; Oguri et al., 2012; Riess et al., 2007; Kowalski et al., 2008; Ade et al., 2013c). Its simplicity on the one hand and its success in passing observational constraints on the other are solidifying its role in the emerging 'standard model' of big bang cosmology (Bartelmann, 2010b). And Λ is not a stranger to theorists. The cosmological constant was introduced as a parameter to general relativity by Einstein (1917), shortly after the theory's formulation. Furthermore, a non-vanishing energy density of the vacuum is expected in quantum field theories. Such an energy density would constitute a contribution to the cosmological constant. Why should we be dissatisfied with this successful story?

Besides the general importance in science to question the standard paradigms and to investigate alternatives, there is a particular reason why many cosmologists mistrust the cosmological constant scenario. The cosmological constant, expressed in particle physics units, is extremely small compared to fundamental mass scales,

$$\rho_\Lambda^{1/4} \sim 10^{-12}\,\mathrm{GeV} \ll M_P,\, M_\mathrm{EW},\, M_\mathrm{QCD}, \tag{3.2}$$

with the (reduced) Planck scale $M_P \approx 2 \times 10^{18}$ GeV, the electroweak scale $M_\mathrm{EW} \approx 2 \times 10^2$ GeV, and the QCD scale $M_\mathrm{QCD} \approx 2 \times 10^{-1}$ GeV. As we shall argue in Sec. 3.1, we would expect the above scales to enter the value of Λ. One might argue that such expectations are not *predictions*. Our fundamental theories, e. g., do not predict the particle masses or coupling constants in the Standard Model of particle physics. Rather, these quantities are inferred from experiments. The same is true, in principle, for the cosmological constant. The difference lies in the concept of *naturalness*. Let us illustrate this with the help of a very simple and well-known example: the self-energy of the electrostatic field around an electron interpreted as a mass

$$m = \frac{1}{2}\int_{|x|>r_e} d^3x\,|\boldsymbol{E}|^2 = \frac{e^2}{8\pi r_e}, \tag{3.3}$$

evaluated according to the rules of classical electrodynamics. For a radius $r_e \to 0$, this quantity diverges. We will see a similar behavior for the expected value of the cosmological constant if we assume quantum field theory to be valid on arbitrarily small scales. To be intellectually honest, we have to assume that classical electrodynamics

breaks down, at the latest, where quantum effects become important. In order to obtain a scale, we choose the Compton wavelength and set $r_e \sim 1/m$. From this, we obtain the expectation

$$e^2 \sim 8\pi \quad \text{or} \quad \alpha \equiv \frac{e^2}{4\pi} \sim 1. \tag{3.4}$$

This very rough estimate is not in good agreement with the actual value $\alpha \approx 1/137$, but the disagreement is not dramatic. The scale seems to be 'natural'. The case for the cosmological constant is extremely different. We conclude: Although our theories do not provide a prediction for Λ, we should still be puzzled by its tiny value.

Weinberg (1987, 1989) noted, however, that — looking at it from a different perspective — we should not be too astonished that the cosmological constant is tiny. If it was much larger than the observed value, its energy density $\rho_\Lambda = \text{const.}$ would have overtaken the matter density $\rho_m \propto a^{-3}$ much earlier in cosmic history. In a Λ-dominated universe ($\Omega_\Lambda \approx 1$), linear (subhorizon) matter perturbations decay (Amendola and Tsujikawa, 2010, p. 303) as

$$\frac{d^2\delta_m}{(d\log a)^2} + 2\frac{d\delta_m}{d\log a} \approx 0. \tag{3.5}$$

If the linearly evaluated density contrast has not, before this decay, reached the critical value $\delta_m \approx 1.69$ (Weinberg, 2008, p. 424), where the nonlinear evolution decouples the collapsing overdensity from the background expansion, no nonlinear structures and, eventually, no galaxies, stars, and planets will have formed. Such a universe would be empty of observers. There would be no physicist feeling comfortable with the more natural value of Λ. With this argument, Weinberg (1987) calculated, for a positive cosmological constant, the rough upper bound

$$\rho_\Lambda \lesssim 10^3 \rho_{\Lambda,\text{obs}}, \tag{3.6}$$

three orders of magnitude larger than the observationally inferred value. Although there still is a considerable discrepancy, this estimate is much closer to the observation than the estimate from fundamental mass scales. Recent refined and very careful calculations suggest a bound much closer to the observational value, both for positive and negative cosmological constants (Tegmark et al., 2006a). As a conceptual improvement, this calculation is not searching for a strict upper bound for Λ compatible with the evolution of life but merely derives a probability distribution with the help of the anthropic principle discussed later.

At first, this merely is an observation but no explanation. Yet, there is a scenario in which the above observation is promoted to a potential explanation for the tiny value of Λ. Such a scenario is:

1. there is a physical mechanism giving rise to the existence of many universes[1];

[1] We keep the expression 'universe' vague here. In the context of inflation, we will use the term to denote *pocket universes* within the inflationary *multiverse*. These pocket universes are just independently evolving regions within the same space-time manifold. In the terminology of Tegmark (2007), they form a *level I* multiverse

2. these universes differ (among, possibly, other things) in the value of the cosmological constant;

3. in some universes, the cosmological constant is such that it allows for the existence of observers.

On a global level, there would be a distribution of different values of Λ depending on the particular universe. From this 'bird perspective', there would not necessarily be a cosmological constant problem. However, all observers measuring values of the cosmological constant would find values consistent with their existence (*anthropic selection*). The cosmological constant problem would be present seen from this 'frog perspective' (adopting the terminology from Tegmark, 2007). The idea is illustrated in Fig. 3.1. Remarkably, a multiverse scenario of the required type is known to cosmol-

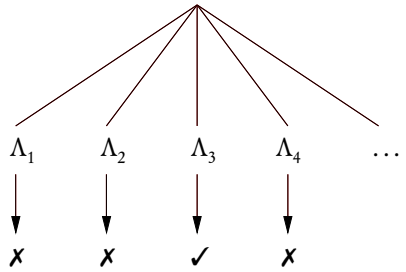

Figure 3.1: Illustration of the anthropic selection mechanism. Only in those realizations with a sufficiently small value of the cosmological constant, observers can exist (indicated by a check mark).

ogists, namely *eternal inflation* (Guth, 2007), which generically arises in a large class of inflationary models (Vilenkin, 1983). Since the theory of inflation is very successful and part of the current standard paradigm in the science of cosmology (cf., e. g., Weinberg, 2008; Mukhanov, 2005), the discussion of eternal inflation and its possible implication for the cosmological constant is in order. We will briefly describe this reasoning in Sec. 3.2.2. The simplest and most predictive models of inflation, however, use a scalar field — the inflaton ϕ — evolving under the rules of quantum field theory and general relativity, assuming that the cosmological constant Λ is irrelevant for the description of inflation. For this to work, the primordial cosmological constant would need to be much below the energy scale of inflation. A severe problem for the tentative explanation of the small observed value of Λ with the help of eternal inflation is the *measure problem*. In our suggestive illustration, Fig. 3.1, it is tempting to just compare the number of cases with a sufficiently small Λ (allowing for the existence of observers) with the number of cases where Λ is too large. Yet, we will see that, as these numbers go to infinity (which is the case for eternal inflation), this naive procedure does not work, and there is no canonical solution.

Although the anthropic line of argument is, with the above-mentioned restrictions, logically viable, it leaves open many questions. It essentially states that very unlikely coincidences can happen because we have to take into account the *selection bias* due to

our role as observers. Still, there might be a fundamental mechanism actually *explaining* the coincidence physically rather than statistically. Usually, the two approaches, anthropic selection on the one side and physical explanation on the other, are regarded as opposites. We wish to emphasize, as a side note, that this need not be the case. It is possible to study both ideas in a unified framework. Let us assume that there is a possible mechanism adjusting the cosmological constant dynamically (to, say, exactly zero). We further assume that the theory space populated by eternal inflation is large enough to allow for both, universes where the cosmological constant is adjusted to zero and universes where the cosmological constant is essentially a free parameter. Then, one could apply anthropic selection to find out where a random observer is most likely located, see Fig. 3.2. The observers located in universes where the physical

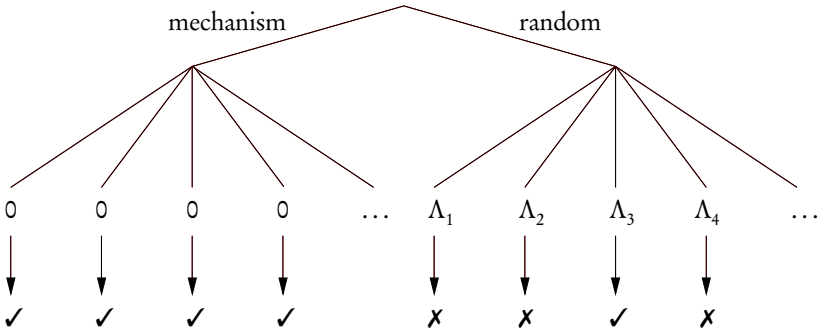

Figure 3.2: A physical mechanism adjusting Λ could, in a unified picture, be preferred by anthropic selection.

mechanism works could outnumber the observers living in the rare universes where Λ is sufficiently small just by chance. In this case, we would expect (according to the self-sampling assumption and the principle of mediocrity introduced in Sec. 3.2.1) to belong to the first group. Studying such a scenario is beyond the scope of this thesis. We just note that, even with anthropic selection, physical explanations rather than pure coincidences can turn out more successful. This line of argument is not only applicable to the cosmological constant problem, and it tells us that, even if the anthropic principle is taken seriously, it is still essential to look for physical explanations for apparent coincidences.

We will not discuss the innumerable mechanisms that have been proposed to resolve the cosmological constant problem (for some incomplete surveys, cf. Martin, 2012; Amendola and Tsujikawa, 2010; Carroll, 2001; Garriga and Vilenkin, 2001; Weinberg, 1989, and references therein). One particular mechanism, however, is of interest for the work in this thesis and should not pass unmentioned. It not only leads to a vanishing of the cosmological constant, it also gives rise to a dark energy scalar field, the cosmon φ, and motivates some of its properties, such as a flat and asymptotically vanishing scalar potential $V(\varphi)$ (Wetterich, 1988, 2009, 2010). Higher-dimensional dilatation symmetry implies a vanishing of the cosmological constant in four dimensions. The spontaneously broken dilatation symmetry then gives rise to a Goldstone boson, which

is — in the presence of a dilatation anomaly — in fact a massive pseudo-Goldstone boson. This will be the dark energy scalar field. For a comprehensive discussion of the mechanism and cosmologically relevant questions, we refer the reader to Wetterich (2008).

3.1 Expected contributions to Λ

If we wish to take the cosmological constant problem seriously, we should first clarify what known physics tells us about the cosmological constant. We shall see that the cosmological constant problem cannot be reduced to a problem of solely general relativity or of solely quantum fluctuations in quantum field theory. In fact, the cosmological constant problem is linked to several distinct effects. These include the free parameter of general relativity (the 'true' cosmological constant), contributions from the quantum vacuum, but also contributions from classical field configurations linked to phase transitions in the early Universe. In the following, we write the observable, effective value of the energy density of the cosmological constant as

$$\rho_\Lambda = \rho_{\Lambda_G} + \sum_i \rho_{\text{vac}}^{(i)} \tag{3.7}$$

with a parameter Λ_G from gravity and various contributions $\rho_{\text{vac}}^{(i)}$ to the vacuum energy. We will discuss the latter in the following subsections. As mentioned in Sec. 2.1.2, it is not clear which value to expect for the purely gravitational parameter Λ_G. If general relativity was a fundamental theory of gravity, a vanishing of Λ_G would seem most natural as it makes the theory both simpler and scale free. If we interpret general relativity instead as an effective theory, we must be prepared that all terms compatible with the symmetries of the theory can be present. In this case, $\Lambda_G \neq 0$ may be expected. If we further assume that the fundamental theory, presumably a quantum theory of gravity, includes the Planck scale as a fundamental scale, one might even find it natural to expect $\rho_{\Lambda_G} \sim M_P^4$ already at this stage.

We shall see that, although no predictions can be made, the natural scales expected to enter the contributions $\rho_{\text{vac}}^{(i)}$ by far exceed the observationally inferred value (Bennett et al., 2012; Ade et al., 2013c) of the cosmological constant,

$$\rho_\Lambda \sim 10^{-47}\,\text{GeV}^4, \tag{3.8}$$

if we attribute the observed accelerated expansion and the missing energy density for the observed spatial flatness of the Universe to a cosmological constant Λ.

By our discussion of the (well-known) expected contributions to the cosmological constant, we wish to emphasize two points that often remain unsaid in purely cosmological treatments. First, we want to clarify that the cosmological constant problem is a hard problem. Since the expected contributions to the cosmological constant originate from very different effects, it is not sufficient to hope that one particular contribution, e. g. the quantum fluctuations in quantum field theory, drops out. Potential solutions

to the cosmological constant problem must address several distinct effects at once. Ad-hoc solutions are probably not enough.

Second, if we take the known physics of the vacuum seriously and thus expect contributions to the cosmological constant, the alluring idea to just postulate a vanishing of the cosmological constant is problematic. In the presence of various contributions that add up to the observable value of Λ, the value $\Lambda = 0$ is not better from a fine-tuning perspective than the tiny positive value assumed in the cosmological concordance model. Instead, phenomenological models that work with $\Lambda = 0$ as a working hypothesis — this concerns works on dark energy and modified gravity — rely on the assumption of a physical mechanism leading to a vanishing of the cosmological constant. As long as the ideas for potential mechanisms of this kind are speculative, the phenomenological models based on them are speculative as well. It is tempting to argue that, although unknown, we must expect that a physical cancellation mechanism leading to a tiny or vanishing cosmological constant is at work. Doran and Jäckel (2002) write:

> "After all, this mechanism must be there, for the observed cosmological constant is far less than the naively calculated $\mathcal{O}(M_P^4)$."

Although there obviously is some cancellation in the value of Λ, there does not need to be a cancellation *mechanism*. We shall see that within eternal inflation, e. g., a tiny value of Λ could find a potential statistical explanation related to the anthropic principle.

In our brief discussion of the different contributions $\rho^{(i)}_{\text{vac}}$, we will closely follow Martin (2012), a pedagogical and fairly comprehensive review.

3.1.1 Quantum fluctuations

The expectation that the cosmological constant should be comparable to the Planck scale, $\rho_\Lambda \sim M_P^4$, is typically attributed to the zero-point energy in quantum field theories (cf., e. g. Copeland et al., 2006). Let us briefly recall the standard argument. We choose a very simple quantum field theory, namely a free massive scalar field χ with Lagrangian

$$\mathcal{L}_\chi = -\frac{1}{2}\partial^\lambda \chi \, \partial_\lambda \chi - \frac{1}{2} m^2 \chi^2 \tag{3.9}$$

in Minkowski space. The argument does not fundamentally change if we go to fermions or vector bosons, or if we consider field theory on curved spacetime (Martin, 2012). As usual, we may expand the field in Fourier space

$$\chi(x) = \int \widetilde{dk} \, \left(a_k e^{ik\cdot x} + a_k^\dagger e^{-ik\cdot x} \right) \tag{3.10}$$

with the invariant momentum-space measure

$$\widetilde{dk} \equiv \frac{d^4k}{(2\pi)^4} 2\pi \, \delta(k^2 + m^2) \Theta(k^0) = \frac{d^3k}{(2\pi)^3 \, 2\omega_k} \tag{3.11}$$

and $\omega_k \equiv k^0 = \sqrt{\boldsymbol{k}^2 + m^2}$. We impose the commutation relations

$$[a_{\boldsymbol{k}}, a_{\boldsymbol{k}'}] = (2\pi)^3\, 2\omega_k\, \delta^3(\boldsymbol{k} - \boldsymbol{k}') \tag{3.12}$$

for the annihilation and creation operators. The energy density of the scalar field is given by the Hamiltonian $\mathscr{H}_\chi$ obtained by the Legendre transform

$$\mathscr{H}_\chi = \pi\dot{\chi} - \mathscr{L}_\chi \tag{3.13}$$

with the canonical momentum $\pi = \partial\mathscr{L}_\chi/\partial\dot{\chi} = \dot{\chi}$. If $|0\rangle$ denotes the vacuum state, i. e. $a_{\boldsymbol{k}}|0\rangle = 0$, the vacuum expectation value of the Hamiltonian can be interpreted as the zero-point energy of the field χ,

$$\rho^\chi_{\text{vac}} = \langle 0|\mathscr{H}_\chi|0\rangle = \frac{1}{(2\pi)^3}\frac{1}{2}\int d^3k\, \omega_k. \tag{3.14}$$

In the language of Feynman diagrams, this expression occurs as a vacuum bubble. For the propagator

$$D(x_1 - x_2) = \langle 0|\mathscr{T}\chi(x_1)\chi(x_2)|0\rangle = \frac{i}{(2\pi)^4}\int \frac{d^4k}{\omega_k^2}\, e^{ik\cdot(x_1 - x_2)}, \tag{3.15}$$

we obtain for $x_1 = x_2$

$$D(0) = \frac{i}{(2\pi)^4}\int \frac{d^4k}{k^2 + m^2} = -\frac{1}{(2\pi)^3}\frac{1}{2}\int \frac{d^3k}{\omega_k} \tag{3.16}$$

after performing the integration over the time component (cf. Martin, 2012). The structure of this expression is very similar to Eq. (3.14). It is directly related to the trace of the energy-momentum tensor (Martin, 2012), i. e.

$$D(0) = \frac{1}{m^2}\langle 0|\left(T_\chi\right)^\lambda{}_\lambda|0\rangle. \tag{3.17}$$

The trace of the energy-momentum tensor is $\left(T_\chi\right)^\lambda{}_\lambda = -\rho_\chi + 3p_\chi = -4\rho_\chi$ if we assume the equation of state $w = -1$ for the vacuum energy. With the Feynman rule

$$D(x_1 - x_2) = \tag{3.18}$$

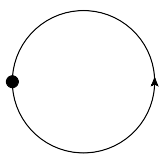

and this result, the vacuum energy (3.14) may also be written as

$$\rho^\chi_{\text{vac}} = -\frac{m^2}{4} \tag{3.19}$$

More complicated vacuum bubbles cannot occur in our free theory. The value of this vacuum energy is divergent unless we impose an ultraviolet cutoff on the integral in Eq. (3.14). The integral is taken over $\omega_k d^3k \sim k^3 dk$. Integrating up to infinity would mean that the field theory is valid up to arbitrary energy scales, which is clearly not expected. A reasonable cutoff scale M would be the energy scale up to which we would trust our field theory. Then

$$\rho_{\text{vac}}^{\chi} \approx \frac{1}{4\pi^2} \int_0^M k^2 dk \, \sqrt{k^2 + m^2} = \frac{M^4}{16\pi^2}. \tag{3.20}$$

The highest cutoff scale we could justify is the Planck scale $M = M_P$ since above this scale, the effects of quantum gravity are expected to become important. But also if we chose a much lower scale M, even known particle physics scales, Eq. (3.20) would give huge values compared to the observed value (3.8). This argument faces a loophole. The quantum field theory Hamiltonian is not uniquely determined by the classical Lagrangian (3.9). In principle, we have the freedom to reorder the operators without changing the corresponding classical field theory. In the case of normal ordering where the creation operators $a_k^\dagger$ are always left from the annihilation operators a_k, the zero-point energy always vanishes because of $a_k|0\rangle = 0$ for the vacuum state.

The result $\rho_{\text{vac}}^{\chi} \sim M^4$ is suggestive on dimensional grounds but not obvious since the field theory itself contains a mass scale m. This is similar in more complex settings where several mass scales exist. Furthermore, a simple cutoff is not the only way to treat infinities. Before we claim that the above estimates are valid, we should check what alternative regularization schemes reveal. A simple cutoff should not be taken too seriously. For example, Martin (2012) notes that such a cutoff breaks Lorentz invariance and, as a consequence, even leads to a wrong equation of state for the vacuum energy.

First, the integrals can become finite if we move from four dimensions $D = 4$ to an arbitrary parameter D. The physical case $D = 4$ will then be a pole of otherwise well-defined expressions. In this *dimensional regularization*, the scalar field is expanded as

$$\chi(x) = \int \frac{d^{D-1}k}{(2\pi)^{D-1} 2\omega_k} \left(a_k e^{ik\cdot x} - a_k^\dagger e^{-ik\cdot x} \right), \tag{3.21}$$

and the repetition of the arguments (Martin, 2012) above yields the vacuum energy in D dimensions,

$$\rho_{\text{vac}}^{\chi} = \frac{\mu^{4-D}}{(2\pi)^{D-1}} \frac{1}{2} \int d^D k \, \omega_k = \sqrt{\pi} M^4 \frac{\Gamma(-D/2)}{\Gamma(-1/2)} \left(\frac{m^2}{4\pi\mu^2} \right)^{\frac{D}{2}}, \tag{3.22}$$

where the mass parameter M is needed for the correct mass dimension in $D \neq 4$ dimensions. The gamma function $\Gamma(z)$ has poles for all negative integers including zero. In particular, the above result is, again, divergent for $D = 4$ because of the term $\Gamma(-D/2)$. Still, we can make an expansion around the pole, i. e. consider $\Gamma(-2+\varepsilon)$ and eventually

obtain

$$\rho^{\chi}_{\text{vac}} \approx -\frac{m^4}{64\pi^2}\left(\frac{1}{\varepsilon}+\frac{3}{2}-\gamma-\log\frac{m^2}{4\pi M^2}\right), \tag{3.23}$$

where γ is the Euler-Mascheroni constant. In an $\overline{\text{MS}}$ renormalization approach (essentially removing the pole at $D=4$), Martin (2012) proceeds to eventually obtain

$$\rho^{\chi}_{\text{vac}} = \frac{m^4}{64\pi^2}\log\frac{m^2}{M^2}. \tag{3.24}$$

The striking feature of this result is that the right mass dimension is now no longer given by a cutoff scale M but rather by the mass m of the field χ. A second mass scale M only enters logarithmically.

We will not comment on whether the above result is more realistic than the estimate obtained by a simple cutoff. Instead, we just note that one cannot make a *prediction* for the value of the cosmological constant based on quantum field theory. Similarly, quantum electrodynamics does not predict the observed electron mass or charge. These values are obtained by experiments. Particle physics theories can, however, give us fundamental energy scales. If a measured energy scale is extremely far away from all relevant fundamental scales, we may find this *unnatural*. This is the case for the cosmological constant. Since it is generally expected that the quantum field theory formalism works until around the Planck scale, there should be fields for which the natural ultraviolet cutoff is indeed the Planck scale M_P. Of course, a more careful discussion should consider fermionic fields and vector bosons or also (broken) supersymmetry. For this, we refer the reader to Martin (2012), but note here that the problem does not fundamentally change.

3.1.2 Classical configurations, phase transitions

Concerning the quantum fluctuations, a widespread speculation is to assume that they do not gravitate. Amendola and Tsujikawa (2010, p. 129) write about the vacuum energy from quantum fluctuations, cf. Eq. (3.14):

> "Whether or not the vacuum energy we have calculated [...] really contributes to dark energy is still a debatable problem. Usually this energy can be eliminated by the normal ordering prescriptions in quantum field theory or it can be normalized to any value."

Amendola and Tsujikawa (2010) then go on to introduce a symmetry to general relativity where the vacuum energy completely decouples from gravity.

We shall now see that the quantum vacuum fluctuations are not the only problematic contribution to the cosmological constant. Instead, there are also classical field configurations, e. g. from the Higgs field in the Standard Model after electroweak symmetry breaking. We will consider this example more closely, following Martin (2012).

Let us first collect the main formulae describing the Standard Model Higgs that we shall need. The Higgs field is the doublet

$$\phi = \frac{1}{\sqrt{2}} \begin{pmatrix} \phi^+ \\ \phi^0 \end{pmatrix} \tag{3.25}$$

of two complex scalars. Its Lagrangian $\mathscr{L}_\phi$ can be written in terms of ϕ, $\phi^\dagger$, and the gauge-covariant derivative ∇:

$$\mathscr{L}_\phi = -\left(\nabla^\lambda \phi\right)^\dagger \nabla_\lambda \phi - V(\phi^\dagger, \phi) \tag{3.26}$$

where V is chosen to be

$$V(\phi^\dagger, \phi) = \frac{\mu^2}{2} \phi^\dagger \phi + \frac{\lambda}{4} \left(\phi^\dagger \phi\right)^2 + V_0 \tag{3.27}$$

with an effective mass squared μ^2 and a parameter $\lambda > 0$. We have added a constant V_0 accounting for our ignorance of the total energy scale. Since the Higgs field is charged under $\mathrm{SU}(2) \times \mathrm{U}(1)$, the gauge-covariant derivative is given by

$$\nabla_\mu \phi = \left(\partial_\mu + i g W_\mu^a \tau^a + i g' Y_\phi B_\mu\right) \phi \tag{3.28}$$

with the generators $\tau_a = \sigma_a/2$ of SU(2) (σ_a are the Pauli matrices), the electroweak gauge bosons W_μ^a and B_μ, coupling constants g, g', and the weak hypercharge Y_ϕ. We choose a gauge such that $\phi^+ = 0$ and ϕ^0 is real. Furthermore, we introduce the vacuum expectation value

$$v = \langle 0 | \phi^0 | 0 \rangle \tag{3.29}$$

in this gauge. Occasionally, we will interpret the potential as a function of this vacuum expectation value, $V = V(v)$.

Before the electroweak phase transition, the effective mass squared μ^2 is positive. The minimum of the potential is at the vacuum expectation value $v = 0$. After the phase transition, the effective mass squared is at a negative value $\mu^2 < 0$, and the minimum of the potential is shifted. The new vacuum expectation value is

$$v = \sqrt{-\frac{2\mu^2}{\lambda}} \neq 0. \tag{3.30}$$

In the Higgs Lagrangian (3.26), after writing out the gauge-covariant derivatives, this vacuum expectation value gives rise to effective mass terms for the $W^\pm$ and Z bosons,

$$M_W = \frac{1}{2} |g| v, \quad M_Z = \frac{1}{2} \sqrt{g^2 + g'^2}\, v, \tag{3.31}$$

where these bosons are linear combinations of W_μ^a and B_μ. This is the well-known mechanism by which the Higgs field provides masses for these vector bosons.

The potential at the new vacuum expectation value is

$$V(v) = V_0 - \frac{\mu^4}{4\lambda}, \tag{3.32}$$

whereas it was $V(0) = V_0$ before. From this, we already see that the vacuum energy — just due to the change in the potential energy of the vacuum expectation value, not regarding vacuum bubbles — changes by an amount

$$\Delta\rho_{\text{vac}} = -\frac{\mu^4}{4\lambda}. \tag{3.33}$$

So, even if the vacuum is tuned to zero in the high-energy limit, we will encounter a non-vanishing cosmological constant after the electroweak phase transition.

Assuming that the recently detected boson at the LHC (Aad et al., 2012; Chatrchyan et al., 2012) indeed is the Standard Model Higgs, the parameters μ and λ are known experimentally, i. e. they are linked to the Higgs mass m_H and to the vacuum expectation value v. We shall briefly recall these results. First, introducing the field H as the perturbation around the vacuum expectation value,

$$\phi^0 = v + H, \tag{3.34}$$

and inserting into the potential, we obtain

$$V(\phi, \phi^\dagger) = V_0 - \frac{\lambda v^4}{16} + \frac{1}{2}\frac{\lambda v^2}{2}H^2 + \frac{\lambda v}{4}H^3 + \frac{\lambda}{16}H^4 \tag{3.35}$$

and hence a mass term with $m_H = \lambda v^2/2$ corresponding to the measured Higgs mass. Furthermore, for the correct low-energy limit for the weak interaction (Martin, 2012), one can establish

$$v^2 = \frac{1}{\sqrt{2}\,G_F^2} \tag{3.36}$$

with Fermi's constant G_F. The numerical values are

$$v \approx 246\ \text{GeV} \quad \text{and} \quad m_H \approx 125\ \text{GeV} \tag{3.37}$$

according to the discovery at the LHC (Aad et al., 2012; Chatrchyan et al., 2012). This gives, by Eq. (3.33), a change in the vacuum energy of

$$\Delta\rho_{\text{vac}} \sim -10^8\ \text{GeV}^4. \tag{3.38}$$

This is huge compared to the observed value (3.8). If there is no physical mechanism solving the cosmological constant problem, we can draw a few conclusions from this result. First, the vacuum energy changes with time, i. e. during phase transitions in the early Universe. Second, assuming $\Lambda = 0$ at one time, e. g. in the late Universe, introduces a non-zero cosmological constant at early times. Or if the cosmological constant is, for some reason, fundamentally zero or close to zero (in the high-energy limit), it will not remain so in the course of the cosmic evolution.

3.2 Anthropic argument

3.2.1 The anthropic principle

As scientists, trying to find universal laws of nature, we should be endowed with a healthy mistrust against anthropocentric ideas reminding us of failed ancient ideas like the Ptolemaic system of the cosmos. Did not Copernicus teach us that our location in the cosmos is not singled out? Yet, Carter (1974) states that

> "[...] our location in the universe is *necessarily* privileged to the extent of being compatible with our existence as observers."

He introduces the term *anthropic principle* into cosmology. In its 'weak' form, it reads

> "[...] what we can expect to observe must be restricted by the conditions necessary for our existence as observers. (Although our situation is not necessarily *central*, it is inevitably privileged to some extent.)"

Logically, we may regard this as quite obvious or even a tautology, rendering it harmless rather than irritating. The anthropic principle as a mere statement is not fruitful. Instead, it should properly be interpreted as a guiding principle how to reason in situations where observation selection effects are important. In this way, anthropic reasoning can be made precise, both conceptually and quantitatively, with the help of adequate tools from probability theory. This has been clarified in some generality by Bostrom (2002, and references therein), restricted, however, to the case of finitely many considered observers. We shall see that the cosmologically relevant case is not that simple since countably infinite universes are generated in eternal inflation; this leads to the complicated *measure problem* (Winitzki, 2009). The connection to probability theory was established independently by cosmologists working on the measure problem and by philosophers analyzing the anthropic principle. The general idea may be called *self-sampling*, i. e. regarding us as observers or as civilization as a random sample from all observers in the multiverse. Vilenkin (1995), describing how to make quantitative predictions in the presence of eternal inflation, formulates the *principle of mediocrity*:

> "The Principle of Mediocrity suggests that we think of ourselves as a civilization randomly picked in the metauniverse."

From the philosophers' side, in more generality, the *strong self-sampling assumption* was proposed (Bostrom, 2002):

> "One should reason as if one's present observer-moment were a random sample from the set of all observer-moments in its reference class."[2]

[2] The strong self-sampling assumption is wrongly attributed to Bostrom. It is the result of applying the idea of self-sampling to observers *at a time*, called *observer-moments*. This was first proposed by Hal Finney in an online discussion group. Bostrom (2002) provides a comprehensive discussion of the idea, its various criticisms, and implications.

These principles suffer from a clear limitation. Once the set of considered observers becomes countably infinite, the prescriptions are ill-defined. This is because there is no uniform probability distribution on a countably infinite set. It is unclear with which probability distribution the above-mentioned self-sampling should be described. The absence of a canonical choice lies at the heart of the measure problem in eternal inflation (Winitzki, 2009).

Unfortunately, there is still a lot of confusion about the anthropic principle and its use. Bostrom (2002, p. 6) summarizes in a historical note:

> "The term 'anthropic' is a misnomer. Reasoning about observation selection effects has nothing in particular to do with homo sapiens, but rather with observers in general. [...] When John Barrow and Frank Tipler introduced anthropic reasoning to a wider audience in 1986 with the publication of *The Anthropic Cosmological Principle*, they compounded the terminological disorder by minting several new 'anthropic principles', some of which have little if any connection to observation selection effects. A total of over thirty anthropic principles have been formulated [...]. Not surprisingly, the result has been some pretty wild confusion concerning what the whole thing is about."

We emphasize that, for the discussion of the measure problem and the anthropic explanation for the small value of the observed cosmological constant, the anthropic principle is only used in the form of the self-sampling assumption or the principle of mediocrity.

3.2.2 Eternal inflation and the measure problem

We shall see that *eternal inflation* is fairly generic in inflationary models. The multiverse scenario with a distribution of cosmological constants mentioned in the beginning of this chapter, cf. Fig. 3.1, might thus be realistic if we assume inflation to be correct. Yet, it is questionable whether this scenario can be scrutinized in the traditional way. First, the energy scale of inflation (typically assumed to be around the GUT scale), is hopelessly far away from the capabilities of accelerators so that we might never be able to conclusively test the physics of inflation in the laboratory. Rather, we are restricted to cosmological probes such as the cosmic microwave background (Bennett et al., 2012; Ade et al., 2013c) and, in principle, gravitational wave astronomy (Schutz, 1999; Grishchuk et al., 2001). Second, we will present the measure problem telling us that there is no canonical way to infer, with the help of the principle of mediocrity, statistical predictions from eternal inflation on, e. g., the most likely observed value of Λ. Third, if we want to use eternal inflation as part of a potential explanation of why the observed late-time cosmological constant is so far away from the Planck scale, we should be able to describe the process of eternal inflation in the presence of a large cosmological constant $\rho_\Lambda \sim M_P^4$ in the first place. Obviously, we cannot expect this to be done in the framework of general relativity and quantum field theory. So,

for our technical discussion, we will assume that the primordial cosmological constant is well below the energy scale of inflation. This still requires considerable fine-tuning.

Slow-roll inflation

Let us start with a brief reminder on the standard picture of inflation. Detailed introductions can be found in recent textbooks (e. g. Mukhanov, 2005; Weinberg, 2008; Lyth and Liddle, 2009). We will follow the presentations by Ayaita (2009); Weinberg (2008). The success of inflationary theory lies in its solution to a couple of puzzling problems in cosmology. Without inflation, the answers to at least some of the following questions would be unclear:

1. Why is the homogeneous and isotropic FLRW metric a good approximation on large scales?

2. Why is the CMB so isotropic — i. e., why was the primordial plasma, apparently, in equilibrium — although angular scales $\gtrsim 1°$ today were superhorizon scales at recombination?

3. Why do we not observe stable 'exotic relics' like magnetic monopoles that we expect from high-energy theories beyond the Standard Model?

4. Why does the large-scale spatial curvature vanish (up to current observational uncertainties) such that the Universe can be described by a flat FLRW metric? According to the Friedmann equations, the importance of curvature grows with time as compared to matter or radiation. Even a small primordial curvature should eventually become important.

5. What is the origin of the observed nearly scale-invariant spectrum of perturbations in the metric and the energy density?

The most striking of the above questions presumably is the *horizon problem* linked to the isotropy of the CMB. The expectation of exotic relics is uncertain due to our ignorance of the correct high-energy theory; and the flatness of the observed Universe might be due to some unknown fundamental reason rather than being fine-tuned.

The horizon problem is due to the fact that, in a universe filled with only radiation and matter, the particle horizon is comparable to the Hubble scale, while the latter never decreases. Fluctuations in the CMB separated by several Hubble scales at recombination (several angular degrees today) were not within one particle horizon and could never establish equilibrium. A solution to this problem would be a phase of accelerated expansion during which the particle horizon grows very fast. Such a period in cosmic history is called *inflation*. It was first studied by Starobinsky (1979); Kazanas (1980). Guth (1981) then made two decisive contributions. First, he showed that a period of accelerated expansion can be obtained in high-energy theories. Second, he described that inflation indeed solves some of the above-mentioned puzzles. He did not consider the question of primordial perturbations. This point was clarified shortly

afterwards (Mukhanov and Chibisov, 1981; Chibisov and Mukhanov, 1982; Lukash and Novikov, 1982) with the help of an adequate quantum theory of cosmological perturbations.

The technically simplest models of inflation are so-called 'new inflation' models (Linde, 1982; Albrecht and Steinhardt, 1982). A single scalar field, the inflaton ϕ, with a canonical action and a scalar potential $V(\phi)$, gives rise to the accelerated expansion. The mechanism is analogous to the description of dark energy as a scalar field which we will consider in more detail in Sec. 3.3.1. We note than an equation of state $w_\phi \approx -1$, and consequently an exponential expansion $a(t) \propto \exp(Ht)$, occurs if $\dot{\phi}^2 \ll V(\phi)$ (hence the term *slow* roll) and if the Universe is dominated by the inflaton,

$$H^2 \approx \frac{1}{3}\left(\frac{\dot{\phi}^2}{2} + V(\phi)\right) \approx \frac{1}{3}V(\phi). \tag{3.39}$$

The slow-roll condition requires

$$\varepsilon \equiv \frac{1}{2}\left(\frac{V_{,\phi}}{V}\right)^2 \ll 1 \quad \text{and} \quad \eta \equiv \frac{V_{,\phi\phi}}{V} \ll 1, \tag{3.40}$$

for the so-called slow-roll parameters ε and η. This tells us that the potential $V(\phi)$ must be sufficiently flat in order for the friction term $\propto 3H\dot{\phi}$ in the equation of motion to effectively reduce the kinetic energy. In order to finish inflation, the field ϕ must reach a steeper part of the potential where the slow-roll conditions are no longer satisfied. A prototypical potential $V(\phi)$ is illustrated in Fig. 3.3 (cf. also Winitzki, 2009; Guth, 2000). The number of 'e-foldings' by which the Universe has expanded

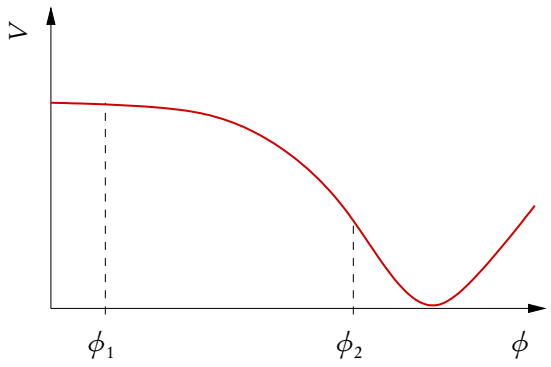

Figure 3.3: Schematic, prototypical potential $V(\phi)$ for new inflation. The field exhibits slow roll between some starting value ϕ_1 and the end of slow roll at ϕ_2. In the end, the field is frozen in the minimum.

during inflation then is

$$N = \log\frac{a_2}{a_1} \approx -\int_{\phi_1}^{\phi_2} d\phi\, \frac{V(\phi)}{V_{,\phi}(\phi)}. \tag{3.41}$$

Quantum perturbations

To this classical analysis, we have to add quantum perturbations. These provide the seed for the classical perturbations described in Sec. 2.2.1 but also generically lead to never-ending, *eternal* inflation. We briefly review the aspect of perturbations following Mukhanov et al. (1992) in order to complete our picture of the evolution of perturbations.

The classical slow-roll trajectory is denoted by $\phi_0(\tau)$. In the conventions of Sec. 2.2.1, the perturbation $\delta\phi$ is related to the gauge-invariant quantity $\delta\phi_{\mathrm{gi}} = \delta\phi + \phi'(B - E')$, which falls together with the perturbation $\delta\phi$ in the Newtonian gauge where $B = E = 0$. Together with the gravitational (Bardeen) potential Φ, this forms the gauge-invariant potential

$$v = a\left(\delta\phi_{\mathrm{gi}} + z\Phi\right) \tag{3.42}$$

with the short-hand $z \equiv \phi_0'/(a'/a)$. In the action of the scalar field minimally coupled to gravity, the perturbation variable v is kept up to quadratic order (for linear equations of motion),

$$S = S_0 + \frac{1}{2}\int d^4x \left(v'^2 - \partial_i v \partial_j v \delta^{ij} + \frac{z''}{z}v^2 + \cdots\right), \tag{3.43}$$

where we have omitted a total divergence. The perturbation v is then promoted to a scalar quantum field with canonical commutation relations with its conjugate momentum $\partial\mathscr{L}/\partial v'$. This can be done similarly for the second Bardeen potential Ψ.

The quantum-to-classical transition can be described by the theory of decoherence (Zeh, 1970). This theory has been applied to the quantum perturbations generated during inflation (Laflamme and Matacz, 1993; Polarski and Starobinsky, 1996; Kiefer, 2000; Castagnino and Lombardi, 2003; Campo and Parentani, 2004; Martin, 2005; Kiefer and Polarski, 2009) in quite different ways. It seems justified to calculate the statistical properties of the classical perturbations, i. e. the two-point correlators $\langle\cdots\rangle$, from the vacuum expectation value of the corresponding quantum operators $\langle 0|\cdots|0\rangle$. Working out the equations of motion (Mukhanov, 2005, p. 355), one arrives at the dimensionless auto-correlation spectrum of the classical metric perturbation Ψ,

$$\Delta^2_\Psi(k) \propto \left(\frac{\rho_\phi}{1+w_\phi}\right)_{k\approx a'/a}, \tag{3.44}$$

where the expression is, for each k, evaluated when k leaves the Hubble horizon. During slow roll, ϕ_0 evolves only slowly whereby $\rho_\phi \approx$ const. and $w_\phi \approx -1$. If these approximations were exact, the dimensionless spectrum were constant (*scale invariant*). This is an explanation for the observed nearly scale-invariant spectrum of primordial perturbations. Furthermore, we can even explain why the spectrum is not exactly scale invariant but has a spectral *tilt* described by the spectral index n_S (Mukhanov, 2005,

p. 347):

$$n_S - 1 \equiv \frac{d\log\Delta_\Psi^2}{d\log k} \approx \left[1 - 3(1+w_\phi) - \frac{a}{a'}\frac{d}{d\tau}\log(1+w_\phi)\right]_{k\approx a'/a}. \tag{3.45}$$

When inflation approaches the end of the slow-roll regime near ϕ_2, cf. Fig. 3.3, the equation of state grows due to the larger kinetic energy. In this way, we naturally expect a tilt given by $n_S < 1$. This is also seen in observations where $n_S \approx 0.96\text{-}0.97$ is found (Bennett et al., 2012; Ade et al., 2013c). This is one of the great successes of the theory of inflation.

Eternal inflation

The quantum perturbations $\delta\phi$ of the inflaton have far-reaching consequences. We have already discussed that they quickly decohere to give classical perturbations of the field. In this way, random 'jumps' are superimposed on the deterministic slow-roll evolution ϕ_0. This becomes important when the quantum jumps are of the same order or even typically larger than the deterministic evolution. In this case, the field ϕ can always step back and go up the potential, delaying the point ϕ_2 where inflation ends. Our discussion of eternal inflation follows the comprehensive review by Winitzki (2009).

The size of the random jumps can be quantified as

$$\langle 0|\phi(t+\Delta t)^2|0\rangle - \langle 0|\phi(t)^2|0\rangle \approx \frac{H^3}{(2\pi)^2}\Delta t. \tag{3.46}$$

If the quantum perturbations decohere within a time scale comparable to the Hubble scale $\Delta t \sim 1/H$, the random steps have a size of $\delta\phi \sim H/(2\pi)$. This has to be compared with the classical solution, which evolves, in one Hubble time $1/H$, by $\dot\phi_0/H$. During slow-roll, the classical equation of motion originating from the scalar field action (cf. Sec. 3.3.1 below) may be approximated as

$$3H\dot\phi_0 \approx -V_{,\phi} \approx -6H\frac{dH}{d\phi}, \tag{3.47}$$

where we have neglected $\ddot\phi_0$ against $V_{,\phi}$ and used, in the last step, approximation (3.39) saying that the energy density is essentially given by the potential energy $V(\phi_0)$ of the inflaton. Equation (3.47) allows us to evaluate the classical evolution $\dot\phi_0/H$ within one Hubble time. The superimposed quantum jumps dominate if

$$H^2 \gg \left|\frac{dH}{d\phi}\right|. \tag{3.48}$$

This condition is closely related to the slow-roll condition. In the extreme case of $\dot\phi = 0$, the Hubble scale would remain constant and the above condition would always

be satisfied. Therefore, it is not surprising that such a regime is fairly generic in models of slow-roll inflation. It is called a *fluctuation-dominated* regime.

Although it is clear that a *random walk* of the above type can lead to a substantial delay until the end of inflation, $\phi \gtrsim \phi_2$, is reached, it is also clear that the random walk will *eventually* reach this point with certainty. The fluctuation-dominated regime will be left (we ignore possible issues at the Planck scale). Nonetheless, the *reproduction* of inflating regions can give rise to eternal inflation in the sense that there will always be inflating regions although every region, individually, will ultimately stop inflating. During the deterministic slow-roll evolution, a region amplifies its 3-volume by a factor

$$n \sim \frac{a(t+\Delta t)^3}{a(t)^3} \sim (1+H\Delta t)^3 . \tag{3.49}$$

If we consider steps $\Delta t \sim 1/H$, this is of order $\sim 10^1$. This is the reproduction of an inflating domain. Since regions separated by several Hubble scales evolve independently of one another, it is not surprising that the above reproduction with individual random walks can lead to eternal inflation. In more precise terms (Winitzki, 2009), the presence of eternal inflation may de defined as follows. Finitely many initial regions of horizon size evolve into infinitely many regions of horizon size, which reach the end of inflation. In this sense, we speak of a *multiverse* consisting of *(pocket) universes* reaching the end of inflation at different times.

Mathematically, the random walk can be described in complete analogy to Brownian motion. The full evolution of the inflaton may be written as

$$\dot{\phi} = \dot{\phi}_0 + N \tag{3.50}$$

with a Gaussian random noise $N = N(x)$ described by its two-point correlator

$$C_\phi(x,x') = \langle N(x)N(x')\rangle, \quad C_\phi(x,x) = \left(\frac{H}{2\pi}\right)^2, \tag{3.51}$$

where the last equation follows from the random jump size $\delta\phi \sim H/(2\pi)$. The independence of regions separated by several Hubble scales is expressed by a fast decrease of C for $|\boldsymbol{x}-\boldsymbol{x}'|$ of several Hubble scales.

The measure problem

We assume that some fundamental constants, among them (a contribution to) the cosmological constant Λ, depend on the values of scalar fields χ_i, which have reached constant values after inflation such that the fundamental constants no longer vary much. We want to answer the question, assuming eternal inflation, which values of the fundamental constants a randomly picked observer is most likely to find. This requires us to find a probability distribution for the values of the scalar fields χ_i in our post-inflationary universe. The cosmological constant, e. g., will depend on the potential energies $V_{\chi_i}(\chi_i)$ of these fields at their frozen values. The probability distribution for

the expected observed values, $p_{\text{obs}}(\chi)$, will thus include the probability distribution for the cosmological constant.

The transition from the ensemble theory (eternal inflation) to a probability distribution is achieved by the anthropic principle in the form of the principle of mediocrity or the self-sampling assumption introduced in Sec. 3.2.1. Essentially, this is an application of Bayesian probability in the schematic form

$$P(\chi|\text{obs}) = \frac{P(\text{obs}|\chi)P(\chi)}{P(\text{obs})}, \tag{3.52}$$

where $p_{\text{obs}}(\chi) \equiv P(\chi|\text{obs})$ is the probability for the values $\chi = (\chi_i)$ under the condition of them being observed by adequate observers, $P(\chi)$ is the prior probability distribution, and $P(\text{observed})$ is a normalization linked to the total number of observers in the ensemble. If we use the principle of mediocrity, the *observers* are replaced by *civilizations*. In the strong self-sampling assumption, instead, observers are replaced by *observer-moments* of some reference class. The two approaches fall together under the approximation that the relation between observer-moments and civilizations is statistically independent from the values χ and if we choose the reference class to include all observers in the inflationary multiverse. For convenience, we shall use the principle of mediocrity here. Following Vilenkin (1995); Winitzki (2009), we write

$$p_{\text{obs}}(\chi) = P(\chi)\, n_{\text{gal}}(\chi) N_{\text{civ}}(\chi) \tag{3.53}$$

decomposing $P(\text{obs}|\chi)$ into a factor described by cosmology (the galaxy number density n_{gal}) and a more involved factor describing how likely it is for life to develop within gravitationally bound structures (the expected number N_{civ} of civilizations in one galaxy). Since the number density of galaxies is normalized by volume, the prior probability distribution here is the volume-weighted probability distribution for the χ_i (at some specific time such as the end of inflation).

The conceptually problematic part is the prior probability distribution $P(\chi)$. It could easily be evaluated in the *finite* case where a number N of pocket universes with 3-volumes V_j (where this value is defined, e. g., at the end of inflation) and scalar field values $\chi^{(j)}$ is generated. Then, we could write

$$P(\chi) \prod_i \Delta\chi_i \approx \frac{\sum_{|\chi_i^{(j)} - \chi_i| < \Delta\chi_i} V_j}{\sum_{k=1}^{N} V_k}. \tag{3.54}$$

When the number N of pocket universes goes to infinity and the intervals $\Delta\chi_i$ are sufficiently small, this expression vanishes exactly (unless the χ_i take the same values in almost all pocket universes). It can then no longer be used for the probability distribution.

At first sight, this might look like a mathematical subtlety, perhaps not crucial for our purposes. Unfortunately, this is not the case. There is no canonical way to extend finite expressions like Eq. (3.54) to the infinite case. Let us discuss this with more

precision. We return, for the moment, to the finite case of N pocket universes. For simplicity, the 3-volumes are assumed to be all equal. Equation (3.54) above is then equivalent to performing an average of a quantity $A(j)$ taking values 0 or 1 on $j = 1, \ldots, N$:

$$A(j) \in \{0, 1\}, \quad \langle A \rangle = \frac{1}{N} \sum_{j=1}^{N} A(j). \tag{3.55}$$

The measure problem in this case is the question how to canonically extend this averaging procedure to the case $N \to \infty$. Although there is no uniform probability distribution on the natural numbers, one is tempted to write

$$A : \mathbb{N} \to \{0, 1\}, \quad \langle A \rangle \equiv \lim_{N \to \infty} \frac{1}{N} \sum_{j=1}^{N} A(j). \tag{3.56}$$

This definition has a severe disadvantage: it is not stable under reordering the natural numbers. A reordering may be expressed as a permutation $\sigma \in S_{\mathbb{N}}$. The averaging then depends on this ordering and should be written as

$$\langle A \rangle_\sigma \equiv \lim_{N \to \infty} \frac{1}{N} \sum_{j=1}^{N} A(\sigma(j)). \tag{3.57}$$

This is not a correction but decisive. If A takes the values 0 and 1 each on infinite points, this average can be made 0 or even 1 for adequately chosen σ. If there was some canonical measure μ of finite mass defined on $S_{\mathbb{N}}$, we could define an average

$$\langle A \rangle \equiv \frac{\int_{S_{\mathbb{N}}} \langle A \rangle_\sigma \, d\mu(\sigma)}{\mu(S_{\mathbb{N}})}, \tag{3.58}$$

where the freedom we had in the ordering is averaged out. The same could be done with an adequate *left-invariant* mean m on $S_{\mathbb{N}}$. This would exist if $S_{\mathbb{N}}$ was an *amenable group*. These two approaches are equivalent. A group is amenable if and only if there is a (finitely additive) left-invariant probability measure μ on it. Unfortunately, in our case, the result is negative: the group $S_{\mathbb{N}}$ of permutations on the natural numbers is not amenable. There is no canonical way to define an average $\langle A \rangle$, which is stable under reordering.

It seems that our intuition given by the principle of mediocrity and the self-sampling assumption fails in the infinite case. These conceptual problems have not entirely intimidated cosmologists. Many researches have not shied away and, instead, proposed various procedures to cope with the infinities occurring when one applies the principle of mediocrity. Winitzki (2008) classifies these approaches into two categories:

1. *Volume-based* measures correspond to our discussion above where we try to look at the ensemble of all observers in the inflationary multiverse. With some prescription, one needs to choose a finite subset of this infinite number of observers or pocket universes. The results will, of course, depend on this prescription leading to inherently ambiguous outcomes.

2. *Worldline-based* measures restrict the reference class used in the self-sampling assumption right from the start. This reference class only consists of observers located near the worldline of a randomly chosen spatial coordinate $\boldsymbol{x}$. This reference class is typically finite and the formal problems are not present. However, since we have quite arbitrarily singled out a reference class, it is not clear how to interpret the results in the terms of actual expectations.

3.3 Accelerated expansion without Λ

As an optimistic interpretation of our discussion in the preceding sections, we might say that there is an emerging potential explanation for the small value of Λ based on the anthropic principle. On the other hand, it has become clear that the arguments are still vague and speculative. Perhaps even more importantly, the anthropic principle does not, as we have noted, remove the need to search for a physical explanation beyond merely statistical arguments. If there is a physical mechanism adjusting the value of Λ, we might assume the simplest and most natural possibility $\Lambda = 0$.

So, from now on, we will assume that the cosmological constant is not responsible for the observed accelerated expansion of the Universe. We assume that the cosmological constant vanishes, does not gravitate, or that the cosmological constant is replaced by a dynamical field in the correct effective theory. We have briefly mentioned these — so far speculative — ideas, and even if they are considered not conclusive, it is still very desirable to have alternative models to the cosmological concordance model. Alternative models will in the end be required to guide observational efforts: they show where to look for possible deviations from the standard scenario. At the present time where many significant observational efforts are planned or already undertaken (Albrecht et al., 2006; Amendola et al., 2012; Amiaux et al., 2012; Ade et al., 2011), there is a pressing need to explore alternative scenarios and their implications.

In this section, we shall see several possibilities to account for the late-time expansion of the Universe without a cosmological constant. We will, throughout this thesis, focus on *quintessence* models, which we consider as a very natural approach. In its very early history, the Universe already experienced a phase of exponential expansion, namely during the inflationary epoch. There, the simplest, most predictive, and successful model is an expansion driven by a scalar field, the inflaton ϕ. A mechanism that worked once could work for the late Universe as well. In this way, the late-time accelerated expansion could be described without the need to introduce completely new concepts to cosmology.

3.3.1 Quintessence

Explaining the late-time expansion by a scalar field, the cosmon φ, is done by *quintessence models* of dark energy, introduced by Wetterich (1988); Ratra and Peebles (1988). At the time of these early works, there was no (clear) observational evidence for a late-time accelerated expansion. This underlines that there are good reasons to investigate

the possible role of scalar fields in late-time cosmology.

The observational evidence for an accelerated expansion boosted the investigation of quintessence models (cf., e. g., Huterer and Turner, 1999; Wang et al., 2000; Doran et al., 2001; Wetterich, 2002). One of the most attractive features is that the models can significantly reduce the fine-tuning required for the right order of magnitude of the 'effective cosmological constant' observed today. We shall see that the smallness of the effective cosmological constant is, in quintessence models, a mere consequence of the large age of the Universe.

If we find it unnatural to explain the accelerated expansion by a component with constant and extremely small energy density, we might, at first, think of a time-dependent cosmological constant '$\Lambda(\tau)$' as an alternative. Yet, general relativity treats time and space on an equal footing whereby, conceptually, we must include the spatial dependence. We are naturally driven to the study of scalar fields $\varphi(x)$. Of course, in this generality, neither the fundamental nature of this 'scalar field' nor its dynamics are known. In fact, even in the cosmological constant model, we have argued that the cosmological constant might take different values after phase transitions or in different patches of the inflationary multiverse — the cosmological constant should therefore properly also be described as space-time dependent. In contrast, in quintessence models, one typically considers the 'canonical' case, i. e. a scalar field with canonical action, minimally coupled to gravity,

$$S = \int d^4x \sqrt{-g} \left[\frac{R}{2} - \frac{1}{2}\partial^\lambda\varphi\partial_\lambda\varphi - V(\varphi) \right] + S_m, \tag{3.59}$$

i. e. with the Lagrangian $\mathscr{L}_\varphi = -\partial^\lambda\varphi\partial_\lambda\varphi/2 - V(\varphi)$ and a self-interaction potential $V(\varphi)$. Most of the material we expose in this section can be found in reviews on the subject (Amendola and Tsujikawa, 2010; Copeland et al., 2006; Peebles and Ratra, 2003).

The action implies the Klein-Gordon equation of motion,

$$\nabla^\lambda\nabla_\lambda\varphi - V_{,\varphi}(\varphi) = 0, \tag{3.60}$$

which is equivalent to the energy-momentum conservation equation

$$\nabla_\nu T^{\mu\nu}_{(\varphi)} = 0 \quad \text{for} \quad T^{\mu\nu}_{(\varphi)} = \partial^\mu\varphi\partial^\nu\varphi + g^{\mu\nu}\mathscr{L}_\varphi. \tag{3.61}$$

If the perturbations of the scalar field can be treated in linear approximation, which we shall assume throughout this thesis, the Klein-Gordon equation can be split into a background and a linear perturbation part,

$$\bar\varphi'' + 2\frac{a'}{a}\bar\varphi' + a^2V_{,\varphi}(\bar\varphi) = 0 \tag{3.62}$$

$$\delta\varphi'' + \Delta\delta\varphi + 2\frac{a'}{a}\delta\varphi' + a^2V_{,\varphi\varphi}(\bar\varphi)\delta\varphi = -2a^2V_{,\varphi}(\bar\varphi)\Psi - 4\bar\varphi'\Psi'. \tag{3.63}$$

In this section, we will only be concerned with the background evolution. We will come back to the perturbation equation in later chapters. For now, we denote by $\varphi \equiv \varphi(\tau)$ simply the background field.

The scalar potential

For the expansion history, the interesting quantity is the equation of state

$$w_\varphi = \frac{p_\varphi}{\rho_\varphi} = -\frac{1}{3}\frac{T^i_{(\varphi)i}}{T^0_{(\varphi)0}} = \frac{\frac{\varphi'^2}{2a^2} - V(\varphi)}{\frac{\varphi'^2}{2a^2} + V(\varphi)}. \tag{3.64}$$

Let us first briefly discuss two extreme cases:

1. If the potential energy dominates, i. e. $V(\varphi) \gg \varphi'^2/2a^2$, we obtain $w_\varphi \approx -1$, and the cosmon acts as an effective cosmological constant of value $\rho_{\Lambda,\text{eff}} = \rho_\varphi = V(\varphi) = \text{const}$.

2. In the other extreme, the kinetic energy dominates, $V(\varphi) \ll \varphi'^2/2a^2$, and we get $w_\varphi \approx +1$. This implies a decrease of the energy density as $\rho_\varphi \propto a^{-6}$, much faster than matter or radiation.

We conclude that the cosmon can act as a cosmological constant or can adopt any other equation of state between -1 and $+1$; which value is taken at early and at late times will depend on the choice of the potential $V(\varphi)$ and, in general, on the initial values of φ and φ'.

In particular, the potential $V(\varphi)$ can be chosen such that we just obtain the correct late-time acceleration. It can even be tuned to mimic a cosmological constant with arbitrary precision. There are, however, a few conditions one would like to impose on $V(\varphi)$ from a theoretical perspective. First, the potential should avoid or reduce the necessity of fine-tuning. If the quintessence scenario required more fine-tuning than the cosmological constant, its theoretical appeal would have more or less gone. Second, it is desirable to choose a potential $V(\varphi)$ that typically arises in (to date speculative) high-energy fundamental theories. A fairly detailed discussion of this point is given by Amendola and Tsujikawa (2010). Third, from an observational perspective, the potential must be chosen such that constraints, e. g. on the early amount of dark energy, are satisfied (Pettorino et al., 2013; Wang, 2012; Grossi and Springel, 2009; Doran and Robbers, 2006).

Two very prominent examples for $V(\varphi)$ already proposed by the earliest works (Wetterich, 1988; Ratra and Peebles, 1988), are the exponential potential

$$V(\varphi) = M^4 e^{-\alpha\varphi} \tag{3.65}$$

and the power-law potential

$$V(\varphi) = \frac{M^{4-\alpha}}{\varphi^\alpha}. \tag{3.66}$$

For both potentials, one assumes $\alpha > 0$. In case of the exponential potential, the mass scale M is essentially arbitrary as a change of M corresponds to a mere shift in the field value φ. The potentials do not have a minimum such that φ always rolls towards larger values (although this rolling can become arbitrarily slow).

These two potentials belong to a large class of potentials with a very favorable feature: they allow for *tracker solutions*.[3] For a wide range of initial conditions, the evolution of the scalar field approaches an attractor thereby reducing the amount of fine-tuning in the model (Wetterich, 1988; Ratra and Peebles, 1988; Steinhardt et al., 1999; Zlatev et al., 1999). Since the initial values of φ and φ' will not matter much, the parameters M and α of the potential determine the late-time evolution completely. We will briefly explain the tracking mechanism for the exponential potential (the argument is given, e. g., by Doran and Wetterich, 2003), which is the potential used in this thesis. The tracker behavior explains why the energy-density of dark energy is comparable to that of matter today because ρ_φ follows the dominant component, $\rho_\varphi \approx \rho_{\text{tot}}$. In particular, since the time evolution of the energy density is given by the equation of state, the tracker solution adopts the equation of state w_{tot} of the dominant component ($w_{\text{tot}} = 1/3$ during radiation domination, $w_{\text{tot}} = 0$ during matter domination). We illustrate the tracking mechanism in Fig. 3.4. The red line indicates the tracking

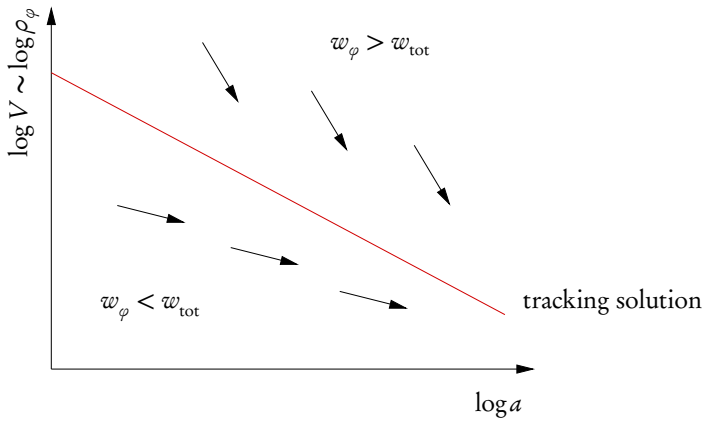

Figure 3.4: Schematic illustration of the tracking mechanism.

solution, $\rho_\varphi \propto a^{-4}$ during radiation domination, $\rho_\varphi \propto a^{-3}$ during matter domination. Let us first discuss the region above this curve. There, the energy density and the potential energy $V(\varphi)$ are large and with them the term $a^2 V_{,\varphi} \propto V(\varphi)$ in the equation of motion. This accelerates the rolling of the field thereby increasing the equation of state w_φ. With a larger w_φ, the energy density will decrease faster. In the region above the curve, the opposite happens. The damping term $2a'\varphi'/a$ in the equation of motion decelerates the rolling thereby lowering the equation of state. The energy density ρ_φ decreases slowly and catches up with the dominant component. In this way, we can qualitatively understand the occurrence of an attractor. Of course, this argument can be made precise (Doran and Wetterich, 2003), and the tracker solution is characterized

[3] Sometimes, the term *tracker solution* is distinguished from *tracking solutions*. While the first refers to an attractor, the latter means that the solution follows the dominant component at the background level (Steinhardt et al., 1999). We will not make this distinction here.

by

$$\varphi(t) = \frac{2}{\alpha} \log \frac{t}{\bar{t}} \tag{3.67}$$

$$\frac{1}{2}\dot{\varphi}(t)^2 = \frac{2}{\alpha^2} t^{-2} \tag{3.68}$$

$$V(\varphi(t)) = \frac{2M^4}{\alpha^2} \frac{1 - w_{\text{tot}}}{1 + w_{\text{tot}}} t^{-2}, \tag{3.69}$$

leading to a fractional energy density of

$$\Omega_\varphi = \frac{3(1 + w_{\text{tot}})}{2\alpha^2}. \tag{3.70}$$

The amount of dark energy is completely determined by the parameter α.

The coincidence problem

The tracking solution of the exponential potential always follows the dominant component. This regime has no end, i. e., there will be no dark energy domination and hence no accelerated expansion. At first sight, this might seem as a clear disadvantage since the possible explanation of the late-time expansion is, today, the main motivation to consider quintessence models. We show the evolution of energy densities with an exponential potential, $\alpha = 10$, in Fig. 3.5.

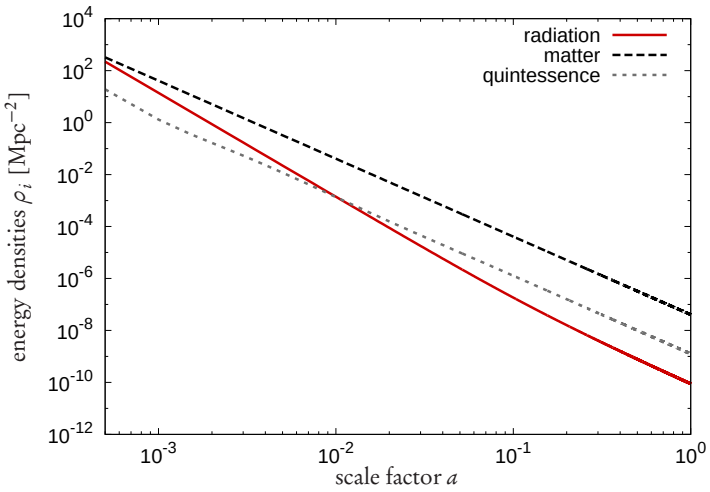

Figure 3.5: Energy densities of radiation, matter, and quintessence for an exponential potential.

The power-law potential $V \propto \varphi^{-\alpha}$, which also allows for tracking solutions, is an example where accelerated expansion is generated. This comes at a price. The parameters of the potentials have to be tuned such that the accelerated expansion sets in just

at the right time. This introduces a new fine-tuning problem. In standard models of quintessence, one need not tune the theory to obtain a small energy density comparable to the energy densities of the other components; the fine-tuning associated to the cosmological constant problem is reduced. However, one needs to put in the starting point for the accelerated expansion. This is called the *coincidence problem* since dark energy domination has started in the very recent cosmic past.

From this point of view, we may interpret it as an advantage that the exponential potential itself does not trigger the accelerated expansion by some explicit or implicit fine-tuning. Instead, it leaves open the mechanism by which the cosmon is stopped and a phase of dark energy domination is initiated. In the growing neutrino quintessence model, we will explore the idea that a coupling of the cosmon to matter, in this case to the neutrinos, is responsible for the onset of dark energy domination. Rather than tuning the potential by hand, there will be a dynamical effect on the cosmon behaving like an effective potential barrier, cf. Fig. 3.6. In such a scenario, the cosmon will

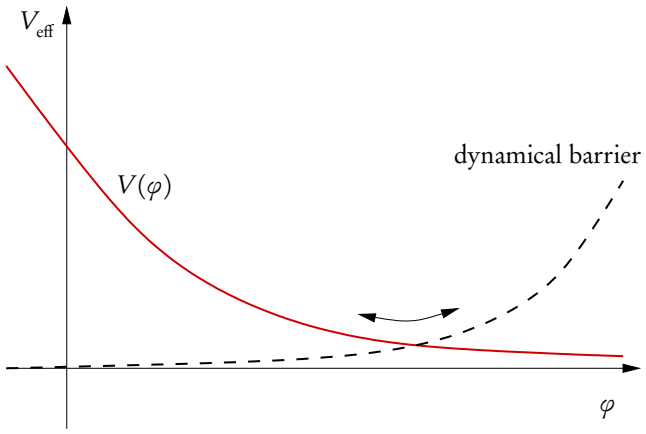

Figure 3.6: Illustration of how additional physics could act as a dynamical barrier.

oscillate around the minimum of the effective potential and be essentially stopped due to the friction term in its equation of motion.

3.3.2 Other approaches

The task of describing the accelerated expansion of the Universe without a cosmological constant is a large area of research, not restricted to quintessence models on which we focus in this thesis. We conclude this section by presenting a few other popular approaches to the problem.

k-essence

Since the fundamental physics of dark energy is not known, we may assume that the effective action of the dark energy scalar field is not canonical. It might have a non-

standard kinetic term. For quintessence models, this possibility has been proposed in order to leave the tracker solution (of the exponential potential) with the help of a 'leaping' kinetic term (Hebecker and Wetterich, 2001). In *k*-essence models, one assumes the scalar field Lagrangian $\mathscr{L}_\varphi$ to include some function of the standard kinetic term $X = -\partial^\lambda\varphi\partial_\lambda\varphi/2$,

$$S_\varphi = \int d^4x\,\sqrt{-g}\,\mathscr{L}_\varphi(X,\varphi). \tag{3.71}$$

This was originally studied for scalar field driven inflation (Armendariz-Picon et al., 1999; Garriga and Mukhanov, 1999) and shortly afterwards also for dark energy (Chiba et al., 2000). The interest in *k*-essence models for dark energy mainly originated from the observation that the onset of dark energy domination can be dynamically triggered by the period of matter domination (Armendariz-Picon et al., 2000, 2001). In this way, the fine-tuning related to the coincidence problem of standard quintessence models can be reduced.

From the energy-momentum tensor

$$T_{\mu\nu} = \frac{-2}{\sqrt{-g}}\frac{\delta\left(\sqrt{-g}\mathscr{L}_\varphi\right)}{\delta g^{\mu\nu}} = \frac{\partial\mathscr{L}_\varphi}{\partial X}\partial_\mu\varphi\partial_\nu\varphi + \mathscr{L}_\varphi g_{\mu\nu}, \tag{3.72}$$

one can read off the expressions for the pressure $p_\varphi = T^i{}_i/3$ and the energy density $\rho_\varphi = -T^0{}_0$ (at the background level) yielding the equation of state

$$w_\varphi = \frac{p_\varphi}{\rho_\varphi} = \frac{\mathscr{L}_\varphi}{2\frac{\partial\mathscr{L}_\varphi}{\partial X}X - \mathscr{L}_\varphi}. \tag{3.73}$$

The behavior of *k*-essence models differs from quintessence particularly in the perturbations where the *k*-essence scalar field has a nontrivial *speed of sound*. The *adiabatic* sound speed $c_a^2 \equiv \bar{p}'_\varphi/\bar{\rho}'_\varphi$ is given by

$$c_a^2 \equiv \frac{\bar{p}'_\varphi}{\bar{\rho}'_\varphi} = \frac{\partial\bar{p}_\varphi/\partial X}{\partial\bar{\rho}_\varphi/\partial X} = \frac{\partial\mathscr{L}_\varphi/\partial X}{\partial\mathscr{L}_\varphi/\partial X + 2X\partial^2\mathscr{L}_\varphi/\partial X^2} \tag{3.74}$$

using Eq. (3.73). The sound speed $c_s^2 \equiv \delta p_\varphi/\delta\rho_\varphi$, related to the energy density and pressure perturbations $\delta\rho_\varphi$ and δp_φ of the scalar field, is

$$c_s^2 \equiv \frac{\delta p_\varphi}{\delta\rho_\varphi} = c_a^2 + \frac{v_{\varphi,\boldsymbol{k}}}{k\delta_{\varphi,\boldsymbol{k}}}\left[3\frac{a'}{a}(1+w_\varphi)(c_a^2 - w) + w'\right] \tag{3.75}$$

with the scalar peculiar velocity perturbation v_φ and the density contrast δ_φ in Fourier space (Erickson et al., 2002). The sound speed thus depends on the Fourier mode $\boldsymbol{k}$. We will consider the dark energy sound speed in more detail in Chapter 4 and just note, at this point, that *k*-essence perturbations can exhibit nontrivial and interesting evolutions. The adiabatic sound speed can even exceed the speed of light although this does not lead to violations of causality (Babichev et al., 2008).

Phantom dark energy

Quintessence models allow, as we have discussed, for any equation of state between $w_\varphi = -1$ and $w_\varphi = +1$. The same is true for k-essence models if the kinetic energy contributes positively to the energy density of the scalar field, i. e. $\partial L_\varphi / \partial X > 0$. From a phenomenological point of view, this has a disappointing aspect: In the observational search for deviations from the cosmological constant scenario, we can, with quintessence, only describe the region $w_\varphi > w_\Lambda = -1$ but the other side $w_\varphi < -1$.

A simple idea to obtain this possibility is to simply choose the 'wrong' sign in the kinetic term, i. e. to write $\mathscr{L}_\varphi = -X - V(\varphi)$. This implies the inverse equation of state as compared to quintessence models, namely

$$w_\varphi = \frac{\frac{\varphi'^2}{2a^2} + V(\varphi)}{\frac{\varphi'^2}{2a^2} - V(\varphi)} \tag{3.76}$$

with $w_\varphi < -1$ for $\varphi'^2/(2a^2) < V(\varphi)$. We call φ a *phantom* or *ghost field* (Caldwell, 2002). If this is interpreted as more than a purely phenomenological parameterization, the scenario is subject to instability concerns (Carroll et al., 2003).

Modified gravity

Although not directly related to the work presented in this thesis, it is in order to mention another very popular approach to describe the accelerated expansion of the Universe without a cosmological constant, namely a modification of Einstein gravity (for recent introductions and reviews, cf. Clifton et al., 2012; Nojiri and Odintsov, 2006a,b; Carroll et al., 2005; Amendola and Tsujikawa, 2010). Rather than introducing components to the cosmic fluid with $w < -1/3$ on the right-hand side of Einstein's equations, one can also establish an accelerated expansion by changing the left-hand side.

The most straightforward way to find modified field equations is to return the Einstein-Hilbert Lagrangian $\mathscr{L}_G = R/2$. It is constructed from the Ricci scalar R, the simplest scalar quantity related to the curvature tensor $R^\mu{}_{\nu\alpha\beta}$. Alternative, more complicated field equations are obtained if we include, in the action, more scalars constructed from $R^\mu{}_{\nu\alpha\beta}$ such as $R^{\alpha\beta}R_{\alpha\beta}$ or $R^{\alpha\beta\gamma\delta}R_{\alpha\beta\gamma\delta}$ or if we allow for a more complex functions of R than the linear term $\mathscr{L}_G = R/2$. The latter option is chosen in the popular '$f(R)$ modified gravity' approach (first introduced by Buchdahl, 1970) where one chooses

$$S_{\mathrm{MG}} = \frac{1}{2}\int d^4x\,\sqrt{-g}\,[R + f(R)] \tag{3.77}$$

for the modified gravitational action, where f is some arbitrary function of R. It is straightforward to show by variation of the action that the field equations are

$$G_{\mu\nu} + \frac{df}{dR}R_{\mu\nu} - \frac{1}{2}\left(f + 2\nabla^\lambda\nabla_\lambda\frac{df}{dR}\right)g_{\mu\nu} - \nabla_\mu\nabla_\nu\frac{df}{dR} = T_{\mu\nu} \tag{3.78}$$

with the usual general-relativistic Einstein tensor $G_{\mu\nu} = R_{\mu\nu} - Rg_{\mu\nu}/2$. For $f \equiv 0$, the above equations specialize to Einstein's field equations. The early inflation model by Starobinsky (1979) uses a quadratic function $f(R) \propto R^2$ (for examples of more complex functions, cf., e. g., Carroll et al., 2005).

At least in the classical theory (ignoring quantum effects), there is a formal relation between $f(R)$ gravity and scalar field theory in Einstein gravity. We call Eq. (3.77), where gravity is modified and there is no dark energy scalar field, the *Jordan frame* action. Following Nojiri and Odintsov (2006a), we introduce an auxiliary field A such that the Lagrangian reads $\mathscr{L}_{\rm MG} = R + f(A) + (R - A)\,df(A)/dR$. Now, we perform the conformal transformation $g_{\mu\nu} \to \hat{g}_{\mu\nu} = e^{2\varphi/\sqrt{3}}$ with $\varphi \equiv -\sqrt{3}\log A$ and obtain

$$S_E = \int d^4x\,\sqrt{-\hat{g}}\left(\hat{R} - \frac{1}{2}\hat{\partial}^\lambda\varphi\hat{\partial}_\lambda\varphi - V(\varphi)\right) \tag{3.79}$$

with a suitably defined potential $V(\varphi)$. This action is called the *Einstein frame* action as the standard general-relativistic action is retained, and the original modification of gravity is expressed as a canonical scalar field with some self-interaction potential. From this formal equivalence, it is already clear that we can obtain accelerated expansion in $f(R)$ models analogously to quintessence models.

An important question is, for these models, how to retain general relativity on small scales such as in the Solar System or in the galaxy (Hu and Sawicki, 2007).

4 Constraints on parametrized dark energy

Before we come to the investigation of growing neutrino quintessence, a dynamical dark energy model proposed as a potential solution to the coincidence problem, we take a more general point of view in this chapter. We ask how well future observations will be able to put constraints on rather generic properties of dark energy, in particular on its possible clustering on very large scales. Of course, this will not lead to model-independent statements. Rather, it gives an idea of the strength and precision of future observations to constrain large-scale gravitational potentials and their time evolution. Once the actual observational data are taken and available, it is essential to check for each dark energy model individually whether the constraints are met or not.

A particular dark energy parametrization, the wCDM parametrization, has become the de-facto standard. The parametrization describes the dark energy fluid with a constant equation of state w (sometimes, a constant time-derivative like dw/da, evaluated at $a = 1$, is added). It is so widely used that it has become virtually obligatory if one studies the constraining power of observational probes. This is because, if another parametrization or a particular dark energy model is used, it is hardly possible to compare the results with other studies in the literature, where the wCDM parametrization is used almost exclusively. Therefore, although we will see a number of drawbacks of the wCDM parametrization, we will choose it in this chapter. The parametrization is discussed in Sec. 4.1, where we will also add a sound-speed parameter c_s^2 in order to study the influence of dark energy clustering. So far, the sound speed parameter c_s^2 is essentially unconstrained (Li and Xia, 2010; de Putter et al., 2010; Bean and Dore, 2004). The question whether dark energy clusters cannot be answered based on present observational data although this possibility has to be investigated if we consider dark energy as a generic fluid (Hu, 2002b; Erickson et al., 2002; DeDeo et al., 2003; Hu and Scranton, 2004). The situation might improve with weak lensing tomography, the Planck satellite, future galaxy surveys, and neutral hydrogen surveys (Sapone et al., 2010; Takada, 2006; Ballesteros and Lesgourgues, 2010; Torres-Rodriguez and Cress, 2007; Torres-Rodriguez et al., 2008). This motivates to look into 3d weak lensing (Heavens, 2003), a method designed to take full advantage of the three-dimensional information of the cosmic shear field, and to analyze what constraints we may expect from it concerning dark energy clustering. As compared to weak lensing tomography, there is less mode coupling in 3d weak lensing, and large scales — where dark energy clustering is present — are better resolved.

We discuss weak gravitational lensing and its three-dimensional version in Sec. 4.2. Weak gravitational lensing by large-scale structure (van Waerbeke et al., 2000) has become, along with the cosmic microwave background, a well-understood cosmological probe which does not sensitively depend on highly complicated astrophysical processes

like the formation and evolution of galaxies (Hu and White, 2001; Refregier, 2003; Huterer, 2010; Bartelmann, 2010a). Instead, the weak gravitational lensing formalism depends only on gravity, and it allows to directly investigate the (dark) matter distribution rather than postulating that the matter distribution is traced by the optically accessible galaxy distribution. If we assume standard general relativity, weak gravitational lensing on sufficiently large scales is thus not plagued by conceptual uncertainties. The situation becomes more complicated on small scales where baryonic physics and hence astrophysical effects have to be taken into account (Duffy et al., 2010). The remarkable potential of weak gravitational lensing to scrutinize properties of dark energy, in particular of its equation of state, is well known (cf. Huterer, 2010; Kilbinger et al., 2008; Hollenstein et al., 2009; Amendola et al., 2008b; Heavens et al., 2006; Hannestad et al., 2006; Takada and Jain, 2004; Bernstein and Jain, 2004; Heavens, 2003; Jain and Taylor, 2003; Huterer, 2002).

The three-dimensional version of weak lensing, *3d weak lensing*, allows, in principle, to use the full three-dimensional information in the cosmic shear field in order to, e. g., constrain cosmological models (Heavens, 2003; Heavens et al., 2006; Castro et al., 2005; Kitching et al., 2007, 2008; Munshi et al., 2011). This might prove useful once sufficiently large weak lensing surveys (provided with redshifts as a distance measure) will have been undertaken. We shall consider the Euclid mission here (Amendola et al., 2012; Laureijs et al., 2011). We will apply a Fisher matrix approach, cf. Sec. 4.3, in order to estimate how well a 3d weak lensing analysis based on future Euclid data will constrain parametrized dark energy, namely the equation of state parameter w and the sound speed c_s^2, both assumed constant. With adequate numerical techniques, presented in Sec. 4.3.2, we will present the estimated constraints in Sec. 4.4. For possible 3d weak lensing constraints on a concrete, k-essence model, cf. Camera et al. (2010). For the question whether a time-dependent sound speed could leave characteristic traces, cf. Ansari and Unnikrishnan (2011).

The results shown in this chapter are already published in the collaborative paper Ayaita et al. (2012a) (whose presentation we will largely follow) and have, partially, been presented by Weber (2012). The focus of this thesis is on the computation of the Fisher information matrix used to estimate potential parameter constraints, and the approximate, analytical understanding of the ingredients of the 3d weak lensing spectrum.

4.1 The wCDM parametrization

The large number of approaches to describe the accelerated expansion without a cosmological constant (cf. Copeland et al., 2006) motivate the search for refuge in a rather indifferent, purely phenomenological parametrization. Unfortunately, the diversity of models (coupled or uncoupled quintessence, k-essence, modified gravity, ...) tells us that there is little hope to find a useful parametrization describing the essential features of all of these models. We will discuss this point by comparing the standard wCDM parametrization to uncoupled quintessence models in Sec. 4.1.1. Then, we concentrate

on wCDM as the de facto standard parametrization and include dark energy clustering by a sound speed parameter in Sec. 4.1.2. The effects of the sound speed are investigated in more detail in Sec. 4.1.3.

4.1.1 Background: equation of state

Regarding only the evolution of the background, a possible alternative is to not constrain model parameters but rather (background) observables directly in a more or less model-independent way. From this, it is relatively straightforward to check the consistency of different cosmological models with these observables. As an observable, one may choose the luminosity distance $D_L(z)$, which is directly related to supernova Ia measurements of the cosmic expansion. Its definition is motivated by the relation $F = L/(4\pi D^2)$ between distance D, luminosity L, and flux F in a Euclidean geometry (corresponding to a static and flat universe). Although this relation will no longer hold in the more general case of an expanding universe, we may use it as an operational definition of a new distance measure, the luminosity distance

$$D_L = \sqrt{\frac{L}{4\pi F}}. \tag{4.1}$$

Taking into account the cosmological redshift (ignoring the peculiar motion of the source), the modified growth of the physical area of a sphere around the source, and the lower rate of photon arrivals, the luminosity distance is $D_L(z) = r\,(1+z)$, where r is the comoving distance of the source and z is its (cosmological) redshift (Weinberg, 2008, p. 31 et seq.). Dark energy models predict the expansion history given by the Hubble function $H(z) = dz/dr$. Using this relation, the Hubble function can be reconstructed from the luminosity distance as

$$H(z) = \frac{1+z}{\frac{dD_L}{dz} - r}. \tag{4.2}$$

In order to put constraints on an entire function like $D_L(z)$, we have to first choose some discretization scheme like constraining $D(z_i)$ for a finite number of redshifts z_i. This naive approach corresponds to approximating the function $D_L(z)$ by a simple step function. Alternatively, we may expand $D_L(z)$ in any set of orthonormal functions f_i,

$$D_L(z) \approx \sum_{i=0}^{N} c_i\, f_i(z), \tag{4.3}$$

and then constrain the coefficients c_i. This approach has been chosen by Mignone and Bartelmann (2007); Benitez-Herrera et al. (2011).

Although such a strategy has the clear advantage of being quite general (essentially, we have just made use of general relativity, i. e. the Friedmann equations), its limitation is that it does not necessarily focus on the particular features of a dark energy model.

One might hope to obtain stronger constraints by concentrating on the particularities of a specific model or a class of models rather than constraining the set of coefficients c_i. For example, one could choose the class of uncoupled quintessence models. Then, the essential free function which one would like to constrain is the potential $V(\varphi)$. Equivalently, one could consider the function $\Omega_\varphi(z)$, the energy fraction in dark energy. The relation between these two functions can be expressed as

$$V(\varphi) = \frac{3}{2}(1-w_\varphi)\Omega_\varphi H^2, \tag{4.4}$$

$$w_\varphi = \frac{d\Omega_\varphi/d\log(1+z)}{3\Omega_\varphi(1-\Omega_\varphi)}, \tag{4.5}$$

following Wetterich (2004). Again, one could try to constrain the entire function Ω_φ. Alternatively, one may concentrate on a few aspects of this function. In the discussion of tracker solutions in Sec. 3.3.1, we have seen that the cosmon φ tracks the dominant component such that $\Omega_\varphi \approx$ const. during a long period in matter domination. For the exponential potential $V(\varphi) \propto \exp(-\alpha\varphi)$, we have $\Omega_\varphi = 3/(2\alpha^2)$ for the tracking solution. This amount of *early dark energy* Ω_e is a natural parameter to constrain. It can be complemented with a parameter describing the deviation from the cosmological constant in recent times, such as the present equation of state $w_{\varphi,0}$. Between the regime of constant $\Omega_\varphi \approx \Omega_e$ and the late-time regime, where quintessence is characterized by an equation of state $w_{\varphi,0}$, some interpolation can be made. Wetterich (2004) proposes to parametrize

$$R(z) \equiv \log\frac{\Omega_\varphi(z)}{1-\Omega_\varphi(z)}, \quad R(z) \approx R_0 + \frac{3w_{\varphi,0}\log(1+z)}{1+b\log(1+z)}, \tag{4.6}$$

where b describes the position of the transitional period. The relation of b and $w_{\varphi,0}$ to the early amount of dark energy is

$$\Omega_e \approx \frac{e^{R(0)+3w_{\varphi,0}/b}}{1+e^{R(0)+3w_{\varphi,0}/b}}. \tag{4.7}$$

This already is a reasonable approximation for many uncoupled quintessence models with the advantage of only three free parameters, $\Omega_{\varphi,0}$, Ω_e, and $w_{\varphi,0}$.

In the late-time Universe, close to $a = 1$, the parametrization is essentially equivalent to the wCDM parametrization. In the earlier parts of matter domination, however, it drastically deviates from wCDM as it approaches a constant energy fraction $\Omega_e > 0$. Unfortunately, it has become the standard to not use Ω_e as a parameter to describe the deviation from the wCDM case, but rather some time derivative of w at $a = 1$, such as dw/da. Such an ad-hoc parametrization cannot reproduce the interesting feature of early dark energy present in quintessence models. We schematically compare the three options in Fig. 4.1. At recent times, $a \approx 1$, the evolution is described by the equation

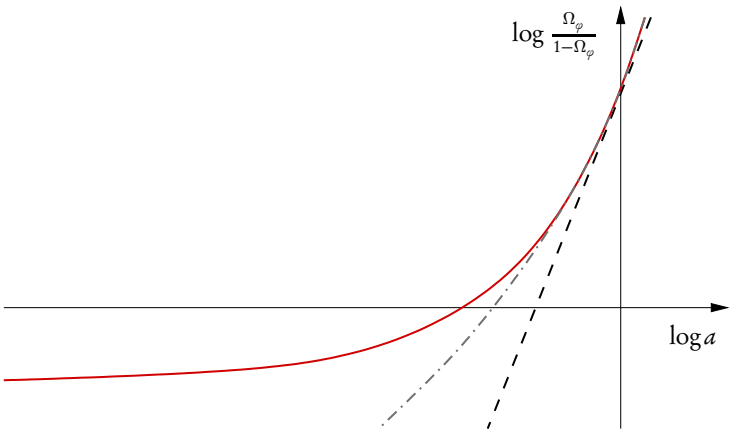

Figure 4.1: Schematic comparison of dark energy parametrizations, the y axis marks $a = 1$. A realistic quintessence scenario (red solid line) approaches a constant early dark energy fraction Ω_e for small a. The pure wCDM parametrization (black dashed line) is a straight line. A naive extension of the wCDM parametrization including a derivative like dw/da at $a = 1$ (grey dot-dashed line) does not reproduce the early behavior of quintessence.

of state $w_{\varphi,0}$ at present. There,

$$\frac{\Omega_\varphi}{1-\Omega_\varphi} = \frac{\rho_\varphi}{\rho_m} \approx \frac{\rho_{\varphi,0} a^{-3(1+w_{\varphi,0})}}{\rho_{m,0} a^{-3}} \propto a^{-3w_{\varphi,0}}. \tag{4.8}$$

This power law is a straight line in the logarithmic plot, and it is observed in all three curves. The pure wCDM parametrization continues along this line leading to a dark energy density completely negligible at early times (similar to a cosmological constant). The realistic case is an approach of Ω_e. This is not at all mimicked by the mere inclusion of a derivative of w_φ at $a = 1$. In general, it seems inadequate to perform just a Taylor expansion of w_φ at $a = 1$.

We conclude that the wCDM parametrization (assuming a constant equation of state) is a reasonable approximation for generic, uncoupled quintessence models in the late-time Universe. It neglects, however, early dark energy. In the wCDM scenario, dark energy becomes irrelevant quickly if we go to larger redshifts. This does not change much if we include in w a linear function in a.

4.1.2 Perturbations: sound speed

Models of dynamical dark energy do not only differ in the predicted expansion of the background. If we model dark energy as a cosmic fluid X with a separately conserved energy-momentum tensor,

$$\nabla_\nu T^{\mu\nu}_X = 0, \tag{4.9}$$

which is the case for *uncoupled* dark energy, we can characterize the fluid by three quantities: the (present) energy-density $\Omega_{X,0}$, the equation of state $w_X(a)$ as a function

of time, and the sound speed $c_s^2 \equiv \delta p_X / \delta \rho_X$ needed for the linear perturbation equations (2.72) and (2.73) (cf. also Gordon and Hu, 2004). The sound speed, in principle, is a function of Fourier mode as well as of time,

$$c_s^2 \equiv c_{s,k}^2(a) = \frac{\delta p_{X,k}(a)}{\delta \rho_{X,k}(a)}. \tag{4.10}$$

The linear perturbation equations (2.72) and (2.73) are only valid in the uncoupled case and under the assumption of general relativity. For coupled dark energy, there will be extra terms. In modified gravity, an important effect visible only in the perturbations is the possibility $\Psi \neq \Phi$ even in the absence of anisotropic shear.

The sound speed as defined by Eq. (4.10) is not a gauge-invariant quantity. So, we still have the freedom to choose a particular frame. In the following, we shall only consider the *rest-frame* speed of sound defined in a frame where the scalar velocity perturbation $v_{X,k}$ vanishes. In the case of quintessence, the linear perturbation of the energy-momentum tensor reads, by Eq. (3.61),

$$\delta T^{\mu}{}_{\nu} = \partial^{\mu}\delta\varphi\partial_{\nu}\bar{\varphi} + \partial^{\mu}\bar{\varphi}\partial_{\nu}\delta\varphi + \delta^{\mu}_{\nu}\,\delta\mathscr{L}_{\varphi}, \tag{4.11}$$

from which we can read off the velocity perturbation defined by $\delta T^{0}{}_{i} = (\bar{\rho}+\bar{p})v_i$, cf. Eq. (2.65),

$$v_i = -\frac{a}{\bar{\varphi}'}\partial_i\delta\varphi \tag{4.12}$$

using $\partial_i\bar{\varphi} = 0$. In the fluid's rest frame, we have established $\delta\varphi = 0$. As a consequence, the (rest-frame) sound speed

$$c_s^2 = \frac{\delta T^{i}{}_{i}/3}{-\delta T^{0}{}_{0}} = \frac{\bar{\varphi}'\delta\varphi' - aV_{,\varphi}\delta\varphi}{\bar{\varphi}'\delta\varphi' + aV_{,\varphi}\delta\varphi} = 1 \tag{4.13}$$

is just unity.

This is not a universal property of dynamical dark energy models. In the case of *k*-essence, we have seen that the speed of sound can take any value, cf. Sec. 3.3.2. The sound speed c_s^2 specializes to the *adiabatic sound speed* c_a^2 for adiabatic perturbations, i. e. if the entropy perturbation $(c_s^2 - c_a^2)\delta/w$ vanishes. The adiabatic sound speed is defined in terms of the background quantities,

$$c_a^2 \equiv \frac{\bar{p}'}{\bar{\rho}'} = w - \frac{w'}{3\frac{a'}{a}(1+w)}. \tag{4.14}$$

For a constant equation of state, we immediately note $c_a^2 = w$.

Let us now turn to the effect of the sound speed on perturbations in the fluid. Following Kodama and Sasaki (1984), we write the evolution of the total density perturbation $\delta\rho$ as

$$\left(\delta\rho a^3\right)'' + \left(1+3c_a^2\right)\frac{a'}{a}\left(\delta\rho a^3\right)' + \left[k^2c_s^2 - \frac{3}{2}(1+w)\left(\frac{a'}{a}\right)^2\right]\left(\delta\rho a^3\right) = 0, \tag{4.15}$$

where we have assumed the vanishing of the anisotropic shear perturbation. The interesting term in this equation is the source term driving the growth of $\delta\rho$, namely

$$s_k \equiv k^2 c_s^2 - \frac{3}{2}(1+w)\left(\frac{a'}{a}\right)^2 . \tag{4.16}$$

Ignoring the equation of state parameter w for a moment, we see that the physical scale $|c_s|k/a$ is compared with the Hubble scale $H = a'/(a^2)$. Consequently, there is an effective horizon no longer given by the Hubble scale but by $H_s = H/|c_s|$. This is called *the sound horizon*. Sapone and Kunz (2009) show, for scales $k/a \ll H_s$ well within the sound horizon and a constant equation of state, that there is a growing mode

$$\delta(a) \propto (1+w)\left(\frac{a}{1-3w} + \frac{\rho_{m,0}}{k^2}\right). \tag{4.17}$$

For scales far outside the sound horizon (assuming a constant sound speed parameter), $k/a \gg H_s$, the density contrast freezes to

$$\delta(a) \propto \frac{1+w}{2}\frac{\rho_{m,0}}{c_s^2 k^2}. \tag{4.18}$$

In both cases, the proportionality constant is just the initial fluctuation amplitude. Taking into account the equation of state w, the source term s_k, Eq. (4.16), compares the physical scale k/a with $\approx \sqrt{1+w}H/|c_s|$. More precisely, we may define a critical physical scale $\lambda_c = a/k_c$ where the source term vanishes,

$$\lambda_c = \sqrt{\frac{2}{3}}\frac{1}{\sqrt{1+w}}\frac{|c_s|}{H}. \tag{4.19}$$

This critical scale should be regarded as an improved definition of the sound horizon. We plot the dependence of this scale (compared to the Hubble horizon) on w and c_s^2 in Fig. 4.2.

A perturbation δ_k can only grow under the gravitational attraction if k/a is, at the same time, within the Hubble horizon H and within the sound horizon $1/\lambda_c$. In particular, there are clustering modes only if the sound horizon does not exceed the Hubble horizon, i. e. if

$$\lambda_c \lesssim H^{-1} \quad \text{or} \quad c_s^2 \lesssim 1+w. \tag{4.20}$$

Since the present dark energy equation of state is close to -1, the sound speed must be close to zero in order to show observable effects. These effects, in turn, are only visible on scales above λ_c. In the case of quintessence models, we have $c_s^2 = 1$ and, accordingly, for an equation of state $w_\varphi \leq 0$, always $\lambda_c \gtrsim H^{-1}$. Quintessence does not cluster on subhorizon scales.

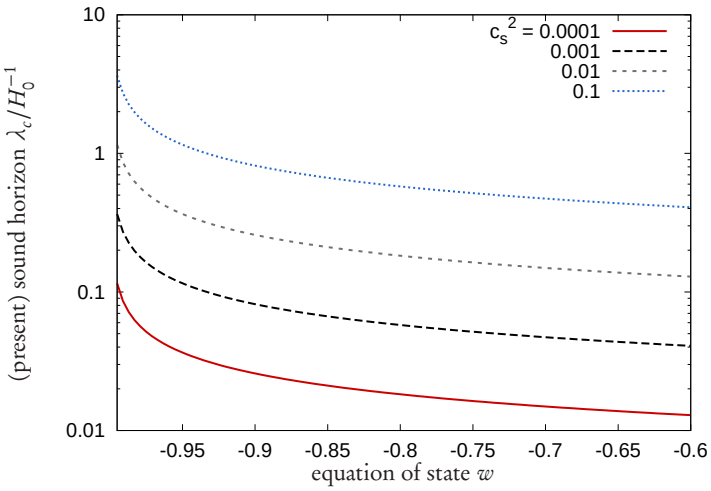

Figure 4.2: The critical scale λ_c at $a = 1$ in units of the Hubble scale for varying w and c_s^2.

4.1.3 Parametrized clustering

In principle, it is straightforward to evolve the linear perturbation equations numerically in the presence of a clustering dark-energy component. Approximate parametrizations of the solutions are, technically, not needed. The slight reduction of numerical effort that can be achieved by a parametrization comes at the cost of a loss of accuracy, which is often not clearly quantified. In our analysis, we will not analyze actual observational data, so that the constraints we give are just rough estimates based on uncertain, assumed properties of the Euclid mission. Moreover, the use of the wCDM parametrization with constant equation of state w and (rest-frame) speed of sound c_s^2 renders our analysis essentially illustrative. Precision is not an issue as long as we can account for all essential effects with reasonable accuracy. For the purpose of illustration, it is then even useful to work with parametrizations which allow some analytical insights that would otherwise remain hidden behind the numerics. Therefore, we do not evolve the linear perturbation equations numerically but rather use approximate, parametrized solutions for them.

The clustering of a dark energy component X due to a nontrivial speed of sound $c_s^2 < 1$ has two important implications, which we will parametrize separately:

1. It leads to a growing density perturbation $\delta\rho_X$ of dark energy on scales below the sound horizon λ_c. These are, in principle, observable via their gravitational potential Φ_X.

2. The gravitational potential Φ_X induced by dark energy perturbations is felt by matter perturbations. Matter perturbations consequently exhibit additional clustering.

We account for the first effect by introducing a quantity $Q(\boldsymbol{k},a)$ by

$$\Phi_{X,\boldsymbol{k}} = [Q(\boldsymbol{k},a) - 1]\, \Phi_{m,\boldsymbol{k}}. \tag{4.21}$$

We will adopt a particular parametrization for $Q(\boldsymbol{k},a)$ proposed by Sapone and Kunz (2009). Let us now turn to the second effect. Using the definition of $Q(\boldsymbol{k},a)$, we can write the Poisson equation of the total gravitational potential as

$$k^2\Phi_{\boldsymbol{k}} = -\frac{a^2}{2}\left(\delta\rho_{m,\boldsymbol{k}} + \delta\rho_{X,\boldsymbol{k}}\right) = -\frac{a^2}{2}Q(\boldsymbol{k},a)\,\delta\rho_{m,\boldsymbol{k}}. \tag{4.22}$$

This equation follows from Eqs. (2.67) and (2.68) if we work, for convenience, in the Newtonian limit. It tells us that the effect of dark energy clustering on the gravitational potential can be expressed as a variable Newton's constant $Q(\boldsymbol{k},a)$. This allows us to make use of parametrizations originally developed for this scenario. The parametrization we shall use is due to Linder and Cahn (2007) and has also been employed by Sapone et al. (2010).

The central function we shall consider is the growth function $D_\delta(k,a)$ defined by

$$\delta\rho_{m,\boldsymbol{k}}(a) = D_\delta(k,a)\,\frac{\delta\rho_{m,\boldsymbol{k}}(a=1)}{a}. \tag{4.23}$$

Following Linder (2005), the growth function $D_\delta(k,a)$ is parametrized by the growth index $\gamma = \gamma(k,a)$,

$$D_\delta(k,a) = \exp\int_0^a \frac{d\tilde{a}}{\tilde{a}}\left[\Omega_m(\tilde{a})^{\gamma(k,\tilde{a})} - 1\right]. \tag{4.24}$$

This means that we have a complete parametrization if we find an approximate relation between $\gamma(k,a)$, the effective Newton's constant $Q(k,a)$, and the parameter w of the model. This task has been performed by Linder and Cahn (2007), whose argument we shall briefly present. The linear perturbation evolution equation (4.15) for dark matter (i. e. $w = c_s^2 = 0$ and a variable Newton's constant Q) is rewritten for the variable

$$G(k,a) = \frac{d\log D_\delta(k,a)}{d\log a}. \tag{4.25}$$

This change of variables has the following advantage. During matter domination, and in the absence of dark energy clustering, $\delta_{m,\boldsymbol{k}}$ grows linearly with a whence $D_\delta(k,a)$ is constant and $G = 0$. So, the effects of dark energy can be treated as a linear perturbation in G. Under this approximation, the evolution equation can be solved to give

$$G(k,a) + 1 = \frac{1}{H}\int_0^a \frac{d\tilde{a}}{\tilde{a}}\left(\frac{\tilde{a}}{a}\right)^4 H\left[1 + \frac{3}{2}Q(k,\tilde{a})\,\Omega_m(\tilde{a})\right]. \tag{4.26}$$

Formally, we have replaced $Q(\boldsymbol{k},a)$ by the corresponding quantity depending on the dimensionless spectra of δ_m and δ_X rather than on the actual (three-dimensional)

perturbation variables, so that it only depends on the absolute value $k = |\boldsymbol{k}|$. The quantity $G(k,a)$ is related to the growth index $\gamma(k,a)$ by Eq. (4.24). If we assume that the effects of clustering dark energy mainly originate from the period of matter domination where Ω_m is close to one, we obtain

$$G(k,a)+1 = \Omega_m^{\gamma(k,a)} = (1-\Omega_X)^{\gamma(k,a)} \approx 1-\gamma(k,a)\Omega_X(a). \tag{4.27}$$

If we combine this with the approximate expression for $G(k,a)$ (4.26), one can deduce, eventually, a useful parametrization for the growth index:

$$\gamma(k,a) \approx \frac{3(1-w-A(k,a))}{5-6w}, \quad \text{with} \quad A(k,a) \equiv \frac{Q(k,a)-1}{\Omega_X(a)}. \tag{4.28}$$

It will be convenient to use, next to the growth function $D_\delta(k,a)$ for the matter density perturbation $\delta\rho_m$, an analogous growth function $D_\Phi(k,a)$ for the gravitational potential,

$$\Phi_k(a) = D_\Phi(k,a)\frac{\Phi_{k,0}}{a}, \quad \text{and hence} \quad D_\Phi(k,a) = \frac{Q(k,a)}{Q_0(k)} D_\delta(k,a). \tag{4.29}$$

We have now expressed all relevant quantities in terms of $Q(k,a)$. It remains to give a useful approximation for $Q(k,a)$. Analyzing modes well below and far outside the sound horizon H_s separately, and then combining the two solutions into an interpolative formula, Sapone and Kunz (2009) find

$$Q(k,a)-1 \approx (1+w)\frac{\Omega_X(a)}{\Omega_m(a)} \frac{a^{-3w}}{1-3w+\frac{2ak^2c_s^2}{3H_0^2\Omega_m(a)}}. \tag{4.30}$$

We show the results for this quantity as a function of k for $w = -0.8$ and varying sound speed parameter c_s^2 at $a = 1$ in Fig. 4.3. This figure already gives an impression where we can hope to see the effects of dark energy clustering. Essentially, it illustrates the relation discussed in Sec. 4.1.2, namely, that the clustering of dark energy is characterized by the critical scale $k_c \sim \sqrt{1+w}\,H/|c_s|$ playing the role of a sound horizon.

Using these results in Eq. (4.28) for the growth index $\gamma(k,a)$ of matter perturbations and eventually in Eq. (4.24) for the growth function, we can quantify the influence of dark energy clustering on the linear matter power spectrum $P(k)$. In Fig. 4.4, we show the effect (obtained by a numerical evolution of the perturbation equations rather than by our parametrizations). On scales outside the Hubble horizon, the result is strongly gauge-dependent. We have chosen the gauge-invariant perturbation variable $\Delta_m \equiv \delta_m + 3Ha/k\,(v_m - B)$ which defines the right-hand side of the Poisson equation for the matter-induced gravitational potential and specializes to δ_m in the Newtonian limit.

On subhorizon scales, $P(k)$ changes only at the percent level, even for sound speeds c_s^2 close to zero. For $c_s^2 = 0.1$, the effect is well below the percent level and only

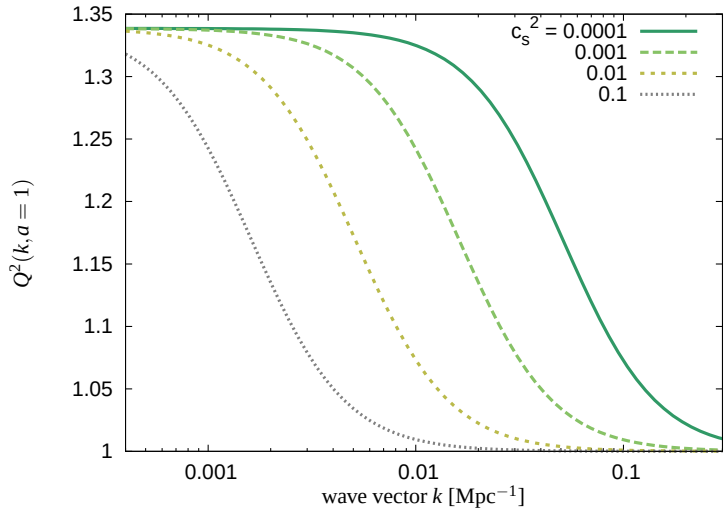

Figure 4.3: Enhancement of the effective Newton's constant (squared) $Q(k,a)^2$ felt by matter perturbations due to the clustering of the dark energy component. For increasing speed of sound c_s^2, the effect is shifted to larger scales (smaller k). The figure is taken from Ayaita et al. (2012a).

visible on scales very close to the Hubble horizon. The situation is more severe for an equation of state w closer to -1. Although current observations prefer an equation of state w very close to -1 (Bennett et al., 2012; Ade et al., 2013c), this should not be taken too seriously as the wCDM parametrization is not a realistic model. Realistically, w will only be close to -1 in the late Universe, hence allowing for dark energy clustering during earlier times in matter domination.

So far, we had quantified the scale where dark energy clustering occurs by the critical scale λ_c in Eq. (4.20). This gives a characteristic scale but does not tell us how large the clustering effect will be. This information is given by the function $Q(k,a)$. We can use this to define another scale telling us where the effect of dark energy clustering exceeds some threshold, which may be motivated by the precision of future experiments. For example, we may ask for which scales

$$Q(k,a=1) \gtrsim 1+\varepsilon \tag{4.31}$$

with some small threshold ε. This yields a physical scale

$$\lambda_\varepsilon = \frac{1}{k_\varepsilon} \gtrsim \sqrt{\frac{2\varepsilon}{3\Omega_{X,0}(1+w)}}\,\frac{|c_s|}{H_0} = \sqrt{\frac{\varepsilon}{\Omega_{X,0}}}\,\lambda_c \tag{4.32}$$

with the same dependence on w and c_s^2 as the critical scale λ_c. For example, if we employ exemplary values $\varepsilon = 1\%$ and $\Omega_{X,0} = 0.7$, we obtain

$$\lambda_\varepsilon \approx 0.1\,\frac{|c_s|}{\sqrt{1+w}}\,H_0^{-1}. \tag{4.33}$$

The condition for an observable effect is then estimated by $\lambda_\varepsilon \lesssim H_0^{-1}$.

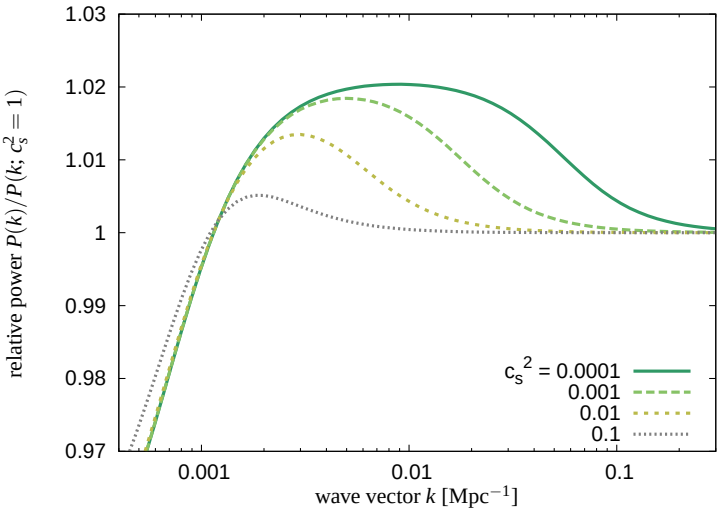

Figure 4.4: Growth of the (subhorizon) linear matter perturbations due to the enhanced effective Newton's constant, i. e. the extra gravitational potential induced by dark energy clustering. The figure is taken from Ayaita et al. (2012a).

4.2 3d weak lensing

4.2.1 Basics of weak gravitational lensing

Let us briefly collect some basic concepts of weak gravitational lensing in the context of cosmology. Our presentation and notations follow the review by Bartelmann and Schneider (2001). Details and clarifications about the range of validity of the formalism used here can also be found there.

Generalizing the standard general-relativistic result for the deflection angle $\hat{\alpha}$ of light passing a point mass m at impact parameter y,

$$\hat{\alpha} = \frac{m}{2\pi} \frac{y}{|y|^2}, \tag{4.34}$$

one obtains, for a nonrelativistic mass distribution ρ and the line-of-sight direction r (assumed unperturbed):

$$\hat{\alpha} = \frac{1}{2\pi} \int d^2y' \int dr\, \rho(y', r) \frac{y - y'}{|y - y'|^2}. \tag{4.35}$$

It is useful to consider the mapping between observed, distorted positions ϑ on the sky and the positions β that would be observed in the absence of the gravitational lens. We show these quantities in Fig. 4.5 in the idealized case of a single thin lens. The geometrical relation between ϑ and β is the *lens equation*

$$\beta = \vartheta - \alpha(\vartheta), \tag{4.36}$$

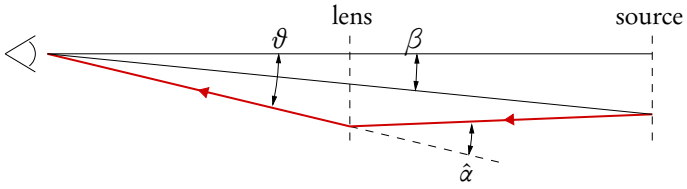

Figure 4.5: Illustration of weak gravitational lensing due to a thin lens. The red line is the actual path taken by a light ray. In the three-dimensional setting, the angles $\hat{\alpha}$, ϑ, and β are promoted to points on the unit sphere.

where $\boldsymbol{\alpha}(\boldsymbol{\vartheta})$ is the *scaled deflection angle*. Here, angles are unit vectors defining a direction on the unit sphere. It is obtained by a straightforward geometrical argument using the concept of *angular diameter distance* D_A, which is observationally defined as the quotient of the actual transverse size l of an object and the angle φ under which it is observed. In a static Minkowski spacetime, D_A is just the distance (for small angles, $\tan\varphi \approx \varphi$). In a flat FLRW metric, we instead have $D_A(r) = a\,r$. If $D_{A,s}$, $D_{A,l}$ denote the angular diameter distance of the source and the lens, respectively, and $D_{A,ls}$ denotes the angular diameter distance of the source from the lens, the scaled deflection angle is

$$\boldsymbol{\alpha}(\boldsymbol{\vartheta}) = \frac{D_{A,ls}}{D_{A,s}}\,\hat{\boldsymbol{\alpha}}(D_{A,l}\,\boldsymbol{\vartheta}). \tag{4.37}$$

We may define a *lensing* or *deflection potential* $\psi(r;\boldsymbol{\vartheta})$ whose angular gradient is the (scaled) deflection angle. Here, $r = r_s$ is the comoving distance of the source and $\boldsymbol{\vartheta}$ is, as before, the angle under which it is observed,

$$\psi(r;\boldsymbol{\vartheta}) = 2\int_0^r dr'\,\frac{r-r'}{r\,r'}\,\Phi(r';\boldsymbol{\vartheta}), \qquad \alpha_i(\boldsymbol{\vartheta}) = \partial_i\psi(r;\boldsymbol{\vartheta}), \tag{4.38}$$

in terms of the gravitational potential Φ in the Newtonian limit and with the abbreviation $\partial_i \equiv \partial/\partial\vartheta^i$. The deflection angle is related to the first derivative of the lensing potential. It is constant for a constant gradient $\partial_i\psi$, corresponding to a mere shift of the image. Since the true position of an object, typically a galaxy, is not known, this will be irrelevant for our analysis. The second derivative $\partial_i\partial_j\psi$ will determine the change of $\boldsymbol{\alpha}$ along the image of a galaxy. This will alter the size and the shape of the image. Even if the shapes of individual galaxies are approximated as intrinsically uncorrelated, the lensing effect induces a correlation since the second derivative $\partial_i\partial_j\psi$ changes more slowly than the fluctuating ellipticity field. In this way, one can detect the lensing signal *statistically*. We illustrate the influence of the lensing potential on the image of a galaxy (approximated as an ellipse) in Fig. 4.6 (inspired by Björn Malte Schäfer, private discussion). We conclude that the observationally relevant quantity, the shearing of the image, is related to the second derivatives of the gravitational potential and hence to the energy perturbation $\delta\rho$. This again expresses that weak gravitational lensing probes the matter distribution.

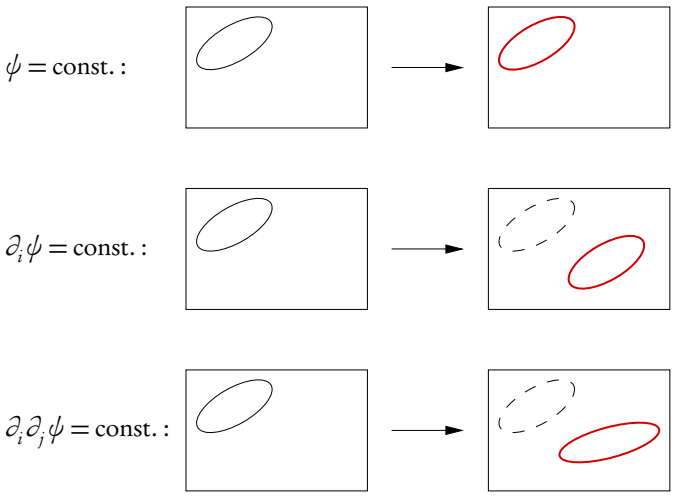

Figure 4.6: Change of a galactic image in weak gravitational lensing. A constant lensing potential leaves the image unchanged, a constant (angular) gradient causes a mere shift. The second derivative leads to an amplification and a shearing of the image. Higher gradients would distort the elliptical shape.

Mathematically, we may express the distortion of the image in a locally linear approximation with the help of the lensing Jacobian

$$\mathcal{A}_{ij} = \partial_j \beta_i = \delta_{ij} - \partial_i \partial_j \psi(r;\vartheta). \tag{4.39}$$

This is a symmetric matrix and may be decomposed into a term $\propto \delta_{ij}$ expressing the amplification of the image and a symmetric trace-free contribution expressing the shear of the image,

$$\mathcal{A} = (1-\varkappa)\begin{pmatrix} 1 & 0 \\ 0 & 1 \end{pmatrix} - \begin{pmatrix} \gamma_1 & \gamma_2 \\ \gamma_2 & -\gamma_1 \end{pmatrix}. \tag{4.40}$$

The parameters are called the *convergence* $\varkappa$ and the *shear* components γ_1, γ_2,

$$\varkappa = \frac{1}{2}\left(\partial_1^2 + \partial_2^2\right)\psi, \quad \gamma_1 = \frac{1}{2}\left(\partial_1^2 - \partial_2^2\right)\psi, \quad \gamma_2 = \partial_1\partial_2\psi. \tag{4.41}$$

The convergence $\varkappa$ quantifies the amplification of the image due to gravitational lensing. The shear, measuring the change in the shape of the image, can be estimated from observations of the ellipticities of galaxies. The complex ellipticity may be defined as

$$\epsilon = \frac{a-b}{a+b} e^{2i\varphi} \tag{4.42}$$

for a galaxy with semi-major axis a, semi-minor axis b, and an orientation on the sky given by the angle φ. Assuming that the orientations of galaxies are, intrinsically, just random, we would have $\langle\epsilon\rangle = 0$ in the absence of gravitational lensing. In *weak*

gravitational lensing, the shape is distorted according to $\epsilon \to \epsilon + \gamma$. Hence, gravitational lensing induces the average

$$\langle \epsilon \rangle = \gamma_1 + i\gamma_2 \tag{4.43}$$

such that the ellipticities are a (noisy) measure of the cosmic shear γ.

So, the observationally important quantity are the statistics of the shear (γ_1, γ_2). The (complex) shear $\gamma \equiv \gamma_1 + i\gamma_2$ is a spin-2 field as can be established by applying a rotation matrix with angle φ,

$$\gamma \mapsto \gamma e^{-2i\varphi}. \tag{4.44}$$

This complicates the analysis and will motivate us to switch to the — observationally less relevant but statistically equivalent — convergence $\varkappa$. The spin-2 quantity γ defined on the sphere may be expanded in spin-weighted spherical harmonics ${}_{\pm 2}Y_{\ell m}$,

$$\gamma(\boldsymbol{\vartheta}) = \sum_{\ell=0}^{\infty} \sum_{m=-\ell}^{+\ell} \left(\varepsilon_{\ell m} \pm i\beta_{\ell m}\right) {}_{\pm 2}Y_{\ell m}(\boldsymbol{\vartheta}), \tag{4.45}$$

and the statistical information is (cf., e. g., Hikage et al., 2011), in the linear case, encoded in the three angular spectra C_ℓ^ε, C_ℓ^β, and $C_\ell^{\varepsilon\beta}$ defined via $\langle \varepsilon_{\ell m} \varepsilon^*_{\ell' m'} \rangle = C_\ell^\varepsilon \delta_{\ell\ell'} \delta_{mm'}$ and so forth. These spectra include statistical information about the weak lensing potential ψ and hence about the matter distribution.

Analogously, an angular spectrum $C_\ell^\varkappa$ may be defined for the convergence $\varkappa$ via

$$\langle \varkappa_{\ell m} \varkappa_{\ell' m'} \rangle = C_\ell^\varkappa \delta_{\ell\ell'} \delta_{mm'}. \tag{4.46}$$

Let us specify the relation between the spectrum $C_\ell^\varkappa$, the spectrum C_ℓ^ψ of the lensing potential, and the power spectrum $P_\Phi(k)$ of the gravitational potential more precisely following Bartelmann (2010a). First, we simply have $\varkappa_{\ell m} = \ell(\ell+1)\psi_{\ell m}/2$ due to $\Delta_\Omega Y_{\ell m} = \ell(\ell+1) Y_{\ell m}$. This implies

$$C_\ell^\varkappa = \frac{[\ell(\ell+1)]^2}{4} C_\ell^\psi. \tag{4.47}$$

The convergence, consequently, contains *all* the statistical information of the lensing potential; it is thus, from a theoretical point of view, not necessary to also consider the shear spectra. Second, by expanding $\psi(r; \boldsymbol{\vartheta})$ given by Eq. (4.38) in spherical harmonics, it is straightforward to see

$$C_\ell^\psi = \frac{2}{\pi} \int_0^r dr' \, \frac{r - r'}{r\, r'} \int_0^r dr'' \, \frac{r - r''}{r\, r''} \int_0^\infty k^2 dk \, P_\Phi(k) \, j_\ell(k r') \, j_\ell(k r'') \tag{4.48}$$

with the power spectrum $P_\Phi(k)$ satisfying $\langle \Phi_{\boldsymbol{k}} \Phi^*_{\boldsymbol{k}'} \rangle = (2\pi)^3 P_\Phi(k) \delta^3(\boldsymbol{k} - \boldsymbol{k}')$. Making use of the approximation

$$j_\ell(kr) \approx \sqrt{\frac{\pi}{2}} \frac{1}{k\sqrt{\nu}} \delta(r - \nu/k) \tag{4.49}$$

with $\nu \equiv \ell + 1/2$ discussed in more detail in the next section (corresponding to a Limber projection), one obtains

$$C_\ell^\psi \approx \int_0^r dr' \left(\frac{r-r'}{r\,r'}\right)^2 P_\Phi(\nu/r'). \tag{4.50}$$

This can also be related to the power spectrum $P(k)$ of matter density perturbations by virtue of the gravitational Poisson equation telling us $k^4 P_\Phi = a^4 \rho_m^2 P/4$ in the absence of an additional clustering component.

4.2.2 The 3d formalism

So far, the lensing potential and with it the spectra of the shear components and of the convergence had an implicit dependence on the comoving distance r of the source. If the source redshifts are known, we can exploit this to obtain spectra for different distances r, hence moving from a 2d analysis to a 3d method. A straightforward approach is *weak lensing tomography* pioneered by Hu (1999, 2002a) where the observed source galaxies are grouped into redshift (or, equivalently, distance) bins (cf. also Ma et al., 2005; Takada and Jain, 2004; Refregier et al., 2004). The shear spectra can then be estimated for each bin separately, and these (auto-correlation) spectra are complemented with the cross-correlation spectra between the bins. Instead of bins, one may, of course, choose another set of orthogonal functions with preferable properties (Schäfer and Heisenberg, 2012).

Instead of choosing a discrete collection of bins, a more direct way is to keep the comoving distance as a continuous variable. The convergence $\varkappa$ and the lensing potential ψ are then three-dimensional fields. In linear perturbation theory, it has proven very useful to study fields and their statistical information (two-point correlators) in Fourier space, i. e. after a Cartesian Fourier transform. Since the measurements of angular properties (position of galaxies on the sky, measurement of ellipticities) are fundamentally different from measurements of redshifts, and since the redshift is not only a measure of distance but also of time, it is more adequate to work in spherical coordinates where angles and radial distances are clearly separated.

Spherical harmonic transform

The (Cartesian) Fourier transform is an expansion in eigenfunctions (plane waves) $f(\boldsymbol{k};\boldsymbol{x}) \propto \exp(i\boldsymbol{k}\cdot\boldsymbol{x})$ of the Laplacian with eigenvalues $\Delta f(\boldsymbol{k};\boldsymbol{x}) = -k^2 f(\boldsymbol{k};\boldsymbol{x})$. We wish to analogously find eigenfunctions of the Laplacian, in spherical coordinates (r,ϑ,φ), which separate according to

$$f(r,\vartheta,\varphi) = R(r)\,\Theta(\vartheta,\varphi). \tag{4.51}$$

The Laplacian in spherical coordinates can be decomposed as $\Delta = \Delta_r + \Delta_\Omega/r^2$ where

$$\Delta_r = \frac{1}{r^2}\frac{\partial}{\partial r} r^2 \frac{\partial}{\partial r} \text{ and } \Delta_\Omega = \frac{1}{\sin\vartheta}\frac{\partial}{\partial\vartheta}\left(\sin\vartheta\frac{\partial}{\partial\vartheta}\right) + \frac{1}{\sin^2\vartheta}\frac{\partial^2}{\partial\varphi^2}. \tag{4.52}$$

A suitable basis of eigenfunctions $\Theta(\vartheta,\varphi)$ of Δ_Ω is well-known: the spherical harmonics $Y_{\ell m}(\vartheta,\varphi)$ satisfying $\Delta_\Omega Y_{\ell m} = -\ell(\ell+1)Y_{\ell m}$. It remains to choose appropriate eigenfunctions $R(r)$ of the radial part Δ_r. These are the spherical Bessel functions $j_\ell(kr)$ satisfying

$$\Delta_r j_\ell(kr) = \left(-k^2 + \frac{\ell(\ell+1)}{r^2}\right) j_\ell(kr). \tag{4.53}$$

They are linked to the (cylindrical) Bessel functions J_ν by

$$j_\ell(x) = \sqrt{\frac{\pi}{2x}} J_\nu(x), \quad \text{for} \quad \nu \equiv \ell + \frac{1}{2}. \tag{4.54}$$

The orthogonality relation for the ordinary Bessel functions then translates into

$$\int_0^\infty r^2 dr\, j_\ell(kr) j_\ell(k'r) = \frac{\pi}{2k^2}\delta(k-k'). \tag{4.55}$$

Due to this result and the orthogonality of the spherical harmonics, we have a set of orthonormal eigenfunctions of the Laplacian:

$$f_{\ell m}(k;r,\vartheta,\varphi) = k\sqrt{\frac{2}{\pi}}\, j_\ell(kr)\, Y_{\ell m}(\vartheta,\varphi), \tag{4.56}$$

$$\Delta f_{\ell m}(k;r,\vartheta,\varphi) = -k^2 f_{\ell m}(k;r,\vartheta,\varphi), \tag{4.57}$$

$$\int r^2 dr \int d\Omega\, f_{\ell m}(k;r,\vartheta,\varphi) f_{\ell' m'}(k';r,\vartheta,\varphi) = \delta(k-k')\,\delta_{\ell\ell'}\,\delta_{mm'}. \tag{4.58}$$

We shall, in the following, expand scalar functions like the convergence $\varkappa(r,\vartheta,\varphi)$ in this basis,

$$\varkappa(r,\vartheta,\varphi) = \sum_{\ell=0}^{\infty}\sum_{m=-l}^{+l}\int dk\, k\, \varkappa_{\ell m}(k) f_{\ell m}(k;r,\vartheta,\varphi), \tag{4.59}$$

$$\varkappa_{\ell m} = \sqrt{\frac{2}{\pi}}\int r^2 dr \int d\Omega\, \varkappa(r,\vartheta,\varphi)\, j_\ell(kr)\, Y^*_{\ell m}(\vartheta,\varphi). \tag{4.60}$$

Note the inclusion of an additional factor k in the integrand of the first equation. This is not necessary, and it will lead to further factors of k or k^2 in later equations. We still define $\varkappa_{\ell m}(k)$ this way in order to use the same convention as Heavens (2003).

An analogous approach can be followed for the spin-2 field γ using spin-weighted spherical harmonics ${}_{\pm2}Y_{\ell m}$ instead of $Y_{\ell m} = {}_0Y_{\ell m}$.

Application to weak lensing

Let us now write the relations between the convergence $\varkappa$, the lensing potential ψ, and the gravitational potential Φ after an expansion in the basis $f_{\ell m}(k;r,\vartheta,\varphi)$. Since we

will use 3d weak lensing to parametrize clustering dark energy, we now also include the effects of the dark energy sound speed. The transformed relations read

$$\varkappa_{\ell m}(k) = -\frac{\ell(\ell+1)}{2}\,\psi_{\ell m}(k), \tag{4.61}$$

$$\psi_{\ell m}(k) = \int k'^2 dk'\,\eta_\ell(k,k')\,\Phi_{\ell m,0}(k'), \tag{4.62}$$

$$-k^2\Phi_{\ell m}(k) = \frac{a^2}{2}\,Q(k,a)\,\rho_m\,\delta_{\ell m}(k), \tag{4.63}$$

with the quantity

$$\eta_\ell(k,k') = \frac{4}{\pi}\int r^2 dr\, j_\ell(kr)\int_0^r dr'\,\frac{r-r'}{r\,r'}\,j_\ell(k'r')\,\frac{D_\Phi(k',a')}{a'} \tag{4.64}$$

and the transformed matter density contrast $\delta_{\ell m}(k)$. The subscript 0 refers to quantities evaluated at the present cosmic time $a = 1$. Here, $Q(k,a)$ is the enhanced, effective Newton's constant in the presence of dark energy clustering, and $g(k,a)$ is the growth function for the gravitational potential as introduced in Sec. 4.1.3. We will often encounter integrals in the form of Eq. (4.62) such that it will be useful to introduce the summation convention

$$A(k,k')B(k',k'') = \int_0^\infty k'^2 dk'\,A(k,k')B(k',k'') \tag{4.65}$$

also used by Heavens (2003).

The cosmologically interesting quantity is the two-point correlator $\langle\varkappa_{\ell m}(k)\varkappa_{\ell' m'}(k')\rangle$ related to the statistics of the lensing potential. This generalizes the two-dimensional case given by Eq. (4.46) and gives the correlation function

$$\langle\varkappa_{\ell m}(k)\varkappa_{\ell' m'}(k')\rangle = \frac{1}{k^2}\,C_\ell^\varkappa(k,k')\,\delta_{\ell\ell'}\,\delta_{mm'}, \tag{4.66}$$

where the factor $1/k^2$ is an artefact of the extra factor k that we introduced in Eq. (4.59) to match the convention of Heavens (2003). The Kronecker deltas are a result of the assumed statistical homogeneity and isotropy. Using the above relations (4.61) to (4.63), this can be linked to the matter power spectrum $P_0(k)$ at the present cosmic time $a = 1$ and the effective Newton's constant $Q(k,a)$ accounting for the effect of dark energy clustering,

$$\varkappa_{\ell m}(k) = \frac{\ell(\ell+1)}{2}\,\eta_\ell(k,k')\,\frac{1}{2k'^2}\,Q_0(k)\,\rho_{m,0}\delta_{\ell m,0}(k') \tag{4.67}$$

and hence

$$C_\ell^\varkappa(k,k') = A_\ell^2\,\eta_\ell(k,k'')\,\frac{Q_0(k'')^2\,P_0(k'')}{k''^4}\,\eta_\ell(k',k'') \tag{4.68}$$

with $A_\ell = \ell(\ell+1)/4 \cdot \rho_{m,0}$.

In practice, the shear field is not observable directly but it is estimated from the ellipticities of individual galaxies. We have to take into account the limitations given by the survey properties. In particular, we have to include the error of the redshift measurement, the survey's galaxy distribution, and the shot noise in the shear estimation due to the random orientations of galaxies. Rather than the shear γ, one will measure an estimator $\hat{\gamma}$. For simplifying the argument, we shall (unrealistically) assume that we could measure the convergences $\varkappa_g$ of galaxies. In that case, an estimator of the convergence $\varkappa$ in some small comoving spatial volume ΔV around the point (r, ϑ, φ) would be the average value

$$\hat{\varkappa}(r,\vartheta,\varphi) = \frac{1}{N_g} \sum_g \varkappa_g, \tag{4.69}$$

where N_g is the number of galaxies located in ΔV, and the sum is taken over these galaxies g. In the limit of a very small ΔV, this relation becomes $\hat{\varkappa} \propto \sum_g \varkappa_g \delta^3(\boldsymbol{x} - \boldsymbol{x}_g)$ (where g runs over all galaxies), and its spherical harmonic transform is, by Eq. (4.60),

$$\hat{\varkappa}_{\ell m}(k) = \sqrt{\frac{2}{\pi}} \sum_g \varkappa_g \, j_\ell(k r_g) \, Y^*_{\ell m}(\vartheta_g, \varphi_g). \tag{4.70}$$

Let us now derive the expectation value of this estimator given the properties of the survey. The sum over the galaxies can be replaced by an integral over the expected (assumed spherically symmetric) number density $n(r)$ of galaxies. In particular, we assume a full-sky survey for simplifying our analysis. The radial part $\delta(r - r_g)$ of the delta function is to be replaced by the redshift uncertainty $p(r_g|r)$ expressing the probability that the galaxy observed at r_g is located at r. The measurement of the angular position is still assumed to be exact. We thus obtain for the expectation value $\bar{\varkappa}$ of the estimator:

$$\bar{\varkappa}(r,\vartheta,\varphi) = \int 4\pi r'^2 dr' \, n(r') \int dr'' \, p(r'|r'') \, \varkappa(r'', \vartheta, \varphi). \tag{4.71}$$

In order to use Eqs. (4.61) to (4.63), we will transform both $\bar{\varkappa}$ and $\varkappa$ to the basis $f_{\ell m}(k)$. Heavens (2003) goes even further and also transforms the individual integrals, over $n(r')$ and $p(r'|r'')$, yielding

$$\bar{\varkappa}_{\ell m}(k) = Z_\ell(k,k') M_\ell(k',k'') \, \varkappa_{\ell m}(k'') \tag{4.72}$$

with the quantities

$$Z_\ell(k,k') = \frac{2}{\pi} \int r'^2 dr' \int dr \, p(r'|r) \, j_\ell(k'r) \, j_\ell(kr'), \tag{4.73}$$

$$M_\ell(k,k') = \frac{2}{\pi} \int r^2 dr \, n(r) \, j_\ell(kr) \, j_\ell(k'r). \tag{4.74}$$

Transforming both integrals in Eq. (4.71) introduces one unnecessary transformation. Therefore, the product $Z_\ell(k,k')M_\ell(k',k'')$ will produce the orthogonality relation of the spherical Bessel functions. We shall use this later in order to improve the numerical efficiency.

Let us specify the functions $n(r)$ and $p(r'|r)$, estimated for the Euclid survey (Amara and Refregier, 2007). We use

$$n(r)\,r^2 dr = C\left(\frac{z}{\bar{z}}\right)^2 \exp\left[-\left(\frac{z}{\bar{z}}\right)^\beta\right] dz, \tag{4.75}$$

with $\beta = 3/2$, $dz = dz/dr \cdot dr = H\,dr$, and the normalization $C = N\beta/\bar{z}$, where N is the total number of galaxies in the (full-sky) survey. We have evaluated the normalization in redshift space according to

$$N = \int_0^\infty dz\, n(z) = \frac{C\bar{z}}{\beta}\int_0^\infty dt\, t^{\zeta-1}e^{-t} = \frac{C\bar{z}}{\beta}\Gamma(\zeta) \quad \text{with} \quad t \equiv \left(\frac{z}{\bar{z}}\right)^\beta \tag{4.76}$$

and $\zeta = 3/\beta$, $\Gamma(\zeta) = \Gamma(2) = (2-1)! = 1$. Assuming a total number of ≈ 100 galaxies per square arcminute, N amounts to $\sim 10^9$. The redshift parameter $\bar{z} \approx 0.64$ corresponds to a median redshift $z_{\rm med} \approx 0.9$ (Amara and Refregier, 2007).

For the redshift uncertainty, we assume a simple Gaussian error with variance σ_z^2,

$$p(r'|r)dr' = \frac{1}{\sqrt{2\pi}\sigma_z}\exp\left[-\frac{(z-z')^2}{2\sigma_z^2}\right] dz' \tag{4.77}$$

with $\sigma_z \approx 0.02$ (Heavens, 2003), equal for all galaxies. A more realistic assumption would be that $\sigma_z/(1+z)$ is approximately constant; in this case, the probability distribution $p(r'|r)$ would not be a function of the redshift difference $(z-z')$, and numerical optimizations regarding convolutions would not be applicable.

The estimator $\hat{x}$ can be expressed by its expectation value $\bar{x}$ plus an unbiased noise (related to the random orientations of galaxies when we wish to infer the shear field). The covariance matrix $C_{\ell\ell',mm'}(k,k') \equiv C^{\hat{x}}_{\ell\ell',mm'}(k,k')$ splits into a signal and a noise contribution,

$$C_{\ell\ell',mm'}(k,k') = \langle \hat{x}_{\ell m}(k)\hat{x}^*_{\ell' m'}(k')\rangle = \langle \bar{x}_{\ell m}(k)\bar{x}^*_{\ell' m'}(k')\rangle + N_{\ell\ell',mm'}(k,k') \tag{4.78}$$

with a noise covariance N. Since we assumed a full-sky analysis and isotropic survey properties, it is clear that the covariance will be diagonal in (ℓ,ℓ') and independent of m and m'. This means

$$C_{\ell\ell',mm'}(k,k') = C_\ell(k,k')\,\delta_{\ell\ell'}\delta_{mm'}. \tag{4.79}$$

The more general case is briefly discussed by Heavens (2003). We may use Eqs. (4.72) and (4.67) to calculate the signal covariance. Introducing the abbreviation

$$B_\ell(k,k') \equiv Z_\ell(k,k'')M_\ell(k'',k''')\eta_\ell(k''',k'), \tag{4.80}$$

we obtain

$$S_\ell(k,k') \equiv \langle \bar{x}_{\ell m}(k) \bar{x}_{\ell m}(k') \rangle = A_\ell^2 \, B_\ell(k,k'') \frac{Q_0(k'')^2 \, P_0(k'')}{k''^4} \, B_\ell(k',k''). \tag{4.81}$$

The signal covariance of the estimator has the same form as the covariance of the (actual) convergence $\varkappa$ from Eq. (4.68). The only difference are the additional multiplications by the matrices Z_ℓ and M_ℓ. The mode coupling $\eta_\ell(k,k')$ due to gravitational lensing is supplemented by additional mode couplings induced by the survey properties, $\eta_\ell \to B_\ell$. The linear matter power spectrum $P_0(k)$ can be obtained by a numerical integration of the linear perturbation equations (as performed, e. g., by CAMB) or by a parametrization (Eisenstein and Hu, 1997, 1998).

The shot noise in the relation between cosmic shear and ellipticities is just related to the number density of galaxies in the survey, which, transformed to spherical harmonic space, is encoded in the matrix M_ℓ. We follow Heavens (2003) and use

$$N_\ell(k,k') = \frac{\sigma_\epsilon^2}{4} M_\ell(k,k') \tag{4.82}$$

with $\sigma_\epsilon^2 \approx 0.1$. Assuming just a shot noise neglects the intrinsic alignments of neighboring galaxies, which lead to a correlation of the ellipticities (Giahi-Saravani and Schäfer, 2013b; Capranico et al., 2012; Giahi-Saravani and Schäfer, 2013a; Joachimi and Bridle, 2010; Joachimi and Schneider, 2010; Kirk et al., 2010; Schäfer, 2009; Heavens et al., 2000). These and other systematic errors are discussed in the literature and are not expected to have a strong impact on parameter estimation (March et al., 2011; Takada and Jain, 2009; Kitching et al., 2008; Huterer et al., 2006). It is justified to ignore these effects in our illustrative forecast.

A closer look at the matrices Z_ℓ, M_ℓ, η_ℓ, and B_ℓ

The covariance $C_\ell(k,k')$ of the estimator $\hat{x}_{\ell m}(k)$ is given by a lengthy product (4.81), involving a large number of integrations. In order to get a better feeling for this quantity, we show the matrices Z_ℓ (linked to the redshift error), M_ℓ (expressing the galaxy distribution), and η_ℓ (the mode coupling induced by weak lensing) in Fig. 4.7.

Let us understand these matrices in more detail analytically. This will also lead to a drastically simplified way to approximate these quantities in numerical calculations. From the ordinary Bessel functions $J_\nu(x)$, one can construct a family of functions $\eta_\varepsilon(x)$ which approach the Dirac delta $\delta(x)$ for small ε,

$$\eta_\varepsilon(x) = \frac{1}{\varepsilon} J_{1/\varepsilon}(\xi), \quad \text{with} \quad \xi \equiv \frac{x+1}{\varepsilon}. \tag{4.83}$$

Choosing $\nu = 1/\varepsilon$ and writing $\nu = \ell + 1/2$, we can translate this to the spherical Bessel functions,

$$\eta_\varepsilon(x) = \sqrt{\frac{2}{\pi}} \, \nu \sqrt{\xi} \, j_\ell(\xi). \tag{4.84}$$

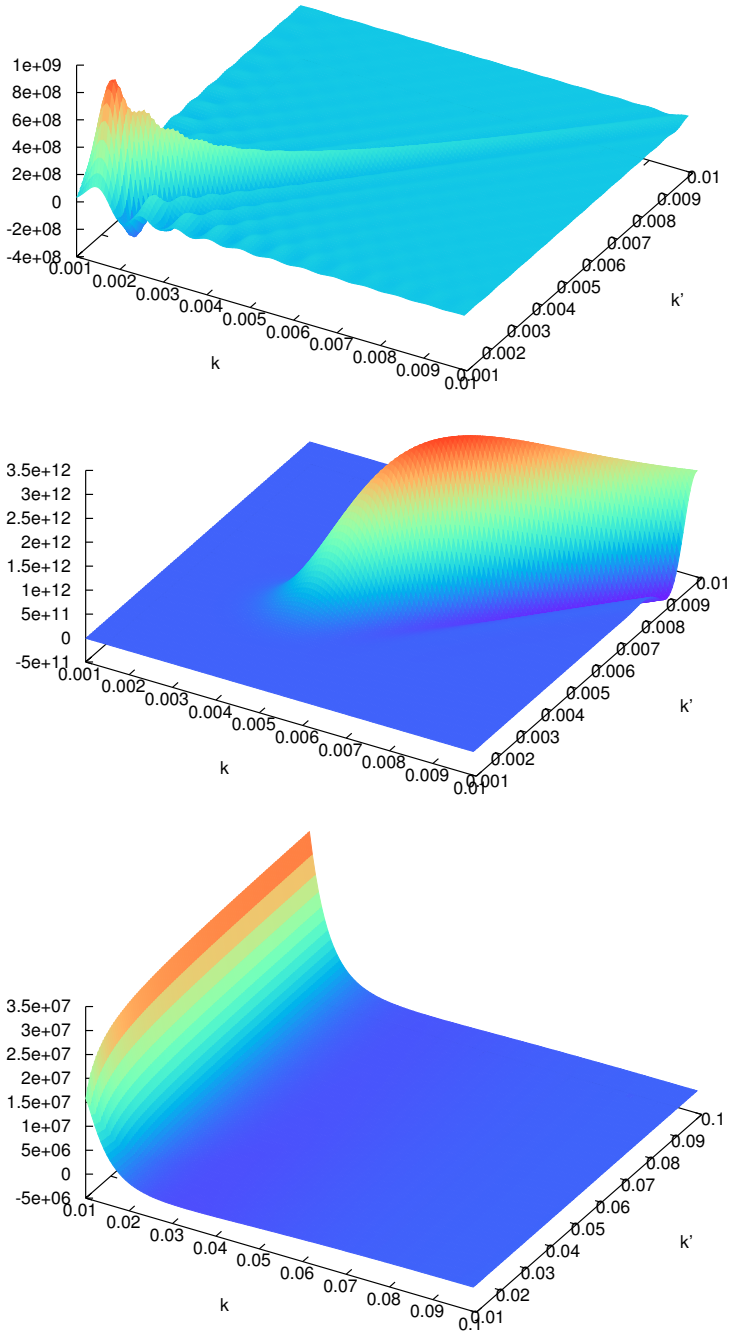

Figure 4.7: The matrices (from top to bottom) $Z_{10}(k,k')$, $M_{20}(k,k')$, and $\eta_{10}(k,k')$. All units in (powers of) Mpc.

In other words, for large ℓ, the spherical Bessel functions essentially reduce to a Dirac

delta,

$$j_\ell(k\,r) \approx \sqrt{\frac{\pi}{2}}\,\frac{1}{k\sqrt{\nu}}\,\delta(r-\nu/k). \tag{4.85}$$

This essentially corresponds to the Limber approximation (cf., e. g., LoVerde and Afshordi, 2008; Kitching and Heavens, 2010; Bartelmann and Schneider, 2001). For convenience, we define $r_{\nu,k} \equiv \nu/k$.

Applying this on the matrices, we immediately find

$$Z_\ell(k,k') \approx \frac{\nu}{k^3 k'}\,p(r_{\nu,k}|\,r_{\nu,k'}), \tag{4.86}$$

$$M_\ell(k,k') \approx \frac{1}{k^2}\,n(r_{\nu,k})\,\delta(k-k'), \tag{4.87}$$

$$\eta_\ell(k,k') \approx 2\frac{k'-k}{k^3 k'}\,\frac{D_\Phi(k',r_{\nu,k'})}{a(r')} \text{ for } k \le k' \text{ and } \approx 0 \text{ else.} \tag{4.88}$$

The matrix Z_ℓ couples modes whose associated distances $r_{\nu,k} = \nu/k$ are within the uncertainty of the redshift measurement. It reduces to a delta function when the redshift error is neglected. The matrix M_ℓ essentially weights each mode with the galaxy number density $n(\nu/k)$. In this approximation, the matrix B_ℓ is given by

$$B_\ell(k,k') \approx 2\frac{\nu}{k^3 k'}\,\frac{D_\Phi(k',a(r_{\nu,k'}))}{a(r_{\nu,k'})}\int_{r_{\nu,k'}}^{\infty} d\,r\;p(r_{\nu,k}|r)\,n(r)\,\frac{r-r_{\nu,k'}}{r\,r_{\nu,k'}}. \tag{4.89}$$

We show the matrix $B_\ell(k,k')$, $\ell = 10$, calculated without this approximation, in Fig. 4.8, where we also plot the difference to the approximate calculation. This difference amounts to $\lesssim 10\%$ of the amplitude.

In our quantitative analysis, we will not make use of the approximative scheme although the accuracy is, at least for large enough ℓ, reasonably good. In the full evaluation of B_ℓ, it is useful to use the orthogonality relation of the spherical Bessel functions j_ℓ. Thereby, the number of nested integrations is reduced considerably, and we get

$$B_\ell(k,k') = \frac{4}{\pi}\int r'^2 d\,r'\,j_\ell(k\,r')\int d\,r\;p(r'|r)\,n(r)\,F_\ell(k',r), \tag{4.90}$$

where

$$F_\ell(k',r) \equiv \int_0^r d\,r''\,j_\ell(k'\,r'')\,\frac{r-r''}{r\,r''}\,\frac{D_\Phi(k',a'')}{a''}. \tag{4.91}$$

Since the probability distribution $p(r'|r)$ can be written as a function of the redshift difference $p(z'-z)$ in redshift space, the inner integral in Eq. (4.90) can be written as a convolution allowing for an efficient calculation with the help of a Fast Fourier Transform, since the Fourier coefficients of the individual functions in the integrand can be multiplied to give the Fourier coefficients of the convolution. The details are explained in Ayaita et al. (2012a).

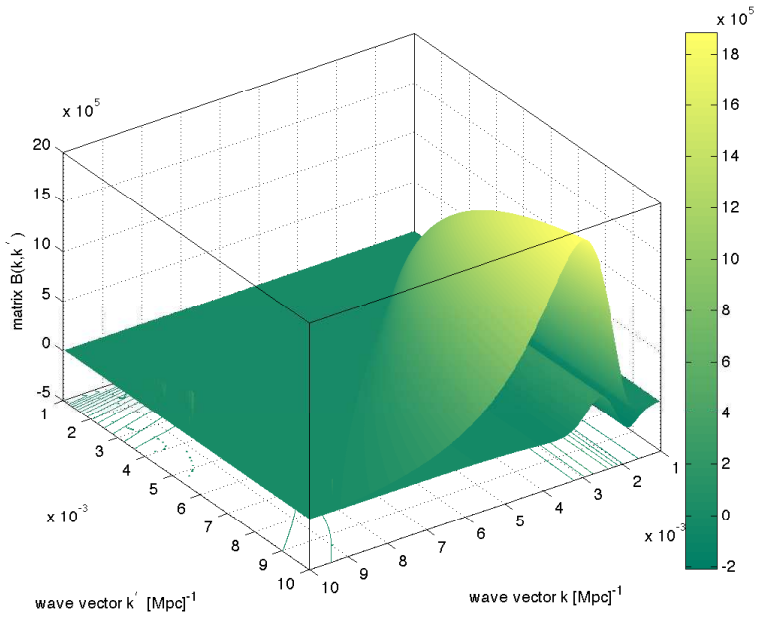

Figure 4.8: The product $B_\ell(k,k') = Z_\ell(k,k'')M_\ell(k'',k''')\eta_\ell(k''',k')$ for $\ell = 10$. The lower surface and the contour lines quantify the difference between the full calculation and the approximation. The figure is taken from Ayaita et al. (2012a).

4.3 Fisher matrix approach

4.3.1 Likelihood and Fisher matrix

Consider an experiment providing a data vector $\boldsymbol{x}$ (such as a list of measured galactic ellipticities). We model the observation as a random experiment yielding data $\boldsymbol{x}$ with some probability, the *likelihood*, given a vector $\boldsymbol{\vartheta}$ of N_ϑ model parameters. In cosmology, as in our case, these parameters will just be the cosmological parameters we wish to consider, $\boldsymbol{\vartheta} = (w_X, c_s^2, \ldots)$. The probability distribution function for the data is the likelihood function $L(\boldsymbol{x};\boldsymbol{\vartheta})$. The 'true' and unknown parameters are labeled $\boldsymbol{\vartheta}^*$. If the experimental data vector $\boldsymbol{x}$ is given, an obvious estimate for $\boldsymbol{\vartheta}^*$ are the *maximum likelihood* parameters $\hat{\boldsymbol{\vartheta}}$ for which

$$\left.\frac{\partial L}{\partial \vartheta_i}\right|_{\vartheta=\hat{\vartheta}} = 0. \tag{4.92}$$

This is not just an arbitrary choice; the maximum likelihood estimator has theoretically appealing properties. It is, in the limit of very large data vectors, the 'best unbi-

ased estimator' (cf. Tegmark et al., 1997) in the sense

$$\langle \hat{\boldsymbol{\vartheta}} \rangle = \boldsymbol{\vartheta}^*, \tag{4.93}$$

$$\Delta \hat{\vartheta}_i^2 \equiv \langle \hat{\vartheta}_i^2 \rangle - \langle \hat{\vartheta}_i \rangle^2 = \min. \tag{4.94}$$

The maximum of the likelihood L is thus of particular importance. Typically, we may even assume that the likelihood falls off quickly for parameters $\boldsymbol{\vartheta}$ away from the maximum $\hat{\boldsymbol{\vartheta}}$. Then, the local neighborhood of $\hat{\boldsymbol{\vartheta}}$ is, essentially, equivalent to the likelihood everywhere. As a first approximation, we may model this neighborhood by a multivariate Gaussian,

$$L(\boldsymbol{x};\boldsymbol{\vartheta}) \approx \frac{1}{\sqrt{(2\pi)^{N_\vartheta} \det T}} \exp\left[-\frac{1}{2}\left(\boldsymbol{\vartheta}-\hat{\boldsymbol{\vartheta}}\right)^T T^{-1} \left(\boldsymbol{\vartheta}-\hat{\boldsymbol{\vartheta}}\right)\right] \tag{4.95}$$

with a covariance matrix T. Given some (not necessarily Gaussian) likelihood L, we may estimate T after expanding at the maximum,

$$\log L(\boldsymbol{x};\boldsymbol{\vartheta}) \approx \log L(\boldsymbol{x};\hat{\boldsymbol{\vartheta}}) + \frac{1}{2} \left.\frac{\partial^2 \log L}{\partial \vartheta_i \partial \vartheta_j}\right|_{\boldsymbol{\vartheta}=\hat{\boldsymbol{\vartheta}}} \left(\vartheta_i - \hat{\vartheta}_i\right)\left(\vartheta_j - \hat{\vartheta}_j\right) \tag{4.96}$$

and then identifying

$$T_{ij}^{-1} = -\left.\frac{\partial^2 \log L}{\partial \vartheta_i \partial \vartheta_j}\right|_{\boldsymbol{\vartheta}=\hat{\boldsymbol{\vartheta}}}. \tag{4.97}$$

Alternatively, rather than approximating L as a Gaussian in the first place, we may write down a similar relation to define a matrix characterizing the likelihood,

$$F_{ij} \equiv \left\langle -\frac{\partial \log L}{\partial \vartheta_i \partial \vartheta_j} \right\rangle. \tag{4.98}$$

This is the *Fisher information matrix*. If the likelihood is indeed Gaussian in the parameters $\boldsymbol{\vartheta}$, it is just the inverse of the covariance matrix T_{ij}.

A crucial property of the Fisher matrix is that it puts stringent bounds on how well an estimator can be. In fact, for any unbiased estimator, the *Cramér-Rao* bound

$$\Delta \vartheta_i^2 \geq \frac{1}{F_{ii}} \tag{4.99}$$

holds (cf. Tegmark et al., 1997, for an introduction and details). For very large data sets, the maximum likelihood estimator approaches the best unbiased estimator and this inequality becomes, approximately, an equality. We will, for simplicity, not sharply distinguish between the Cramér-Rao bound and the actual uncertainty of the estimator.

Estimating the Fisher matrix for a future experiment allows us to forecast how well we will be able to constrain cosmological parameters. In order to visualize not only

the individual constraints $\Delta\vartheta_i$ but also the correlation between different parameters, it has become conventional to show confidence regions for multiple parameters. If we assume a Gaussian likelihood (in the parameters), a contour of constant likelihood enclosing a confidence region is given by the constraint

$$\left(\boldsymbol{\vartheta} - \hat{\boldsymbol{\vartheta}}\right)^T F \left(\boldsymbol{\vartheta} - \hat{\boldsymbol{\vartheta}}\right) = \text{const.} \tag{4.100}$$

Since F is symmetric, this equation defines an N_ϑ-dimensional ellipsoid. For two parameters ϑ_1, ϑ_2 (e. g. after marginalizing over the remaining parameters), this can be visualized as an ellipse, cf. Fig. 4.9. Conventionally, one chooses 1σ or 2σ confidence

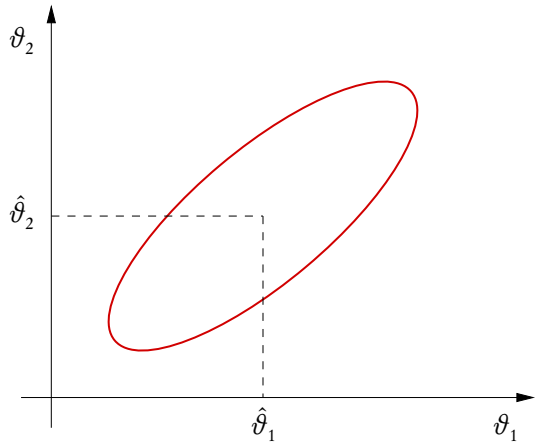

Figure 4.9: A contour enclosing a confidence region or, more precisely, the Cramér-Rao bound, for parameters ϑ_1, ϑ_2, also called *Fisher ellipse*.

regions. The projections of the ellipse on the axes give the individual uncertainties $\Delta\vartheta_1$, $\Delta\vartheta_2$.

We expect that, typically, the shape and size of the ellipse will not be very sensitive to the precise assumed maximum likelihood point $\hat{\boldsymbol{\vartheta}}$, which is, before the experiment is performed, not known. Hence, we can forecast constraints without precise knowledge of $\hat{\boldsymbol{\vartheta}}$.

Let us assume that the likelihood $L(\boldsymbol{x};\boldsymbol{\vartheta})$, as function of the data $\boldsymbol{x}$, is also approximately Gaussian with a covariance C and an average value $\mu = \langle \boldsymbol{x} \rangle$. Then, following Tegmark et al. (1997), as a function of $\boldsymbol{x}$, we write

$$\log L(\boldsymbol{x};\boldsymbol{\vartheta}) \approx -\frac{1}{2}\log\det C - \frac{1}{2}(\boldsymbol{x}-\mu)^T C^{-1}(\boldsymbol{x}-\mu) - \frac{1}{2}N_x \log 2\pi. \tag{4.101}$$

Using $\log\det C = \operatorname{tr}\log C$, this becomes

$$\log L \approx -\frac{1}{2}\operatorname{tr}\left[\log C + C^{-1}(\boldsymbol{x}-\mu)(\boldsymbol{x}-\mu)^T\right] - \frac{1}{2}N_x \log 2\pi. \tag{4.102}$$

If $L(\boldsymbol{x};\boldsymbol{\vartheta})$ is also Gaussian in the parameters $\boldsymbol{\vartheta}$, it is straightforward to obtain the Fisher matrix via the second derivatives of $\log L$. This further simplifies for observables normalized such that $\boldsymbol{\mu} = \langle \boldsymbol{x} \rangle = 0$. This is the case for a shear measurement, and we shall use this simplification. The Fisher matrix then reads

$$F_{ij} = \frac{1}{2}\mathrm{tr}\left[C^{-1}\frac{\partial C}{\partial \vartheta_i}\cdot C^{-1}\frac{\partial C}{\partial \vartheta_j}\right]. \tag{4.103}$$

4.3.2 3d weak lensing Fisher matrix

In our analysis, we choose the cosmological parameters $\boldsymbol{\vartheta} = (\Omega_m, A_s, h, n_s, w, \log_{10} c_s^2)$; here, Ω_m also determines $\Omega_X = 1-\Omega_m$ due to the flatness condition and neglecting radiation. The present Hubble parameter H_0 is included as the dimensionless quantity h, cf. Eq. (2.17). The primordial scalar adiabatic perturbations (i. e. the initial conditions for linear perturbation theory) are characterized by the amplitude A_s and the spectral index n_s, cf. Sec. 3.2.2. The dynamics of the dark energy component (its background and its linear perturbation evolution) is described by the equation of state $w \equiv w_X$ and the (rest-frame) sound speed c_s^2, both assumed constant. Choosing $\log_{10} c_s^2$ as a parameter rather than c_s^2 has two reasons. First, regarding Figs. 4.3 and 4.4, we may not expect tight constraints on c_s^2 but rather constraints for the order of magnitude of c_s^2, i. e. on $\log_{10} c_s^2$. Second, the likelihood is not expected to have an approximately Gaussian shape if c_s^2 is taken as a parameter. The weak constraints on c_s^2 will be reflected in a likelihood extending over a wide region. This likelihood will be fitted by a very flat Gaussian around the maximum, and this Gaussian extends to values $c_s^2 < 0$ where we would expect a very different behavior. In other words, in a wide region, the dependence of the matter power spectrum $P_0(k)$ on the sound speed c_s^2 will not be linear (Ballesteros and Lesgourgues, 2010). The parameter $\log c_s^2$ avoids this to some extent.

We will use Eq. (4.103) for the computation of the 3d weak lensing Fisher matrix. The trace is performed over ℓ, m, and k. Since the convergence covariance $C_\ell(k,k')$ is independent of m, the sum over m just returns a factor $2\ell+1$; this just reflects the fact that, due to statistical isotropy, we have $2\ell+1$ independent modes m. The sum over ℓ runs, in principle, from 0 to ∞. We will, however, use a finite range from some $\ell_{\min}$ to $\ell_{\max}$ discussed later. The Fisher matrix is thus

$$F_{ij} = \sum_{\ell=\ell_{\min}}^{\ell_{\max}} \frac{2\ell+1}{2}\mathrm{tr}_k\left[C^{-1}\frac{\partial C}{\partial \vartheta_i}\cdot C^{-1}\frac{\partial C}{\partial \vartheta_j}\right] \tag{4.104}$$

where the summation convention (4.65) is implied, and the covariance $C_\ell(k,k')$ is given by a signal and a noise part, $C_\ell(k,k') = S_\ell(k,k') + N_\ell(k,k')$ defined by Eqs. (4.81) and (4.82).

Since the trace is a basis-independent operation, we have the freedom to transform the expression to another basis such that the computation becomes manageable. Recalling Eqs. (4.81) and (4.90), the calculation of $C_\ell(k,k')$ already requires several nested

integrals. The additional matrix products in Eq. (4.104) for the Fisher matrix correspond to further integrations. This shows that an optimization is very useful.

Working with linear algebra, we prefer to switch to the usual notations of discrete matrices $A^\ell_{kk'}$ (where k, k' now label discrete, equidistant modes) rather than using the continuous quantities $A_\ell(k,k')$. Further, we want to use standard matrix multiplications rather than the summation convention (4.65). This is achieved by the definition

$$A^\ell_{kk'} = \sqrt{k^2\Delta k}\, A_\ell(k,k')\, \sqrt{k'^2\Delta k}. \tag{4.105}$$

A matrix product then automatically reproduces the summation convention:

$$\sum_{k''} A^\ell_{kk''} B^\ell_{k''k'} = \sqrt{k^2\Delta k} \left[\sum_{k''} k''^2 \Delta k\, A_\ell(k,k'') B_\ell(k'',k')\right] \sqrt{k'^2\Delta k} \tag{4.106}$$

$$\approx \sqrt{k^2\Delta k} \left[\int k''^2 dk''\, A_\ell(k,k') B_\ell(k,k')\right] \sqrt{k'^2\Delta k}. \tag{4.107}$$

Let us know look for an orthogonal transformation O^ℓ of the covariance matrix $C^\ell_{kk'} = \sqrt{k^2\Delta k} C_\ell(k,k') \sqrt{k'^2\Delta k}$ such that the transformed matrix

$$\tilde{C}^\ell = \left(O^\ell\right)^T\, C^\ell\, O^\ell \tag{4.108}$$

can be calculated more efficiently, i. e. with less nested integrals. A way to obtain this is to produce, by O^ℓ, the orthogonality relation of the spherical Bessel functions avoiding one integration. This is done by

$$O^\ell_{k\rho} = \sqrt{k^2\Delta k} \sqrt{\frac{2}{\pi}}\, j_\ell(k\rho) \sqrt{\rho^2\Delta\rho}. \tag{4.109}$$

The orthogonality is easily verified:

$$\left(O^\ell\right)^T\, O^\ell = \sum_k O^\ell_{\rho k} O^\ell_{k\rho'} \tag{4.110}$$

$$= \sqrt{\rho^2\Delta\rho}\, \frac{2}{\pi} k^2 \Delta k\, j_\ell(k\rho)\, j_\ell(k\rho') \sqrt{\rho'^2\Delta\rho} \tag{4.111}$$

$$\approx \sqrt{\rho^2\Delta\rho}\, \frac{2}{\pi} \int k^2 dk\, j_\ell(k\rho)\, j_\ell(k\rho') \sqrt{\rho'^2\Delta\rho} \tag{4.112}$$

$$= \delta(\rho-\rho')\Delta\rho \approx \delta_{\rho\rho'}. \tag{4.113}$$

The transformed noise part, $N^\ell_{kk'} \propto M^\ell_{kk'}$, even becomes diagonal,

$$\tilde{M}^\ell_{\rho\rho'} = \sum_{k,k'} O^\ell_{k\rho} M^\ell_{kk'} O^\ell_{k'\rho'} = n(\rho)\, \delta_{\rho\rho'}. \tag{4.114}$$

For the signal part $S^\ell_{kk'}$, we recall that the signal can be written in the form $S^\ell = (B^\ell)^T \cdots B^\ell$ according to Eq. (4.81). Transforming the signal corresponds to transforming B^ℓ just from the left side,

$$\tilde{B}^\ell_{\rho k'} = \sum_k O^\ell_{k\rho} B^\ell_{kk'} = \sqrt{\rho^2 \Delta\rho}\, 2\sqrt{\frac{2}{\pi}} \int_0^\infty dr\; p(\rho|r)\, n(r) F_\ell(k', r) \sqrt{k'^2 \Delta k}. \quad (4.115)$$

This means that one integral less has to be calculated than in Eq. (4.90). We will make use of this transformation in the calculation of the Fisher matrix.

There is also an intuitive reason for the transformation O^ℓ. Since the effects of redshift error (encoded in the matrix Z_ℓ) and of the galaxy distribution (in M_ℓ) are most directly expressed in position space, a Fourier transform unnecessarily complicates the calculations. Our transformation essentially undoes these unnecessary transformations. It would have been possible to avoid them right from the start. In this case, angles (ϑ, φ) would have been transformed to multipoles (ℓ, m) in harmonic space, but we would have kept the radial distance r rather than the Fourier mode k. As a consequence, the covariance matrix would be of the form $C_\ell(r, r')$. The Fourier transformation is only essential in one part of the calculation: relating the gravitational potential to the matter power spectrum $P_0(k)$ in Eq. (4.81). In our analysis, this is reflected in the fact that the matrix $B_\ell(k, k')$ is only transformed back to real space on one side, i. e. to $\tilde{B}_\ell(r, k')$. The right index acts on the matter power spectrum, which is given in Fourier space.

4.4 Results

We now come to the application of the Fisher-matrix approach to the parametrized clustering dark energy component described by two constant parameters, the equation of state w and the rest-frame speed of sound c_s^2. This will enable us to estimate how well the weak lensing data of Euclid, analyzed with the 3d weak lensing method, will be able to constrain these parameters.

Concerning the sound speed c_s^2, we immediately face a complication. Usually, the Fisher matrix analysis has the advantage of not being very sensitive to the maximum likelihood parameters, which are, before the experimental data are taken, not known. This means that the dependence of the Fisher matrix F_{ij} on the maximum likelihood parameters $\hat{\boldsymbol{\vartheta}}$, at which the derivatives defining F_{ij} are calculated, cf. Sec. 4.3.1, is typically not strong so that the Cramér-Rao bounds are meaningful even if the maximum likelihood parameters $\hat{\boldsymbol{\vartheta}}$ are not known to high precision. This advantage is not present in our analysis of the sound speed. According to our analytic investigation of dark energy clustering due to a nontrivial sound speed, we found the physical sound horizon λ_c as a critical scale, cf. Eq. (4.20). We have seen that dark energy clustering is only expected to have observable effects if $\lambda_c < H_0^{-1}$, i. e. if the sound horizon lies

within the Hubble horizon. This requires

$$c_s^2 \lesssim 1 + w, \tag{4.116}$$

showing a critical behavior for values w close to $w_\Lambda = -1$, which are preferred by current observations (Bennett et al., 2012; Ade et al., 2013c). For $w = -1$, no clustering can be observed, and for $w = -1 + \varepsilon$ with a small deviation $\varepsilon > 0$, the expected constraints on c_s^2 will strongly depend on the precise value of ε.

Our strategy is thus to vary the assumed maximum likelihood points for w and c_s^2. In such a way, we will see how well 3d weak lensing observed by Euclid will constrain these parameters for different assumptions of the maximum likelihood values. In this calculation, we keep the other cosmological parameters fixed at fiducial values, taken as the WMAP-7 recommended ΛCDM parameters (Komatsu et al., 2011). So, the parameter vector reads $\boldsymbol{\vartheta} = (w, \log_{10} c_s^2)$, where we choose to constrain the order of magnitude of c_s^2 rather than c_s^2 itself, for reasons discussed in Sec. 4.3.2. The uncertainty $\Delta \log_{10} c_s^2$ is related to the relative error

$$\frac{\Delta(c_s^2)}{c_s^2} \approx \log 10 \, \Delta \log_{10} c_s^2. \tag{4.117}$$

We compute the 3d weak lensing Fisher matrix as explained in Sec. 4.3. This Fisher matrix is complemented by a CMB prior based on forecasts for the Planck satellite.[1] Therefor, we can use the additivity Fisher matrices. For independent experiments A and B, the likelihoods obviously multiply. So, if $\boldsymbol{x} \equiv (\boldsymbol{x}^{(A)}, \boldsymbol{x}^{(B)})$, we have

$$L(\boldsymbol{x}; \boldsymbol{\vartheta}) = L^{(A)}(\boldsymbol{x}^{(A)}; \boldsymbol{\vartheta}) L^{(B)}(\boldsymbol{x}^{(B)}; \boldsymbol{\vartheta}) \tag{4.118}$$

and consequently for the total Fisher matrix

$$F_{ij} = \left\langle -\frac{\partial \log L}{\partial \vartheta_i \partial \vartheta_j} \right\rangle \tag{4.119}$$

$$= \left\langle -\frac{\partial \log L^{(A)}}{\partial \vartheta_i \partial \vartheta_j} \right\rangle + \left\langle -\frac{\partial \log L^{(B)}}{\partial \vartheta_i \partial \vartheta_j} \right\rangle \tag{4.120}$$

$$= F_{ij}^{(A)} + F_{ij}^{(B)} \tag{4.121}$$

by linearity of the derivatives and the expectation value. A CMB prior is then simply included by adding a CMB Fisher matrix. Our construction of this matrix, $F_{ij}^{(\mathrm{CMB})}$, follows the prescription by Perotto et al. (2006) (including temperature, polarization, and their cross-correlation) with expected properties of the Planck data (Hollenstein et al., 2009; Knox, 1995) and spectra calculated with the Boltzmann code CAMB (Lewis et al., 2000; Lewis and Bridle, 2002), which has built-in facilities for our $w\mathrm{CDM} + c_s^2$ parametrization. The multipole range included for the CMB prior is $\ell = 2$ to $\ell = 2250$.

[1] This work preceded the first data release of the Planck collaboration (Ade et al., 2013a).

Detailed explanations for our calculation of $F_{ij}^{(\mathrm{CMB})}$ are found in Ayaita et al. (2012a); Weber (2012).

As we have to scan the two-dimensional parameter space spanned by w and $\log_{10} c_s^2$, we calculate the 3d weak lensing Fisher matrix with reduced numerical precision. Concretely, we use $\ell_{\mathrm{min}} = 2$, $\ell_{\mathrm{max}} = 50$ for the multipole range (we will argue later that high multipoles do not play an important role), wave modes k from $k_{\mathrm{min}} = 10^{-3}\ \mathrm{Mpc}^{-1}$ to $k_{\mathrm{max}} = 10^{-1}\ \mathrm{Mpc}^{-1}$ in $N_k = 200$ (equidistant) steps. This roughly spans from the limit of the linear regime k_{max} to scales comparable to the Hubble horizon at k_{min}. The redshift range is adapted to the depth of the survey and is chosen to be $z_{\mathrm{min}} = 10^{-4}$ to $z_{\mathrm{max}} = 10$ in $N_z = 1000$ equidistant steps.

Figure Fig. 4.10 shows the results for the Cramér-Rao bound $\Delta \log_{10} c_s^2$ (upper figure) and for the relative uncertainty $\Delta w/|w|$ (lower figure). In addition, we show the scale λ_ε at which the effective Newton's constant felt by matter perturbations is enhanced by $\varepsilon = 1\%$, i. e. $Q = 1 + \varepsilon$, cf. Eq. (4.32). At this scale, the gravitational potential induced by dark energy perturbations amounts to a fraction of $\varepsilon = 1\%$ of the total gravitational potential. The red lines mark the values $(w, \log_{10} c_s^2)$ for which

$$\lambda_\varepsilon = 10^{-n} H_0^{-1} \quad \text{for} \quad n = 1, 2, 3, \tag{4.122}$$

and thereby relate λ_ε to the Hubble horizon. In the upper figure, we see that the contours in uncertainty in $\log_{10} c_s^2$ as a function of w qualitatively follow these red lines.

The constraints improve for w further away from -1 and hence for a smaller sound horizon, as expected. On the other hand, the constraints become weak if w is very close to -1. Only for $w \gtrsim -0.95$ and very small sound speeds c_s^2, the error $\Delta \log_{10} c_s^2$ is below 1; so, we may only hope that, at best, the order of magnitude of c_s^2 can be determined. Stated differently, the weak lensing data of Euclid will perhaps only be able to determine whether c_s^2 vanishes, $c_s^2 = 0$, or not.

Since the effects of a nontrivial sound speed, i. e. $c_s^2 \neq 1$, are very small, it comes as no surprise that the expected uncertainty $\Delta w/|w|$ is almost independent of the assumed maximum likelihood value for c_s^2. The contour lines are almost parallel to the y axis. Moreover, the error on the equation of state is not very sensitive to the assumed value of w either. 3d weak lensing combined with a CMB prior will be able to put tight constraints on the equation of sate in the wCDM model, below the percent level. We shall see later that 3d weak lensing is more important, here, than the CMB prior.

In our following calculations, we shall fix the fiducial values instead of scanning the full parameter space. We choose them such that the effects of dark energy clustering are not tiny. This requires a small sound speed, we take $c_s^2 = 10^{-2}$, and an equation of state w not very close to -1, our choice is $w = -0.8$. This might seem unnatural given that $w \approx -1$ is the observationally preferred choice corresponding to a cosmological constant. Yet, this neglects the fact that the wCDM parametrization is only, at best, an effective description. In Sec. 4.1.1, we have argued that, in realistic models, the dark energy equation of state w_X was far away from -1 at high redshifts. For dark energy

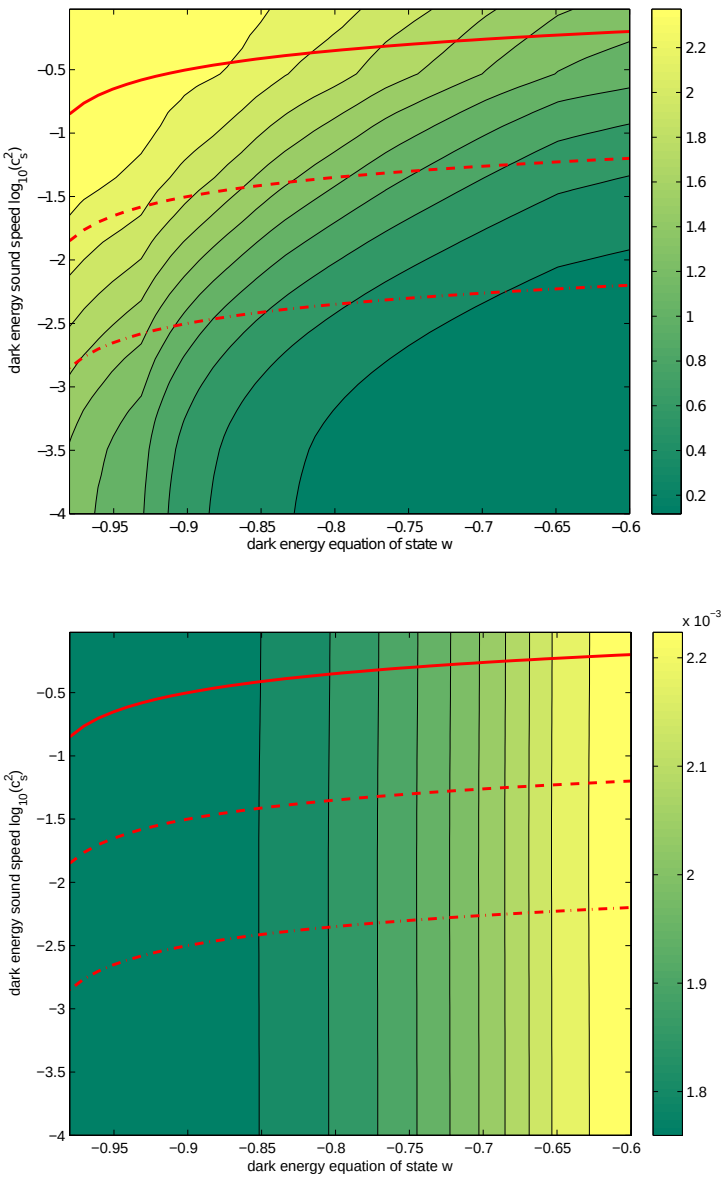

Figure 4.10: Estimated uncertainties $\Delta \log_{10} c_s^2$ of the sound speed parameter (upper figure) and of the equation of state $\Delta w/|w|$ (lower figure). The three red lines ($n = 1,2,3$) show parameters for which $\eta_\varepsilon = 10^{-n} H_0^{-1}$. The figures are taken from Ayaita et al. (2012a).

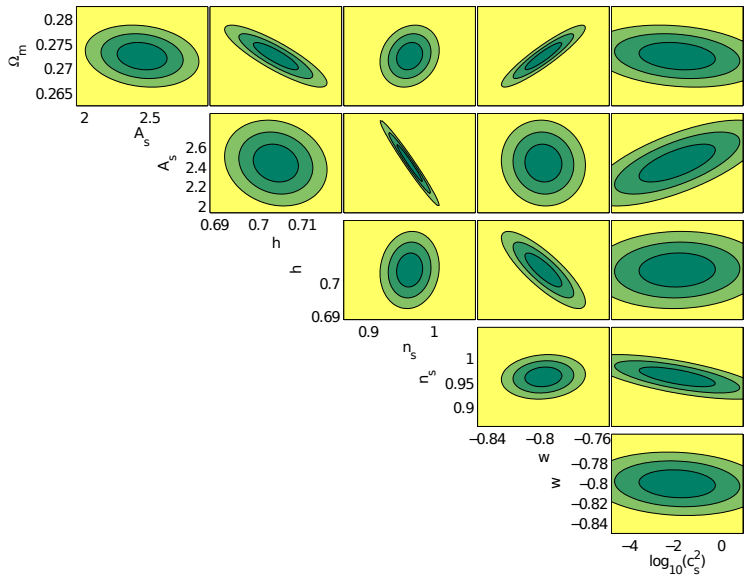

Figure 4.11: Cramér-Rao bounds as estimated confidence ellipses from the 3d weak lensing Fisher matrix. The contours show the 1σ, 2σ, and 3σ intervals. The values on constraints on A_s in the figures are scaled by a factor 10^9. The figure is taken from Ayaita et al. (2012a).

clustering and its impact on matter perturbations, the entire growth history is important. Seen from this perspective, the choice $w = -0.8$ is still conservative as it leads to a negligible amount of dark energy (and hence no effect on matter perturbations) at high redshift. The constant value chosen here will, in the end, correspond to an effective time-average of the true value $w_X(z)$.

We now include further cosmological parameters such that $\boldsymbol{\vartheta}$ is composed of Ω_m, A_s, h, n_s, w, and $\log_{10} c_s^2$. The assumed maximum likelihood values are taken from Komatsu et al. (2011). We can improve the numerical precision and include multipoles up to $\ell_{\max} = 300$ and use $N_k = 500$ steps for the wave modes from $k_{\min}$ to $k_{\max}$. The maximum wave mode $k_{\max}$ is related to the scale where nonlinear effects become very important. A maximal k also motivates a maximum multipole ℓ. Recalling the approximation of spherical Bessel functions $j_\ell(kr)$ with a Dirac delta $\propto \delta(r - \nu/k)$, $\nu = \ell + 1/2$, we see that values ℓ and k are related to distances $r \approx \ell/k$. Since the depth of the survey is limited, the galaxy distribution $n(r)$ will drop off quickly for large r. So, for fixed $k = k_{\max}$, too large values of ℓ will not give contributions because $n(\ell/k)$ will approach zero. We will see this in more detail when quantifying the 3d convergence covariance matrix.

We show the estimated confidence ellipses for pairs $(\vartheta_i, \vartheta_j)$ of the chosen cosmological parameters from the 3d weak lensing Fisher matrix alone (i. e. without a CMB prior) in Fig. 4.11. All the parameters, with the exception of the sound speed c_s^2, are reasonably well constrained. Of course, the constraints by the CMB on the primor-

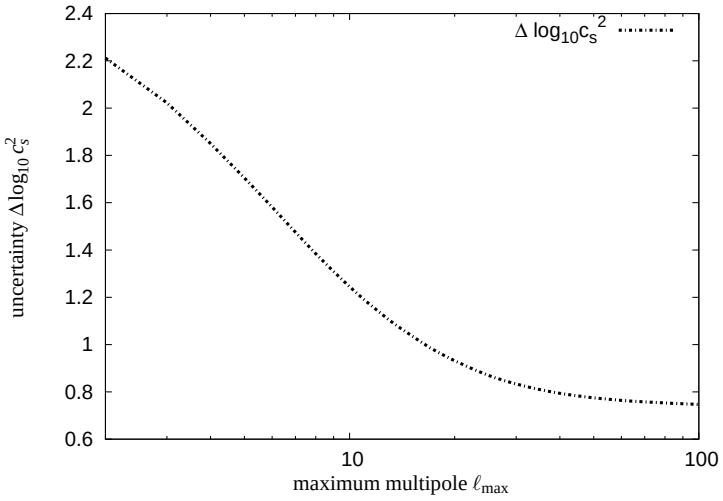

Figure 4.12: The Cramér-Rao bound $\Delta \log_{10} c_s^2$ as a function of the maximum multipole $\ell_{\max}$ included in the calculation of the 3d weak lensing Fisher matrix. The figure is taken from Ayaita et al. (2012a).

dial perturbations (characterized by the scalar amplitude A_s and the spectral index n_s) will be much stronger. This is not true for the remaining parameters, where 3d weak lensing can be a powerful tool.

Let us now turn to the question which multipoles ℓ are important for the sound speed constraints. Therefor, we show the Cramér-Rao bound $\Delta \log_{10} c_s^2$ as a function of the maximum multipole $\ell_{\max}$ in the calculation of the 3d weak lensing Fisher matrix in Fig. 4.12. We see that the first multipoles are of particular importance whereas multipoles $\ell \gtrsim 30$ do not contribute significantly to the constraints. This is reflected in the behavior of the covariance $C_\ell(k,k')$ for different multipoles, qualitatively shown in Fig. 4.13. With increasing ℓ, the region in (k,k') space where the covariance is important shifts to larger wave modes. This is linked to the galaxy distribution $n(r)$. The highest sensitivity is reached around the peak of the distribution $n(r)$. This peak position r^* corresponds to $r^* \sim \ell/k$. So, while we increase ℓ, the important contribution shifts to larger k as well. If we do not go above $k_{\max}$ in order to avoid the nonlinear regime, the galaxy distribution relates this cut to a cut in ℓ.

The covariance $C_\ell(k,k')$ shows where the 3d weak lensing signal is strong. This does not necessarily mean that the parameter constraints are mainly given by this region. For clustering dark energy, only scales above the characteristic scale λ_ε are important. So, for the constraints, we need both a strong 3d weak lensing signal and a signal peaked at large scales $\lambda \sim \lambda_\varepsilon$. According to Fig. 4.13, this means that the first multipoles are decisive, as confirmed by the calculation of the Fisher matrix, cf. Fig. 4.12.

Another way to look at the dependence of the parameter constraints on the multipole ℓ is to consider the summands of the Fisher matrix for each ℓ. Here, we concen-

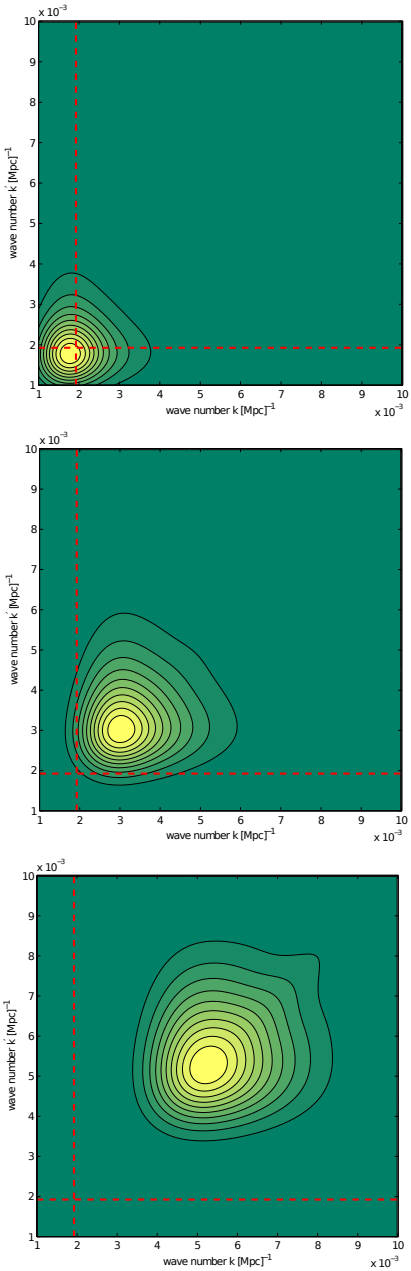

Figure 4.13: The 3d convergence covariance matrices $C_\ell(k,k')$ for multipoles $\ell = 5, 10, 20$ (top to bottom). The red lines again show the effective scale λ_ε (here, $k \equiv 1/\lambda_\varepsilon$ and $c_s^2 = 1$), above which the clustering of dark energy becomes significant. Brighter regions indicate larger values of the covariance matrix. The figures are taken from Ayaita et al. (2012a).

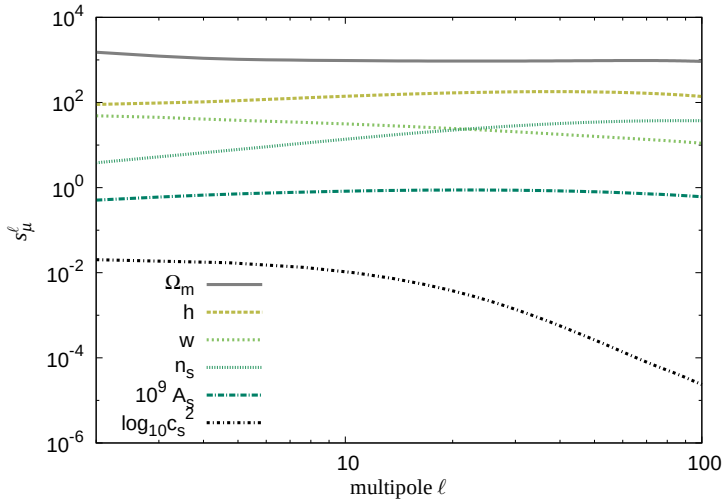

Figure 4.14: The contribution of modes $\varkappa_{\ell m}$ to the diagonal elements of the Fisher matrix, interpreted as the sensitivity of $\varkappa_{\ell m}$ on the parameters. The figure is taken from Ayaita et al. (2012a).

trate on the diagonal elements F_{ii},

$$F_{ii} = \sum_\ell \frac{2\ell+1}{2} \mathrm{tr}_k \left(C_\ell^{-1} \frac{\partial C_\ell}{\partial \vartheta_i} \right)^2 \tag{4.123}$$

and define the *sensitivity* s_i^ℓ as

$$s_i^\ell \equiv \mathrm{tr}_k \left(C_\ell^{-1} \frac{\partial C_\ell}{\partial \vartheta_i} \right)^2 , \tag{4.124}$$

quantifying how much a mode $\varkappa_{\ell m}$ of the 3d convergence contributes to the constraint of parameter ϑ_i; the factor $2\ell+1$ is then just the number of modes $\varkappa_{\ell m}$ for fixed ℓ. The sensitivity for the cosmological parameters $\boldsymbol{\vartheta}$ is plotted in Fig. 4.14. First of all, we notice that the sensitivity for the sound speed is very weak again telling us that no strong constraints can be obtained. Further, all parameters except c_s^2 acquire important contributions for large multipoles ℓ. In contrast, the sensitivity on the sound speed falls off quickly for large ℓ.

Let us briefly comment on the results presented in this section. First of all, given the smallness of the effect a sound speed $c_s^2 < 1$ has on the growth of perturbations, it is remarkable that 3d weak lensing, with the data of Euclid, leads to noticeable constraints at all. This underlines the accuracy with which this method will probe the statistics of the gravitational potential, free from assumptions about the galaxy bias. We shall keep this in mind when investigating the structure formation process in the growing neutrino quintessence model.

On the other hand, we may critically conclude that a dark energy sound speed substantially above zero will not be detected. This even worsens if the equation of state

parameter w is very close to -1. There is no chance to observe dark energy clustering if $c_s^2 \gg 1 + w$ since the dark energy perturbations then lie outside the horizon. We again emphasize that, in realistic dark energy models, the value of w will undergo a time evolution. Even if $w \approx -1$ at the present time to a very good approximation, this can have been different in the past. There will be early dark energy perturbations, and these will leave an imprint on the dark matter distribution.

In the full range of considered fiducial values, $-0.99 \lesssim w \lesssim -0.6$ and $10^{-4} \lesssim c_s^2 \lesssim 1$, our calculated Cramér-Rao bounds on $\Delta \log_{10} c_s^2$ are between 0.1 and 3 implying relative errors $\Delta(c_s^2)/c_s^2$ of roughly 0.3 to 7. Clearly, these weak constraints will not tell us the actual value of the sound speed; instead, one can hope to rule out the trivial case $c_s^2 = 1$ provided that the actual sound speed is sufficiently close to zero. How we interpret this result depends on our expectation. If we are completely ignorant about the actual value of the sound speed and consider it as an entirely free parameter, there is a fair chance that 3d weak lensing with Euclid data will tell us something new, i. e. ruling out either $c_s^2 \approx 0$ or $c_s^2 \approx 1$. If our expectation, however, is $w \approx -1$ and $c_s^2 \approx 1$ (corresponding, approximately, to a cosmological constant), we might ask whether small deviations from these values would be observable. For the sound speed parameter, the answer is clearly negative.

In accordance with forecasts based on weak lensing tomography (Sapone et al., 2010), we find that the constraints on the sound speed parameter with Euclid data will significantly improve as compared to the current status (de Putter et al., 2010; Li and Xia, 2010). In a comparison with tomography (Sapone et al., 2010), it seems that 3d weak lensing performs slightly better. Alternative methods that will be used to improve constraints on the sound speed parameter base on galaxy surveys (Takada, 2006; Ballesteros and Lesgourgues, 2010) and neutral hydrogen surveys (Torres-Rodriguez and Cress, 2007; Torres-Rodriguez et al., 2008).

5 Growing neutrino quintessence

When we introduced quintessence in Sec. 3.3.1, we found that it naturally predicts a small present energy density in the dark energy, with an order of magnitude roughly comparable to that of matter. Although this constitutes an important step in addressing the fine-tuning issues of the cosmological constant scenario, the *coincidence* or *why now* problem remained. As compared to matter, the early energy density of dark energy was small in the past, $\rho_\varphi \ll \rho_m$, for typically $a \lesssim 0.2$, but then quickly grew to $\rho_\varphi \gtrsim \rho_m$ today at $a = 1$. Of course, such a transition can be reproduced with a suitable choice of the cosmon potential $V(\varphi)$. In the absence of a physical motivation for such a choice, the implied fine-tuning would, however, spoil much of the theoretical attractiveness of quintessence. Growing neutrino quintessence (Amendola et al., 2008a; Wetterich, 2007) replaces the need for a fine-tuned potential by proposing another, dynamical mechanism for the onset of dark energy domination. A coupling between the cosmon and the neutrinos, somewhat larger than gravity, automatically stops the evolution of the cosmon and thereby converts quintessence to an effective cosmological constant. The trigger for this event is set by the moment when the cosmic neutrinos become nonrelativistic.

The growing neutrino quintessence model and the physical understanding, theoretical modeling, and quantitative analysis of its effects will be the central topics throughout the remainder of this thesis. The uninitiated reader will find a first introduction in the next section (Sec. 5.1), where the mechanism, by which growing neutrino quintessence naturally accounts for a recent onset of dark energy domination, is explained in detail. Key considerations that will be used frequently are summarized in Secs. 5.2, 5.3, and 5.4.1. These sections provide the basic ideas and intuitions on which we will build later. The particularities of growing neutrino quintessence at the perturbation level are illustrated by explaining the main steps and problems of earlier studies (Sec. 5.2). Both, crucial fundamental equations and the cornerstones of the comprehensive simulation method are explained in Sec. 5.3. We physically motivate the picture of a cosmon-neutrino lump fluid in Sec. 5.4.1.

Coupled quintessence, in particular the form of the coupling used in growing neutrino quintessence, goes back to early works (Wetterich, 1995; Amendola, 2000). In the absence of a symmetry forcing couplings to vanish, we generally have to expect coupled dark energy. Many examples of coupled dark energy, often proposed with the coincidence problem in mind, are studied in the literature (examples include Comelli et al., 2003; Gumjudpai et al., 2005; Zhang, 2005; Koivisto, 2005; Huey and Wandelt, 2006; Hu and Ling, 2006; Barrow and Clifton, 2006) or are investigated in the light of observational constraints (cf., e. g., Olivares et al., 2005; Guo et al., 2007; Bean et al., 2008; Quartin et al., 2008; Caldera-Cabral et al., 2009). The approaches are too nu-

merous and too diverse to do justice to in these few lines. A class of models with many similarities to growing neutrino quintessence are mass-varying neutrino (MaVaN) scenarios (cf. Afshordi et al., 2005; Bi et al., 2005; Peccei, 2005; Weiner and Zurek, 2006; Spitzer, 2006; Chitov et al., 2011).

5.1 Introduction and homogeneous evolution

The growing neutrino quintessence model (Amendola et al., 2008a; Wetterich, 2007) aims at a natural explanation why the expansion of the Universe has started to accelerate so recently in cosmic history. Let us briefly explain why the standard ΛCDM model but also standard models of quintessence do not provide an explanation for the recent onset of dark energy domination. A flat ΛCDM universe with a nonvanishing cosmological constant Λ has to enter, eventually, a Λ-dominated epoch since the constant energy density ρ_Λ associated to the cosmological constant necessarily catches up with the energy densities of radiation and matter,

$$\frac{\rho_\Lambda}{\rho_\gamma} \propto a^4, \quad \frac{\rho_\Lambda}{\rho_m} \propto a^3. \tag{5.1}$$

The scale factor of equality $\rho_\Lambda = \rho_m$ is given by (neglecting radiation)

$$a_{\mathrm{eq}} = \sqrt[3]{\frac{\rho_{m,0}}{\rho_\Lambda}} \sim \sqrt[3]{\frac{10^{-46}\mathrm{GeV}^4}{\rho_\Lambda}}. \tag{5.2}$$

Although the onset of dark energy domination is guaranteed in the ΛCDM model, the cosmological constant needs to be of an unnaturally tiny value in order to obtain $a_{\mathrm{eq}} \sim 1$ and hence a recent onset of dark energy domination, cf. the cosmological constant problem discussed in Chapter 3.

In quintessence models of dark energy, which we have presented in Sec. 3.3.1, the small energy density of dark energy as compared to fundamental physics scales is easily explained by the dynamical evolution of the dark energy scalar field, the cosmon φ. Its energy density ρ_φ decays analogously to those of radiation and matter and naturally comes close to the right order of magnitude needed for the accelerated expansion today. The smallness of the energy density of dark energy is then simply a consequence of the large age of the Universe. Although standard quintessence models successfully predict a small energy density ρ_φ, they do not naturally account for an onset of dark energy domination. In the case of a purely exponential potential, Eq. (3.66), we have seen that the energy density of quintessence in the tracker solution always follows the dominant component, i. e. $\rho_\varphi \propto \rho_\gamma$ during radiation domination and then $\rho_\varphi \propto \rho_m$ during matter domination. There will be no accelerated expansion in this model, cf. Fig. 3.5. The power-law potential, Eq. (3.66), does lead to dark energy domination, but the timing when this happens has to be fine-tuned.

The growing neutrino quintessence model is a potential solution to this *coincidence problem* of dark energy. Amendola et al. (2008a) speculate that there is a way to guarantee the onset of dark energy domination even in the case of a purely exponential potential. A coupling of the cosmon φ to another species, e. g. the neutrinos, might act as an effective contribution to the potential and kick the cosmon out of its tracker behavior, cf. Fig. 3.6. We shall see that the most straightforward type of a coupling leads to a varying mass $m_\nu(\varphi)$ of the species coupled to the cosmon, which we assume to be the neutrinos. If this mass grows while the cosmon rolls down its potential, the energy density in neutrinos will decay less fast than in the uncoupled case or even increase (Amendola et al., 2008a),

$$\rho_\nu \propto a^{n(\gamma-2)}, \quad \gamma > 1, \tag{5.3}$$

where $n = 4$ for relativistic neutrinos and $n = 3$ once the neutrinos have become non-relativistic. So, at some point, the energy density ρ_ν will have an order of magnitude similar to the other components and then have a significant effect on the evolution of the cosmon by virtue of the cosmon-neutrino coupling.

Basic equations

Let us investigate this mechanism in more detail. The proposed covariant coupling (Wetterich, 1995; Amendola, 2000) can be expressed by an exchange of energy and momentum between the two species and reads

$$\nabla_\lambda T^{\mu\lambda}_{(\nu)} = -\beta \mathrm{tr} T_{(\nu)} \partial^\mu \varphi, \tag{5.4}$$

$$\nabla_\lambda T^{\mu\lambda}_{(\varphi)} = +\beta \mathrm{tr} T_{(\nu)} \partial^\mu \varphi. \tag{5.5}$$

The individual energy-momentum tensors $T^{\mu\lambda}_{(\nu)}$ of the neutrinos and $T^{\mu\lambda}_{(\varphi)}$ of the cosmon do not satisfy conservation equations but their sum does,

$$\nabla_\lambda \left(T^{\mu\lambda}_{(\nu)} + T^{\mu\lambda}_{(\varphi)} \right) = 0. \tag{5.6}$$

We will see that Eqs. (5.4) and (5.5) are realized, at the particle physics level, as a dependence of the neutrino mass m_ν on the scalar field φ. This dependence is quantified by the coupling parameter β,

$$\beta = -\frac{d \log m_\nu}{d\varphi}. \tag{5.7}$$

Here, m_ν denotes the average neutrino mass, and the cosmon-neutrino coupling β is assumed to be equal for the different neutrino species. This can be generalized (Wetterich, 2007).

The evolution of the cosmon can be obtained by varying the action

$$S = \int d^4x \sqrt{-g} \left(\mathscr{L}_G + \mathscr{L}_m + \mathscr{L}_\nu + \mathscr{L}_\varphi \right) \tag{5.8}$$

of the model (here, $\mathscr{L}_m$ includes matter and radiation) with respect to φ, or by using the energy-momentum tensor

$$T^{\mu\lambda}_{(\varphi)} = \partial^\mu\varphi\partial^\lambda\varphi + g^{\mu\lambda}\mathscr{L}_\varphi, \quad \mathscr{L}_\varphi = -\frac{1}{2}\partial^\lambda\varphi\partial_\lambda\varphi - V(\varphi) \tag{5.9}$$

and inserting it into the energy-momentum exchange equation (5.5). The result is a modified Klein-Gordon equation

$$\nabla^\lambda\nabla_\lambda\varphi - V_{,\varphi}(\varphi) = \beta\,\mathrm{tr}T_{(\nu)}. \tag{5.10}$$

On the background level, $\varphi(x) \to \bar{\varphi}(\tau)$, this equation becomes (cf. Sec. 3.3.1)

$$\bar{\varphi}'' + 2\frac{a'}{a}\bar{\varphi}' + a^2 V_{,\varphi}(\bar{\varphi}) = a^2\beta\,(\bar{\rho}_\nu - 3\bar{p}_\nu). \tag{5.11}$$

Similarly, by using the background energy-momentum tensor of the neutrinos,

$$T^\mu{}_{(\nu)\,\lambda} = \mathrm{diag}(-\bar{\rho}_\nu, \bar{p}_\nu, \bar{p}_\nu, \bar{p}_\nu) \tag{5.12}$$

in Eq. (5.4), the background evolution of the neutrino energy density is given by

$$\bar{\rho}_\nu' + 3\frac{a'}{a}\,(\bar{\rho}_\nu + \bar{p}_\nu) = -a^2\beta\,(\bar{\rho}_\nu - 3\bar{p}_\nu)\,\bar{\varphi}'. \tag{5.13}$$

If β is negative and $\bar{\varphi}$ rolls down the potential $V(\varphi)$ towards larger values, the right-hand side of this equation exactly causes the behavior we demanded in Eq. (5.3).

Onset of dark energy domination

In the background Klein-Gordon equation (5.11), the 'force term' is now given by

$$f = -a^2\left[V_{,\varphi} - \beta\,(\bar{\rho}_\nu - 3\bar{p}_\nu)\right] \tag{5.14}$$

consisting of the potential gradient and the coupling term. Once the (positive) coupling term overtakes the (negative) potential gradient, the cosmon is stopped due to an effective, dynamical barrier, cf. Fig. 3.6. Afterwards, the approximately frozen value $V(\bar{\varphi})$ acts as an effective cosmological constant and leads to an onset of dark energy domination. We will next discuss this mechanism.

Let us first investigate the case of a constant β. Then, the neutrino mass evolves simply according to

$$m_\nu(\varphi) = \bar{m}\,e^{-\beta\varphi}, \tag{5.15}$$

with a mass $\bar{m}$ normalized at $\varphi = 0$. This mass parameter can be adjusted such that the neutrino mass in the early universe matches a natural neutrino mass scale. For later use, we express Eq. (5.15) in terms of the potential,

$$m_\nu(\varphi) = \bar{m}\,V_0^{-\frac{\beta}{\alpha}}\,[V(\varphi)]^{\frac{\beta}{\alpha}}, \quad V(\varphi) = V_0\,e^{-\alpha\varphi}. \tag{5.16}$$

At some point, the growing mass $m_\nu(\varphi)$ will overtake the decaying neutrino temperature $T_\nu \propto a^{-1}$, and the neutrinos become nonrelativistic, $\bar{p}_\nu \approx 0$. The coupling term in the Klein-Gordon equation (5.11), which is proportional to $\beta(\bar{\rho}_\nu - 3\bar{p}_\nu)$, will then become important (whereas it is negligible in the ultrarelativistic case $\bar{p}_\nu \approx \bar{\rho}_\nu/3$). The potential gradient $V_{,\varphi}(\bar{\varphi})$ falls with a^{-3} during matter domination. This is a consequence of the tracker behavior,

$$\Omega_\varphi \approx \frac{3}{2\alpha^2} = \text{const.}, \quad \text{and} \quad \Omega_\varphi = 2\frac{V(\bar{\varphi})}{\rho_{m,0}a^{-3}}, \tag{5.17}$$

where we have used $\bar{\rho}_\varphi = 2V(\bar{\varphi})$ during the tracker behavior in matter domination where $w_\varphi = 0$ and $\rho_{\text{tot}} = 3H^2 \approx \rho_{m,0}a^{-3}$. Hence

$$V_{,\varphi}(\bar{\varphi}) = -\alpha V(\bar{\varphi}) \propto a^{-3}. \tag{5.18}$$

On the other hand, once the neutrinos are nonrelativistic, their energy density decays slower than a^{-3} due to the growing mass. Using the scaling behavior of quintessence and Eq. (5.15) for the neutrino mass, Amendola et al. (2008a) derive

$$\bar{\rho}_\nu \propto a^{3(\gamma-2)} \quad \text{with} \quad \gamma = 1 - \frac{\beta}{\alpha}. \tag{5.19}$$

This means that, for negative coupling β, the coupling term $\propto \beta\bar{\rho}_\nu$ will eventually overtake the potential gradient, the force term f switches its sign, the rolling of the cosmon is stopped, and a phase of accelerated expansion will eventually set in.

For the asymptotic late-time evolution, Amendola et al. (2008a) find the future attractor

$$w = -1 + \frac{1}{\gamma}, \quad \Omega_\varphi = 1 - \Omega_\nu = 1 - \frac{1}{\gamma} + \frac{3}{\alpha^2\gamma^2}. \tag{5.20}$$

If the present Universe is close to this attractor, the present fraction of dark energy is, by this equation, directly related to Ω_ν and hence to the present neutrino mass (Amendola et al., 2008a),

$$\Omega_{\varphi,0} \approx \frac{\gamma\, m_\nu(\bar{\varphi}_0)}{16\,\text{eV}}. \tag{5.21}$$

The situation is completely different from the cosmological constant where the scale of dark energy has to be fine-tuned to many orders of magnitude. Here, the smallness of the neutrino mass automatically gives roughly the correct order of magnitude for the energy density in dark energy. The precise evolution is then determined by the dimensionless parameters α and β.

We show the late-time evolution of the fractional energy densities Ω_φ, Ω_ν, and Ω_m in Fig. 5.1. Here, we have chosen $\alpha = 10$ to ensure a sufficiently small amount of early dark energy,

$$\Omega_e \sim \frac{1}{\alpha^2} = 10^{-2}, \tag{5.22}$$

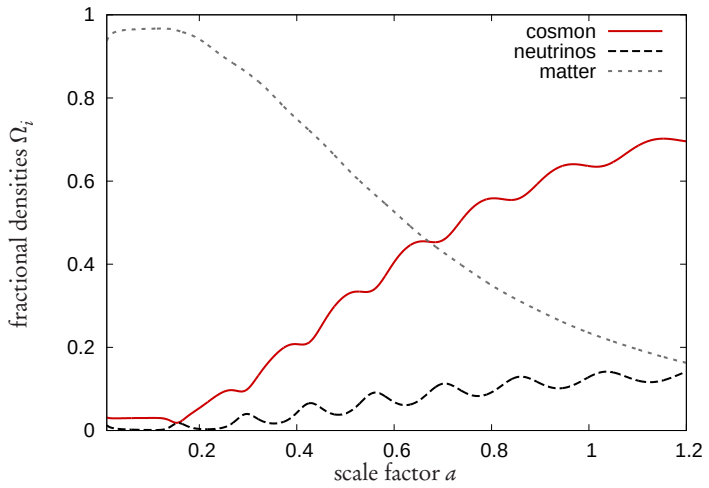

Figure 5.1: The late-time evolution of the fractional energy densities Ω_φ, Ω_ν, and Ω_m in the constant β model. The parameters are $\alpha = 10$ and $\beta = -52$.

as required to match observational constraints (Doran et al., 2007; Reichardt et al., 2012; Pettorino et al., 2013). The value of β has then to be chosen large enough in order to realize the onset of dark energy domination at the right time, we take $\beta = -52$. These parameters lead to a rather large present-day neutrino mass as can be seen in Fig. 5.2. The present value reaches $m_\nu \approx 2$ eV, which is, essentially, the current upper limit allowed by laboratory constraints (Beringer et al., 2012). A consequence of this large mass is a rather high energy density in neutrinos, $\Omega_{\nu,0} \gtrsim 10\%$. Smaller present-day neutrino masses can be obtained for larger values of β — large values of β compensate a smaller mass in the coupling term $\propto \beta\bar{\rho}_\nu$. So, the above scenario can be regarded as the case of a minimal $|\beta|$ leading to an expansion history similar to the ΛCDM model while at the same time respecting constraints on early dark energy and the neutrino mass. In Fig. 5.2, we also see the characteristic feature of the model that the neutrino mass was small in early cosmic history. Cosmological upper limits for the neutrino mass (Goobar et al., 2006; Ade et al., 2013c) are easily passed.

Varying coupling parameter

For the purpose of simplicity, we have assumed a constant coupling parameter β. We have seen that sufficiently small present-day neutrino masses require typically $\beta \sim -10^2$, which might seem an unnaturally large value. In general, however, β should be regarded φ-dependent, $\beta = \beta(\varphi)$, and the approach of large values can find a dynamical explanation. The constant β model is then merely an approximation in the case that the function $\beta(\varphi)$ is sufficiently flat in late-time cosmology. Wetterich (2007) considers a cascade mechanism for explaining the neutrino masses (Magg and Wetterich, 1980; Lazarides et al., 1981; Schechter and Valle, 1980), according to which the neutrino mass

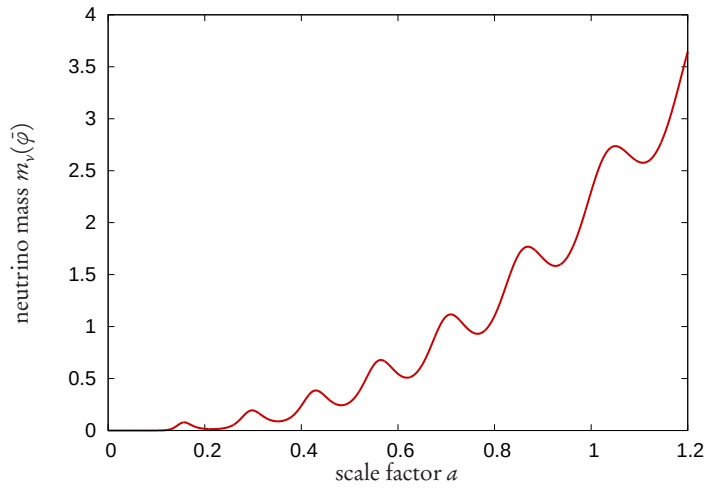

Figure 5.2: The evolution of the neutrino mass $m_\nu(\bar{\varphi})$ in the constant β model.

acquires a contribution proportional to M_t^{-2}, where M_t is the mass of a scalar SU(2) triplet field, and generically $M_t \sim M_{\rm GUT} \sim 10^{16}$ GeV. Wetterich (2007) then assumes that M_t depends on φ and has a zero, $M_t(\varphi_{\rm crit}) = 0$. When φ, in the course of its cosmological evolution, approaches $\varphi_{\rm crit}$, this automatically leads to growing neutrino masses and large couplings $\beta(\varphi)$. A concrete realization is

$$m_\nu(\varphi) = \frac{\bar{m}}{\varphi_{\rm crit} - \varphi}, \tag{5.23}$$

which may approximate the (fundamental and more complex) function close to the pole (Wetterich, 2007), with

$$\beta(\varphi) = -\frac{d\log m_\nu}{d\varphi} = \frac{1}{\varphi - \varphi_{\rm crit}}. \tag{5.24}$$

In such a model, we will naturally encounter large couplings. It is also appealing from the particle physics perspective; the scale of neutrino masses would, from a comparison of fundamental scales in the neutrino mass generation mechanism, naively be estimated (Wetterich, 2007) as

$$m_\nu \sim \frac{v^2}{M_{\rm GUT}} \sim 10^{-3}\,\text{eV}, \tag{5.25}$$

with the Higgs vacuum expectation value $v \approx 246$ GeV, cf. Sec. 3.1.2, and the GUT scale. Yet, observations indicate that at least one neutrino mass eigenstate is above $m_i \gtrsim 0.04$ eV (Beringer et al., 2012). In the growing neutrino quintessence model, a more natural value $m_\nu \sim 10^{-3}$ can be realized in the early Universe, while the neutrino mass can be much larger today.

This varying β model also leads to realistic expansion histories. We again show the energy fractions Ω_φ, Ω_ν, and Ω_m in Fig. 5.3. The expansion history is very similar to

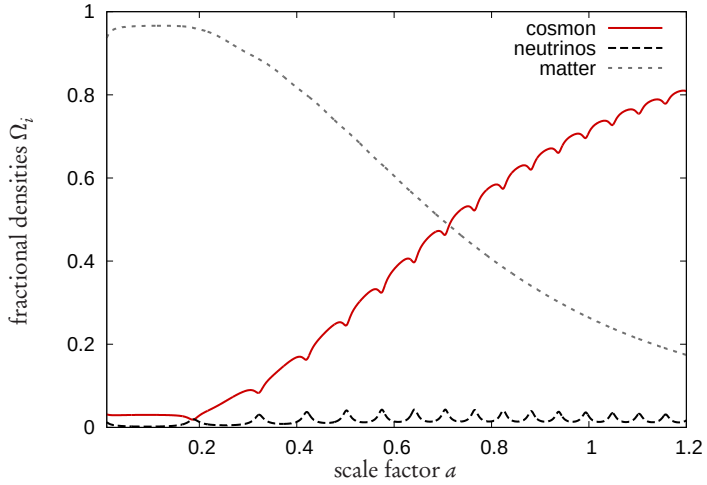

Figure 5.3: The late-time evolution of the fractional energy densities Ω_φ, Ω_ν, and Ω_m in the varying β model.

the ΛCDM model. The stopping mechanism is even more pronounced than in the constant β model since the effective potential barrier is steeper. Moreover, in this example, the present-day neutrino mass is smaller as is expressed by a much smaller energy fraction Ω_ν. The evolution of the neutrino mass is shown in Fig. 5.4. It reaches $m_\nu \approx 0.3$ eV at the present cosmic time.

Aspects of the cosmon-neutrino coupling

We have already mentioned that the dependence of a fundamental mass scale in the mechanism of neutrino mass generation on the cosmon φ leads to the cosmon-neutrino coupling assumed in the growing quintessence model. On a particle physics level, the neutrinos (we do not, for simplicity, discriminate between the different neutrino species) can be described with a Majorana Lagrangian

$$\mathscr{L}_\nu = i\bar{\psi}\left[\gamma^\lambda \nabla_\lambda + m_\nu(\varphi)\right]\psi \tag{5.26}$$

on curved spacetime (Brill and Wheeler, 1957), where γ^λ denote the gamma matrices contracted with the vierbeins, $\gamma^\lambda = \gamma^a e_a^\lambda$, and $g^{\mu\nu} = e_a^\mu e_b^\nu \eta^{ab}$. Working out the equations of motion following from this action and the usual scalar field action, Ayaita et al. (2012b) find that the coupling defined by the energy-momentum exchange equations (5.4) and (5.5) is exactly reproduced. The details of the derivation can be found in Ayaita et al. (2012b); Weber (2012).

A concern one has to consider is that the cosmon-neutrino coupling changes the Fermi scale of the weak interactions due to loop contributions. The effect of the

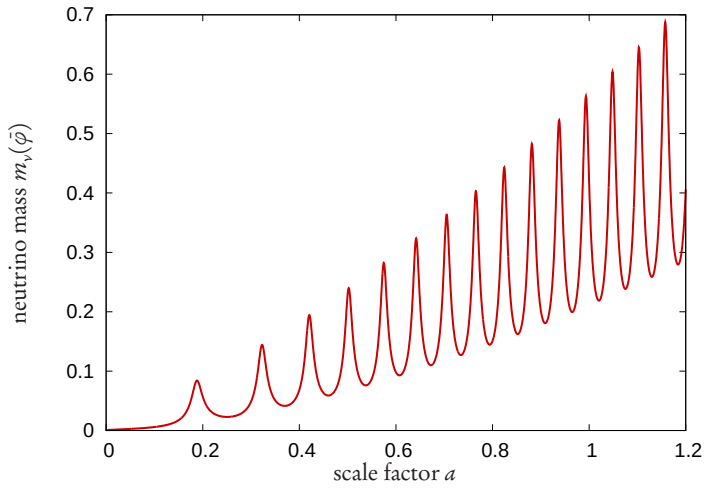

Figure 5.4: The evolution of the neutrino mass $m_\nu(\bar{\varphi})$ in the varying β model.

cosmon-neutrino coupling on the electron mass has been analyzed by Wetterich (2007). In fact, if the cosmon-neutrino coupling is realized by a dependence of the triplet mass M_t on the cosmon φ, a rather strong variation of the Fermi scale is possible. The situation is different if the cosmon-neutrino coupling is realized, e. g., by the dependence of the right-handed neutrino mass on φ.

Although we will not go into the details of the fundamental physics realization of the growing neutrino quintessence model, we briefly mention an early criticism of models with an exponential potential and a fermion coupling of the type $m_\nu(\varphi) \propto \exp(-\beta\varphi)$. Doran and Jäckel (2002) argue that fermion fluctuations as shown in Fig. 5.5 would effectively contribute to the scalar potential and even dominate. The

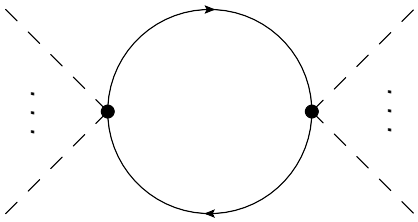

Figure 5.5: Solid lines indicate neutrinos, dashed lines the (scalar) cosmon field. In the case of a linear approximation, $m_\nu(\varphi) \approx m_\nu(\hat{\varphi})(1-\beta\hat{\varphi})$, only one external line on each side would appear.

potential $V(\varphi)$ would be unstable under quantum fluctuations in the presence of a coupling to fermions. A response to this criticism has been given by Wetterich (2008): If the quintessence theory is properly constructed from a broken dilatation symmetry — the cosmon is then the pseudo-Goldstone boson of this spontaneously broken symmetry —, the exponential potential can already be the full, effective potential including

all quantum contributions. In this scenario, the cosmological constant problem is addressed on a fundamental level.

5.2 Studies of inhomogeneities

Linear perturbations

After having found a promising background evolution with an expansion history very similar to the standard ΛCDM model, the 'canonical' next task is the study of linear perturbations. Typically, linear perturbation theory already allows to draw a lot of important conclusions and to make contact with a variety of observational probes and constraints. This is because linear perturbation theory is, typically, a good approximation on large scales even if small scales already undergo a nonlinear evolution. One might hope to predict, with the help of linear perturbations, an angular power spectrum C_ℓ of CMB temperature fluctuations and a large-scale matter power spectrum $P(k)$ as probed by galaxy surveys. We shall see in this section that this does not work in the growing neutrino quintessence model. Nonlinearities become important even on large scales. The investigation of linear perturbations is, nonetheless, an important task as it will provide the initial conditions for a thorough nonlinear treatment. We now briefly review the application of linear perturbation theory to the growing neutrino quintessence model as worked out by Mota et al. (2008). The resulting modified version of the Boltzmann code CAMB, capable of treating growing neutrino quintessence at the linear level, will be used later for the generation of initial conditions.

Linear perturbations in the cosmon φ are described by the linearly perturbed part of the modified Klein-Gordon equation (5.10). In Fourier space, it reads (Mota et al., 2008)

$$\begin{aligned}&\delta\varphi'' + 2\frac{a'}{a}\delta\varphi' + \left[k^2 + a^2 V_{,\varphi\varphi}(\bar{\varphi})\right]\delta\varphi + 2a^2 V_{,\varphi}(\bar{\varphi})\Psi - \left(\Psi' + 3\Phi'\right)\bar{\varphi}' = \\ &= a^2\left[\beta(\bar{\varphi})(\delta\rho_\nu - 3\delta p_\nu) + \beta_{,\varphi}(\bar{\varphi})(\bar{\rho}_\nu - 3\bar{p}_\nu)\delta\varphi + 2\beta(\bar{\varphi})(\bar{\rho}_\nu - 3\bar{p}_\nu)\Psi\right]. \qquad (5.27)\end{aligned}$$

For the neutrinos, we need the evolution of the density perturbation $\delta\rho_\nu$ and also of the pressure perturbation δp_ν. The linear evolution equations (2.72) and (2.73) discussed in Sec. 2.2.1 only provide both perturbations if we assume a sound speed $c_s^2 = \delta p_\nu / \delta\rho_\nu$. Since the latter is not known a priori, one has to take a different approach. This is done by perturbing the neutrino phase-space distribution (Mota et al., 2008; Ma and Bertschinger, 1995),

$$f_\nu(\tau, x^i, p_j) = f_{\nu,0}(p)\left[1 + \psi(\tau, x^i, p_j)\right], \qquad (5.28)$$

where $p = |\boldsymbol{p}|$ denotes the absolute value of the spatial comoving momentum. Inserting this linear expansion into the phase-space conservation equation, cf. Eq. (2.84), in

Fourier space gives the first-order Boltzmann equation (Mota et al., 2008)

$$\psi' + i\frac{\boldsymbol{k}\cdot\boldsymbol{p}}{E}\psi + \frac{d\log f_{\nu,0}}{d\log p}\left(\Phi' - i\frac{E}{p^2}\boldsymbol{k}\cdot\boldsymbol{p}\,\Psi\right) = \\ = -i\frac{\boldsymbol{k}\cdot\boldsymbol{p}}{E}\frac{k}{p^2}a^2 m_\nu(\bar\varphi)^2\beta(\bar\varphi)\frac{d\log f_{\nu,0}}{d\log p}\delta\varphi \tag{5.29}$$

with the energy $E = E(p,\varphi) = \sqrt{p^2 + a^2 m_\nu(\bar\varphi)^2}$. The density and the pressure perturbations are then, cf. Eqs. (2.32) and (2.33), obtained as integrals, e. g.

$$\delta\rho_\nu = \int d^3p\,\frac{1}{\sqrt{-g}}\left[E(p,\bar\varphi+\delta\varphi)f_{\nu,0}(1+\psi) - E(p,\bar\varphi)f_{\nu,0}\right], \tag{5.30}$$

where $E(p,\bar\varphi+\delta\varphi) \approx E(p,\bar\varphi) + E_{,\varphi}(p,\bar\varphi)\delta\varphi$ in linear approximation. In a numerical computation, rather than evolving the full function $\psi = \psi(\tau, x^i, p_j)$, it is adequate to expand ψ in Legendre polynomials (Mota et al., 2008).

We apply the linear perturbation equations to show the dimensionless spectra $\Delta_\nu(k)$ and $\Delta_m(k)$ of neutrino and matter density perturbations at $a = 1$ in the constant β model ($\beta = -52$ and $\alpha = 10$) in Fig. 5.6. Obviously, the cosmon-neutrino coupling

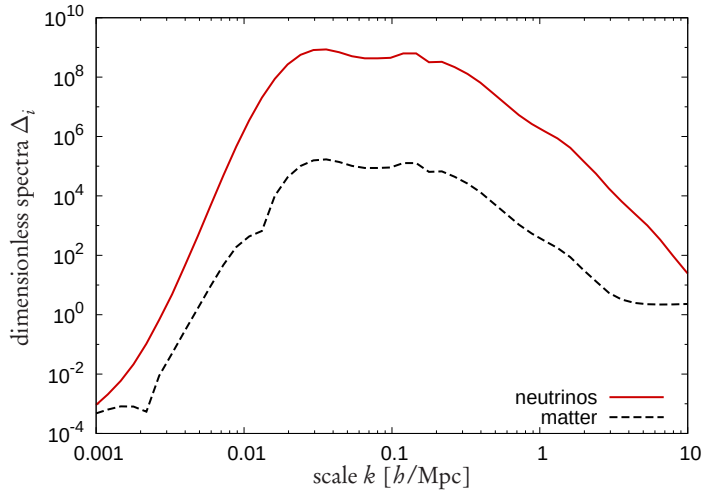

Figure 5.6: The dimensionless spectra $\Delta_\nu(k)$ and $\Delta_m(k)$ (in the synchronous gauge) according to linear perturbation theory of the growing neutrino quintessence model with constant coupling parameter β. Confer the corresponding figure in Mota et al. (2008).

has led to a rapid growth of neutrino perturbations exceeding the boundary between the linear and the nonlinear regime, $\Delta_\nu \sim 1$, even on large scales. Recalling that the coupling becomes only effective once the neutrinos are nonrelativistic, which happens around $z \approx 5$ or $a \approx 0.2$, we get an impression of the enormous impact of the cosmon-neutrino coupling. In Fig. 5.7, we show the scale factor $a_{\rm nl}(k)$ where the neutrino

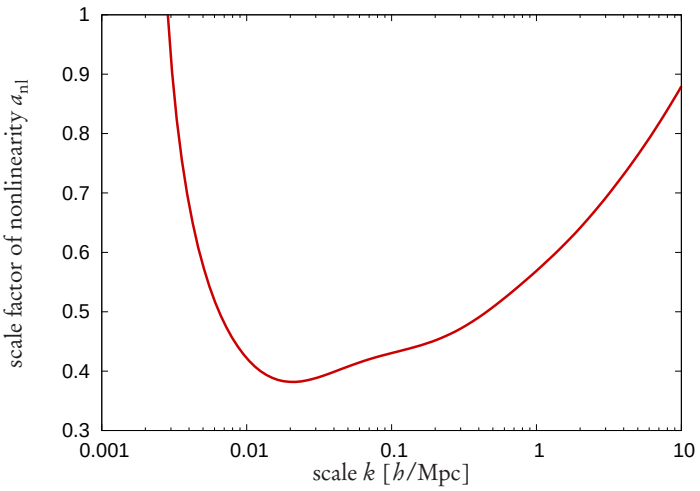

Figure 5.7: The scale factor $a_{\rm nl}$ where neutrino perturbations start to become nonlinear, as a function of scale. Confer the corresponding figure in Mota et al. (2008).

density perturbations start to become nonlinear, i. e. $\Delta_\nu(k;a_{\rm nl}) = 1$. In stark contrast to cold dark matter, whose perturbations enter the nonlinear regime on small scales first and then form, from there, larger structures, the neutrino density becomes first nonlinear at the comoving scale $\lambda \sim 100h^{-1}$Mpc. We thus have to expect the formation of very large structures first. In particular, linear perturbation theory breaks down even on large scales. Hence, the formation of large-scale nonlinear neutrino structures has been a prediction by Mota et al. (2008).

First nonlinear attempts

A first, tentative investigation of these structures has been performed by Wintergerst et al. (2010). In order to include at least some nonlinear contributions and to model the neutrino density of an idealized, forming lump in position space, a hydrodynamic approach was chosen, cf. Sec. 2.2.2. The velocity dispersion σ_{ij} quantifying the 'microscopic' velocity of the neutrinos, cf. Eq. (2.92), which — as we shall see in Sec. 5.4.4 — is essential in stabilizing the neutrino structures and which encodes the effect of shell crossing, has been neglected. The calculation was necessarily unstable and only reasonably accurate as long as σ_{ij} is small and the Newtonian limit holds. The hydrodynamic equations in the Newtonian limit (ignoring matter) that were used (Wintergerst et al.,

2010) read

$$\delta_\nu' = -v_\nu \cdot \nabla\delta_\nu - (1+\delta_\nu)\nabla\cdot v_\nu, \tag{5.31}$$

$$v_\nu' = -\left(\frac{a'}{a} - \beta\bar{\varphi}'\right) v_\nu - (v_\nu\cdot\nabla)v_\nu - \nabla\Phi + \beta\nabla\delta\varphi, \tag{5.32}$$

$$\Delta\delta\varphi = -a^2\beta\bar{\rho}_\nu\delta_\nu, \tag{5.33}$$

$$\Delta\Phi = \frac{a^2}{2}\bar{\rho}_\nu\delta_\nu. \tag{5.34}$$

These equations show that, in the Newtonian limit, the cosmon-neutrino coupling is completely analogous to gravity. The cosmon perturbation $\delta\varphi$ plays the roll of a gravitational potential, with an enhanced coupling constant. Obviously, $\delta\varphi = -2\beta\Phi$, and the force term in Eq. (5.32) picks up another factor of β. We see that the cosmon-mediated force between neutrinos is, in the Newtonian limit,

$$|\boldsymbol{F}| = 2\beta^2\,|\boldsymbol{F}_G|, \tag{5.35}$$

a factor $2\beta^2$ larger than the gravitational interaction. This is of order 10^4 for $\beta \sim -10^2$. This very strong attractive force explains the rapid neutrino clustering that we observed already in linear theory. This clustering has also been seen in the hydrodynamic approach (Wintergerst et al., 2010) for an initially spherically symmetric overdensity. It has also been investigated in a spherical collapse approach (Wintergerst and Pettorino, 2010). Since the calculations are unstable, no physical properties of the final sate of the neutrino structures could be inferred.

Nonetheless, Pettorino et al. (2010) have tried, essentially with intelligent guesses about the properties of the structures and with modeling the neutrino density by a collection of point-shaped peaks, to get an idea of the impact of these structures on the CMB temperature fluctuation spectrum C_ℓ. Although the quantitative results are clearly speculative and hard to interpret, the authors emphasized the importance of the *backreaction* in growing neutrino quintessence, with which we shall be concerned later:

> "[...] the neutrino mass within a virialized lump may differ from the cosmological value outside the lump. As an effect, the fluctuations on larger length scales may 'see' a modified effective neutrino mass and a modified φ-dependence of $\bar{m}_\nu(\varphi)$."

As a consequence, large scales, and even the background solution, cannot be calculated accurately without taking into account the *backreaction* from small scales which manifests itself in a modified neutrino mass. We will see later in a full nonlinear treatment that this effect is quantitatively very important and leads to drastic consequences, e. g. for the expansion of the Universe.

The possibility of even a mass freezing within neutrino lumps — decoupling the lumps from the background evolution of the cosmon — has been investigated by Nunes

et al. (2011). The idea was to model a spherical neutrino structure and to consider the Klein-Gordon equation for a spherically symmetric cosmon $\varphi(r)$ with boundary conditions

$$\left.\frac{\partial\varphi}{\partial r}\right|_{r=0} = 0 \quad \text{and} \quad \lim_{r\to\infty}\varphi(r) = \bar{\varphi}, \tag{5.36}$$

i. e. with regularity in the center of the structure and an approach of the cosmological background value far outside the structure. For the neutrino number density, an NFW-type profile has been assumed, Eq. (2.103). Nunes et al. (2011) discussed two important effects.

First, the radial Klein-Gordon equation for a static field indeed leads to a mass freezing in the sense that the value inside the lump $\varphi_l = \varphi(r = 0)$ is not sensitive to the background value $\bar{\varphi} = \varphi(r \to \infty)$,

$$\frac{d\varphi_l}{d\bar{\varphi}} \ll 1. \tag{5.37}$$

We illustrate this effect in Fig. 5.8. As the background cosmon rolls down the potential

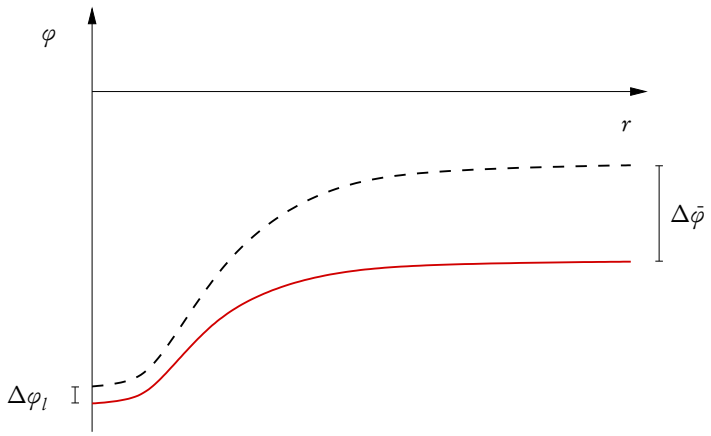

Figure 5.8: Schematic illustration of the mass-freezing effect. The cosmon field within the lump does not follow the background value far outside the lump.

towards larger values, the cosmon field within the lump reacts only mildly. This has severe consequences for the background expansion since the stopping mechanism is significantly reduced.

Second, Nunes et al. (2011) argue that, depending on the steepness of the neutrino number density close to the center, it is possible that the neutrinos become relativistic again. This is due to the mass suppression induced by the local cosmon field $\varphi(r)$ which shows a potential well as illustrated in Fig. 5.8.

Newtonian N-body simulation

The next big step forward in investigating the cosmological dynamics of the model and, in particular, the formation of neutrino structures, was due to Baldi et al. (2011) (cf. also Baldi, 2011, 2012), who overcame the instability of the purely hydrodynamic approach by switching to a Newtonian N-body treatment. The backreaction effect (Pettorino et al., 2010), the dependence of the neutrino mass on the local cosmon field $\varphi(x)$ (rather than merely on the background value $\bar{\varphi}(\tau)$), and the possibility of relativistic neutrino velocities (Nunes et al., 2011) have not been included in this early work. Nonetheless, Baldi et al. (2011) could successfully simulate the beginning of the neutrino lump formation in an adapted GADGET-2 N-body simulation (Baldi et al., 2010; Springel, 2005).

The equation of motion for effective neutrino particles in the N-body simulation reads

$$v' = -\left(\frac{a'}{a} - \beta\bar{\varphi}'\right) v - \boldsymbol{\nabla}\Phi + \beta\boldsymbol{\nabla}\delta\varphi, \tag{5.38}$$

where the cosmon perturbation is given by the Poisson equation (5.33). Instead of solving it on a grid, it is implemented as a two-body force in complete analogy to Newtonian gravity. The mass variation — in this simulation only taken into account at the background level, $m_\nu = m_\nu(\bar{\varphi})$ — is reflected in a modified Hubble damping term now including a contribution $\propto \beta\bar{\varphi}'$. If $\bar{\varphi}$ oscillates, this modified damping can change its sign and lead to accelerations of the N-body particles. This is a strong effect and can even tear forming structures apart. Baldi et al. (2011) hence observed what they called an "oscillating structure formation". We show the modified damping term from Eq. (5.38) as compared to the usual Hubble damping $\propto a'/a$ in Fig. 5.9. As we

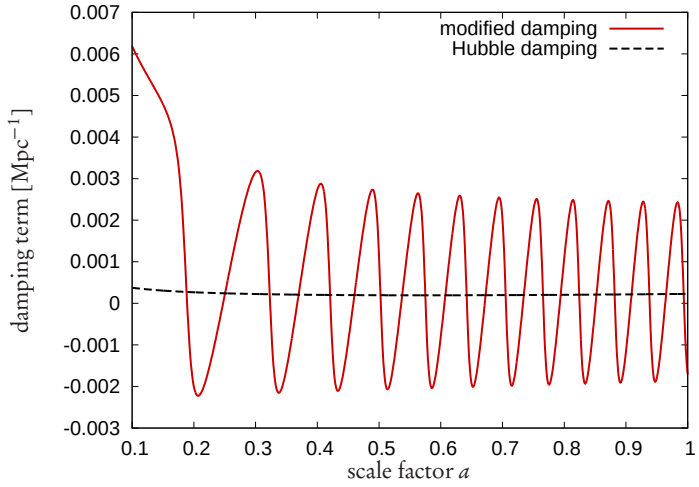

Figure 5.9: The modified Hubble damping from Eq. (5.38) compared to the usual Hubble damping a'/a.

shall see later, this result is not physical but, instead, an artefact of neglecting local

mass variations. As already speculated by Nunes et al. (2011), an effective mass freezing occurs in the lumps, and the background oscillation of $\bar{\varphi}$ is effectively shielded, i. e. compensated by the perturbations.

The simulations performed by Baldi et al. (2011) also verified that, indeed, the effective N-body particles are accelerated to relativistic velocities, hence leaving the Newtonian limit. At redshift $z = 1$ (corresponding to $a = 0.5$), already 20% to 30% of the effective N-body particles have reached the speed of light. Here, at the latest, the Newtonian N-body simulation can no longer be used.

5.3 Cornerstones of the full simulation

The considerable amount of original work to understand the cosmological evolution of growing neutrino quintessence, which we have briefly summarized in the preceding section, has not given a comprehensive picture, nor does it enable us to make quantitative predictions; instead, it underlines that a variety of drastic and initially unexpected effects are decisive for any quantitative description of growing neutrino quintessence cosmology (Amendola et al., 2008a; Wetterich, 2007; Brouzakis et al., 2008; Mota et al., 2008; Dent et al., 2009; Pettorino et al., 2009; Wetterich and Pettorino, 2009; Ayaita et al., 2009; Wintergerst et al., 2010; Wintergerst and Pettorino, 2010; Pettorino et al., 2010; Baldi et al., 2010; Brouzakis et al., 2011; Schrempp and Brown, 2010; Nunes et al., 2011; Baldi et al., 2011). This motivates the development of a unified approach, designed from scratch to include all essential effects in a comprehensive and self-consistent method, starting from the fundamental equations of the theory. This has been achieved by Ayaita et al. (2012b); encouraged by the promising, yet incomplete results of the Newtonian N-body simulations (Baldi et al., 2011), an N-body based approach has been chosen.

This new N-body simulation scheme for growing neutrino quintessence is the topic of Chapter 6. Here, we will anticipate several key points of these simulations in order to investigate the physics of the model, in particular of the forming neutrino structures, more closely. In fact, we shall see that many aspects of these structures or *lumps* can be understood analytically, providing a clear framework of concepts that we can employ later to interpret the results of the full simulation runs.

This section serves both as an (incomplete) introduction to the simulation method and as the basis for our analytical investigations. The results of the simulations will guide us to some extent and allow us to numerically test our analytical hypotheses. Therefore, we briefly explain which effects are included in the simulations and quote some fundamental equations on which we will rely in the course of this chapter. The technical details are postponed to Chapter 6.

We will build upon this section when we argue that the cosmon-neutrino lumps can be treated as effective, nonrelativistic particles in Sec. 5.4.1. Once the neutrinos are bound in structures, the cosmological dynamics depends on the nonrelativistic fluid of lumps (not only the neutrinos, as we will see, but also the local cosmon field sourced by them has to be regarded as a part of the cosmon-neutrino lump).

Relativistic neutrinos

In order to fully account for the possibility of relativistic neutrino velocities, we describe the motion of effective neutrino N-body particles with a fully relativistic equation of motion. The energy density ρ_ν and the pressure p_ν have to be calculated including relativistic effects. They are given by the $T^0{}_{(\nu)0}$ and the $T^i{}_{(\nu)i}$ components, respectively. In a realistic treatment, also the off-diagonal components $T^i{}_{(\nu)j}$ are important, as they account for the anisotropic shear perturbation, cf. Eq. (2.66). We model $T^{\mu\lambda}_{(\nu)}$ by a collection of neutrino particles with standard one-particle energy-momentum tensors

$$T^{\mu\nu} = \frac{1}{\sqrt{-g}} \int d\eta\, m_\nu(\varphi)\, u^\mu u^\nu\, \delta^4(x-\xi) \tag{5.39}$$

with the proper time η, the particle trajectory $\xi(\eta)$, the cosmon-dependent neutrino mass $m_\nu(\varphi)$ evaluated at the particle position $\xi(\eta)$, and the four-velocity $u^\mu \equiv d\xi^\mu/d\eta$, cf. Eq. (2.41). This manifestly covariant expression can be rewritten in a simpler form by performing the integration over proper time, i. e. writing

$$\int d\eta \delta^4(x-\xi) = \int \frac{d\eta}{d\xi^0} d\xi^0 \delta(x^0-\xi^0)\delta^3(\boldsymbol{x}-\boldsymbol{\xi}) = \frac{d\eta}{d\xi^0}\delta^3(\boldsymbol{x}-\boldsymbol{\xi}). \tag{5.40}$$

The derivative of proper time η with respect to coordinate time $\xi^0 = \tau$ is linked to the special-relativistic Lorentz factor

$$\gamma = \frac{\sqrt{-g_{00}}\, d\xi^0}{d\eta} = \frac{1}{\sqrt{1-(1-2\Psi-2\Phi)\,\boldsymbol{v}^2}}. \tag{5.41}$$

The term $\sqrt{-g_{00}}$ absorbed in γ just changes the factor $\sqrt{-g}$ to its spatial version $\sqrt{{}^{(3)}g}$,

$${}^{(3)}g = \det(g_{ij}) \quad \text{and hence} \quad \sqrt{{}^{(3)}g} = a^3(1-3\Phi). \tag{5.42}$$

The one-particle energy-momentum tensor then reads

$$T^{\mu\nu} = \frac{1}{\sqrt{{}^{(3)}g}} \frac{m_\nu(\varphi)}{\gamma}\, u^\mu u^\nu\, \delta^3(\boldsymbol{x}-\boldsymbol{\xi}). \tag{5.43}$$

Several approaches of deriving the equation of motion for these particles will be mentioned in Sec. 6.3. The simplest approach just uses the standard relativistic one-particle action, supplemented by a φ-dependent mass,

$$S = \int d^4x\, \sqrt{-g}\, T^\lambda{}_\lambda = -\int d\eta\, m_\nu(\varphi(\xi)), \tag{5.44}$$

which has to be varied with respect to the trajectory $\xi(\eta)$. By derivatives acting on $m_\nu(\varphi(\xi))$, this variation will induce extra terms to the usual general-relativistic geodesic equation expressing the cosmon-neutrino coupling:

$$\frac{du^\mu}{d\eta} + \Gamma^\mu_{\rho\sigma} u^\rho u^\sigma = \beta \partial^\mu \varphi + \beta u^\lambda \partial_\lambda \varphi \, u^\mu, \tag{5.45}$$

where β is the cosmon-neutrino coupling parameter. With the Christoffel symbols from Eqs. (2.58) and (2.59), this fully relativistic equation of motion is used in the N-body approach for the effective N-body particles, and the neutrino energy momentum tensor is evaluated as the sum over the one-particle contributions.

Local mass variation

Another crucial ingredient is to include local variations of the neutrino mass, which will be decisive for the backreaction effect discussed in Sec. 5.2. The local mass is a function of the local cosmon field,

$$m_\nu(\varphi) = m_\nu(\bar\varphi(\tau) + \delta\varphi(\tau, \boldsymbol{x})) = \bar m \, e^{-\beta\bar\varphi} e^{-\beta\delta\varphi}, \tag{5.46}$$

where the last equation holds for the constant β model, with a background mass and a local fluctuation. Although we will see that cosmon perturbations are linear in the sense $\delta\varphi \ll 1$, the term $\beta\delta\varphi$ in the mass perturbation can reach order one; the mass function $m_\nu(\bar\varphi + \delta\varphi)$ can thus not be linearized.

The cosmon perturbation $\delta\varphi$ is obtained by solving the linearly perturbed Klein-Gordon equation, cf. Eq. (5.27). Numerically, we have to neglect the time derivatives $\delta\varphi''$ and $\delta\varphi'$ against the spatial derivatives (in a time integration, the small quantity $\delta\varphi''$ would be calculated as the difference of two large quantities, namely $\Delta\delta\varphi$ and the source perturbation $\delta(\beta \mathrm{tr} T_{(\nu)})$ — this cancellation effect cannot be resolved numerically). So, the equation for $\delta\varphi$ is approximately given by

$$\Delta\delta\varphi - a^2 V_{,\varphi\varphi}(\bar\varphi)\delta\varphi + 2\left(\bar\varphi'' + 2\frac{a'}{a}\bar\varphi'\right)\Psi = a^2\delta\left(\beta \mathrm{tr} T_{(\nu)}\right). \tag{5.47}$$

The left-hand side has been linearized in $\delta\varphi$, but the right-hand side is a complicated, nonlinear function of $\delta\varphi$. Even in the constant β model, where β can be taken out of the perturbation, $\delta \mathrm{tr} T_{(\nu)}$ contains the neutrino mass $\propto \exp(-\beta\delta\varphi)$. The solution of this equation is a crucial part of the N-body method.

Backreaction

The coupling term in the background part of the Klein-Gordon equation (5.11) has been given by $a^2\beta(\bar\rho_\nu - 3\bar p_\nu)$. The usual procedure of calculating the cosmological evolution would go as follows. First, the pure background equations are integrated, providing the results that we have already shown in Sec. 5.1. Then, on this precomputed background, the perturbations are evolved. This procedure is only exact in the

linear case, since the averaging is, as well, a linear operation. In the case of nonlinear structure formation, averaging the nonlinear equations first and then evolving them leads, in general, to a different result than evolving the full nonlinear equations first and averaging thereafter. We have discussed this in the case of gravity in Sec. 2.2.2, illustrated in Fig. 2.3. In our case, the averaging problem can be stated as the inequality

$$\beta(\bar{\varphi})\mathrm{tr}T_{(\nu)}(\bar{\varphi}) \neq \overline{\beta(\varphi)\mathrm{tr}T_{(\nu)}(\varphi)}, \tag{5.48}$$

since both, $\beta(\varphi)$ and the mass function $m_\nu(\varphi)$ can lead to nonlinear contributions in the cosmon perturbation $\delta\varphi$. Most neutrinos will be located in lumps where $\delta\varphi$ is negative and the mass is consequently suppressed. In the varying β model, $|\beta|$ grows with φ and is, accordingly, also suppressed in lumps, $|\beta(\bar{\varphi}+\delta\varphi)| < |\beta(\bar{\varphi})|$. So, the local cosmon perturbations systematically suppress the right-hand side of Eq. (5.48) as compared to the background calculation given by the left-hand side.

Moreover, Eq. (5.48) veils another important contribution to the backreaction effect. In a background calculation, the neutrino equation of state $w_\nu = \bar{p}_\nu/\bar{\rho}_\nu$ decreases because of the growing mass. This means that $w_\nu \approx 0$ in the late-time evolution. Thus, the background computation gives $\mathrm{tr}T_{(\nu)}(\bar{\varphi}) \approx -\bar{\rho}_\nu$. In the perturbations, neutrinos can again accelerate to relativistic velocities, and the absolute value of the trace is smaller, $\mathrm{tr}T_{(\nu)} = -\rho_\nu + 3p_\nu$. This intensifies the suppression of the right-hand side.

Formation of lumps

The technical details of the simulation and a quantitative analysis of its results are given in Chapter 6. We conclude this section with a qualitative discussion of one essential and characteristic result of the constant β model. Once the neutrinos have become nonrelativistic, the perturbations in the neutrino density grow quickly to become nonlinear on comoving scales $\lambda \sim 100h^{-1}$Mpc, cf. Fig. 5.7 at $a \gtrsim 0.3$. Subsequently, large nonlinear, stable neutrino lumps form until $a \approx 0.5$. We show these structures in a simulation box of size $L = 600h^{-1}$Mpc and for the model parameters $\beta = -52$ and $\alpha = 10$ at $a = 0.5$ in Fig. 5.10. Nearly all the cosmic neutrinos are collected in these lumps. This tells us that a thorough analysis of the physics of these lumps is essential for understanding the subsequent cosmological evolution.

We next give some quantitative results of the lump distribution as obtained by Ayaita et al. (2013). In 10 simulation runs, lumps at $a = 0.5$ have been identified as local maxima of the neutrino number density. This lump identification scheme is also well-known for finding dark matter halos, where it is called the DENMAX method (Gelb and Bertschinger, 1994). This lump identification agrees with visually identifying the lumps in, e. g., Fig. 5.10; the concrete procedure chosen is not essential for our purposes.

We characterize the lumps l by the number of neutrinos $N_\nu(V_l)$ in the volume V_l of the lump l. This can be normalized by the total number of neutrinos in the (present) Hubble horizon, $N_\nu(V_{H_0})$, defining the fraction

$$f_l = \frac{N_\nu(V_l)}{N_\nu(V_{H_0})} \tag{5.49}$$

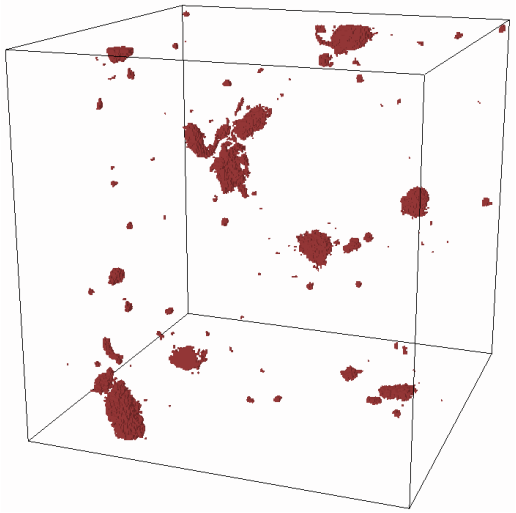

Figure 5.10: Neutrino lumps in the full N-body simulation at $a = 0.5$, in a box of size $L = 600h^{-1}$Mpc. Indicated are regions with a neutrino number density contrast $\delta n_\nu/\bar{n}_\nu \geq 5$. The figure is taken from Ayaita et al. (2013).

where the Hubble volume is of size H_0^{-3}. The simulation boxes have the dimension $L = 600h^{-1}$Mpc. The average abundance N_l of lumps in V_{H_0} exceeding a neutrino number fraction threshold, $N_l(f_l > f)$, is shown in Fig. 5.11.

We divide the number fraction f_l in bins and also calculate the average lump mass M_l in each bin, as well as the standard deviation σ_M. We plot the result in Fig. 5.12. We have found a number of 10^3 to 10^4 lumps in the present Hubble volume; the largest lumps we have observed reach $\sim 10^{17}$ solar masses. As we will see in detail in Sec. 5.4, the lump mass consists of two contributions, a neutrino part $M_{\nu,l}$ and a (subdominant) cosmon part $M_{\delta\varphi,l}$ given by the local cosmon contribution. If we denote by $\hat{\varphi}$ the external cosmon field (not attributed to the lump) and by γ_l the Lorentz factor of the lump (although to a good approximation $\gamma_l \approx 1$), the masses are given by integrating the energy density in the lump volume V_l (cf. the next section for details),

$$\gamma_l M_{\nu,l} = \int_{V_l} d^3x \sqrt{{}^{(3)}g}\, \rho_\nu \approx \sum_p \gamma_p\, m_\nu(\varphi(\boldsymbol{x}_p)), \tag{5.50}$$

$$\gamma_l M_{\delta\varphi,l} = \int_{V_l} d^3x \sqrt{{}^{(3)}g}\, (\rho_\varphi - \rho_{\hat{\varphi}}), \tag{5.51}$$

where the sum is performed over particles labeled by the index p, and the cosmon energy density is

$$\rho_\varphi = \frac{\dot{\varphi}^2}{2} + \frac{|\nabla\varphi|^2}{2a^2} + V(\varphi). \tag{5.52}$$

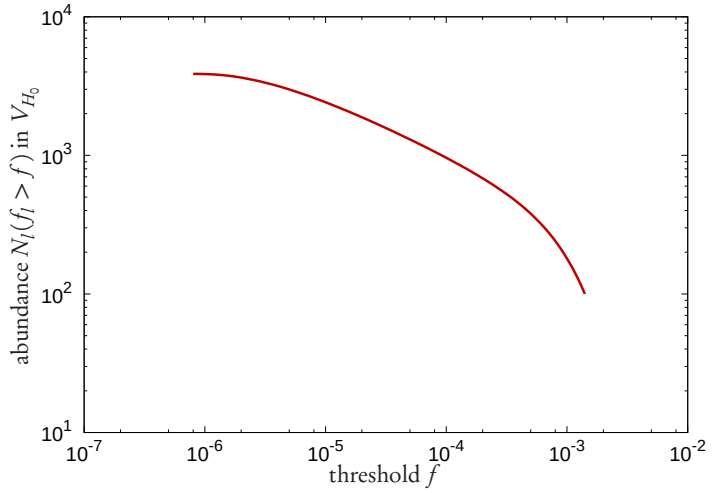

Figure 5.11: Lump abundances as a function of the neutrino number fraction f_l defined in Eq. (5.49) at $a = 0.5$. The figure is taken from Ayaita et al. (2013).

5.4 Cosmon-neutrino lump fluid

5.4.1 Lumps as particles

The question whether the cosmological evolution of growing neutrino quintessence in the constant β model (which we will assume throughout this section), after the lump formation has finished at $a \approx 0.5$, can be modeled with the help of a 'fluid of lumps' is, at first sight, not easy to answer. It is tempting to think, considering Fig. 5.10, that the lumps can be treated as particles forming a cosmic fluid. Yet, the particle description relies on an important condition. The one-particle energy-momentum tensor $T^{\mu\nu}$, cf. Eq. (5.39), is pressureless in the rest frame where $u^i = 0$:

$$p = \frac{1}{3} T^i{}_i \propto u^i u_i = 0, \tag{5.53}$$

which means: particles have no internal pressure.

This condition seems to be clearly violated for neutrino lumps. As we have already discussed, the neutrinos within lumps can reach relativistic velocities, both due to the cosmon-mediated attractive force and due to the mass suppression. In the sum over the particles forming the lump, there will, accordingly, be a considerable pressure contribution due to the nonnegligible dispersion $\langle \boldsymbol{u}^2 \rangle$. It amounts to typically $w_\nu \approx 0.1$ (Ayaita et al., 2012b). So, if the lumps were only *neutrino lumps*, they could not be treated as particles.

In fact, we have to also count the local cosmon perturbation $\delta\varphi$, sourced by the neutrinos of the lump, as part of the lump. Although the energy density of this cosmon perturbation is subdominant as compared to the neutrinos, the pressure contribution

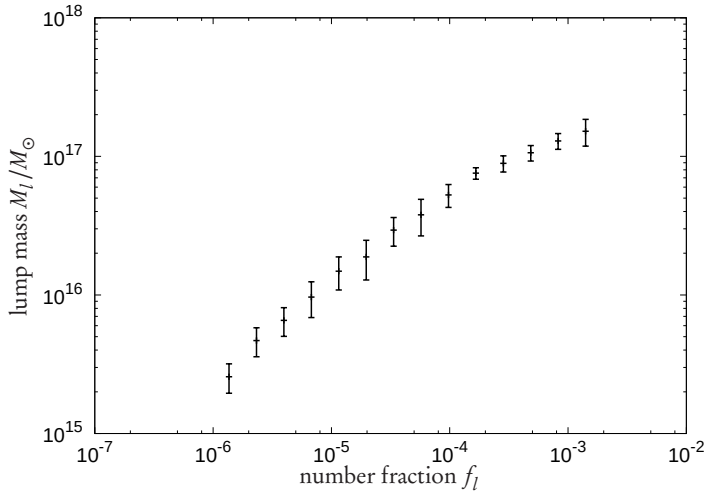

Figure 5.12: Lump masses (in solar masses) and standard deviations for different neutrino number fractions at $a = 0.5$. The figure is taken from Ayaita et al. (2013).

is important. We will see that it leads to a cancellation of the neutrino pressure at sufficiently large distances from the center of the lump. Lumps are thus properly considered as *cosmon-neutrino lumps*, and they are approximately pressureless in this description, which allows a particle treatment. This idea was established by Ayaita et al. (2013), and we repeat the reasoning as well as the analysis based on it here.

A well-known physical example with an analogous behavior is a gas of nonrelativistic atoms. This fluid obeys $T^i{}_i = 0$ — it has no relativistic pressure. Still, the electrons within the atoms have a small but nonnegligible pressure contribution. How can these two aspects be reconciled? We have ignored the electromagnetic field. In fact, the electromagnetic field around the atom exactly cancels the pressure contribution due to the electrons such that, at sufficiently large distances, the atoms are pressureless. Properly defined, the atom does not only consist of the nucleus and the electrons, but also of the local electromagnetic field. Another example are the nuclei themselves, where one would naively expect many pressure contributions from quarks and gluons but eventually finds that a nucleus at rest is pressureless.

The universality of this observation indicates that there is a fundamental principle behind it. Indeed, we will give an argument in Sec. 5.4.2 that guarantees the pressure cancellation under very general conditions. For our discussion, we may neglect the gravitational potential against the cosmon-mediated attractive force such that the argument can be formulated without metric perturbations (i. e. in Minkowski space or a flat FLRW metric). The conditions for a pressure cancellation of an object are:

1. The energy-momentum tensor $T^{\mu\nu}$ describing the object obeys the conservation equation $\nabla_\nu T^{\mu\nu} = 0$.

2. The object can be completely localized in a finite volume V such that $T^{\mu\nu} = 0$

outside V.

3. The object is static in the sense $\partial_0(\sqrt{{}^{(3)}g}\, T^{\mu\nu}) = 0$.

To a more or less good approximation, these conditions are applicable to a large class of stable objects. Before we briefly discuss the restrictions, let us perform a numerical check for lumps in the growing neutrino quintessence model.

Ayaita et al. (2013) have simulated a single lump in a simulation box. The lump was constructed such that it remains static due to an exact balance between the cosmon-mediated force and the local neutrino velocity dispersion σ_{ij}. We will give this balance equation in Sec. 5.4.4. Matter and gravity have been neglected, and the lump was chosen spherically symmetric such that the field equation for $\delta\varphi$ becomes a one-dimensional differential equation in the distance r from the lump's center, which is straightforward to solve for the boundary condition of a vanishing perturbation at infinity. If the neutrinos are modeled by a sum over one-particle energy-momentum tensors of the form of Eq. (5.43), their pressure contribution, integrated up to a radius r, reads

$$P_\nu(r) = \frac{1}{3}\int_0^r 4\pi r'^2 dr' \sqrt{{}^{(3)}g}\, T^i{}_{(\nu)i} = \frac{1}{3}\sum_p \frac{m_{\nu,p}}{\gamma_p} u_p^i u_{p,i}, \tag{5.54}$$

where the index p labels the particles. The cosmon pressure can be calculated from the cosmon energy-momentum tensor. We can assume a static cosmon perturbation here:

$$P_{\delta\varphi}(r) = -\int_0^r 4\pi r'^2 dr' \sqrt{{}^{(3)}g}\left[\frac{1}{6a^2}\left(\frac{\partial\delta\varphi}{\partial r}\right)^2 + V_{,\varphi}(\bar\varphi)\,\delta\varphi\right]. \tag{5.55}$$

We already see the opposite signs of the contributions in these equations. The measurement of $P_\nu(r)$, $P_{\delta\varphi}(r)$, and their sum is shown in Fig. 5.13. The neutrino contribution grows quickly as r increases and becomes constant at $aR_\nu \gtrsim 5h^{-1}\mathrm{Mpc}$. This simply reflects the fact the neutrino number density has fallen off to a small value above R_ν. The cosmon contribution, however, extends to $aR_{\delta\varphi} \gtrsim 20h^{-1}\mathrm{Mpc}$. This also defines the size R_l of the cosmon-neutrino lump at which the lump can be modeled as a pressureless particle. The total pressure $P_\nu + P_{\delta\varphi}$ has fallen to almost zero at this distance.

The particle description of lumps is thus applicable if the effective cosmon-neutrino lump size R_l is smaller than the typical distance D between neighboring lumps. Then, the lump fluid can be described by the mutual interactions between cosmon-neutrino lump particles. In the simulation, we observe typically $D \sim 100h^{-1}\mathrm{Mpc}$. This can be explained by our observation, already in linear theory, that the neutrino perturbations become nonlinear first at scales $\sim 100h^{-1}\mathrm{Mpc}$, cf. Fig. 5.7. These initial nonlinearities then shrink to the lumps we see at $a \approx 0.5$.

The hierarchy of scales is visualized in Fig. 5.14 and may be stated as

$$R_\nu \ll R_l \ll D. \tag{5.56}$$

We introduce an intermediate scale λ with $R_l < \lambda < D$. On scales $\sim\lambda$, the particle description of neutrino lumps is useful since the cosmon-neutrino lumps are smaller

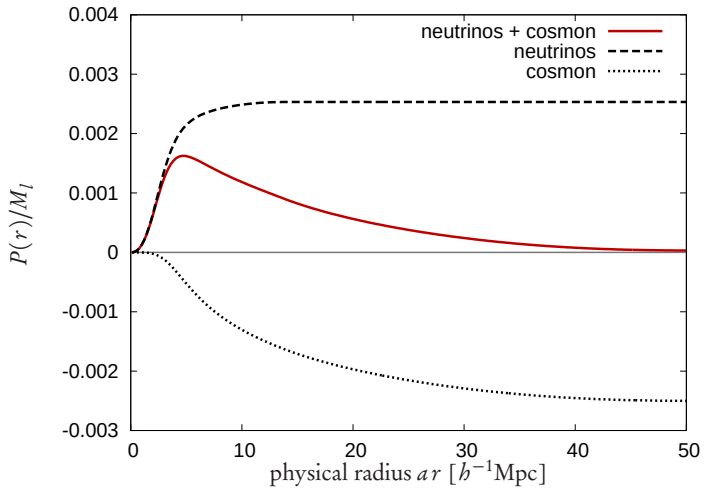

Figure 5.13: Pressure contributions $P_\nu(r)$, $P_{\delta\varphi}(r)$, and their sum integrated to the radius r and normalized by the mass M_l of the static lump. The figure is taken from Ayaita et al. (2013), cf. also Fig. 7.2 in Weber (2012).

than λ but the typical distance between the lumps is larger than λ such that different lumps are clearly separated. This intermediate scale will play an important role in our analysis.

In the idealized, static lump, the pressure cancellation was exact. The three conditions necessary for the general argument are met. Realistically, however, all conditions are only satisfied approximately; strictly speaking, there are effects violating each of them. The neutrino lumps are then not exactly pressureless but they keep a residual, small pressure. The simulations show that the pressure cancellation works to roughly one order of magnitude such that there is a small deviation of order $\sim 10\%$. This quantifies the error of the particle description although a part of the deviation might simply be due to limitations of the numerics, e. g. regarding the spatial resolution. Let us discuss the three conditions in a realistic context.

1. Only the total energy-momentum tensor of the neutrinos, the local cosmon field attributed to the lump, and the outside cosmon field satisfies a conservation equation. Consequently, the cosmon-neutrino lump energy-momentum tensor is not exactly conserved — the deviation is essentially given by the background evolution of the cosmon.

2. The cosmon perturbation behaves similarly to the gravitational potential around a point mass, i. e. approximately $\delta\varphi \propto r^{-2}$ (due to the very small scalar mass term $V_{,\varphi\varphi}$ that becomes only important at large distances). But the particle description assumes $R_l \ll D$; the typical distance between neighboring lumps sets a limit up to which we can attribute the local cosmon perturbation to the lump.

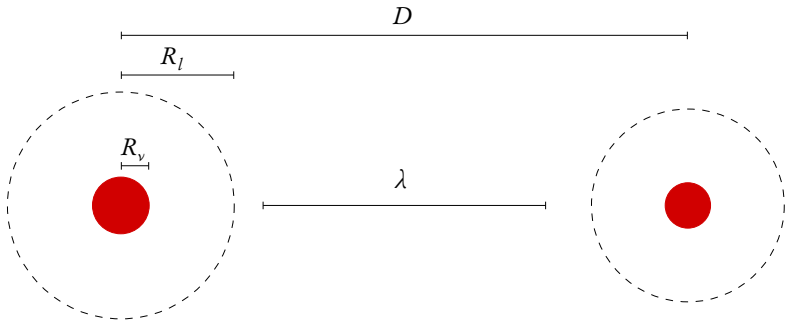

Figure 5.14: Illustration of the hierarchy of scales in the cosmon-neutrino lump picture. The two red circles indicate two neighboring neutrino lumps. The size of the red circle is the typical extension R_ν of the neutrino number density. The pressure of the local cosmon perturbation extends until R_l (indicated by the dashed circle). Above this scale, the lump can be modeled as a (pressureless) particle. This scale can be compared to the typical distance D between the lumps. We also define an intermediate scale λ.

3. The staticity of the energy-momentum tensor is again violated by the effect of the outside cosmon, even if the lump has virialized. The internal cosmon field still 'feels' the outside field, which essentially plays the role of a boundary condition, cf. Fig. 5.8. The approximate mass freezing within neutrino lumps shows that this effect is small.

The corrections due to these restrictions are expected to be small since the external field evolves on a time scale much larger than the dynamical time scale of the lump. In the limit of a static background, the cancellation would be exact (neglecting the second point). The second point only plays a small role since we have established that the lump pressure has fallen off to a good approximation on scales well below D.

5.4.2 Pressure cancellation in detail

We now give the technical argument why stable objects, under the general conditions given in the previous section, are pressureless at sufficiently large distances. Although the derivative is fairly general, we will employ the example of a lump in an unperturbed FLRW metric (neglecting the gravitational potential). For most systems, even for cosmon-neutrino lumps, the expansion is not important and a pure Minkowski background could be used instead. The scale factor a in the FLRW metric could also describe some local property of the metric, which does not vary on the length scale of the object; hence, the argument works also for a perturbed metric as long as the perturbations are spatially approximately constant in the considered volume.

We assume that the lump is described by an energy-momentum tensor $T^\mu{}_\nu$ (consisting of a concentrated neutrino contribution and a more extended cosmon contribution) and that it is completely localized in a volume V, i. e. $T^\mu{}_\nu(\boldsymbol{x}) = 0$ for $\boldsymbol{x}$ outside

V (this is not satisfied in an exact sense for neutrino lumps). We consider the amplitude

$$A^{\mu}{}_{\nu} = \int_V d^3x \sqrt{{}^{(3)}g}\, T^{\mu}{}_{\nu}, \tag{5.57}$$

which characterizes the lump on scales larger than V. With the lump being 'pressureless', we mean that the integrated pressure

$$P = \frac{1}{3} A^{i}{}_{i} = 0 \tag{5.58}$$

vanishes in the rest-frame of the lump. Of course, the coherent motion of the lump will lead to a pressure contribution as it does for ordinary particles. In addition, we will show $A^{i}{}_{j} = 0$ in the rest frame. This can be stated as

$$A^{\mu}{}_{\nu} = -M_l\, \delta^{\mu}_{0} \delta^{0}_{\nu} \tag{5.59}$$

in the rest frame. Of course, $A^{0}{}_{0} = -M_l$ simply by the definition of the rest mass. Furthermore, A^{i0} is the total spatial momentum of the lump, and hence $A^{i0} = 0$ in a system where the lump is at rest. The above equation is then equivalent to $A^{i}{}_{j} = 0$ as we have claimed.

We assume, next to the localization of the lump in the volume V, two further conditions:

- *Staticity* in the sense that the energy-momentum content in a physical volume is constant,
$$\partial_0 \left(\sqrt{{}^{(3)}g}\, T^{\mu}{}_{\nu} \right) = 0. \tag{5.60}$$
This will not hold exactly due to the reaction of the lump to the evolving external cosmon field.

- *Energy-momentum conservation* stated as
$$0 = \nabla_{\lambda} T^{\lambda}{}_{j} = \partial_0 T^{0}{}_{j} + \partial_i T^{i}{}_{j} + 3\frac{\dot{a}}{a} T^{0}{}_{j} \tag{5.61}$$
with the help of the Christoffel symbols for the unperturbed FLRW metric. For cosmon-neutrino lumps, this equation only holds under the assumption that the energy-momentum exchange with the external field can be neglected.

Taken together, the conditions give $\partial_i T^{i}{}_{j} = 0$ and hence the vanishing of the 3-divergence for the vector

$$\boldsymbol{v} \equiv (T^{1}{}_{j}, T^{2}{}_{j}, T^{3}{}_{j}), \quad \boldsymbol{\nabla} \cdot \boldsymbol{v} = 0 \tag{5.62}$$

for all $j = 1,2,3$. For the sake of simplicity, we choose $i = j = 1$ without loss of generality. We thus consider the component $A^{1}{}_{1}$, which we write as

$$A^{1}{}_{1} = a^3 \int dx \int dy\, dz\, v_1 = a^3 \int dx \int_{S_x} d\boldsymbol{S} \cdot \boldsymbol{v}. \tag{5.63}$$

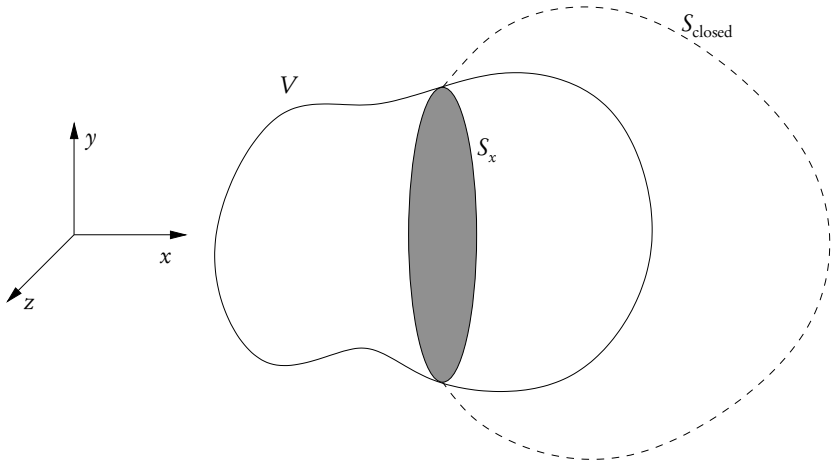

Figure 5.15: The geometrical situation for our analytic argument. It shows a generic lump volume V, the slice S_x and its closure outside V.

Here, S_x is the slice of V of constant x. The situation is illustrated in Fig. 5.15. As indicated in the figure, we extend the slice S_x to a closed surface S_{closed} outside V such that $S_{\text{closed}} \cap V = S_x$. Since the energy-momentum tensor vanishes outside V, the inner integral in Eq. (5.63) can equally be performed over the closed surface S_{closed},

$$A^1{}_1 = a^3 \int dx \oint_{S_{\text{closed}}} d\boldsymbol{S} \cdot \boldsymbol{v} = a^3 \int dx \int d^3x' \boldsymbol{\nabla} \cdot \boldsymbol{v} = 0, \tag{5.64}$$

where we have used that the divergence of $\boldsymbol{v}$ vanishes everywhere in the enclosed volume. Along the same lines, one obtains $A^i{}_j = 0$ for arbitrary i and j.

If the lump exhibits a coherent motion quantified by the four-velocity u^μ, the straightforward generalization of the rest-frame result reads

$$A^\mu{}_\nu = \frac{M_l}{\gamma} u^\mu u_\nu. \tag{5.65}$$

This means that the lump, located at ξ, on scales much larger than V, indeed looks like a point particle with the standard energy-momentum tensor

$$T^\mu{}_\nu \approx \frac{A^\mu{}_\nu}{\sqrt{{}^{(3)}g}} \delta^3(\boldsymbol{x} - \xi) = \frac{1}{\sqrt{{}^{(3)}g}} \frac{M_l}{\gamma} u^\mu u_\nu \delta^3(\boldsymbol{x} - \xi). \tag{5.66}$$

5.4.3 The effective coupling

Based on the above argument, we assume that a lump looks, on scales $\sim \lambda$, effectively point-shaped with a standard one-particle energy-momentum tensor and a mass M_l. We shall now introduce the effective coupling parameter which will turn out decisive

for the interaction between lumps and the equation of motion of the lumps. The lump interaction is mediated by the cosmon φ. On scales $\lesssim \lambda$, we attribute the local cosmon field to the lumps. So, for the interaction between the lumps, only the large-scale cosmon, averaged on the scale λ, is important. This large-scale or *external* cosmon field $\hat{\varphi}$ may be defined by

$$\hat{\varphi}(\boldsymbol{x}) = \int d^3y \, \sqrt{{}^{(3)}g} \, W_\lambda(\boldsymbol{x}-\boldsymbol{y}) \, \varphi(\boldsymbol{y}) \tag{5.67}$$

with some window function W_λ satisfying

$$\int d^3x \sqrt{{}^{(3)}g} \, W_\lambda(\boldsymbol{x}) = 1, \quad \text{and} \quad W_\lambda(\boldsymbol{x}) \approx \begin{cases} \text{const.} & \text{for } |\boldsymbol{x}| \ll \lambda, \\ 0 & \text{for } |\boldsymbol{x}| \gg \lambda. \end{cases} \tag{5.68}$$

The freedom we have in choosing such a window function and in defining the intermediate scale $R_l < \lambda < D$ contributes to the quantitative uncertainty inherent to our approach.

In complete analogy to the (fundamental) cosmon-neutrino coupling parameter β, we define the effective coupling by

$$\beta_l = -\frac{d \log M_l}{d\hat{\varphi}}, \tag{5.69}$$

which will be characteristic for each lump l. The fundamental coupling β quantifies the dependence of the fundamental neutrino mass m_ν on the local value of the cosmon φ; the effective coupling β_l, in turn, describes the dependence of the lump mass M_l on the large-scale cosmon $\hat{\varphi}$, evaluated at the lump position. We will see that, in the equation of motion of the lumps and in the field equation for the large-scale cosmon $\hat{\varphi}$, the effective coupling appears in complete analogy to the fundamental coupling.

In the same ten simulation runs as for Figs. 5.11 and 5.12, cf. Sec. 5.3, we have measured the effective couplings β_l of the lumps by varying the large-scale cosmon field $\hat{\varphi}$ at the lump positions and each time measuring the resulting rest-frame lump mass M_l according to Eqs. (5.50) and (5.51). The lumps are again classified according to the fraction f_l of neutrinos in the present Hubble volume that they contain, cf. Eq. (5.49). These fractions are grouped in bins; we show the average effective coupling parameters together with their standard deviations for all bins in Fig. 5.16. We have used a smoothing scale $\lambda = 30h^{-1}\text{Mpc}$. The effective couplings are substantially smaller than the fundamental coupling, and their values decrease for larger lump sizes, which is explained by the steeper cosmon potentials $\delta\varphi$ and, accordingly, a more severely nonlinear field equation.

5.4.4 Aspects of stability

A crucial assumption of the particle description is the approximate stability of virialized lumps. In the end, this point has to be clarified numerically. Our N-body based

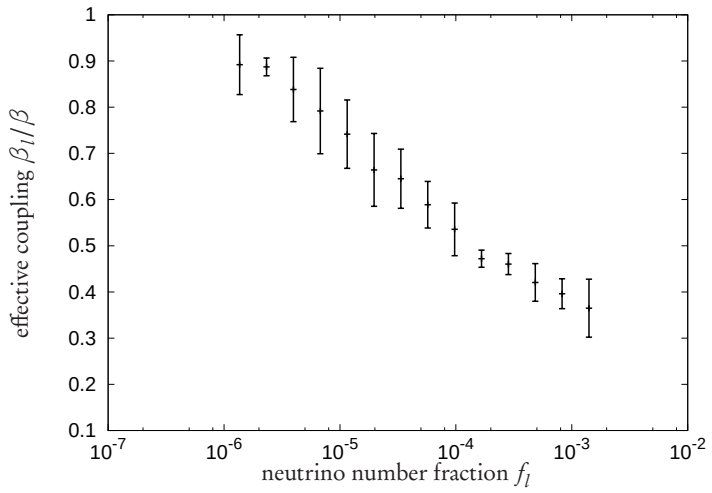

Figure 5.16: The effective couplings as compared to the fundamental coupling β for lumps characterized by their size, i. e. the amount of bound neutrinos f_l. The figure is taken from Ayaita et al. (2013).

simulations do not possess the required spatial resolution to ultimately answer this question in the full cosmological context. This is left open for future work with refined numerical methods. What we can do, is to simulate isolated cosmon-neutrino lumps, and there, we indeed observe stability and, eventually, staticity of the lumps. We will show an example at the end of this section.

Moreover, the question of stability deserves attention from a physical perspective. It is instructive to collect some basic considerations that motivate the assumption that cosmon-neutrino lumps are, indeed, long-lived structures. Essentially, we show a couple of similarities to the case of gravitationally bound dark matter halos. If the latter become approximately static, we then have to assume the same for the cosmon-neutrino lumps. The stability of dark matter halos is, of course, well established both numerically and observationally, although the problem is difficult to fully understand analytically. Unlike physical systems in minima of a thermodynamic potential, dark matter halos have a negative heat capacity C_V. Bartelmann et al. (2013) explain this with the behavior of the total energy U in the virialized case,

$$2E_{\mathrm{kin}} = -E_{\mathrm{pot}} \quad \text{and thereby} \quad U = -E_{\mathrm{kin}}. \tag{5.70}$$

Their argument goes as follows. The kinetic energy plays the role of a temperature, $T \sim \alpha E_{\mathrm{kin}}$, $\alpha > 0$. If the system loses energy, the total energy decreases and hence the kinetic energy, as seen in the above equation, increases. The heat capacity

$$C_V = \left(\frac{\partial U}{\partial T}\right)_V \sim -\frac{1}{\alpha} \tag{5.71}$$

in this schematic definition is negative. This shows that the question of stability is

already involved for self-gravitating systems. The situation for the cosmon-neutrino coupling is, at first sight, even more complex since, in addition to an attractive force, we have to take into account the mass variation. We will argue in this section that, despite of this additional complication, the situation is essentially analogous to a self-gravitating system.

Angular momentum

A suitably defined total angular momentum of a cosmon-neutrino lump is conserved in the limit of the lump being decoupled from the evolution of the external cosmon field. We will see that, in the case of a spherically symmetric lump, the angular momentum is completely given by the neutrino motion. In this case, a total neutrino angular momentum is conserved, similar to the matter angular momentum in self-gravitating halos. Of course, even in the absence of such a dynamical stabilization, the lumps would, ultimately, stabilize due to the degeneracy pressure; this scenario has been investigated by Brouzakis et al. (2008). We argue that this scenario is not realistic.

Before we give our general argument, we briefly mention the motion of a test particle moving under the influence of the cosmon-mediated attraction to a spherical neutrino overdensity. The details are worked out by Weber (2012), and we repeat the main argument here. Indeed, there is an angular momentum barrier just as in the gravitational case which stabilizes the particle against falling into the center. The motion of a test particle in a spherically symmetric, static cosmon field $\varphi(r)$ is mathematically analogous to the motion in a gravitational potential $\Phi(r)$, with the exception of the varying mass

$$\dot{m}_\nu = -\beta m_\nu \frac{u^\lambda \partial_\lambda \varphi}{u^0}, \tag{5.72}$$

where we are working with cosmic time t. Still, it is straightforward to see that the relativistic angular momentum

$$L = \gamma m_\nu r^2 \dot{\vartheta} \tag{5.73}$$

is conserved, simply since the angle ϑ in the plane of motion is a cyclic variable, and L is the corresponding canonical momentum. This conserved angular momentum implies an angular momentum barrier in the radial equation of motion, i. e. for the radial momentum $p_r = \gamma m_\nu \dot{r}$:

$$\dot{p}_r = \frac{L^2}{\gamma m_\nu r^3} + \frac{\beta m_\nu}{\gamma} \frac{\partial \varphi}{\partial r}. \tag{5.74}$$

Remarkably, the angular momentum barrier is even more effective than for gravity since $m_\nu(\varphi(r))$ decreases as r approaches 0 if the assumed neutrino distribution peaks at $r = 0$.

We now turn from the test particle to the full distribution of particles forming a cosmon-neutrino lump with energy-momentum tensor $T^{\mu\lambda} = T^{\mu\lambda}_{(\nu)} + T^{\mu\lambda}_{(\varphi)}$. As in

special relativity, we define the angular momentum density as the rank 3 tensor

$$l^{\mu\nu\alpha} = x^\mu T^{\nu\alpha} - x^\nu T^{\mu\alpha}. \tag{5.75}$$

This definition is, obviously, not useful in general spacetimes since we have arbitrarily singled out coordinates x^μ (in our case the comoving coordinates with cosmic time $t = x^0$). Since, however, we can assume (an even unperturbed) FLRW metric (neglecting the gravitational interaction), which is sufficiently similar to a Minkowski spacetime, we may motivate the use of a special-relativistic definition. This is analogous to considering the classical angular momentum for a distribution of (slow-moving) particles in Newtonian gravity. The nonvanishing Christoffel symbols of the unperturbed FLRW metric read

$$\Gamma^0_{ii} = a\dot{a}, \quad \text{and} \quad \Gamma^i_{i0} = \Gamma^i_{0i} = \frac{\dot{a}}{a}, \tag{5.76}$$

cf. Eqs. (2.58) and (2.59).

We assume the conservation equation for the energy-momentum tensor $T^{\mu\nu}$, which corresponds to neglecting the energy-momentum exchange with the external field. Then, this conservation equation implies

$$\nabla_\lambda \left(\frac{1}{a} l^{ij\lambda} \right) = -\frac{\dot{a}}{a^2} l^{ij0} + \frac{1}{a} \left(T^{ji} - T^{ij} + \Gamma^i_{\lambda\alpha} x^\alpha T^{j\lambda} - \Gamma^j_{\lambda\alpha} x^\alpha T^{i\lambda} \right) = 0 \tag{5.77}$$

with the above Christoffel symbols and the symmetry of the energy-momentum tensor. This local conservation equation can be translated to the total spatial angular momentum

$$L^{ij} = \int d^3x \sqrt{{}^{(3)}g}\, l^{ij0}, \tag{5.78}$$

for which one obtains, after a straightforward calculation, the conservation law

$$\partial_0 \left(a^2 L^{ij} \right) = 0. \tag{5.79}$$

The total cosmon-neutrino angular momentum, rescaled with a^2, is thus conserved. In spherically symmetric lumps, this implies the conservation of $a^2 L^{ij}_{(\nu)}$ for the neutrino part of the angular momentum. This is because a spherically symmetric canonical scalar field $\varphi(r)$ does not carry spatial angular momentum. In general, the angular momentum density is given by

$$l^{ij0}_{(\varphi)} = x^i T^{j0} - x^j T^{i0} = -\dot{\varphi} \left(x^i \partial^j \varphi - x^j \partial^i \varphi \right) = 0. \tag{5.80}$$

The nonvanishing components of the density l^{ij0}_φ are contained in the usual vector product

$$\boldsymbol{l}_\varphi = -\frac{\dot{\varphi}}{a^2} \boldsymbol{x} \times \boldsymbol{\nabla} \varphi, \tag{5.81}$$

which vanishes in the case of spherical symmetry where $\boldsymbol{\nabla}\varphi = \partial\varphi/\partial r\, \boldsymbol{e}_r$. In the absence of spherical symmetry, the cosmon-neutrino coupling can lead to an angular momentum exchange between the neutrinos and the cosmon. Using the energy-momentum exchange equation (5.4), it is straightforward to derive

$$\nabla_\lambda \left(\frac{1}{a} l^{ij\lambda}_{(\nu)}\right) = -\frac{\beta}{a} \mathrm{tr} T_{(\nu)} \left(x^i \partial^j \varphi - x^j \partial^i \varphi\right), \tag{5.82}$$

$$\partial_0 \left(a^2 L^{ij}_{(\nu)}\right) = \int d^3x \sqrt{{}^{(3)}g}\, a^2 \beta \mathrm{tr} T_{(\nu)} \left(x^i \partial^j \varphi - x^j \partial^i \varphi\right). \tag{5.83}$$

In our derivation, we have again neglected the interaction between the lump and the external field. The angular momentum conservation is only exact for an isolated lump and will be violated due to the effective coupling β_l. Since the gradients $\partial^i \hat{\varphi}$ are rather small compared to the concentration of the lump, this will not induce very large corrections.

Hydrodynamic balance equation

In our consideration of the static lump configuration, cf. Fig. 5.13, for showing the pressure cancellation between the neutrino and the cosmon contributions, we have made use of a hydrodynamic balance equation. This equation shows that concrete, static lump configurations exist. We will also see the dynamical stability of these configurations in a numerical test. A detailed derivation can be found in Weber (2012). We closely follow the presentation by Ayaita et al. (2013).

The idea is to start from the neutrino phase-space conservation equation

$$\frac{df_\nu}{dt} = \frac{\partial f_\nu}{\partial t} + \frac{\partial (f_\nu \dot{x}^i)}{\partial x^i} + \frac{\partial (f_\nu \dot{p}_j)}{\partial p_j} = 0 \tag{5.84}$$

and to find, from it, the hydrodynamic equations of motion by taking the first moments (including the dispersion σ_{ij}, which is responsible for stabilizing the neutrino distribution against the cosmon-mediated attractive force). We already saw the general procedure of obtaining the hydrodynamic equations in Sec. 2.2.2. The only difference here is that we define f_ν such that its zeroth moment gives the number density n_ν rather than the energy density ρ_ν (which is because ρ_ν, in contrast to ρ_m, also accounts for the varying mass). Consequently, the velocity dispersion, originating from the second moment, is defined with the number density,

$$\sigma_{ij} = \int d^3p \frac{(p_i - \bar{p}_i)(p_j - \bar{p}_j)}{a^2 m_\nu^2} f_\nu(t, \boldsymbol{x}, \boldsymbol{p}) = n_\nu(\boldsymbol{x}) \left\langle v_{\mathrm{micro},i}(\boldsymbol{x}) v_{\mathrm{micro},j}(\boldsymbol{x}) \right\rangle_f, \tag{5.85}$$

with the local, 'microscopic' velocity $\boldsymbol{v}_{\mathrm{micro}}$ whose local average vanishes. This is, of course, completely analogous to Eq. (2.92). We also define the scalar quantity $\sigma = \sigma^k{}_k/3$ related to the trace of the tensor σ_{ij}.

We do not include higher moments than the second one such that no equation of motion will be obtained for σ_{ij}. Instead, we will infer σ_{ij} from a staticity condition for the number density, $\dot{n}_\nu = 0$. The evolution equations for n_ν and the fluid velocity v are obtained, analogously to Sec. 2.2.2, with the one-particle equations of motion. These are simplified to only account for first-order relativistic corrections, such that they read

$$\dot{x}^i = \frac{p^i}{m_\nu}, \quad \dot{p}_j = \left(1 - \frac{p^k p_k}{2m_\nu^2}\right) \beta m_\nu \partial_j \varphi. \tag{5.86}$$

This yields, for the zeroth moment n_ν, the spatial continuity equation

$$\dot{n}_\nu + \frac{1}{a}\partial_i(n_\nu v_i) = 0. \tag{5.87}$$

Stability of the number density profile in the sense $\dot{n}_\nu = 0$ is obviously given if $v = 0$, i. e. if the microscopic velocities in every fluid cell add up to zero. With this condition, the equation of motion for the first moment is stated as

$$a n_\nu \dot{v}_i = -\partial_j \sigma_{ij} + \beta \partial_i \varphi \left(n_\nu - \frac{3\sigma}{2}\right) + \beta \partial_j \varphi \, \sigma_{ij}. \tag{5.88}$$

For a completely static lump, we demand, in addition to a constant n_ν, that also the fluid velocity field v is constant. For spherically symmetric lumps, the above equation can then be written as the condition

$$\frac{\partial \sigma}{\partial r}(r) = \beta \frac{\partial \varphi}{\partial r}(r) \left[n_\nu(r) - \frac{\sigma(r)}{2}\right] \tag{5.89}$$

with the radial comoving coordinate r. This is the hydrodynamic balance equation we used for the construction of static lump configurations. The velocity dispersion σ plays the role of a pressure working against the contraction of the lump. If this effect is dynamically stable, we have to expect that the neutrino lumps are stabilized by the velocity dispersion rather than by the degeneracy pressure, which will only play a role for extremely concentrated lumps (Brouzakis et al., 2008). It is most straightforward to check the dynamical stability of the staticity condition in a numerical simulation. An analytic investigation would require to consider the quite involved equation for $\ddot{v}$ and, in principle, should also take into account the equation of motion for σ_{ij} from higher moments. Ayaita et al. (2013) have simulated an isolated lump, where the balance equation has been perturbed (by lowering σ to a value too small to compensate the cosmon-attracted fifth force). In a realistic context, this corresponds to a lump which is not yet virialized, i. e. the kinetic energy has not yet built up completely. As a consequence, the lump can still shrink. However, we see the dynamical stabilization in the number density profile, cf. Fig. 5.17. We observe a quick stabilization of the profile in the core, which then extends to the outskirt. The approached staticity is also expressed by the development of a pressure cancellation between the cosmon and neutrino contributions. We show the emerging pressure cancellation in Fig. 5.18.

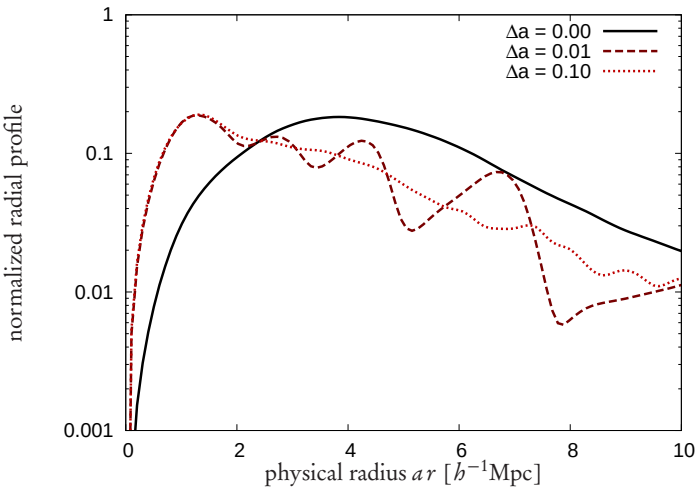

Figure 5.17: The normalized radial profile $4\pi r^2 n_\nu(r)/N_\nu$ starting with a perturbed balance equation. For illustration, time differences dt have been converted to scale-factor differences $da = aHdt$ by the Hubble parameter H at $a = 0.5$. The figure is taken from Ayaita et al. (2013).

The neutrino pressure starts at a rather low value (since we have lowered the velocity dispersion in order to violate the balance equation). In the total pressure, the cosmon contribution dominates, and the total lump pressure is negative. As the lump starts to evolve, the neutrinos are accelerated to the center of the lump, and their pressure contribution quickly increases and surpasses the cosmon pressure. Afterwards, the situation quickly stabilizes and a cancellation between the cosmon and the neutrino pressures can be observed. This cancellation is better at larger distances.

5.4.5 Evolution of the lump fluid

We will now derive and discuss the cosmological evolution equations in the regime where the picture of a cosmon-neutrino lump fluid is valid. This means that essentially all neutrinos have to be bound in stable lumps, and that the typical distance between the lumps has to be larger than the characteristic extension of the local cosmon field sourced by them. In this case, we have seen that the lumps are approximately pressureless due to the cancellation of pressure between the neutrinos and the cosmon and may be described by one-particle energy-momentum tensors with rest masses M_l. The intermediate scale λ, smaller than the typical distances between the lumps, but larger than their typical sizes, can be regarded as the scale where the lump picture can be used. The cosmon field can be smoothed at this scale to give the *external* or *large-scale* cosmon $\hat{\varphi}$, defined by Eq. (5.67), which is not regarded as part of the cosmon-neutrino lumps. The reaction of the lump mass M_l to the external field $\hat{\varphi}$ is expressed by the effective coupling β_l, cf. Eq. (5.69).

We will discuss the motion of the lumps in the external field $\hat{\varphi}$, the field equation

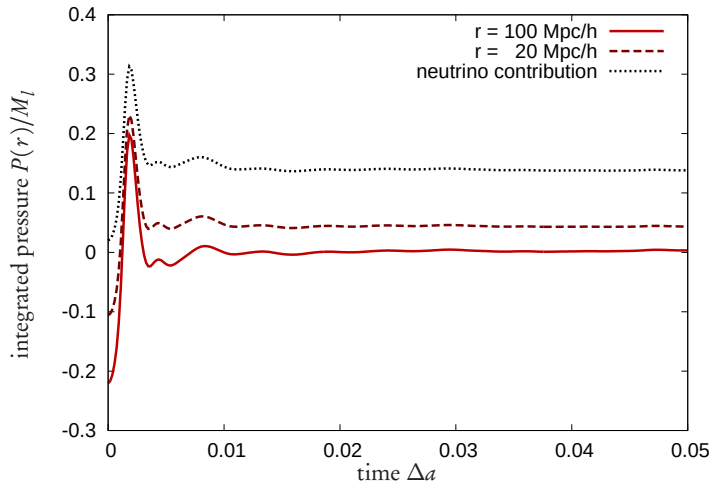

Figure 5.18: Cancellation of the neutrino pressure at different distances from the lump center. Time differences are expressed as scale-factor differences as in Fig. 5.17. The figure is taken from Ayaita et al. (2013).

for $\hat{\varphi}$, and the evolution for the background quantities (taking into account the back-reaction effect). These equations will provide, under the assumption that the effective couplings β_l are known, a full description of the cosmological dynamics. We thus also propose a simplified simulation scheme applicable once the cosmon-neutrino lump picture can be assumed.

Lump motion

For the equation of motion of approximately point-shaped lumps, we can start from the usual one-particle action (in the presence of a mass dependence on the external field),

$$S = \int d^4x \sqrt{-g}\, T_l^{\mu\nu} g_{\mu\nu} = -\int d\eta\, M_l(\hat{\varphi}), \tag{5.90}$$

where η denotes the proper time of the lump. This is in complete analogy to the fundamental one-particle action (5.44) and consequently leads to equations of motions of the same form, cf. Eq. (5.45), just with the effective coupling β_l instead of the fundamental coupling and the external field $\hat{\varphi}$ instead of the total cosmon field φ,

$$\frac{du^\mu}{d\eta} + \Gamma^\mu_{\rho\sigma} u^\rho u^\sigma = \beta_l \partial^\mu \hat{\varphi} + \beta_l u^\lambda \partial_\lambda \hat{\varphi}\, u^\mu. \tag{5.91}$$

The left-hand side is the gravitational interaction, and since the lumps do not move at relativistic velocities, this is essentially the Newtonian equation of motion on an FLRW background. On the right-hand side, the second term is subdominant as it is

quadratic in the (small) lump velocity. The first term gives the cosmon-mediated attractive force between the lumps, which now is $\beta_l \nabla\hat{\varphi}$. As compared to the fundamental fifth force, it is suppressed by the fact that $|\beta_l| < |\beta|$ and, typically, $|\nabla\hat{\varphi}| < |\nabla\varphi|$.

Field equation for the external cosmon

The external cosmon field $\hat{\varphi}$ can be separated into the background part and a smoothed perturbation, $\hat{\varphi} = \bar{\varphi} + \delta\hat{\varphi}$. The perturbation is given as the smoothed solution to the field equation for $\delta\varphi$, Eq. (5.47). In this equation, the right-hand side is the perturbation of the trace $\mathrm{tr}T_{(\nu)}$ of the neutrino energy-momentum tensor. In order to use this equation, we have to express the right-hand side by the lumps. Let us first turn to the left-hand side. Since the left-hand side is linear, the differentiation commutes with the smoothing, i. e.

$$\widehat{\Delta\delta\varphi}(\boldsymbol{x}) = \int d^3y \sqrt{{}^{(3)}g}\, W_\lambda(\boldsymbol{x}-\boldsymbol{y})\Delta_{\boldsymbol{y}}\delta\varphi(\boldsymbol{y}) \tag{5.92}$$

$$= \Delta_{\boldsymbol{x}} \int d^3y \sqrt{{}^{(3)}g}\, W_\lambda(\boldsymbol{x}-\boldsymbol{y})\delta\varphi(\boldsymbol{y}) \tag{5.93}$$

$$= \Delta\delta\hat{\varphi}(\boldsymbol{x}), \tag{5.94}$$

neglecting the metric perturbation, $\sqrt{{}^{(3)}g} = a^3$, and where hats now in general denote quantities smoothed by the window function W_λ. In this way, again neglecting the gravitational potentials against the cosmon perturbation, the smoothed field equation for $\delta\hat{\varphi}$ reads

$$\Delta\delta\hat{\varphi} - a^2 V_{,\varphi\varphi}(\bar{\varphi})\delta\hat{\varphi} = a^2\beta\left(\mathrm{tr}\hat{T}_{(\nu)} - \mathrm{tr}\bar{T}_{(\nu)}\right), \tag{5.95}$$

where we have smoothed $\delta\mathrm{tr}T_{(\nu)}$ on the right-hand side and split it into the full quantity and the background part. The smoothed trace of the neutrino energy-momentum tensor is, again, simply obtained by smoothing with the window function W_λ.

The essential step is to relate the right-hand side of Eq. (5.95) to lump properties. We will next show that this relation can be stated as

$$\beta\mathrm{tr}\hat{T}_{(\nu)} \approx \sum_l \beta_l \mathrm{tr}\hat{T}_l, \tag{5.96}$$

where the sum is performed over all lumps. Since the field equation for $\delta\varphi$ has its origin in the energy-momentum exchange equation (5.5), it is natural to go back to the energy-momentum exchange to motivate this relation. Moreover, the relation essentially states that the coupling β_l originally defined by how the lump reacts to the external field $\hat{\varphi}$ is the same coupling by which the lump acts, as a source, to the field $\hat{\varphi}$. This is similar to the case of mechanics where an action is accompanied by an equal (but opposite) reaction. Mechanical force laws are, in general relativity, related to energy-momentum exchange equations. The crucial difference between the lump

picture and the fundamental picture lies in how the total energy-momentum tensor $T^{\mu\nu}$ is separated into two components:

$$T^{\mu\nu} = T^{\mu\nu}_{(\nu)} + T^{\mu\nu}_{(\varphi)} = T^{\mu\nu}_{\text{lumps}} + T^{\mu\nu}_{(\hat{\varphi})}. \tag{5.97}$$

The first equation is the fundamental picture, describing a neutrino and a cosmon contribution. The second equation is the lump picture, where we consider a cosmon-neutrino lump contribution and the contribution of the external cosmon $\hat{\varphi}$. Energy-momentum conservation in the lump picture can be expressed as

$$\nabla_\lambda T^{\mu\lambda}_{(\hat{\varphi})} = -\nabla_\lambda T^{\mu\lambda}_{\text{lumps}}. \tag{5.98}$$

The term $\nabla_\lambda T^{\mu\lambda}_{\text{lumps}}$ can be obtained under the approximation of the lumps as effective particles, with the one-particle energy-momentum tensor, Eq. (5.66), and the equation of motion, Eq. (5.91). This gives

$$\nabla_\lambda T^{\mu\nu}_{\text{lumps}} \approx -\sum_l \beta_l \text{tr} T_l \, \partial^\mu \hat{\varphi}. \tag{5.99}$$

It remains to consider the contribution of the external cosmon. If we write the total cosmon as $\varphi = \hat{\varphi} + \delta\varphi_{\text{loc}}$, where $\delta\varphi_{\text{loc}}$ accounts for the local fluctuations of the field on scales smaller than λ, we can see — in a linear approximation in $\delta\varphi_{\text{loc}}$ — which part of the total cosmon energy-momentum tensor $T^{\mu\nu}_{(\varphi)}$ is only related to the external field. This is interpreted as the energy-momentum tensor of $\hat{\varphi}$ and given by

$$T^{\mu\nu}_{(\hat{\varphi})} = \partial^\mu \hat{\varphi} \partial^\nu \hat{\varphi} - g^{\mu\nu} \left[\frac{1}{2} \partial^\lambda \hat{\varphi} \partial_\lambda \hat{\varphi} + V(\hat{\varphi}) \right], \tag{5.100}$$

which has exactly the same form as the energy-momentum tensor of the fundamental field φ. In Eq. (5.99), it leads to the term

$$\nabla_\lambda T^{\mu\lambda}_{(\hat{\varphi})} = \left[\nabla^\lambda \nabla_\lambda \hat{\varphi} - V_{,\varphi}(\hat{\varphi}) \right] \partial^\mu \hat{\varphi}. \tag{5.101}$$

The brackets enclose the left-hand side of the Klein-Gordon equation for $\hat{\varphi}$. It just corresponds to the left-hand side of the usual Klein-Gordon equation, cf. Eq. (5.10), smoothed at the scale λ if it is linearized in the local perturbation $\delta\varphi_{\text{loc}}$ (such that the nonlinear potential can be written as $V(\varphi) \approx V(\hat{\varphi}) + V_{,\varphi}(\hat{\varphi})\delta\varphi_{\text{loc}}$). We may thus replace the bracket in Eq. (5.101) by the smoothed right-hand side of the modified Klein-Gordon equation (5.10). This yields

$$\nabla_\lambda T^{\mu\lambda}_{(\hat{\varphi})} = \beta \text{tr} \hat{T}_{(\nu)} \, \partial^\mu \hat{\varphi}. \tag{5.102}$$

Together with Eq. (5.99), this eventually verifies Eq. (5.96) and allows us to write the field equation for the smoothed perturbation $\delta\hat{\varphi}$ as

$$\Delta\delta\hat{\varphi}(\boldsymbol{x}) - a^2 V_{,\varphi\varphi}(\bar{\varphi})\delta\hat{\varphi}(\boldsymbol{x}) = a^2 \sum_l \beta_l \text{tr} \hat{T}_l - a^2 \beta \text{tr} \bar{T}_{(\nu)}. \tag{5.103}$$

Here, also the background part $\propto \mathrm{tr}\bar{T}_{(\nu)}$ can be related to the lumps analogously by

$$\beta \mathrm{tr}\bar{T}_{(\nu)} = -\frac{1}{V}\sum_l \beta_l \frac{M_l}{\gamma_l} \tag{5.104}$$

in some (physical) volume V large enough so that the quantity has converged.

External cosmon and gravitational potential

We will now explain how to solve the field equation for the external field in the lump picture. In particular, we will see that a calculation of $\hat{\varphi}$ on a grid is not necessary. The calculation of the gravitational potential will be similar. First, we consider more closely the right-hand side of the field equation for $\delta\hat{\varphi}$, Eq. (5.103). The smoothed trace of the lump energy-momentum tensor is just

$$\mathrm{tr}\hat{T}_l = -\frac{M_l}{\gamma_l} W_\lambda(\boldsymbol{x}-\boldsymbol{x}_l) \tag{5.105}$$

for the lump l located at $\boldsymbol{x}_l$. This follows by using the delta function in the effective one-particle energy-momentum tensor. If we are mainly interested in the solution $\delta\hat{\varphi}$ on scales larger than λ, the window function can, to a good approximation, be replaced by a Dirac delta. Every lump then sources, in the field equation for $\delta\hat{\varphi}$, a simple Yukawa potential, and the solution can be given as

$$\delta\hat{\varphi}(\boldsymbol{x}) \approx \sum_l \frac{\beta_l}{4\pi a}\frac{M_l}{\gamma_l|\boldsymbol{x}-\boldsymbol{x}_l|} e^{-aV_{,\varphi\varphi}(\bar{\varphi})|\boldsymbol{x}-\boldsymbol{x}_l|} - \delta\varphi_{\mathrm{res}}(\boldsymbol{x}), \tag{5.106}$$

where we have added a residual term $\delta\varphi_{\mathrm{res}}$ sourced by the background contribution $\beta\mathrm{tr}\bar{T}_{(\nu)}$. It is easily verified that a solution is given by

$$\delta\varphi_{\mathrm{res}} = C\frac{e^{aV_{,\varphi\varphi}(\bar{\varphi})|\boldsymbol{x}|}}{2aV_{,\varphi\varphi}(\bar{\varphi})|\boldsymbol{x}|} + \frac{\beta\mathrm{tr}\bar{T}_{(\nu)}}{\left(V_{,\varphi\varphi}(\bar{\varphi})\right)^2}, \tag{5.107}$$

where the proportionality constant C has to be chosen such that the average value $\overline{\delta\hat{\varphi}}$ vanishes in a large simulation volume. Near the lump locations, the residual term will, of course, be subdominant.

Smoothing the gravitational Poisson equation for the metric perturbation Φ induced by lumps (in the limit of nonrelativistic, point-shaped lumps and in the subhorizon regime) yields

$$\Delta\hat{\Phi}(\boldsymbol{x}) \approx \frac{a^2}{2}\sum_l \left(M_l\frac{\delta^3(\boldsymbol{x}-\boldsymbol{x}_l)}{\sqrt{{}^{(3)}g}} - \frac{M_l}{V}\right). \tag{5.108}$$

A solution to this equation is then given by

$$\hat{\Phi}(\boldsymbol{x}) = -\sum_l \frac{1}{8\pi a}\frac{M_l}{|\boldsymbol{x}-\boldsymbol{x}_l|} - \Phi_{\mathrm{res}}(\boldsymbol{x}), \tag{5.109}$$

where the residual contribution $\Phi_{\rm res}$ again accounts for the background part of the right-hand side and can be evaluated according to

$$\Phi_{\rm res}(\boldsymbol{x}) = \frac{1}{V}\sum_l a^2 M_l |\boldsymbol{x} - \boldsymbol{x}_l|^2. \tag{5.110}$$

This equation only accounts for the gravitational potential induced by cosmon-neutrino lumps. If matter is to be included, a usual Newtonian N-body approach can be used in addition to the cosmon-neutrino lump description presented here.

The background cosmon $\bar{\varphi}$ is evaluated with the background equation

$$\bar{\varphi}'' + 2\frac{a'}{a}\bar{\varphi}' + a^2 V_{,\varphi}(\bar{\varphi}) = \frac{1}{V}\sum_l a^2 \beta_l \frac{M_l}{\gamma_l}, \tag{5.111}$$

cf. Eq. (5.11). In the limit where β_l and M_l are approximately constant over time (corresponding to perfect mass freezing) and where $\gamma_l \approx 1$ (nonrelativistic lumps, which is, indeed, found in the simulations), this background equation can be solved independently of the perturbations. More realistically, the change of the mass M_l due to the changing value of the external field $\hat{\varphi}$ has to be taken into account. The background equation can then not be solved separately from the perturbation equations. This reflects the backreaction of the perturbations on the background evolution.

Proposed simulation scheme

We conclude our discussion of the cosmon-neutrino lump fluid by proposing a simplified simulation scheme of growing neutrino quintessence. It can be employed once a collection of stable cosmon-neutrino lumps has formed, characterized by masses M_l and effective couplings β_l. The time where this picture becomes appropriate is around $a \approx 0.5$. The period of rapid lump formation from $a \gtrsim 0.3$ to $a \approx 0.5$ has still to be treated with the help of an N-body type nonlinear treatment. A mere Press-Schechter type approach (Press and Schechter, 1974), which is useful in the cold dark matter case to estimate the mass function of halos, is not sufficient. In the purely gravitational case, the total number of dark matter particles forming the halo completely determines the long-range gravitational properties. This is not the case for cosmon-neutrino lumps where the internal lump configuration determines both the cosmon-dependent lump mass and the effective coupling parameter by which the lump interacts with the external cosmon field. Consequently, a Press-Schechter approach could only, at best, predict a number function of lumps (characterized by their amount of neutrinos f_l), but not the masses M_l and couplings β_l.

In this section, we have provided a complete set of equations characterizing the cosmological dynamics of the cosmon-neutrino lump fluid, the external cosmon field, and the gravitational potential. Rather than relying on a grid where one could solve the field equations, we have seen that the knowledge of the fields (and their gradients) at the lump positions can easily be evaluated by sums over lumps $l' \neq l$. The change

of the lump mass due to its motion in the external field and due to the change of the external field itself is then computed according to

$$\frac{dM_l}{dt} = -\beta_l M_l \frac{d\hat{\varphi}}{dt} = -\beta_l M_l \frac{u^\lambda \partial_\lambda \hat{\varphi}}{u^0}. \tag{5.112}$$

The cosmological evolution equations form a set of coupled differential equations, which have to be solved together.

The quantitative reliability of the proposed simulation scheme depends on the stability of the lumps. The masses M_l of the lumps change due to the effective coupling β_l. But can the coupling β_l be assumed constant, or should it also be regarded as a function of $\hat{\varphi}$? Figure 5.16 suggests that the effective coupling follows a rough functional dependence on the neutrino number fraction f_l. In the limit where there are exact functional relations $\beta_l(f_l)$, $M_l(f_l;\hat{\varphi})$, the simulation scheme is complete. Even mergers could be treated by adding the corresponding number fractions $f_l = f_{l_1} + f_{l_2}$ and looking up the new coupling and mass parameters in the corresponding functional relations. The open issue that remains then is the question whether β_l and M_l are also functions of time, i. e. whether the internal structure of the lumps still evolves significantly after $a \approx 0.5$. Although we have collected arguments why lumps are expected to ultimately stabilize, it is, a priori, not clear when this complete virialization is reached. It is also not straightforward to apply detailed virialization criteria to the full simulation code since it is questionable whether the resolution of the current simulations allows to infer detailed properties of the lumps in the cosmological context.

A first hint that the properties of the lumps stabilize is the time evolution of the total neutrino energy

$$E_{(\nu)} = -\int d^3x \sqrt{{}^{(3)}g}\, T^0_{(\nu)0}(\boldsymbol{x}) \propto \bar{\rho}_\nu a^3 \tag{5.113}$$

shown, until $a \gtrsim 0.5$, in Fig. 5.19. At $a \approx 0.45$, a transition is made from a steep increase to a stabilization of the total energy with a residual, small slope. This corresponds to an approximate mass freezing of the neutrino lumps; the mass still follows the growing external cosmon field, but with a suppressed effective coupling.

5.5 A first look at observable consequences

A central goal of the efforts presented in this thesis is to provide the basis for confronting the growing neutrino quintessence model with observational constraints. The methods we present, in particular in the next chapter, allow to investigate the cosmological evolution quantitatively and thus to explore the parameter space of growing neutrino quintessence and to find parameters yielding a realistic cosmological evolution. Yet, at the current stage, this task has just begun, and we leave the ultimate answer whether growing neutrino quintessence eventually passes observational constraints to

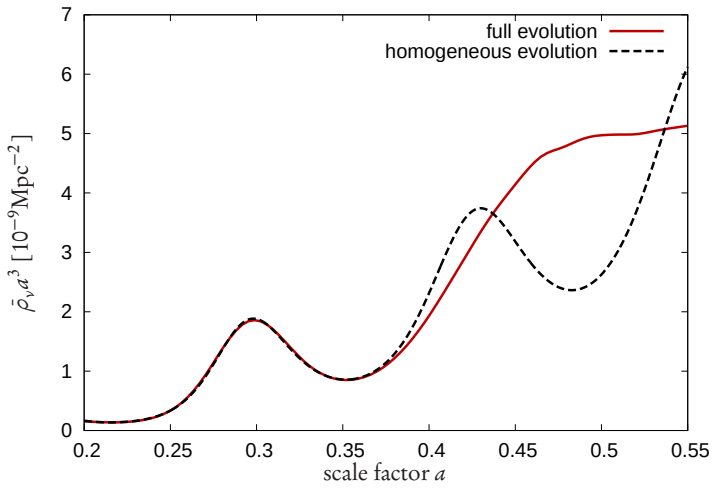

Figure 5.19: The total energy in neutrinos obtained from the full N-body method and from the pure background equations. The figure is taken from Ayaita et al. (2013).

future work. Still, the question of observational consequences is so tempting to ask and of utmost importance that we may not ignore it, even if our results are preliminary.

In this section, we will briefly discuss which observational probes are most important and most directly related to characteristic properties of the growing neutrino quintessence model. We will also give a few preliminary estimates. Some results, at least for exemplary parameter choices, will be obtained in the next chapter, where the full simulation method is presented and used. For now, we will leave aside constraints on the expansion history. In the homogeneous approximation, we have seen that growing neutrino quintessence yields background evolutions very similar to the ΛCDM case, cf. Sec. 5.1. We shall see, in the next chapter, that this becomes much more complicated once the backreaction is fully taken into account.

5.5.1 Neutrino mass and motion

A clear indication for a varying neutrino mass would be conflicting constraints on the neutrino masses from cosmology (related to earlier times in cosmic history) and from laboratory experiments. In such a case, a time-dependent neutrino mass, as in growing neutrino quintessence, would be a natural explanation. At present, cosmological constraints, assuming a constant neutrino mass and the cosmological concordance model ΛCDM, indicate a limit $\sum_i m_i < 0.2$–0.4 eV for the sum of the neutrino mass eigenvalues m_i (cf. Goobar et al., 2006, and Sec. 2.1.2); the Planck collaboration has recently tightened this constraint to the upper limit 0.23 eV (Ade et al., 2013c). The laboratory constraints are much weaker. For the beta decay of tritium, the Mainz experiment

found an upper bound $m(\nu_e) \leq 2.3$ eV (Kraus et al., 2005), where $m(\nu_e)$ is defined by

$$m(\nu_e)^2 = \sum_j \left|U_{ej}\right|^2 m_j^2 \tag{5.114}$$

with the mass eigenvalues m_j and the MNS matrix U_{ai} (a labels the flavor and i the mass eigenstates, cf. Sec. 2.1.2). This tells us that there is still room for surprises if a neutrino mass substantially larger than the cosmological upper limits is detected. As a side remark, we mention the controversy about a claim of a part of the Heidelberg-Moscow collaboration to have an indication for a relevant neutrino mass between 0.1 eV and 0.9 eV (Klapdor-Kleingrothaus et al., 2001, 2004; Goobar et al., 2006; Giuliani and Poves, 2012). Of course, if a tension between cosmological constraints and laboratory detections occurs, it is still possible that — instead of a varying neutrino mass — the assumption of a pure ΛCDM universe, or details regarding the primordial perturbation spectrum, might be wrong and could be adjusted.

Another possibility of a direct hint for models like growing neutrino quintessence would be the detection of an additional force felt by the neutrinos. For example, from the supernova SN1987A, several neutrinos have been detected together with the incoming photons (Hirata et al., 1987; Bionta et al., 1987). If the neutrinos are subject to an additional force, the changing line-of-sight velocity and the additional bending lead to a difference in the arrival time as compared to photons or uncoupled neutrinos. The situation is illustrated in Fig. 5.20. The distance d between the Earth and the

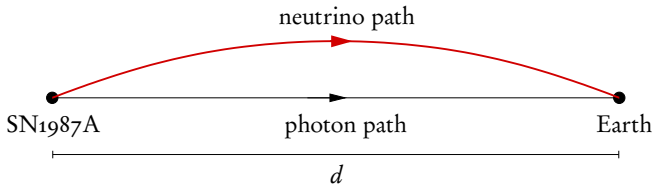

Figure 5.20: Photons and neutrinos arriving on Earth from SN1987A. The photon path is disturbed along the line-of-sight (Shapiro delay) and due to gravitational lensing. We still illustrate it as an approximately straight line. The neutrino path is disturbed, additionally, due to the cosmon-neutrino coupling. A similar illustration for photons is due to Longo (1988).

supernova amounts to $d \approx 50$ kpc.

At first sight, one might expect interesting constraints for growing neutrino quintessence from this observation; already for uncoupled neutrinos, a remarkable upper limit of about 16 eV could be derived for the effective neutrino mass from the fact that no significant extra time delay of the neutrinos as compared to the photons and between neutrinos of different energies could be detected (Arnett et al., 1989). The time delay of a neutrino i due to a nonvanishing mass is estimated to

$$\Delta t_i = 2.57 \text{ sec} \left(\frac{d}{50 \text{ kpc}}\right) \left(\frac{E}{E_i}\right)^2 \left(\frac{m_{\text{eff}}}{10 \text{ eV}}\right)^2, \tag{5.115}$$

where E_i is the energy of the neutrino compared to the characteristic energy scale $E \sim 10$ MeV. We conclude that the observation is very sensitive regarding differences in the arrival time.

Moreover, for the photons as well as for uncoupled neutrinos, the gravitational Shapiro delay already amounts to $\sim 10^6$ sec (Krauss and Tremaine, 1988). If pure gravity has such a large effect, we should check whether the cosmon-mediated fifth force is important as well (motivated by Rocky Kolb, private discussion).

Therefore, we look at the predictions given by the neutrino equation of motion, Eq. (5.45). We consider two distinct effects separately. First, we concentrate on the acceleration and deceleration along the line-of-sight. Second, we consider the time delay due to bending transverse to the line-of-sight. In our discussion, we ignore gravity; still, our calculations can be interpreted as providing the deviations from the geodesic path.

In the first case, the spatial part $\boldsymbol{u}$ of the neutrino four-velocity is parallel to the cosmon gradient, which we assume static,

$$\boldsymbol{u} \,||\, \nabla\varphi \quad \text{and} \quad \dot{\varphi} = 0, \tag{5.116}$$

for a simple approximation. The delay Δt in the arrival time as compared to the uncoupled case is approximately equal to the path difference after a time $t = d$ (since $|v| \approx 1$):

$$\Delta t \approx v_0 d - \int_0^d dt\, v(t), \tag{5.117}$$

where v_0 is the initial velocity, and we can write $v = 1 - 1/\gamma^2$ with the Lorentz factor γ. Then,

$$\Delta t \approx \int_0^d dt \left(\frac{1}{\gamma(t)^2} - \frac{1}{\gamma_0^2} \right). \tag{5.118}$$

Since $\gamma = u^0$ at $a = 1$, the equation of motion for $\gamma(t)$ is just given by the equation of motion for u^0,

$$\frac{du^0}{d\eta} = \beta u |\nabla\varphi| u^0, \tag{5.119}$$

neglecting gravity and using the parallelity condition. Hence,

$$\dot{\gamma} = \beta v |\nabla\varphi| \gamma, \tag{5.120}$$

and since $v \approx 1$,

$$\gamma \approx \gamma_0 e^{\beta v |\nabla\varphi| t} \tag{5.121}$$

if the gradient is assumed to be constant along the short path d. This is justified due to

the large size of cosmon-neutrino lumps. We calculate the delay to

$$\Delta t = \int_0^d \frac{dt}{\gamma_0^2}\left(e^{-2\beta|\nabla\varphi|t} - 1\right) \tag{5.122}$$

$$\approx -\int_0^d \frac{dt}{\gamma_0^2} 2\beta|\nabla\varphi|\, t \tag{5.123}$$

$$= -\frac{1}{\gamma_0^2}\beta|\nabla\varphi|\, d^2. \tag{5.124}$$

For neutrino energies $E \sim 10$ MeV and even rather large neutrino masses ~ 1 eV, we have $\gamma_0 \sim 10^7$. This leads to a large suppression as compared to the gravitational Shapiro delay. In our simulations, we measure typical values $|\nabla\varphi| \sim 10^{-5}\,\mathrm{Mpc}^{-1}$. This leads to a time delay of order

$$\Delta t \sim 10^{-6}\,\mathrm{sec}, \tag{5.125}$$

too small to lead to observational constraints.

Let us turn to the second effect, i. e. the bending due to a transverse gradient $\nabla\varphi$,

$$\boldsymbol{u} \perp \nabla\varphi. \tag{5.126}$$

We separate, in the plane of motion, the velocity $\boldsymbol{v}$ into a parallel component $v^{\parallel}$ along the line-of-sight and a transverse component $v^{\perp}$ aligned with the cosmon gradient. Since there is no acceleration in the line-of-sight direction, we can write

$$\frac{du^{\parallel}}{d\eta} = 0, \quad v^{\parallel}(t) = \frac{\gamma_0 v_0^{\parallel}}{\gamma(t)}, \quad \gamma(t) = \frac{\gamma_0}{\sqrt{1 - v^{\perp}(t)^2}}. \tag{5.127}$$

In the last equation, we may linearize in $(v^{\perp})^2$ since the bending can be assumed small. Again, the time delay is estimated by the (parallel) path distance after time d,

$$\Delta t \approx v_0^{\parallel} d - \int_0^d dt\, v_0^{\parallel}\left(1 - \frac{v^{\perp}(t)^2}{2}\right) \approx \frac{1}{2}\int_0^d dt\, v^{\perp}(t)^2. \tag{5.128}$$

We need to solve the equation of motion for $v^{\perp}$. This reads

$$\frac{du^{\perp}}{d\eta} = \frac{d\left(\gamma v^{\perp}\right)}{dt/\gamma} = \beta|\nabla\varphi|. \tag{5.129}$$

On the left-hand side, after applying the Leibniz rule, the terms $\dot{\gamma}v^{\perp}$ and $\gamma\dot{v}^{\perp}$ occur. We note

$$\dot{\gamma}v^{\perp} = \frac{\partial\gamma}{\partial v^{\perp}}\frac{dv^{\perp}}{dt}v^{\perp} = \gamma\dot{v}^{\perp}\frac{(v^{\perp})^2}{1-(v^{\perp})^2} \ll \gamma\dot{v}^{\perp}, \tag{5.130}$$

whence we may neglect it. We conclude

$$\gamma\dot{v}^{\perp} \approx \frac{1}{\gamma}\beta|\nabla\varphi| \tag{5.131}$$

with the solution

$$v^{\perp}(t) = \frac{e^{\frac{2}{\gamma_0^2}\beta|\nabla\varphi|t} - 1}{e^{\frac{2}{\gamma_0^2}\beta|\nabla\varphi|t} + 1} \approx \frac{1}{\gamma_0^2}\beta|\nabla\varphi|\,t. \tag{5.132}$$

This gives the time delay

$$\Delta t \approx \frac{1}{6\gamma_0^4}\beta^2|\nabla\varphi|^2\,d^3, \tag{5.133}$$

which is severely suppressed by four powers of γ_0 and by an additional comparison between $|\nabla\varphi|$ and d^{-1}. With the numbers used before, we get

$$\Delta t \sim 10^{-25}\ \text{sec}. \tag{5.134}$$

Although the cosmon-mediated fifth force is, for nonrelativistic neutrinos, substantially stronger than gravity, this reverses in the limit of high-energy neutrinos. For the latter, the cosmon-mediated fifth force vanishes, i. e. it is suppressed by powers of the Lorentz factor γ, as compared to gravity. In the equation of motion (5.45), this is clearly visible. Gravity is described by the term $\Gamma^{\mu}_{\rho\sigma}u^{\rho}u^{\sigma}$, and the four-velocity carries a factor of γ as compared to the coordinate velocity. These factors of γ do not occur in the fifth-force term $\beta\partial^{\mu}\varphi$ on the right-hand side of the modified geodesic equation. So, once $\gamma^2 \gg \beta$, gravity is more important. This is not true for the second force term $\beta u^{\lambda}\partial_{\lambda}\varphi u^{\mu}$, which is, if Lorentz factors are counted, similar to gravity. This term, however, only accelerates or decelerates neutrinos parallel to their velocity. If this velocity is very close to the speed of light, the effects will be small since velocity differences scale with γ^{-2}. Consequently, it is difficult to constrain growing neutrino quintessence with high-energy neutrinos. The analysis could be refined by having a closer look on the effect of the coupling on neutrino oscillatons (cf., e. g., Rossi-Torres et al., 2011).

5.5.2 Large-scale gravitational potentials

The most striking difference between growing neutrino quintessence cosmology and the standard ΛCDM scenario lies in the evolution of neutrino perturbations. In the constant β model, with the exemplary value $\beta = -52$, we have seen the formation of very large neutrino lumps, with a total number of 10^3 to 10^4 in the Hubble volume and masses from 10^{15} to 10^{17} solar masses. The gravitational potentials induced by these lumps have observational consequences for probes directly related to gravitational potentials, namely the (late-time) integrated Sachs-Wolfe (ISW) effect and weak gravitational lensing. Moreover, they can be observed due to their influence on the

growth of matter perturbations, i. e. in the dark matter density power spectrum or in the peculiar velocities. Of course, all statements will depend on the parameters considered for the growing neutrino quintessence model. For larger constant β, the stopping power of the cosmon-neutrino coupling regarding the rolling background field $\bar{\varphi}$ is strong enough even for smaller neutrino masses. So, in this case, we expect less massive cosmon-neutrino lumps and, accordingly, reduced potential wells. We shall even see preliminary results indicating that, for varying β models, there is a regime where no stable cosmon-neutrino lumps form and hence the large-scale potentials remain small. This again tells us that reliable and quantitative predictions regarding observations can only be made after a thorough analysis of the parameter space of growing neutrino quintessence with the help of the full N-body based method.

Direct probes

Let us briefly discuss the observational probes directly related to the gravitational potentials. First of all, this is weak gravitational lensing, in detail presented in Chapter 4. With future weak lensing surveys, weak lensing tomography and 3d weak lensing will allow to probe the large-scale gravitational potentials to high accuracy. In Chapter 4, we have even seen that very small effects due to a parametrized dark energy clustering might be observable with the Euclid survey. Clearly, large gravitational potentials induced by cosmon-neutrino lumps would be either verified or ruled out by these methods.

Another observational probe is the (late-time) integrated Sachs-Wolfe effect (Sachs and Wolfe, 1967). It predicts a change in the observed temperature fluctuation of the CMB due to the evolution of the metric perturbations along the line-of-sight direction,

$$\left(\frac{\Delta T}{T}\right)_{\mathrm{ISW}} = -\int d\tau \, \left(\Psi' + \Phi'\right). \tag{5.135}$$

During matter domination, the evolution equations for linear perturbations tell us that the large-scale potentials remain constant, i. e. $\Psi' = \Phi' = 0$. In the standard ΛCDM model, the onset of Λ-domination then leads, by the accelerated expansion, to a slow decay of the large-scale potentials. In the regime of the cosmon-neutrino lump fluid, the formation of lumps implies growing large-scale gravitational potentials, with a subsequent approximate stabilization after the lumps have formed. Thus, we expect the opposite behavior as compared to ΛCDM. This has consequences for the CMB angular power spectrum, as it gives a contribution

$$C_\ell^{\mathrm{ISW}} = \frac{2}{\pi}\int k^2 dk \, \frac{|\Theta_\ell^{\mathrm{ISW}}(k)|^2}{(2\ell+1)^2} \tag{5.136}$$

with the quantity

$$\frac{\Theta_\ell^{\mathrm{ISW}}(k)}{2\ell+1} = \int d\tau \, \left[\Delta_\Psi'(k) + \Delta_\Phi'(k)\right] \, j_\ell(k(\tau_0 - \tau)) \tag{5.137}$$

and with the dimensionless spectra $\Delta_\Psi(k)$ and $\Delta_\Phi(k)$.

The effect of cosmon-neutrino lumps on the CMB spectrum via the ISW effect has first been analyzed by Pettorino et al. (2010) based on very rough estimates in the absence of a full simulation method. More precisely, we should speak of a Rees-Sciama effect (Rees and Sciama, 1968) instead of an ISW effect since the change of the potential is not due to the modified expansion history but due to the nonlinear growth of structure. Pettorino et al. (2010) find that the signal strongly depends on the details of the nonlinear evolution and on the model parameters. This analysis will have to be redone when the parameter space of the model is sufficiently explored.

The ISW effect can also be observed in the cross-correlation between the CMB temperature and large-scale structure. This means, it is observed in the cross-correlation spectrum between the (projected) galaxy density $\delta_{g,\ell m}$ in harmonic space and the CMB temperature $T_{\ell m}$,

$$C_{gT,\ell} = \langle \delta_{g,\ell m} T^*_{\ell m} \rangle \approx \frac{2T}{\int r^2 d\, r\, n(r)} \int d\, r\, n(r) P_{g\Phi'} \left(\frac{\ell + 1/2}{r} \right) \tag{5.138}$$

with the galaxy number density n, in the absence of anisotropic shear ($\Psi = \Phi$), and in the Limber approximation (Afshordi, 2004). Since the primordial CMB is uncorrelated with the large-scale structure along the line-of-sight, it drops out of the cross-correlation. In this way, the ISW effect measured by cross-correlations does not sensitively depend on, e. g., assumptions about the primordial spectrum of perturbations. The ISW effect has recently been detected in this way (Ho et al., 2008; Giannantonio et al., 2008), and one of the groups found a stronger signal than expected in the ΛCDM model at the 2σ level (Ho et al., 2008). This led to further studies with the tendency to agree with ΛCDM (Giannantonio et al., 2012; Ade et al., 2013b) although deviations are reported (at the 3σ level) when measuring the ISW effect by a correlation between individual voids and the CMB temperature (Cai et al., 2013); this result is discussed by Ilic et al. (2013).

The question whether these cross-correlation measurements could constrain growing neutrino quintessence has first been raised by Ayaita et al. (2009). This study briefly discusses the sensitivity of the cross-correlation measurements which typically peaks in a small redshift range. In the growing neutrino quintessence model, the time evolution of the gravitational potentials is nontrivial. The potentials grow during the period of lump formation, and this growth becomes mild once the lumps have stabilized. Moreover, we might expect — depending on the model parameters — oscillatory features in the mass and thereby in the potentials if the lumps still sufficiently react to the outside cosmon. Any analysis has to take into account carefully the redshift dependence of both the cross-correlation signal and the gravitational potentials.

Another point we mention here is that it is not obvious how the cross-correlation spectrum $C_{gT,\ell}$ is affected by the cosmon-neutrino lumps. If the lumps and the galaxy density are completely uncorrelated, the effect of the cosmon-neutrino lumps on $T_{\ell m}$ just drops out of $\langle \delta_{g,\ell m} T^*_{\ell m} \rangle$ as does the primordial CMB. We first need to know the precise correlation between the galaxy density and the distribution of cosmon-

neutrino lumps. Since the latter form at very late times, they have influenced the galaxy distribution only little. So, this point is essentially related to the question to which extent the cosmon-neutrino lumps form in the potential wells given by cold dark matter. The estimation of the cross-correlation spectrum $P_{g\Phi'}$, which determines $C_{gT,\ell}$ by Eq. (5.138), is, in principle, possible by N-body based simulations including both neutrinos and matter. However, this is complicated by the fact that the gravitational potential Φ evolves only very slowly. The estimation of Φ' is thus difficult as the fluctuations due to purely numerical effects might dominate over the true time derivative. This is why such an analysis should be postponed until simulations with higher precision are performed.

Peculiar velocities

In the regime of stable cosmon-neutrino lumps, a promising probe are large-scale peculiar velocities or bulk flows of matter. The gravitational potential induced by cosmon-neutrino lumps is felt by the matter perturbations, which consequently undergo an additional growth. Since this additional growth has only started recently, the effect on the density power spectrum $P_\delta(k)$ of matter is small. The effect on the peculiar velocities can be much larger. This has been argued by Ayaita et al. (2009), and it was verified both in Newtonian N-body simulations of growing neutrino quintessence (Baldi et al., 2011) and in the full simulation method (Ayaita et al., 2012b). For the matter peculiar velocity power spectrum $P_v(k)$ defined by

$$\langle v_{\boldsymbol{k}} v^*_{\boldsymbol{k}'}\rangle = (2\pi)^3 P_v(k)\,\delta^3(\boldsymbol{k}-\boldsymbol{k}'), \tag{5.139}$$

Ayaita et al. (2009) wrote, for the linear regime,

$$P_v(k) = \left(\frac{a'}{a}\right)^2 \frac{f_k^2}{k^2} P_\delta(k), \quad f_k \equiv \frac{d\log\delta_k}{d\log a}. \tag{5.140}$$

The matter power spectrum is constrained quite accurately by galaxy surveys, but much less is known about $P_v(k)$ and f_k. If an excess in $P_v(k)$ as compared to the ΛCDM scenario will be observed, this will constitute a strong hint for a recent growth of matter perturbations.

For a first and rough estimate — in the absence of a full simulation method — the gravitational potential Φ_ν due to neutrino clustering has been assumed to be sourced by point-shaped neutrino lumps of average number density $n_{\text{lumps}} = N_{\text{lumps}}/V$ (in a sufficiently large cosmological volume) and located at random positions, instantaneously formed at $a \approx 0.4$. The dimensionless shot-noise spectrum is then

$$\Delta_{\Phi_\nu}(k) = \frac{\rho_\nu}{2\pi\sqrt{2n_{\text{lumps}}}} k^{-1/2} \tag{5.141}$$

following Ayaita et al. (2009); Pettorino et al. (2010). This neglects the correlation of lump positions, the motion of the lumps, the relativistic corrections, the mass suppression of neutrinos within lumps, the cosmon contribution to the lump masses, and the

distribution of different lump masses. Still, it might give an idea of the importance of the effect. In a constant β model with $\beta = -275$ and a present neutrino mass $m_{\nu,0} \approx 0.5$ eV, Ayaita et al. (2009) estimated the effect on the matter scalar peculiar velocity perturbation v_k as compared to the ΛCDM case. The result is a function of the number density n_{lumps} or, equivalently, of the fraction f of neutrinos (in the Hubble volume) bound in every lump. It is shown in Fig. 5.21 for the scale $k = 0.01$/Mpc. We observe that the peculiar velocities of matter can be enhanced by a considerable

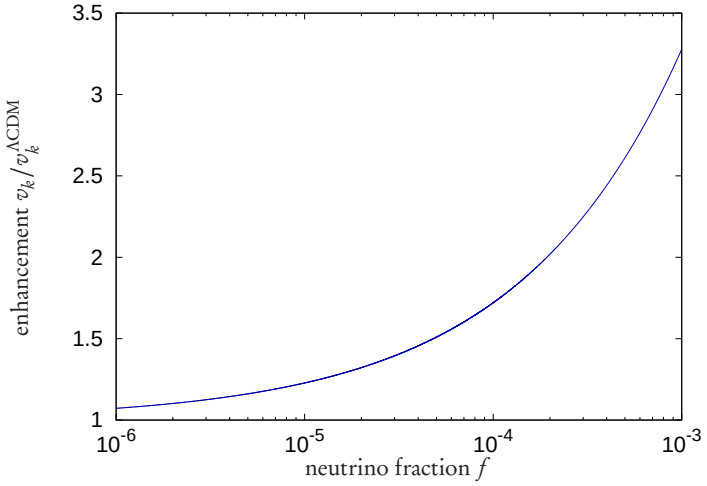

Figure 5.21: The enhancement of matter peculiar velocities at $a = 1$ due to the rough estimate of the lump-induced gravitational potential according to Eq. (5.141). The comoving scale was fixed to $k = 0.01$/Mpc, and the enhancement is a function of the fraction f of neutrinos in the Hubble volume bound in each lump. The number of lumps in the Hubble volume is $N = 1/f$. The figure is taken from Ayaita et al. (2009).

factor if the number of neutrino lumps is sufficiently small. The more lumps form, the smaller will be the effect. We will have a closer look at the peculiar velocity of matter in the next chapter with the full simulation method.

The observational status regarding large-scale peculiar velocities is somewhat controversial. Watkins et al. (2009); Feldman et al. (2010) reported a large-scale bulk flow, i. e. an averaged peculiar velocity

$$\boldsymbol{u}(\boldsymbol{x}) = \int d^3y\, W(\boldsymbol{x}-\boldsymbol{y})\, \boldsymbol{v}(\boldsymbol{y}) \tag{5.142}$$

in a Gaussian window W of size $\sim 100h^{-1}$Mpc; this bulk flow exceeded the ΛCDM root mean square expectation obtained by

$$\langle u^2 \rangle = \frac{1}{2\pi^2} \int k^2 dk\, |\tilde{W}(k)|^2 P_v(k) \tag{5.143}$$

by a factor of about two and was anomalous at the 2σ level. In later works, however, the authors claim to have retained consistency with ΛCDM at the 1σ level (Macaulay

et al., 2010, 2012), although the error budget is still substantial. There is an active debate about the claim of a coherent bulk flow on scales $\gtrsim 300h^{-1}$Mpc and beyond, which would be in direct conflict with the ΛCDM expectation (Kashlinsky et al., 2009; Atrio-Barandela et al., 2010; Kashlinsky et al., 2011; Atrio-Barandela et al., 2012). The analysis has been criticized by Keisler (2009); Osborne et al. (2011); Mody and Hajian (2012). It seems we will have to wait until generally accepted, reliable, and reasonably accurate results for large-scale peculiar velocities will have emerged.

6 Cosmological simulation

The technical challenge of understanding the cosmological evolution in growing quintessence models lies in the particular role of nonlinearities. The standard repertoire of analytical and numerical techniques, such as the calculation of the Friedmann equations (together with some additional homogeneous equations describing the new components of the model), the study of linear perturbation theory, nonlinear estimates based on a spherical collapse and a Press-Schechter approach, and Newtonian N-body simulations, will not give reliable predictions. The standard procedure assumes the following hierarchical picture. The limit of very large scales is described by homogeneous equations, a correction to large scales is provided by linear perturbation theory, and a further correction for small scales is obtained by, e. g., the Newtonian N-body method. This step-by-step approach is not applicable to the growing neutrino quintessence model. The nonlinear regime affects even the largest scales by virtue of a backreaction effect — the homogeneous part $\bar{\varphi}$ of the cosmon sensitively depends on small-scale properties of the neutrinos, in particular on their local mass distribution. Linear theory of neutrino perturbations is only useful in a very small temporal window. The cosmon-neutrino coupling typically becomes effective around $a \approx 0.2$, and the nonlinearities become important around $a \lesssim 0.4$, even on very large scales.

The absence of a reliable numerical technique has not only prohibited any quantitative analysis of the cosmological evolution; it was also a major obstacle for understanding the physics of growing neutrino quintessence. In particular, it remained unclear how to account for the various effects of the theory, which are absent in the standard ΛCDM model and standard models of uncoupled (or weakly coupled) quintessence. Most of the early works, consequently, started from wrong assumptions about the model, neglecting effects that, in the end, turned out to be decisive. For example, the background studies neglected the backreaction effect (Amendola et al., 2008a; Wetterich, 2007), which has an important impact on the background evolution; the hydrodynamic approach neglected the 'microscopic' velocity dispersion (Wintergerst et al., 2010) responsible for the stabilization of cosmon-neutrino lumps; the first study of properties of cosmon-neutrino lumps assumed a stabilization due to the degeneracy pressure rather than due to the velocity dispersion (Brouzakis et al., 2008); the Newtonian N-body simulations did not account for the possibility of relativistic neutrinos and neglected local mass variations (Baldi et al., 2011). These are just some examples, and we have discussed these and other early studies of growing neutrino quintessence in detail in Sec. 5.2. Of course, these early and important works are not to blame; quite the contrary. In retrospect, it is a remarkable accomplishment that these works have already identified and partially discussed many interesting and important effects of the model, cf. Sec. 5.2. Although they did not provide a comprehensive picture,

they sketched several key points around which a full simulation scheme can be built, cf. Sec. 5.3.

Consequently, the development of a full simulation scheme (Ayaita et al., 2012b) was not only a breakthrough regarding its capability to provide the first quantitatively reliable results for growing neutrino quintessence. The simulation also established the basis for a physical understanding of the model. Section 5.4 documents this aspect. Many physical properties of the cosmon-neutrino lumps and of the cosmological evolution have been understood. This would not have been possible without the simulation technique. The latter served as a major inspiration and clarified which effects are important and which are not. It also allowed us to test analytical hypotheses numerically, i. e., it played the role of a laboratory where physical 'experiments' guide the development of theories. And the simulations provide the parameters (such as the effective couplings or the masses of cosmon-neutrino lumps) that enter the semi-analytical descriptions.

From this perspective, it becomes clear that the simulations of growing neutrino quintessence serve a completely different purpose than simulations of, e. g., the ΛCDM model. For the latter, simulations are mainly used to obtain precision results on small scales. For the former, simulations are bitterly needed for any quantitative treatment of the model and also as an indispensable basis for understanding its physics. This fundamental difference has several consequences for the design of the simulation techniques:

1. When a dark matter N-body simulation of the ΛCDM model is developed, the physics that will be implemented is completely known beforehand. The implementation entirely focusses on numerical precision and efficiency. For growing neutrino quintessence simulations, it has not been clear a priori which effects would have to be taken into account. The design of the simulation has to be simple, modular, and flexible. There will be an interplay between understanding the physics and implementing the corresponding numerics.

2. Since, in ΛCDM, large scales are understood already at the linear level, N-body simulations focus on the precise modeling of small scales. Small-scale resolution is of utmost importance, also because cold dark matter starts to form structures on the smallest scales. As a consequence, these N-body simulations need to include as many N-body particles as possible and clever techniques to resolve the gravitational forces at small distances. In growing neutrino quintessence, the focus is not on small scales. The simulation technique is needed to understand large scales and even the background evolution. The smallest scales are less important because the neutrinos cluster on large scales first. The numerical optimization, the number of N-body particles, and the spatial resolution are not crucial.

3. As a consequence of these two points, ΛCDM simulations typically describe the gravitational interaction on small distance scales as a two-body force; in this way, the calculation is not limited by the resolution of a lattice on which the potential gradients would be calculated. In growing neutrino quintessence simulations, we may calculate the fields on a lattice instead. This is even important because the

explicit field value of the cosmon is needed for the calculation of the neutrino mass.

These points make clear that it is inadequate to build upon a standard N-body simulation for simulating growing neutrino quintessence. The standard simulations are so specialized to their particular scope of application (Newtonian description of cold dark matter) that substantial and repeated modifications are complicated to realize. This motivates the development of a new method, worked out from scratch, taking account for the necessities of the growing neutrino quintessence model.

The resulting simulation scheme that we shall present in this chapter does not aim at high precision (although, of course, on quantitative reliability in the sense that all important effects are consistently treated). This already tells us that the simulation results cannot be confronted with the constraints given by precision observations. This is an essential task for future work. The simulation scheme has just reached the necessary maturity and reliability such that it can serve as a model for a precision simulation based on state-of-the-art N-body simulations like GADGET-2 (Springel, 2005). Before this step, the simulation scheme presented here will be used to explore the growing neutrino quintessence parameter space and to find interesting regions with a realistic cosmological evolution. At the end of this chapter, we will show the first results in this regard.

The simulation method is a collaborative work and detailed descriptions are found in Ayaita et al. (2012b); Weber (2012). Our presentation mainly follows Ayaita et al. (2012b). This thesis focusses on the backreaction effect and the calculation of the cosmon field whereas the modeling of the neutrino component and related quantitative results are worked out in more detail by Weber (2012). In addition to the results of Ayaita et al. (2012b) restricted to cosmic times $a \leq 0.5$, we will give the first results until $a = 1$ in this thesis. We also present preliminary results for the varying coupling model at the end of this chapter.

The chapter is organized as follows. We start with a brief technical overview describing the main steps that are performed by the simulation method in Sec. 6.1. A more pedagogical introduction describing the key points of the simulation method that highlight the differences as compared to a standard Newtonian N-body simulation has been given in Sec. 5.3 and was motivated by the discussion of earlier works on growing neutrino quintessence, cf. Sec. 5.2. In the more technical chapter, here, we already assume familiarity with the growing neutrino quintessence model and with the requirements it sets for the simulation method. The initial conditions of the nonlinear simulation technique are obtained somewhat differently than in standard N-body methods. This is why we explain the procedure in detail in Sec. 6.2. The derivation and the implementation of the equation of motion for (potentially relativistic) neutrinos are reviewed in Sec. 6.3, and we refer the reader to Weber (2012) for more details on this point. We also briefly describe the motion of matter particles. In Sec. 6.4, we turn to the calculation of the cosmon field φ and the two gravitational potentials Ψ and Φ on the lattice. We also describe how to evolve the background in the presence of the backreaction effect due to nonlinearities. The results until $a = 0.5$ for the constant

coupling model, first published by Ayaita et al. (2012b), are presented and discussed in Sec. 6.5. We then describe how to overcome the numerical problems associated to late cosmic times ($a > 0.5$), and we present the first results at $a = 1$. At this early stage of the analysis, we do not systematically explore the parameter space of the constant coupling model. Rather, we discuss the influence of exemplary modifications in the parameters and show analytically how the parameter choices affect the expansion history of the model. We will then turn to the varying coupling model, where we find a completely new regime of growing neutrino quintessence. Depending on the precise model parameters, no stable cosmon-neutrino lumps form. Thus, the growing neutrino quintessence model does not show large deviations from the standard ΛCDM model in the perturbations. Also the expansion of the Universe is very similar to ΛCDM. The further investigation of this point in future works is a very promising endeavor.

6.1 Overview

In order to facilitate the understanding of the technical details covered by the following sections, we first describe the overall framework of the simulation design. Let us briefly list the main components of the simulation.

Effective particles in the N-body approach represent the matter and the neutrino component. They are the entities obtained by sampling the phase-space distributions f_m and f_ν with a number of N_m and N_ν particles. These particles can be thought of as collections of a large number of fundamental dark matter and neutrino particles, respectively. They obey the fundamental equations of motion whereby their motion is expected to approximate the true time evolution of the full phase-space distributions. At every time step, each particle p is equipped with a position $\boldsymbol{x}_p$ (which is more precise than a grid cell), a coordinate velocity $\boldsymbol{v}_p = d\boldsymbol{x}_p/d\tau$, and a mass M_p. For the effective neutrino particles, we evolve the four-velocity $u_p^\mu = dx_p^\mu/\eta_p$ instead. It is related to the coordinate velocity via the Lorentz factor γ_p. The mass parameter M_p is constant for effective matter particles but is a function of the local cosmon field $\varphi(\boldsymbol{x}_p)$ for the effective neutrino particles.

Fields and their gradients are needed in the equations of motion of the effective particles and for obtaining the mass of the neutrinos. We solve the field equations on a fixed comoving lattice of volume V and with N_c cells. We use periodic boundary conditions (also for the particles; a particle leaving the simulation box at one side enters again at the opposite side). The side length of the simulation box is $L = \sqrt[3]{V}$. The comoving side length of a cell, $\Delta x = L/\sqrt[3]{N_c}$, quantifies the resolution at which the fields are known. Scales below Δx are not resolved. The fields we calculate on the lattice are the two gravitational potentials Ψ and Φ and the cosmon perturbation $\delta\varphi$. The collections of effective particles are also related to fields, namely to their energy-momentum tensors. Specific components of these energy-momentum tensors appear on the right-hand sides of the field equations for Ψ, Φ, and $\delta\varphi$. They are evaluated on the lattice. The lattice in position space is complemented by a reciprocal lattice

on which the discrete Fourier transforms of the fields are represented. The reciprocal lattice is used, partially, for solving the field equations and for obtaining the gradients $\boldsymbol{\nabla}\Psi$, $\boldsymbol{\nabla}\Phi$, $\boldsymbol{\nabla}\delta\varphi$. At every time step, both the field values and their gradients are known.

Background quantities are defined as spatial averages of fields taken over the full simulation volume. This concerns, in particular, the energy-momentum tensors of the collection of effective particles. They appear on the right-hand sides of homogeneous, background evolution equations, e. g. for the background cosmon $\bar{\varphi}$. Also the Hubble parameter H is given by the averaged energy density. At every instant, the background quantities H, $\bar{\varphi}$, $\bar{\varphi}'$, $\bar{\rho}_\nu$, $\bar{p}_\nu$, $\bar{\rho}_m$ are known. In the varying β model, we also use the average $\overline{\beta \mathrm{tr} T_{(\nu)}}$.

The main steps of the simulation are illustrated in Fig. 6.1. The first building block

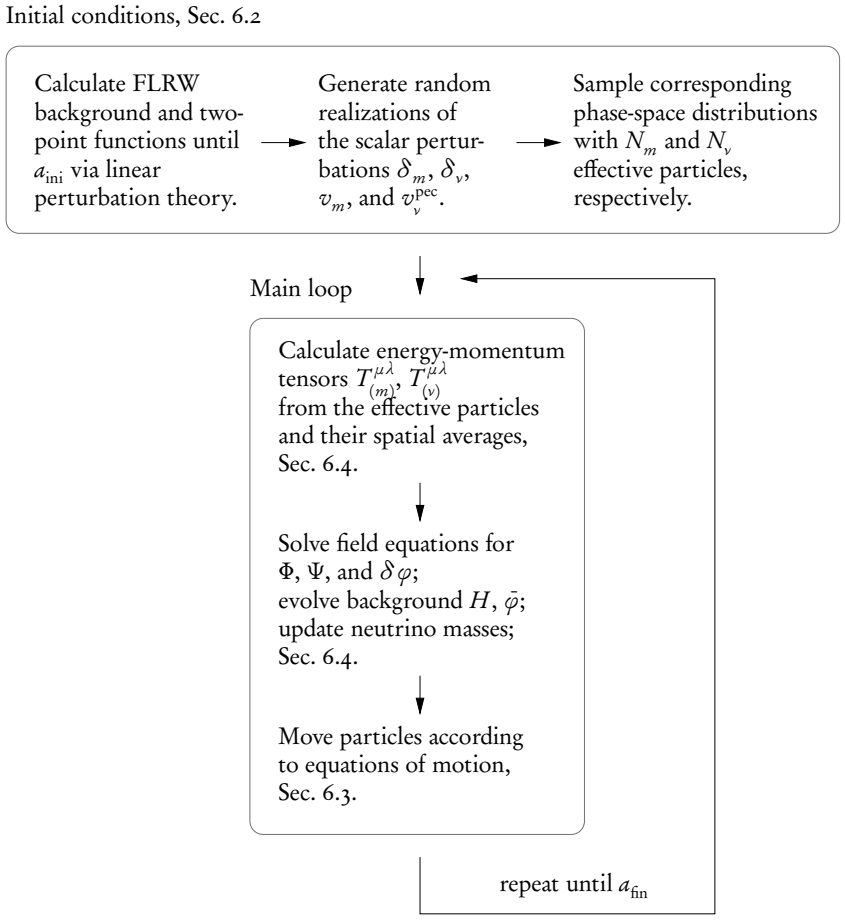

Figure 6.1: Schematic, simplified description of the simulation design. We divide the method into two main parts: first, the linear evolution and the generation of initial conditions; second, the main loop, which evolves the fields and the effective particles within the simulation volume.

refers to the generation of initial conditions, discussed in detail in Sec. 6.2. Here, linear

perturbation theory plays an important role. It is used to provide initial scalar perturbation spectra. While linear perturbation theory is valid, the background evolution decouples from the perturbations such that the homogeneous Friedmann equations together with the background cosmon equation (5.11) can be used to calculate the FLRW background. The spectra and the background are then passed to the N-body based simulation technique. There, random realizations of the perturbation spectra respecting the Gaussian statistics are generated. The resulting hydrodynamic fields correspond to the first moments of the phase-space distribution functions for matter and neutrino particles. Neglecting higher moments (except for the thermal velocities, which we add for the neutrino component), these first moments approximately define the full phase-space distributions. We can use them to sample the phase-space distributions with effective particles. Afterwards, we can switch to an N-body based simulation. An important point we have not mentioned is that we use different initial times $a_{\mathrm{ini},m}$, $a_{\mathrm{ini},\nu}$ for the matter and the neutrino components. A nonlinear treatment of matter is important at much earlier times. The initial conditions are thus obtained separately, and we have to ensure the correct correlation between the initial perturbations (e. g., the linear neutrino density perturbations, with which we start, will have formed in large-scale matter potential wells). Moreover, as long as only matter is evolved in the N-body treatment, the precomputed background solution is used. Only after $a_{\mathrm{ini},\nu}$, the background quantities are evolved within the N-body based simulation.

The second and most important part is the main simulation loop. It evolves the particles, the fields, and the background quantities in global, discrete time steps Δa. For the constant β model, we typically use equidistant steps in the scale factor. As a rough prescription, the steps are chosen such that the displacement of a relativistic particle $|v| \approx 1$ within one step is small compared to the cell size Δx, which corresponds to the condition $\Delta\tau \approx \Delta a/(a^2 H) \ll 1$. Of course, rather than relying on this rule of thumb, we check different step sizes and ensure that convergence is reached. For the varying β case, the dynamical time scale of the model is proportional to $1/|\beta|$ (cf. Baldi et al., 2011). In this case, we will adapt the step size to the varying coupling parameter. The main loop first transforms the particle distributions (given by positions, velocities, and masses) to the relevant components of the energy-momentum tensors on the lattice, cf. Sec. 6.4, and it computes the corresponding spatial averages in the full box. Thereby, the right-hand sides of the field equations for Φ, Ψ, $\delta\varphi$, and for the background equations for $\bar{\varphi}''$ and H are obtained. At this stage, simulation outputs regarding the particle distribution (e. g. the number density fields, the perturbation spectra, the velocities, etc.) can be obtained as outputs. The next step is the solution of the field equations on the lattice, and the evolution of the background quantities. Now, outputs related to the fields and to the background are made. Once the fields are known, their gradients are calculated on the reciprocal lattice, and the neutrino masses are updated. Eventually, the particle velocities are updated by the equations of motion, and the particles are displaced by these updated velocities. This differs from the common (second-order symplectic) leapfrog integration scheme explained in Sec. 2.2.3. The leapfrog iteration relies on the fact that, for Newtonian gravity, the acceleration

of particles does not depend on their velocity. This allows to calculate accelerations and velocities at different times. In our case, however, the neutrinos are relativistic, and the acceleration depends on the value of the velocity. Our integration method is, consequently, not a second-order method. It can be characterized as a (first-order) symplectic Euler method.

6.2 Initial conditions

The simulation scheme includes both neutrinos and matter, while the latter is completely modeled as cold dark matter. Both species differ in the way we obtain initial conditions for them. The most important difference concerns the time at which the nonlinear treatment has to start. Cold dark matter becomes nonlinear at very early times, and in order to describe the clustering with reasonable accuracy, one has to start sufficiently early; we typically choose $a = 0.02$. This early time, however, is somewhat pathological for the neutrino component. The neutrinos are highly relativistic at these early times and become nonrelativistic, typically, around $a \lesssim 0.2$. Although our simulation scheme is capable of treating relativistic neutrinos, we prefer, for the sake of numerical precision, to avoid the limit of highly relativistic neutrinos. Still, these are well described in the linear code such that a later switch to the N-body method, e. g. at $a = 0.2$, is appropriate. The N-body method starts at (typically) $a_{\mathrm{ini},m} = 0.02$ for matter and at $a_{\mathrm{ini},\nu} = 0.2$ for the neutrinos. In the constant coupling model with $\beta = -52$, the neutrinos are already well in the nonrelativistic regime (with an equation of state $w_\nu \sim 10^{-2}$) at $a_{\mathrm{ini},\nu} = 0.2$, and the perturbations are still linear. Of course, the matter and the neutrino perturbations are correlated, and the initial conditions cannot be obtained independently. In our method, the perturbations match at the linear level. We will mention at the end of this section how this is achieved in practice.

In contrast to standard N-body simulations, we do not use a displacement field, obtained from the growing mode, to place particles according to the Zel'dovich approximation (as explained in Efstathiou et al., 1985; Dolag et al., 2008). Rather, we first calculate a Gaussian random realization of the hydrodynamic fields in linear approximation, i. e. the density and the scalar peculiar velocity, and then sample the particle phase-space distribution corresponding to this realization with a finite number of effective N-body particles.

Let us consider this in more detail, and we exemplary focus on the neutrino component. We assume that we have, at the initial time $a_{\mathrm{ini},\nu}$, realizations $\delta_\nu(\boldsymbol{x})$ and $\boldsymbol{v}_{\mathrm{pec},\nu}(\boldsymbol{x})$ for the density perturbation and the peculiar velocity field. We then illustrate the procedure of obtaining the initial conditions in Fig. 6.2. The thermal velocities, which are only included for the neutrinos (and neglected for matter), follow a Fermi-Dirac distribution $f_{\mathrm{th}}(|\boldsymbol{v}_{\mathrm{th}}|)$, cf. Eq. (2.31). Then, we may approximate, for nonrelativistic neutrinos, the phase-space distribution, defined as in Sec. 5.4.4, as

$$f_\nu(x^i, v_j) = \bar{n}_\nu f_{\mathrm{th}}(|\boldsymbol{v} - \boldsymbol{v}_{\mathrm{pec},\nu}(\boldsymbol{x})|)(1 + \delta_\nu(\boldsymbol{x})). \tag{6.1}$$

This is only valid in the nonrelativistic regime where the energy density is equivalent

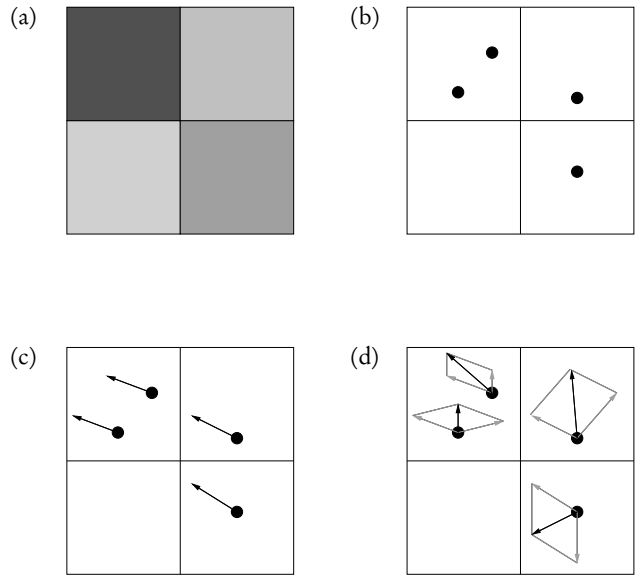

Figure 6.2: Illustration of obtaining initial conditions for effective N-body particles, after a realization of the hydrodynamic fields has been obtained. We show four schematic simulation cells represented by squares. Darker shades of grey (a) indicate larger values of the density field $\bar{\rho}(1+\delta)$. Then, a number of particles is distributed whose expectation value is related to the field value (b). The (smooth) peculiar velocity field $\boldsymbol{v}_{\mathrm{pec}}$ is used (c), and random thermal velocities $\boldsymbol{v}_{\mathrm{th}}$ are added following Fermi-Dirac statistics (d). More precisely, the velocities are added following the rules of relativistic physics. Optionally, we split every particle in two with opposite thermal velocities such that the peculiar velocity field is retained even at the level of a single cell.

to the number density; in the relativistic case, the Lorentz factor has to be taken into account. Although we may assume that most N-body particles are well within the nonrelativistic regime, there will be outliers for which the random thermal velocity just happens to be very large. In a Newtonian addition of velocities, $\boldsymbol{v} = \boldsymbol{v}_{\mathrm{pec},\nu}(\boldsymbol{x})+\boldsymbol{v}_{\mathrm{th}}$, there is thus a small but nonzero probability of obtaining superluminal values. For the purpose of robustness, it is preferable to use a fully relativistic velocity addition law. Although we will typically not work with initially highly relativistic neutrino velocities, we still — at least approximately — allow for this possibility by a simplified scheme. There, the thermal velocity clearly dominates over the peculiar velocity, and the latter can be neglected. The velocity is then completely given by the thermal velocity, and in a simplified approach, all neutrinos are attributed the same absolute value of the velocity, and only the orientations are chosen at random. This can be useful as a very robust and simple first approximation.

The phase-space distribution (6.1) just produces, in the nonrelativistic regime, local

averages in accordance with the hydrodynamic quantities,

$$\langle \rho_\nu(\boldsymbol{x}) \rangle_{f_\nu} = \int d^3v\, m_\nu f_\nu(x^i, v_j) = m_\nu \bar{n}_\nu (1 + \delta_\nu), \tag{6.2}$$

$$\langle \boldsymbol{v}_\nu(\boldsymbol{x}) \rangle_{f_\nu} = \frac{1}{n_\nu(\boldsymbol{x})} \int d^3v\, \boldsymbol{v}\, f_\nu(x^i, v_j) = \boldsymbol{v}_{\mathrm{pec},\nu}. \tag{6.3}$$

The number $N_{\mathrm{part}}(\boldsymbol{x})$ of effective N-body particles with masses M_ν (we will use a capital letter when we emphasize that we consider the mass of an N-body particle rather than of a fundamental neutrino) located in a cell $\boldsymbol{x}$ of physical size $a^3 \Delta V$ should then be chosen such that the expectation value just gives the right energy in the cell,

$$M_\nu \langle N_{\mathrm{part}} \rangle = m_\nu \bar{n}_\nu (1 + \delta_\nu) a^3 \Delta V. \tag{6.4}$$

Since the number of particles is discrete (the average number of particles per cell is, typically, of order one), a random fluctuation is inevitable. In order to minimize it, we distribute the largest number $N_{\mathrm{min}} \leq \langle N_{\mathrm{part}} \rangle$ for sure; N_{min} is just the number obtained by rounding down the expectation value. We then merely have to decide whether to add one additional particle or not. This is done by respecting the expectation value. Once the number of particles in a cell $\boldsymbol{x}$ is known, we randomly distribute the particles within the cell; this means that the three coordinates are just drawn from a uniform random distribution defined in the cell volume. This reduces the amount of artificial power that would be obtained by a completely regular distribution of particles. The result is illustrated in Fig. 6.2 (b).

As a next step, the peculiar velocities $\boldsymbol{v}_{\mathrm{pec}}$ are attributed to the particles. This means that all particles located in one cell get, at first, the same peculiar velocity corresponding to the field value $\boldsymbol{v}_{\mathrm{pec}} = \boldsymbol{v}_{\mathrm{pec},\nu}(\boldsymbol{x})$ at the cell position $\boldsymbol{x}$. To this hydrodynamic peculiar velocity, we add the thermal velocity — or, equivalently, we draw the full velocity $\boldsymbol{v}$ according to $f_{\mathrm{th}}(|\boldsymbol{v} - \boldsymbol{v}_{\mathrm{pec}}|)$. Afterwards, the initial conditions for the N-body particles are complete, cf. Fig. 6.2 (d). If we look at only a few cells, the thermal velocity seems to have destroyed the peculiar velocity field. This changes if we average over a sufficiently large number of cells; then, the coherent motion given by the peculiar velocity field is retained. We optionally refine this by splitting N-body particles in two with opposite thermal velocities. Quantitatively, the effect of this refinement is small.

Matter N-body particles can be distributed in complete analogy, with the only difference that the thermal velocity can be neglected. In this limit, the phase-space distribution function reads

$$f_m(x^i, v_j) = \bar{n}_m\, \delta^3(\boldsymbol{v} - \boldsymbol{v}_{\mathrm{pec},m}(\boldsymbol{x}))(1 + \delta_m(\boldsymbol{x})). \tag{6.5}$$

It remains to describe how we obtain the random realizations of the hydrodynamic fields δ_ν, δ_m, $\boldsymbol{v}_{\mathrm{pec},\nu}$, and $\boldsymbol{v}_{\mathrm{pec},m}$. The peculiar velocity fields are related to scalar perturbation variables $v_{s,\nu}$, $v_{s,m}$. The statistics of the scalar fields are encoded in the two-point correlator, the power spectrum, under the assumption of Gaussianity. We obtain the power spectra from the linear evolution. We discussed the necessary details of random

fields and spectra in Sec. 2.2.1. There, we introduced the vector $y_k^a(\tau)$ including as its components (labeled by a) the different linear scalar perturbation quantities. If we denote by τ_2 the conformal time related to the start of the N-body method and by τ_1 the time where the perturbations were described by the primordial spectrum $P_{\text{prim}}(k)$, we may write, according to Sec. 2.2.1,

$$y_k^a(\tau_2) = F_k^{ab}(\tau_1 \to \tau_2) y_k^b(\tau_1) = \left[F_k^{ab}(\tau_1 \to \tau_2)\eta^b\right] \alpha_k. \tag{6.6}$$

Here, F^{ab} denotes the time evolution operator, and η^a is a vector encoding the relations between the different scalar perturbations for adiabatic initial conditions. The bracket in the last equation is obtained from the linear evolution equations together with the adiabatic condition, and the random realization is then encoded in the scalar-valued coefficients α_k, whose power spectrum is just the primordial perturbation spectrum

$$P_{\text{prim}} = \frac{2\pi^2}{k^3} A_s \left(\frac{k}{k_{\text{pivot}}}\right)^{n_s - 1} \tag{6.7}$$

with the scalar perturbation amplitude A_s, the spectral index n_s, and the pivot scale k_{pivot}. In the N-body code, we need realizations of the scalar perturbations in position space and on a discrete grid of equidistant points $\boldsymbol{x}_n = (n_1, n_2, n_3)\Delta x$. On the discrete grid, we use a discrete Fourier transform to the reciprocal grid $\boldsymbol{k}_n = (n_1, n_2, n_3)\Delta k$ instead of a continuous Fourier transform. The relation between the two transforms f_k (continuous) and $\tilde{f}_n$ (discrete) can be obtained by approximating the Fourier integral by a sum,

$$\begin{aligned} f_{k_n} &= \int d^3x\, e^{-i\boldsymbol{k}_n \cdot \boldsymbol{x}} f(\boldsymbol{x}) && (6.8)\\ &\approx \frac{V}{N^3} \sum_{\boldsymbol{m}} e^{-2\pi i\, \boldsymbol{n}\cdot\boldsymbol{m}/N} f(\boldsymbol{x}_{\boldsymbol{m}}) && (6.9)\\ &= \frac{V}{N^3} \tilde{f}_{\boldsymbol{n}} && (6.10) \end{aligned}$$

with the number $N = \sqrt[3]{N_c}$ of cells in each dimension. The statistics of the discrete realization $\tilde{\alpha}_{\boldsymbol{n}}$ are then obtained by

$$\begin{aligned} \langle \tilde{\alpha}_{\boldsymbol{n}} \tilde{\alpha}^*_{\boldsymbol{m}} \rangle &\approx \left(\frac{N^3}{V}\right)^2 \langle \alpha_{k_{\boldsymbol{n}}} \alpha^*_{k_{\boldsymbol{m}}} \rangle && (6.11)\\ &\approx \left(\frac{N^3}{V}\right)^2 (2\pi)^3 P_{\text{prim}}(k_{\boldsymbol{n}}) \delta^3(\boldsymbol{k}_{\boldsymbol{n}} - \boldsymbol{k}_{\boldsymbol{m}}) && (6.12)\\ &\approx \frac{N^6}{V} P_{\text{prim}}(k_{\boldsymbol{n}}) \delta_{\boldsymbol{nm}} && (6.13) \end{aligned}$$

with the discretization of the Dirac delta,

$$\delta^3(\boldsymbol{k}_n - \boldsymbol{k}_m) \approx \frac{\delta_{nm}}{\Delta k^3}, \tag{6.14}$$

and the relation between the wave number difference Δk and the one-dimensional spatial size $L = \sqrt[3]{V}$ of the grid, $\Delta k = 2\pi/L$.

With the help of this result, it is straightforward to generate a random realization $\tilde{\alpha}_n$ under the Gaussian assumption, as described in Sec. 2.2.1. This can be used, together with the result from linear perturbation theory, to generate the vector of scalar linear perturbations $\tilde{y}^a_n$, which can be transformed to real space by a discrete Fourier transform to give the hydrodynamic initial fields $\delta_\nu(\boldsymbol{x})$, $\boldsymbol{v}_{\mathrm{pec},\nu}$, $\delta_m(\boldsymbol{x})$, $\boldsymbol{v}_{\mathrm{pec},m}$. A minor technical subtlety lies in the fact that the position space fields have to take real values. To ensure this, one has to implement symmetry between mirrored wave modes. In terms of continuous variables, this reads $\alpha^*_{\boldsymbol{k}} = \alpha_{-\boldsymbol{k}}$. The correct correlation between the initial perturbations for matter and for neutrinos is ensured by employing the same coefficients $\alpha_{\boldsymbol{k}}$ for both (although the vector $y^a_{\boldsymbol{k}}$ is calculated at different times $a_{\mathrm{ini},m}$ and $a_{\mathrm{ini},\nu}$ respectively).

6.3 Particle motion

The motion of effective neutrino particles differs from that of matter in two respects. First, we have to take into account the cosmon-mediated attractive force, which, in the Newtonian limit, is a factor of $2\beta^2$ stronger than the gravitational interaction between the neutrinos. Second, as a consequence of this enormous accelerating force, we have to switch to a fully relativistic treatment. In a Newtonian approach, a large fraction of the effective particles quickly reaches the speed of light (Baldi et al., 2011). Including only, e. g., first-order relativistic corrections is not sufficient either. Even in the fully relativistic treatment, we have to choose our numerical strategy with care in order to robustly enforce the speed of light limit. In particular, it is inadequate to formulate the equation of motion for the effective particles as a differential equation in the coordinate velocity $\boldsymbol{v} = d\boldsymbol{x}/d\tau$. Such a differential equation, even if fully relativistic, could — due to finite numerical steps — lead to superluminal velocities and pathological effects when, e. g., trying to calculate the Lorentz factor γ.

In this section, we will show how to derive the fully relativistic equation of motion, discuss the terms it contains in more detail, and explain how to implement it numerically. A more detailed presentation can be found in Weber (2012).

If $T^{\mu\nu}$ denotes the one-particle energy-momentum tensor, cf. Eq. (5.39), we have already mentioned in Sec. 5.3 that the equation of motion can be obtained directly from the one-particle action

$$S = \int d^4x \sqrt{-g}\, T^\lambda{}_\lambda = -\int d\eta\, m_\nu(\varphi(x)), \tag{6.15}$$

with the proper time η and the cosmon-dependent neutrino mass, evaluated at the particle trajectory $x^\mu(\eta)$; this means that the condition $\delta S/\delta x = 0$, in a straightforward manner, yields the equation of motion (Weber, 2012). Another approach proposed in the appendix of Baldi et al. (2011) makes use of a conformal transformation. In order to explain the relation between the two approaches, let us first write the proper time element as

$$d\eta = \sqrt{-g_{\mu\nu} dx^\mu dx^\nu} \tag{6.16}$$

and use — in the constant β model — the explicit mass function $m_\nu(\varphi) = \bar{m} \exp(-\beta\varphi)$. Inserting this, the action reads

$$S = -\int \sqrt{-g_{\mu\nu} dx^\mu dx^\nu}\, \bar{m}\, e^{-\beta\varphi} \tag{6.17}$$

$$= -\int \sqrt{-\left(e^{-2\beta\varphi} g_{\mu\nu}\right) dx^\mu dx^\nu}\, \bar{m} = -\int d\hat{\eta}\, \bar{m}. \tag{6.18}$$

This is of the same form as the standard action of a particle with constant mass and moving only under the gravitational force; yet, we have performed the conformal transformation

$$g_{\mu\nu} \mapsto \hat{g}_{\mu\nu} = e^{-2\beta\varphi} g_{\mu\nu}. \tag{6.19}$$

The equation of motion then simply is the standard geodesic equation in the transformed frame,

$$\frac{d\hat{u}^\mu}{d\hat{\eta}} + \hat{\Gamma}^\mu_{\rho\sigma} \hat{u}^\rho \hat{u}^\sigma = 0, \tag{6.20}$$

and it can be transformed back by using the identities

$$\hat{u}^\mu = \frac{dx^\mu}{d\hat{\eta}} = \frac{d\eta}{d\hat{\eta}} \frac{dx^\mu}{d\eta} = e^{\beta\varphi} u^\mu, \tag{6.21}$$

$$\hat{\Gamma}^\mu_{\rho\sigma} = \Gamma^\mu_{\rho\sigma} - \beta \left(\partial_\sigma \varphi \delta^\mu_\rho + \partial_\rho \varphi \delta^\mu_\sigma - \partial^\mu \varphi\, \hat{g}_{\rho\sigma} \right). \tag{6.22}$$

A third way of arriving at the equation of motion is to use the one-particle energy-momentum tensor, Eq. (5.39), together with the energy-momentum exchange equation (5.4). One can show (Ayaita et al., 2012b; Weber, 2012) for the left-hand side of this equation evaluated at x and with the particle trajectory ξ:

$$\nabla_\nu T^{\mu\nu} = \frac{1}{\sqrt{-g}} \int d\eta\, m_\nu(\varphi) \delta^4(x - \xi) \left(\frac{du^\mu}{d\eta} + \Gamma^\mu_{\rho\sigma} u^\rho u^\sigma - \beta u^\lambda \partial_\lambda \varphi\, u^\mu \right). \tag{6.23}$$

For the exchange term on the right-hand side, one obtains, by inserting the one-particle energy-momentum tensor:

$$-\beta \mathrm{tr} T\, \partial^\mu \varphi = \frac{1}{\sqrt{-g}} \int d\eta\, m_\nu(\varphi)\, \beta \partial^\mu \varphi\, \delta^4(x - \xi). \tag{6.24}$$

Together, these equations also give the equation of motion that we have already seen in Sec. 5.3; we repeat it here, since we will go on discussing it in more detail,

$$\frac{du^\mu}{d\eta} + \Gamma^\mu_{\rho\sigma} u^\rho u^\sigma = \beta \partial^\mu \varphi + \beta u^\lambda \partial_\lambda \varphi \, u^\mu. \tag{6.25}$$

The left-hand side describes the motion under gravity, which, since the particles can be relativistic, differs from the usual Newtonian relation. With the help of the Christoffel symbols from Eqs. (2.58) and (2.59) for the linearly perturbed FLRW metric, the gravitational part of the equation of motion of the spatial components $\boldsymbol{u}$ is

$$\boldsymbol{u}'_G = -2\frac{a'}{a}\boldsymbol{u} - \frac{\gamma}{a}\boldsymbol{\nabla}\Psi - \frac{a\boldsymbol{u}^2}{\gamma}\boldsymbol{\nabla}\Phi + \frac{2a}{\gamma}(\boldsymbol{u}\cdot\boldsymbol{\nabla}\Phi)\,\boldsymbol{u}. \tag{6.26}$$

The first term on the right-hand side describes the usual Hubble damping; the factor of two originates from the fact that an additional scale factor occurs in the relation between the four-velocity $u^\mu = dx^\mu/d\eta$ and the coordinate velocity $\boldsymbol{v} = d\boldsymbol{x}/d\tau$,

$$u^i = \frac{dx^i}{d\eta} = \frac{d\tau}{d\eta}\frac{dx^i}{d\tau} = \frac{(1-\Psi)}{a}\gamma v^i \tag{6.27}$$

with the Lorentz factor defined according to Eq. (5.41).

The relation between the Lorentz factor γ and $\boldsymbol{u}$ can, e. g., be derived from the normalization $u^\lambda u_\lambda = -1$ and reads

$$\gamma = (1-\Psi)\sqrt{1+(1-2\Phi)a^2\boldsymbol{u}^2}. \tag{6.28}$$

Calculating γ this way is numerically robust even in the highly relativistic limit of very large $\boldsymbol{u}^2$. This is strongly preferred over the calculation via the coordinate velocity $\boldsymbol{v}$, which approaches a pole for relativistic velocities. Obviously, for large $|\boldsymbol{u}|$, $\gamma \sim a|\boldsymbol{u}|$. This means that γ scales linearly, for relativistic particles, with the spatial components of the four-velocity. As a consequence, all terms in Eq. (6.26) scale equally, which means that they all remain relevant for relativistic particles. For nonrelativistic particles, $\gamma \approx 1$ and $|\boldsymbol{u}|^2 \ll |\boldsymbol{u}|$ to a good approximation. In this case, only the Hubble damping term and the Newtonian force term $-\boldsymbol{\nabla}\Psi$ remain important. This is the usual case known for cold dark matter.

Let us include the cosmon-mediated fifth force. The total equation of motion can be written as

$$\boldsymbol{u}' = \boldsymbol{u}'_G + \beta\bar{\varphi}'\,\boldsymbol{u} + \frac{\beta}{a\gamma}(1+2\Phi)\,\boldsymbol{\nabla}\delta\varphi + \frac{a\beta}{\gamma}(\boldsymbol{u}\cdot\boldsymbol{\nabla}\delta\varphi)\,\boldsymbol{u}. \tag{6.29}$$

Here, the first additional term leads to a modified Hubble damping. Due to the typically large values of β, it is expected to dominate over the gravitational damping term, cf. Fig. 5.9. The second term $\propto \boldsymbol{\nabla}\delta\varphi$ is analogous to Newtonian gravity. However, as compared to the other terms, it is suppressed by a net factor γ^{-1} for relativistic

particles. In the relativistic limit, this part of the cosmon-mediated coupling becomes irrelevant, even against gravity. Only the modified Hubble damping term and the term $\propto (\boldsymbol{u}\cdot\boldsymbol{\nabla}\delta\varphi)\boldsymbol{u}$ remain important. These contributions accelerate or decelerate particles only parallel to their motion. Although the cosmon-mediated attraction is very important for nonrelativistic particles, this effect is essentially switched off in the relativistic regime.

In order to move the particles in the simulation volume, we still need their coordinate velocities $\boldsymbol{v}$. These are obtained by Eq. (6.27).

We use the equation of motion implemented according to Eq. (6.29) for evolving the effective neutrino particles in our simulation. Note that the derivation relies on the description via the one-particle energy momentum tensor. Regarding our discussion of whether cosmon-neutrino lumps can be treated as particles, cf. Sec. 5.4.1, we have to keep in mind a limitation: particles have no internal pressure. Since effective particles in the N-body simulation are thought of as collections of large numbers of fundamental neutrinos, it is not obvious whether the condition is met. If the thermal velocities of the neutrinos are large, we expect a residual internal pressure attributed to each effective particle. The energy-momentum tensor of effective particles would not be of the one-particle form, and the equations of motion derived from it would not be valid. This is one of the reasons why it is preferred to add the neutrinos to the simulation only once they are well within the nonrelativistic regime. The residual equation of state at $a \approx 0.2$ is of order $w_\nu \sim 10^{-2}$, and potential corrections that follow from it are small. In the course of the evolution, the effective particles are accelerated again, but this acceleration is spatially smooth — it is given by gradients on the grid — so that it does not induce thermal velocities below the effective size of the N-body particles.

Matter particles are evolved as usual in Newtonian N-body simulations. Their equation of motion can, e. g., be obtained by the above equations with $\gamma \approx 1$, $|\boldsymbol{u}|^2 \ll |\boldsymbol{u}|$, and $\beta = 0$. The result is the well-known force law

$$\boldsymbol{v}' = -\frac{a'}{a}\boldsymbol{v} - \boldsymbol{\nabla}\Psi. \tag{6.30}$$

6.4 Fields and background

While the neutrino and matter components are modeled by effective particles, the perturbation fields Ψ, Φ, and $\delta\varphi$ are calculated on a fixed spatial comoving lattice, and the corresponding background quantities H and $\bar{\varphi}$ are evaluated via homogeneous, i. e. averaged equations. The field equation for Φ is just the usual Poisson equation; Ψ is obtained by including the anisotropic shear perturbation, cf. Sec. 2.2.1, i. e.

$$k^2\left(\Phi_{\boldsymbol{k}} - \Psi_{\boldsymbol{k}}\right) = -\frac{a^2}{2}\left(3\frac{k_i k^j}{k^2} - \delta_i^j\right)\Sigma^i_{\boldsymbol{k}\,j}, \tag{6.31}$$

$$\Sigma^i_{\boldsymbol{k}\,j} = T^i_{(\nu)\,j} - \frac{1}{3}\delta^i_j T^k_{(\nu)\,k}, \tag{6.32}$$

in Fourier space and with the fact that only the neutrinos contribute to this relativistic perturbation.

The cosmon perturbation $\delta\varphi$ is determined by the linearly perturbed part of the modified Klein-Gordon equation under suitable approximations, Eq. (5.47). Finally, the Hubble parameter is given by the flatness condition

$$3H^2 = \rho_{\mathrm{tot}}, \tag{6.33}$$

and the averaged cosmon $\bar{\varphi}$ obeys Eq. (5.11).

The right-hand sides of all these equations are given by components of energy-momentum tensors. In the gravitational Poisson equation, this is the total density perturbation

$$\delta\rho_{\mathrm{tot}} = -\delta T^0_{(m)0} - \delta T^0_{(\nu)0} - \delta T^0_{(\varphi)0}; \tag{6.34}$$

in the field equation for $\Phi - \Psi$, the pressure components $T^i_{(\nu)j}$; in the field equation for $\delta\varphi$, the trace perturbation $\delta\mathrm{tr}T_{(\nu)}$; for the Hubble parameter, the total density $-T^0_{\mathrm{tot}\,0}$; and, finally, in the background equation for $\bar{\varphi}$, the averaged trace $\mathrm{tr}\bar{T}_{(\nu)}$. In order to implement the equations numerically, we have to write the quantities in terms of the effective particles. This is even true for the right-hand sides of the background equations. As explained in Secs. 5.2 and 5.3, the background equations cannot be solved independently of the perturbation equations due to the backreaction effect. The calculation of the energy-momentum tensors is straightforward if we go back to the one-particle form of the energy-momentum tensor (5.43). It can be used for every individual effective particle. The energy density ρ_ν (and, analogously, ρ_m) is then

$$\rho_\nu(\boldsymbol{x}) = -T^0_{(\nu)0}(\boldsymbol{x}) = \sum_p \frac{1}{\sqrt{{}^{(3)}g}}\gamma_p M_p(\varphi)\,\delta^3(\boldsymbol{x}-\boldsymbol{x}_p) \tag{6.35}$$

as a sum over particles p with Lorentz factors γ_p and φ-dependent masses $M_p(\varphi)$ evaluated at the particle positions $\boldsymbol{x}_p$. The density perturbation is simply $\delta\rho_\nu = \rho_\nu - \bar{\rho}_\nu$, where $\bar{\rho}_\nu$ is obtained by averaging $\rho_\nu(\boldsymbol{x})$ in the simulation volume V; of course, this volume has to be large enough such that the average has converged. Similarly, the trace $\mathrm{tr}T_{(\nu)}$ is obtained as

$$\mathrm{tr}T_{(\nu)} = T^\lambda_{(\nu)\lambda} = -\sum_p \frac{1}{\sqrt{{}^{(3)}g}}\,\frac{M_p(\varphi)}{\gamma_p}\,\delta^3(\boldsymbol{x}-\boldsymbol{x}_p), \tag{6.36}$$

and the remaining components $T^i_{(\nu)j}$ are evaluated analogously.

Linear field equations are solved in Fourier space where derivatives are transformed to simple multiplications. This can be used for the gravitational potentials Ψ and Φ. Moreover, once the field equation is solved in Fourier space, we obtain the gradients for free using the transformation

$$i\boldsymbol{k}\Psi_{\boldsymbol{k}} \mapsto \boldsymbol{\nabla}\Psi. \tag{6.37}$$

The price to pay for a fixed grid is the limitation it imposes on the resolution. As we have already argued, this is not as crucial for modeling the neutrinos as it is for matter. Cosmon-neutrino lumps form on relatively large scales. A moderate improvement can be obtained by linearly interpolating the force between the grid points and by attributing each particle, in the field calculation, to its neighboring grid points weighted by distance; this cloud-in-cell method has been explained in Sec. 2.2.3. Although this is implemented in our simulation technique as a numerical option, we have not seen significant quantitative effects.

The field equation for $\delta\varphi$ is of a different kind; the left-hand side has been linearized in $\delta\varphi$, but the right-hand side includes, via $\mathrm{tr}T_{(\nu)}$, mass terms, cf. Eq. (5.47). In the constant β model, they are proportional to $\exp(-\beta\delta\varphi)$. And although $\delta\varphi \ll 1$, the rescaled quantity $\beta\delta\varphi$ by the large coupling constant β can be of order one, cf. Sec. 5.3. The field equation remains nonlinear, and a robust solution is not obtained in a straightforward manner. We will discuss this problem in Sec. 6.6.1 but already note here that the numerical complications due to this equation hindered Ayaita et al. (2012b) from evolving the growing neutrino quintessence model beyond $a = 0.5$. The problem has been solved recently, and we show preliminary results beyond $a = 0.5$ in Sec. 6.6.

Let us now turn to the evolution of the background cosmon $\bar{\varphi}$. Usually, studies of perturbations, and in particular N-body simulations, first solve the purely homogeneous equations and then evolve the perturbations on the precomputed background. This would be exact if the time evolution commuted with the averaging procedure. Since the averaging is linear, this is the case for linear perturbation theory. In the standard ΛCDM scenario, the corrections due to nonlinearities are small. This is, essentially, a consequence of the metric perturbations Ψ and Φ being small even when the matter density perturbations are nonlinear. Accordingly, the corrections to the averaged gravitational field equations, i. e. to the Friedmann equations, are generally estimated to be negligible, cf. our discussion in Sec. 2.2.2.

In the growing neutrino quintessence model, this remains true for gravity. Still, for the cosmon-mediated force, the quantity $\beta\delta\varphi$ is decisive, and it does reach order unity. As a consequence, the backreaction is neither negligible nor a mere correction. It is a decisive effect, even if we are not interested in precision calculations. As we have already mentioned, the nonlinearity in $\delta\varphi$ arises in the homogeneous equation for $\bar{\varphi}$, Eq. (5.11). The right-hand side is — in the constant β model — proportional to $\mathrm{tr}\bar{T}_{(\nu)}$. The correct averaging of this quantity, based on the effective particles p, reads

$$\mathrm{tr}\bar{T}_{(\nu)} = \frac{\int d^3x\sqrt{{}^{(3)}g}\,\mathrm{tr}T_{(\nu)}}{\int d^3x\sqrt{{}^{(3)}g}} \approx -\frac{1}{a^3V}\sum_p \frac{M_p}{\gamma_p}, \tag{6.38}$$

neglecting the metric perturbations for a simple discussion. If, instead, the purely homogeneous evolution equations were used, one would obtain an estimate $\mathrm{tr}\bar{T}^{\mathrm{est}}_{(\nu)}$; since the background equations predict nonrelativistic neutrinos for $a \gtrsim 0.2$, cf. Sec. 5.1, we have $\mathrm{tr}\bar{T}^{\mathrm{est}}_{(\nu)} \approx -\bar{\rho}^{\mathrm{est}}_{\nu}$. The neutrino mass entering this estimate is the background

value depending only on $\bar{\varphi}$. If we assume (which, dynamically, becomes inaccurate quickly) that $\bar{\varphi}$ from the estimation still quite well corresponds to the true averaged value, we may write for the quotient between the true right-hand side, Eq. (6.38), and the estimate:

$$\frac{\mathrm{tr}\bar{T}_{(\nu)}}{\mathrm{tr}\bar{T}^{\mathrm{est}}_{(\nu)}} \sim \sum_p \frac{e^{-\beta\delta\varphi(\boldsymbol{x}_p)}}{\gamma_p}. \tag{6.39}$$

This quantifies the error in the right-hand side when the background equations are used independently of the perturbations. We identify two effects:

1. Most neutrinos are located in overdensities and, eventually, in lumps. There, $\delta\varphi$ is negative and $\exp(-\beta\delta\varphi)$ is substantially smaller than one.

2. The relativistic velocities reached during the nonlinear structure formation process lead to substantially enhanced Lorentz factors $\gamma_p > 1$ for many particles.

Both of these effects lead to a suppression of the right-hand side as compared to the homogeneous estimate. We quantify the effects in the full simulation run until $a = 0.5$ in Fig. 6.3. All three quantities agree well until $a \gtrsim 0.35$ where nonlinear effects become

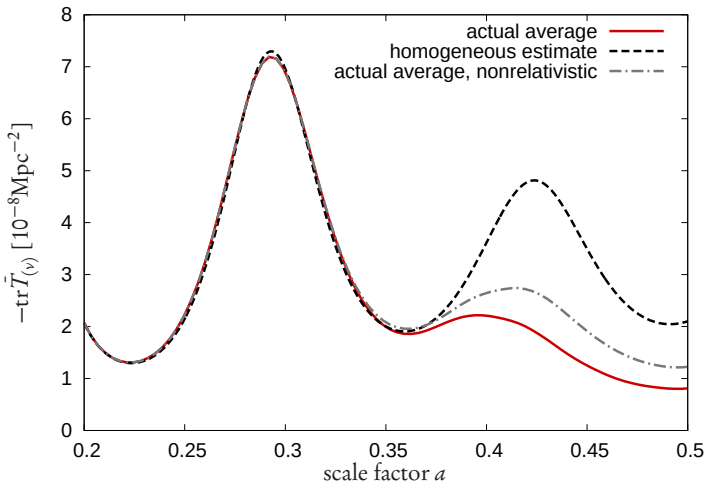

Figure 6.3: The importance of the backreaction effect in the calculation of the right-hand side of Eq. (5.11). The homogeneous evolution not taking into account the perturbations strongly deviates from the correct average. Also the effect of relativistic velocities is important. An equivalent plot can be found in Ayaita et al. (2012b).

important. The actual average $\mathrm{tr}\bar{T}_{(\nu)}$ is substantially suppressed as compared to the pure background calculation. The difference between the actual average $\mathrm{tr}\bar{T}_{(\nu)}$ and the quantity obtained by neglecting the relativistic effect (this would assume $\mathrm{tr}\bar{T}_{(\nu)} \approx -\bar{\rho}_\nu$), is also significant. Both effects, the mass suppression and the relativistic velocities,

have to be included in the computation of the background quantities. Our simulation method thus evolves the coupled system of the perturbations and the background.

The mechanism by which growing neutrino quintessence realizes the onset of dark energy domination and, consequently, initiates the phase of accelerated expansion relies on the cosmon-neutrino coupling constituting an effective potential barrier. By the backreaction effect, this barrier is severely reduced. As a consequence, we will see that the backreaction shifts the onset of accelerated expansion to much later times. The choice of adequate model parameters β and α then has to take into account the nonlinear evolution. This means that the parameter space of the model has to be explored in the full simulations.

6.5 Results until $a = 0.5$

After having reviewed the most important technical aspects of the simulation method, we can have a look at the quantitative results. In this section, we present the results obtained by Ayaita et al. (2012b) based on, essentially, a single simulation run with specific, exemplary model parameters. These are the same parameters we have used in Sec. 5.4 when quantifying the properties of cosmon-neutrino lumps. The model parameters and numerical choices are listed in Table 6.1. These parameters are only exemplary. First, we emphasize that we use a constant coupling parameter $\beta = -52$. In Sec. 6.6, we will see that this implies a particular regime of the growing neutrino quintessence model, where the picture of cosmon-neutrino lumps is valid; whereas, for varying β models, this regime can be left, and the evolution of perturbations is very different both quantitatively and qualitatively. In a sense, the constant β model is an extreme case where cosmon-neutrino lumps dominate the cosmological evolution and the backreaction effect is very large.

Second, the constant coupling is relatively small such that a large average neutrino mass $m_{\nu,0}^{\mathrm{est}} = 2.3$ eV is needed in order for the cosmon-neutrino coupling to be strong enough for initiating a phase of accelerated expansion. This is, as well, a rather extreme choice, and it essentially coincides with the laboratory constraints on the neutrino mass, cf. Sec. 5.5.1. As a consequence, the homogeneous estimate of the present-day neutrino fraction is large, $\Omega_{\nu,0}^{\mathrm{est}} \approx 0.15$. This means that the energy density concentrated within cosmon-neutrino lumps is significant, and correspondingly, their gravitational potentials and their effects on potential observables will be very large.

We conclude that the parameters used here correspond to a choice where the particular effects of growing neutrino quintessence, i. e. the formation of cosmon-neutrino lumps and the backreaction effect, are very pronounced. In addition, the cosmological parameters have been chosen such that the homogeneous estimates provide a realistic expansion history. The deviations induced by the backreaction effect will lead to an unrealistic expansion history as compared to observational constraints. The results we will obtain are thus essentially illustrative. We emphasize again that, in order to obtain more realistic results, an exploration of the parameter space has to be performed.

Parameter	*Value*
Cosmon-neutrino coupling	$\beta = -52$
Scalar potential parameter	$\alpha = 10$
Present-day neutrino mass	$m_{\nu,0}^{\text{est}} = 2.3$ eV
Dark energy fraction	$\Omega_{\varphi,0}^{\text{est}} = 0.6$
Hubble parameter	$H_0^{\text{est}} = 70 \frac{\text{km}}{\text{sec}}\,\text{Mpc}^{-1}$
Scalar perturbation amplitude	$A_s = 2.3 \times 10^{-9}$
Pivot scale	$k_{\text{pivot}} = 0.05\ \text{Mpc}^{-1}$
Spectral index	$n_s = 0.96$
Comoving simulation box size	$V = L^3 = \left(600 h^{-1}\text{Mpc}\right)^3$
Number of grid cells	$N_c = 256^3$
Number of effective neutrino particles	$N_\nu = 2 \times 10^7$
Number of effective matter particles	$N_m = 2 \times 10^7$
Initial scale factor	$a_{\text{ini},m} = 0.02$
Adding the neutrinos	$a_{\text{ini},\nu} = 0.2$
Final scale factor	$a_{\text{fin}} = 0.5$

Table 6.1: Basic growing neutrino quintessence model parameters, cosmological parameters, and numerical parameters of the simulation. The superscript 'est' indicates that the corresponding parameter is obtained by a purely homogeneous evolution of the model; it will differ from the true value due to the backreaction effect, cf. Sec. 6.4.

6.5.1 Formation of cosmon-neutrino lumps

We start our presentation of the simulation results with the most striking finding. This is the formation of large cosmon-neutrino lumps. Their occurrence was first predicted by Mota et al. (2008) on the grounds of linear perturbation theory, tentative studies of their properties followed (Brouzakis et al., 2008; Wintergerst et al., 2010; Nunes et al., 2011) and were applied to first estimates for their influence on the cosmological evolution (Pettorino et al., 2010). The first clear numerical evidence for their formation was shown by Baldi et al. (2011), but due to the neglect of local mass variations and the backreaction effect, the lumps in those simulations did not stabilize, cf. Sec. 5.2 for more details. The clear verification of the formation of cosmon-neutrino lumps and the first numerically reliable results regarding their properties is a key result of the simulation method presented in this chapter. It served as a starting point for the development of a comprehensive physical picture of the cosmon-neutrino lump fluid, which we explained in Sec. 5.4.

The visual impression of the lump formation process within our simulation box is shown in Fig. 6.4. Regarding the size of our simulation box ($L = 600h^{-1}$Mpc side length), it becomes clear that the cosmon-neutrino lumps are a large-scale phenomenon. Let us go through the figures. In the beginning, after the neutrinos are added to the simulation at $a_{\mathrm{ini},\nu}$, the neutrino perturbations are still linear to a good approximation as suggested by the results from linear perturbation theory, cf. Sec. 5.2. The neutrinos are nonrelativistic, and the cosmon-mediated attractive force leads to a rapid growth of the inhomogeneities. Between $a = 0.25$ and $a = 0.30$, the neutrino density perturbations have grown by a substantial factor. The results not only qualitatively, but also quantitatively agree with the linear calculation. The nonlinearities have then clearly emerged at $a = 0.35$, and they are seen on relatively large scales. This is also in accordance with linear theory, where we have seen in Fig. 5.7 that neutrino perturbations pass the nonlinear boundary first for $a \gtrsim 0.35$ and on scales of about $\sim 100h^{-1}$Mpc. After this period, the linear approximation breaks down, and we rely on a nonlinear method. We find very large filaments at $a = 0.40$. At this time, where the nonlinearities have become essential, the acceleration due to the cosmon-mediated attraction already causes many effective neutrino particles to leave the nonrelativistic regime. The average equation of state w_ν grows to $\sim 10^{-1}$. Not only linear theory, but also Newtonian N-body methods can no longer describe the cosmological evolution. At the same time, the cosmon perturbation grows, and the quantity $\beta\delta\varphi$ approaches order one in the overdense regions. The mass suppression $\propto \exp(-\beta\delta\varphi)$ becomes important and can no longer be linearized; the backreaction effect explained in Sec. 6.4 starts to affect the cosmological evolution. Already at $a = 0.45$, we clearly identify a collection of lumps. The large lumps remain stable and are again seen at $a = 0.5$ at essentially unaltered positions. Many of the smaller lumps have merged, and the total number of lumps is reduced. Now, the picture of a cosmon-neutrino lump fluid as developed in Sec. 5.4 can be applied.

Many properties of the lumps, like their distribution, their masses, and their effective couplings (which determine their dynamics), have been studied in Sec. 5.4. There,

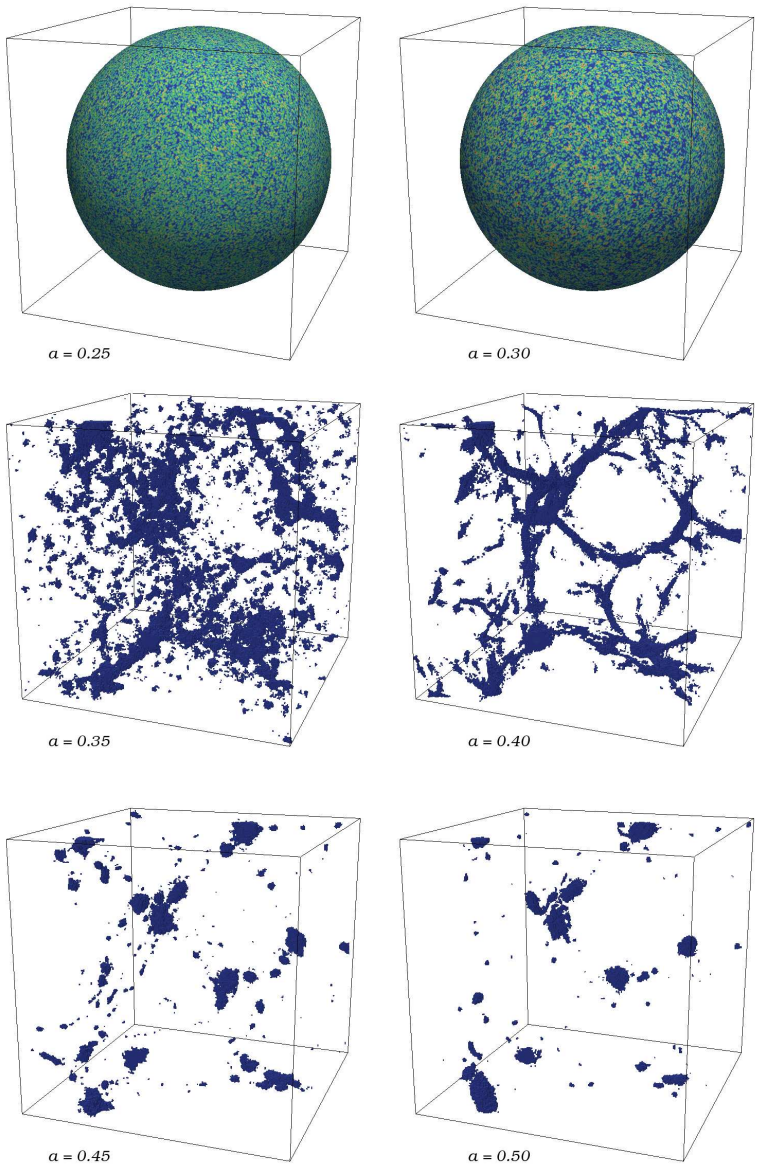

Figure 6.4: Snapshots of the neutrino number density field. The first two figures indicate the (still linear) fluctuations on a two-dimensional surface. The color range goes from $n_\nu(\boldsymbol{x}) = 0$ (blue color) to $n_\nu(\boldsymbol{x}) \geq 5\bar{n}_\nu$ (red color). The remaining figures indicate regions where $n_\nu(\boldsymbol{x}) \geq 5\bar{n}_\nu$. While these nonlinearities are still diffuse at $a = 0.35$, large filaments have formed at $a = 0.40$, and a collection of lumps is observed subsequently. The figure has been taken from Ayaita et al. (2012b).

we also showed simulation results for single, isolated lumps, filling an entire simulation volume. The full cosmological simulations are limited by their resolution, so the information on single lumps is less precise. However, the full simulations allow to study lumps in a realistic cosmological context. Although we were able to generate lumps based on a hydrodynamic balance equation, cf. Sec. 5.4.4, it is a priori unclear which profile and which lump size is to choose realistically. Therefore, it is instructive to actually measure the profile of a lump in the full simulation. We choose a comparatively large lump at $a = 0.5$. A slice through the simulation box at its position (showing the number density $n_\nu(\boldsymbol{x})/\bar{n}_\nu$) and the measured radial number density profile around the center of the lump are shown in Fig. 6.5. We observe a number density contrast in the neutrino component of order 10^5 to 10^6 in the center of the lump. The inner core extends to about $3h^{-1}$Mpc in physical coordinates, and at a distance of $\gtrsim 5h^{-1}$Mpc, the concentration is still two orders of magnitude above the average. If we compare the size of the inner core with the cell size amounting to $\approx 1h^{-1}$Mpc, indicated by the blue-shaded region, we infer that resolution effects might be important. The measurement of the profile is limited by the resolution, and we do not know quantitatively how the profile really looks close to the center.

We analyze the effect of the resolution by performing a new simulation run with identical parameters, except for a lower resolution, $N_c = 128^3$ corresponding to cells twice as extended in each spatial direction. The simulation uses the same random seed, i. e. the same initial perturbations such that we can compare the results of both simulations for the shown neutrino lump. The profile obtained in the low-resolution simulation is shown as the grey-dashed line in Fig. 6.5. As expected, there is a disagreement in the inner core, which now seems less concentrated; the neutrino number density contrast is suppressed by one order of magnitude and only reaches 10^4 to 10^5. However, on scales $\gtrsim 5h^{-1}$Mpc, a remarkable agreement is reached. This is already a first hint for the large-scale properties of the simulation being robust against resolution effects.

In addition to the number density profile, we can have a look at the cosmon profile $\delta\varphi(r)$ or, equivalently, at the mass profile $m_\nu(r) \propto \exp(-\beta\delta\varphi(r))$. For the same lump as in Fig. 6.5, we show the mass profile in both simulation runs (normal and low resolution) in Fig. 6.6. The mass suppression in the inner core amounts, for both resolutions, compared to larger distances, to one order of magnitude. This verifies that the quantity $\beta\delta\varphi$ reaches order one, which is the condition for backreaction effects being important. Since most neutrinos are located in lumps, the cosmologically averaged neutrino mass is substantially suppressed as compared to the homogeneous estimate based on the background cosmon field $\bar{\varphi}$. We will see the influence of this effect on the evolution of background quantities in the next section. It is an important statement, here, that the resolution does not seem to play a crucial role. If the resolution was important for quantifying the mass suppression, this would — by virtue of the backreaction effect — have an impact also on the evolution of large scales and even on the cosmological background, i. e. the dynamics of expansion.

The question whether the resolution of our simulation is sufficient deserves a closer

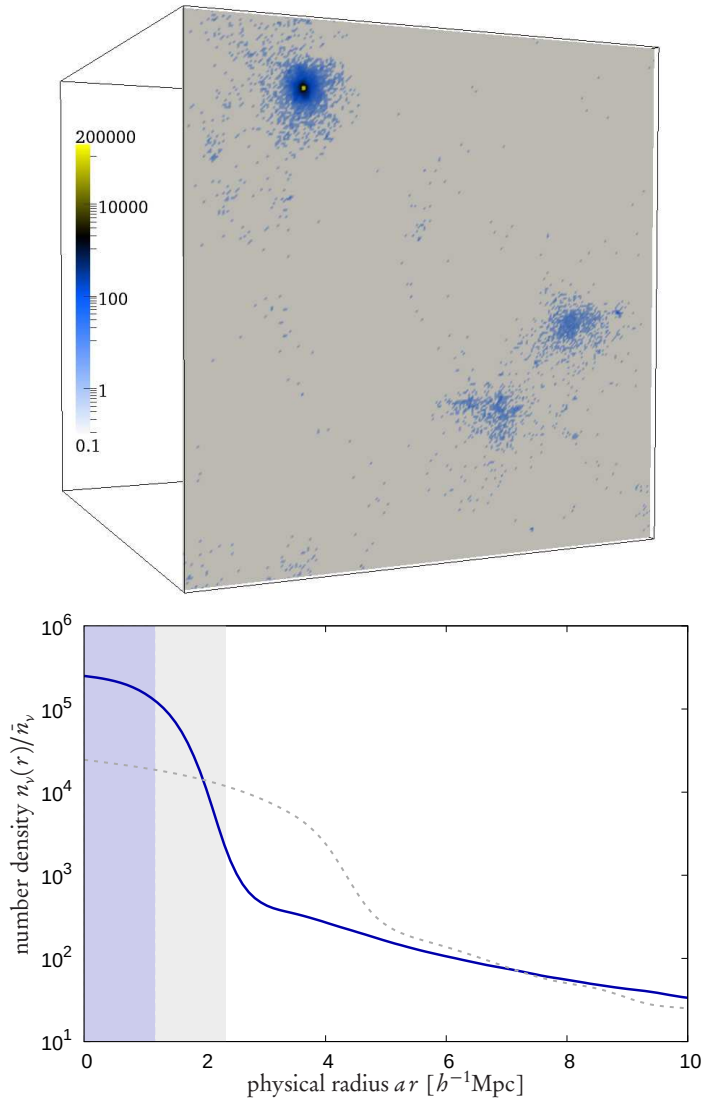

Figure 6.5: Profile of a neutrino lump in the simulation volume at $a = 0.5$. The upper figure shows the number density $n_\nu(\boldsymbol{x})/\bar{n}_\nu$ (normalized to the background value) on a slice through the center of the lump. We observe that the lump is approximately spherical. The spherical number density profile is shown in the lower figure (blue solid line). The blue-shaded region indicates the physical size of a simulation cell. The spatial resolution is comparable to the concentration of the lump. A low-resolution run is shown for comparison (grey dashed line); the grey-shaded region shows the larger cell size. The figures are taken from Ayaita et al. (2012b).

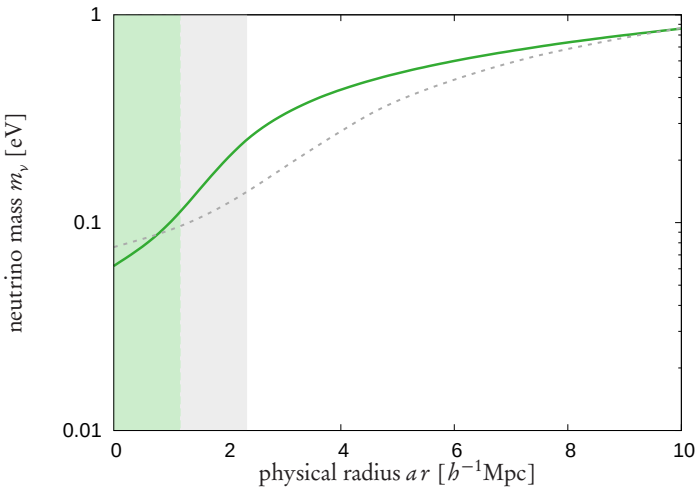

Figure 6.6: The mass profile $m_\nu(r) \propto \exp(-\beta\delta\varphi(r))$ in the neutrino lump of Fig. 6.5. The original simulation run is indicated by a green color, and the low-resolution run is shown in grey. The figure is taken from Ayaita et al. (2012b).

look. Rather than only investigating profiles of individual lumps, we should consider the effect of a resolution change on important cosmological quantities regarding the neutrinos. For example, we may be interested in the effect of the resolution on the neutrino energy-density perturbation spectrum $P_\nu(k)$ or, equivalently, on the dimensionless spectrum $\Delta_\nu(k)$. It is shown, for the two different resolutions, $N_c = 256^3$ and $N_c = 128^3$, in Fig. 6.7. We observe a good agreement between the two spectra on scales larger than the lower resolution, indicated by the vertical line (for smaller scales, of course, the resolution effect is very important, and the power is substantially reduced in the low resolution run). This supports our argument that the evolution on large scales is not sensitive to the smallest scales. We have also checked that the evolution of the FLRW background is not sensitive to the resolution of the simulation. Although the nonlinear evolution necessarily induces couplings between different modes k, this effect is not very pronounced for the smallest scales, which again tells us that neutrino clustering is, in contrast to dark matter clustering, most important on larger scales.

We finish our discussion of cosmon-neutrino lump properties in the realistic cosmological context by having a look at the stability. In Sec. 5.4.4, we have shown that stable lump configurations exist, and we have tested this for isolated neutrino lumps, taken out of the cosmological context and generated with the help of a hydrodynamic balance equation. The full simulations clearly lack the resolution to obtain a detailed picture of the stabilization process. Nonetheless, we wish to check whether the results roughly confirm the expectation of stabilizing lumps. Visually, this expectation seems to apply if we have a look at Fig. 6.4. In order to be quantitative, Ayaita et al. (2012b) identified a lump that does not undergo merging processes between $a = 0.45$ and $a = 0.5$. Such a lump is an ideal object for studying the evolution of the inner

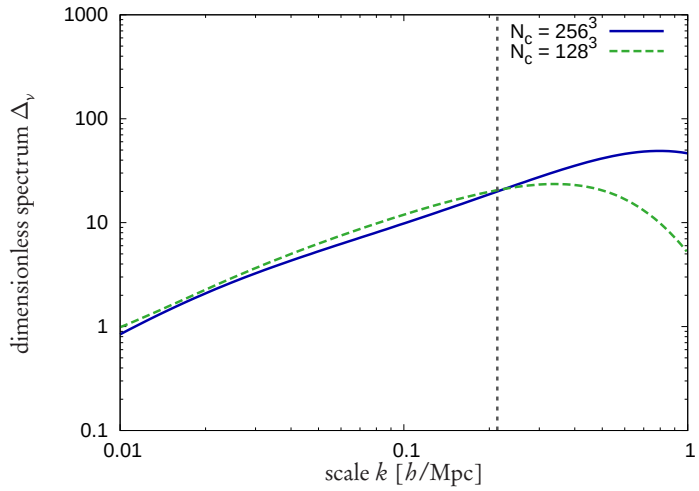

Figure 6.7: The dimensionless neutrino energy-density perturbation spectrum $\Delta_\nu(k)$ at $a_{\rm fin} = 0.5$ for two simulations, $N_c = 256^3$ and $N_c = 128^3$. The vertical line indicates the cell size of the low resolution run, $k \equiv 1/\Delta x$, where $\Delta x = \sqrt[3]{V/N_c} \approx 4h^{-1}$Mpc. The figure is taken from Ayaita et al. (2012b).

profile. We show the result in Fig. 6.8. Of course, we may only expect a stabilization in physical coordinates. This is why we show the profile as a function of the physical radius from the lump's center. If comoving coordinates were used, we would see significant deviations from the rather stable picture we see in Fig. 6.8. Although the stabilization is not precise, we only observe a slow and moderate continuing concentration of the lump. It is not clear whether the continued shrinking is real or an artefact of the numerical limitations.

6.5.2 Backreaction effect

We are now in a position to eventually quantify the backreaction effect in growing neutrino quintessence about which Pettorino et al. (2010) first speculated. We have discussed this effect already in Secs. 5.2, 5.3, and 6.4. The drastic importance of this effect will become clearer in Sec. 6.6, where we will be able to follow the cosmological evolution beyond $a = 0.5$. Since the nonlinearities only start at $a \gtrsim 0.35$, the deviation of the background evolution from the estimate based on the averaged equations is not very pronounced until $a = 0.5$, where the simulation stops. Still, we will see in this section that the effect is already quantitatively important.

In Sec. 6.4, we identified two reasons for the backreaction effect. These are the local mass suppression $\propto \exp(-\beta\delta\varphi)$ and the relativistic neutrino velocities $\gamma > 1$. Both effects lead to a substantial deviation of the averaged neutrino energy-momentum tensor $\bar{T}^{\mu\lambda}_{(\nu)}$ from the estimate obtained by solving the purely homogeneous equations. The averaged energy-momentum tensor enters the calculations of the background cosmon

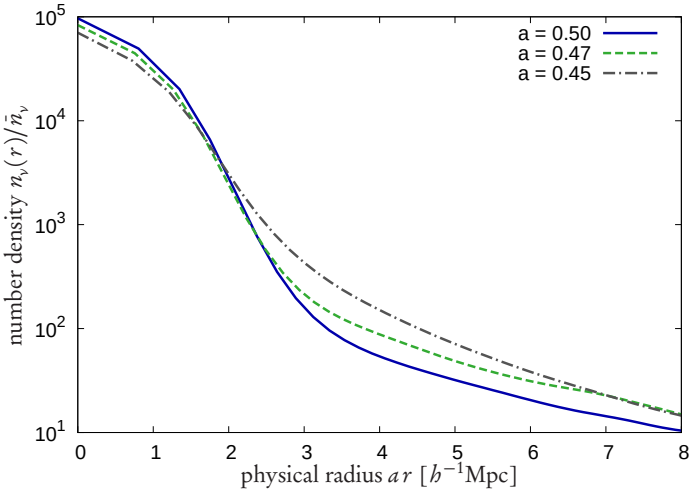

Figure 6.8: The evolution of the number density profile $n_\nu(r)/\bar{n}_\nu$ of a lump between $a = 0.45$ and $a = 0.50$ that does not undergo merging processes. Each profile is taken around the (moving) center of the lump. The figure is taken from Ayaita et al. (2012b).

$\bar{\varphi}$ and of the Hubble parameter H, cf. Sec. 6.4. The effect on the background cosmon in the background modified Klein-Gordon equation (5.11) is most pronounced. Here, both effects, the mass suppression and the relativistic velocities lead to a suppression of the source term $\propto \mathrm{tr}\bar{T}_{(\nu)}$. The strength of the coupling is reduced, and the cosmon is less effectively stopped. As a consequence, the onset of dark energy domination is shifted to later times and with it the accelerated expansion.

The effect on the expansion history can be quantified by the deceleration parameter q already introduced in Sec. 2.1.1, which we rewrite here in conformal time,

$$q = -\frac{a''a}{a'^2} + 1. \tag{6.40}$$

The expansion of the Universe accelerates, i. e. $\ddot{a} > 0$, in the case $q < 0$. In the purely homogeneous evolution, the crossing of $q = 0$ happens shortly after $a = 0.5$. The comparison to the actually measured value in the full simulation run is plotted in Fig. 6.9. Until $a \approx 0.35$, the backreaction effect is irrelevant since the mass suppression can be described in linear approximation and since the neutrinos are still in the nonrelativistic regime. Thereafter, the effect becomes important, and due to the less effective stopping of the cosmon, the Universe continues to significantly decelerate until $a = 0.5$. Yet, in the homogeneous estimate, the expansion has almost switched to the accelerating phase. The effect on the expansion is drastic, and we may not expect agreement with observational constraints on the accelerated expansion. Of course, this does not imply that fitting observational constraints is impossible in general, but it does tell us that the model parameters have to be changed quite substantially. The purely homogeneous estimate — on which the parameter choices here are based — is clearly inaccurate.

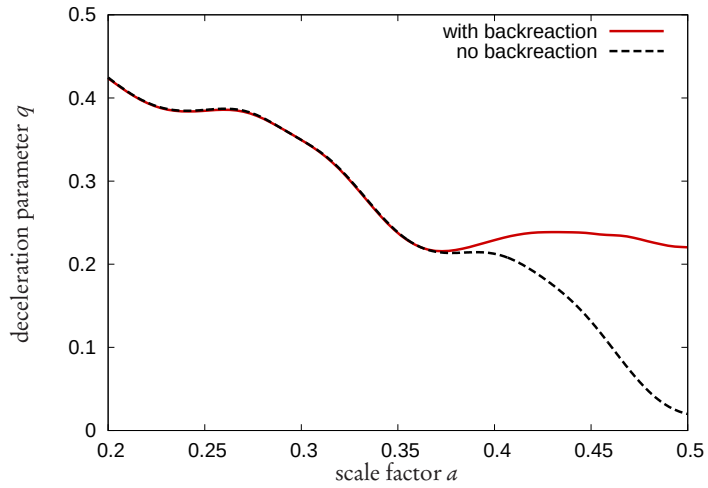

Figure 6.9: The evolution of the deceleration parameter q in the full simulation run as compared to the estimate based on evolving the pure background equations. An equivalent figure can be found in Ayaita et al. (2012b).

The deceleration is directly related to the evolution of the background cosmon $\bar{\varphi}$. Using the Friedmann equations, we can generally write

$$q = \frac{a^4}{6a'^2}\left(\bar{\rho}_{\mathrm{tot}} + 3\bar{p}_{\mathrm{tot}}\right), \tag{6.41}$$

and the background cosmon contributes to the sum by

$$\frac{a^4}{6a'^2}(\bar{\rho}_\varphi + 3\bar{p}_\varphi) \propto \bar{\varphi}'^2 - a^2 V(\bar{\varphi}). \tag{6.42}$$

Although we may not linearize the mass function $m_\nu(\varphi)$ in the perturbation $\delta\varphi$, we can linearize the potential $V(\varphi)$ since the perturbation in the exponent $\alpha\delta\varphi$ is below order one. The relative difference between $\overline{V(\varphi)}$ and $V(\bar{\varphi})$ is only of order 10^{-2}. This shows that the backreaction effect is really due to the mass function and not important for the potential. The cosmon contribution to the deceleration parameter again expresses what we have seen a couple of times for the expansion history in the presence of a canonical scalar field. The comparison between the kinetic energy and the potential energy is decisive. Only if the evolution of $\bar{\varphi}$ is effectively stopped, the potential dominates and we get a contribution that can accelerate the expansion of the Universe.

The comparison between the kinetic term and the potential is encoded in the equation of state w_φ, and we obtain $w_\varphi \approx -1$ if the potential term dominates. The evolution of the equation of state for the full simulation as compared to the homogeneous estimate is quantified in Fig. 6.10. Although still close to the cosmological constant

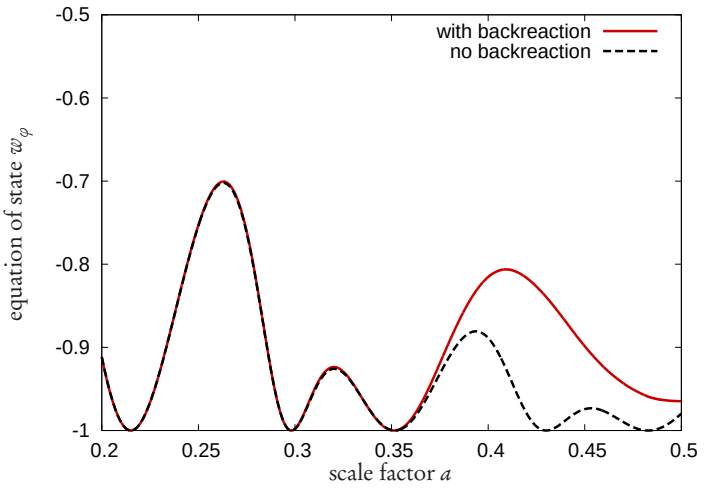

Figure 6.10: The evolution of the equation of state w_φ of the background cosmon field. An equivalent figure can be found in Ayaita et al. (2012b).

value -1, the equation of state w_φ is further away when the backreaction effect is taken into account. This is a consequence of the effective potential barrier provided by the cosmon-neutrino coupling being suppressed. Without the backreaction effect, the equation of state oscillates with values very close to -1 for $a \gtrsim 0.4$.

We can have an even closer look at the evolution of the background cosmon by looking at the evolution of $\bar{\varphi}$ and its time derivative $\bar{\varphi}'$ directly. This is done in Fig. 6.11. Of course, the absolute value of the field $\bar{\varphi}$ is a matter of convention. Any shift can be compensated by adjusting the normalization of the potential and of the neutrino mass accordingly. We have chosen a value such that $\bar{\varphi}$ is close to zero at the present cosmic time; the prefactor of the potential is, consequently, comparable to the cosmological constant value in ΛCDM, $V_0 = V(\varphi = 0) \approx 10^{-120}$ in reduced Planck units. Without the backreaction effect, the background cosmon is clearly stopped at $a \gtrsim 0.4$. This means that the dynamical potential barrier induced by the cosmon-neutrino coupling has produced a minimum in an effective potential where the cosmon is caught. It merely oscillates around this minimum, and the oscillations are continuously reduced due to the damping term in the background equation (5.11). This does not happen if the backreaction effect is included. The potential barrier is suppressed, the minimum in the effective potential is shifted to larger field values. Rather than a stopping, we observe that the field continues to roll down its potential towards larger field values. This also means that the background neutrino mass $m_\nu(\bar{\varphi})$ grows although the mass within the lumps is approximately frozen. The same can also be seen in more detail in the plot of the time derivative $\bar{\varphi}'$.

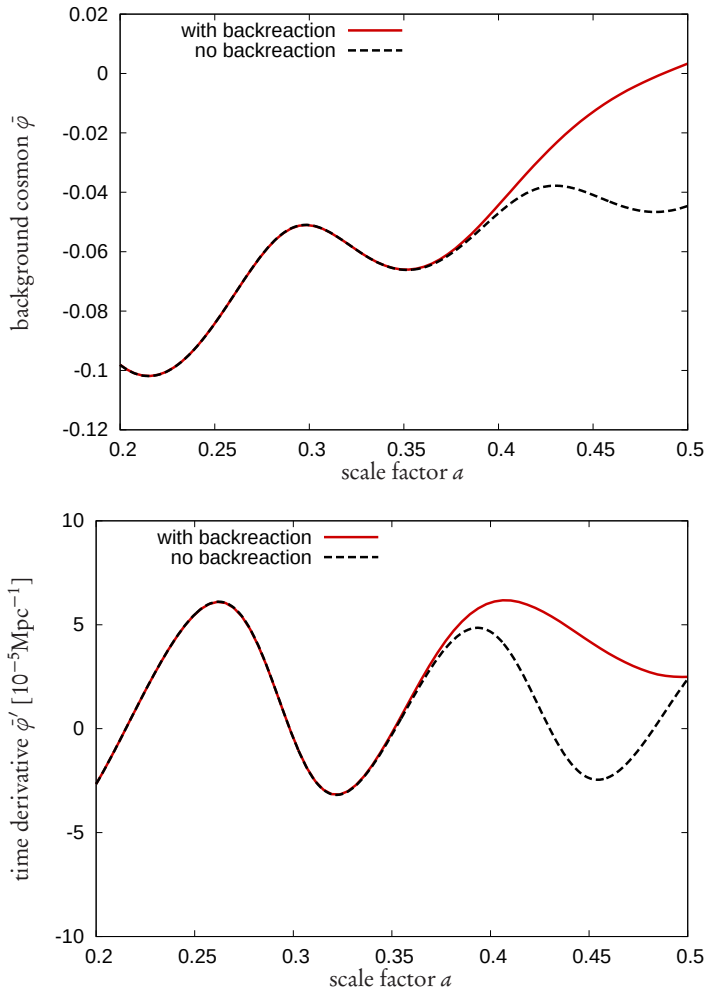

Figure 6.11: The evolution of the background cosmon $\bar{\varphi}$ and its time derivative $\bar{\varphi}'$ with and without taking the backreaction effect into account. Equivalent figures can be found in Ayaita et al. (2012b).

6.5.3 Gravitational potential

Although the parameters chosen for the growing neutrino quintessence model, here, are just exemplary, it is tempting to investigate the consequences of our results for observations. Of course, this investigation is preliminary and mainly illustrative. As we have explained in the beginning of Sec. 6.5, the chosen constant coupling parameter $\beta = -52$ corresponds to an extreme case where the effects of the model are most pronounced. The results that we will show here can thus be interpreted as upper limits for the deviations from the standard ΛCDM model that are induced by the cosmon-neutrino coupling. In Sec. 6.6, we will see hints for the existence of an opposite regime where the deviations from the ΛCDM scenario are expected to be very small.

We have discussed possible observable consequences of the growing neutrino quintessence model in Sec. 5.5. Next to direct probes like measurements of the neutrino mass, we argued that cosmological probes linked to the gravitational potential induced by cosmon-neutrino lumps are promising tools to constrain the model. The gravitational potential is observable directly via the integrated Sachs-Wolfe (ISW) effect, visible both in the CMB and in the cross-correlation between the CMB and large-scale structure and weak gravitational lensing. Indirect probes of the gravitational potential are related to the evolution of matter perturbations. An additional gravitational potential induced by cosmon-neutrino lumps is felt by matter perturbations which, as a consequence, exhibit enhanced growth. This is first visible in the large-scale peculiar velocities, as we have argued in Sec. 5.5. The effect on the matter density power spectrum is delayed.

The evolution of the large-scale gravitational potential, as measured in the simulation run, is quantified in Fig. 6.12. Note that we choose the cosmological redshift $z = 1/a - 1$ as the time variable in this section since it is a common choice made by observers. The simulation ends at $z_{\mathrm{fin}} = 1$, and the neutrinos are added at $z_{\mathrm{ini},\nu} = 4$. The gravitational potential shown here is, more precisely, the dimensionless spectrum defined via

$$\Psi^2(k;z) = \frac{k^3}{2\pi^2} P_\Psi(k;z), \tag{6.43}$$

as usual. We follow Ayaita et al. (2012b) showing the potential normalized to a 'ΛCDM case'. Here, we do not really employ the ΛCDM model but merely use it as a label indicating that the cosmon-neutrino coupling has been switched off in the perturbations. This means that the perturbation evolution is equivalent to the ΛCDM case although the background evolution is not. In order for a clear quantification of the effect of the cosmon-neutrino coupling, we evolved the 'ΛCDM run' on the same FLRW background. This means that we have used the background obtained by the full simulation run as an input for a standard Newtonian N-body simulation which only evolves cold dark matter on a precomputed background. So, the enhancement of the potential shown in Fig. 6.12 is exclusively due to the extra potential induced by cosmon-neutrino lumps and, to a small amount, due to the consequently enhanced matter densities. We also exclude possible numerical effects by using the same numerical parameters in both simulations. The obtained result is, consequently, robust. In

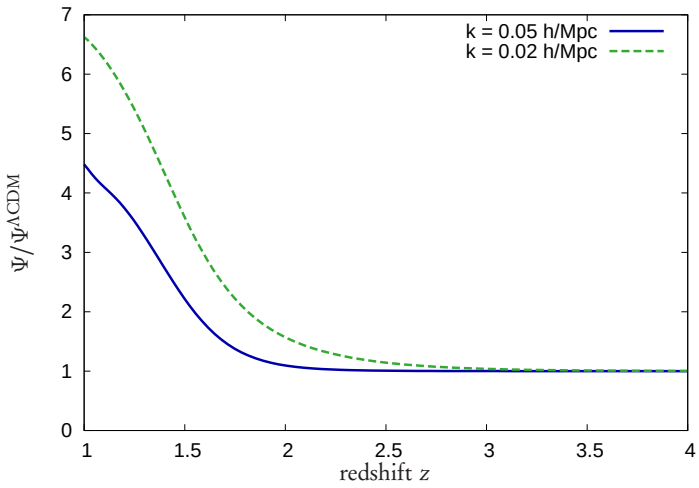

Figure 6.12: The enhancement of the gravitational potential as compared to the ΛCDM scenario (corresponding to switching off the cosmon-neutrino coupling in the perturbations) for two different modes, $k = 0.05h/\mathrm{Mpc}$ and $k = 0.02h/\mathrm{Mpc}$. The figure is taken from Ayaita et al. (2012b).

the presence of relativistic neutrinos, one has, in principle, to discriminate between the two gravitational potentials Ψ and Φ. The difference between the two is, however, only significant on small scales (at the size of the neutrino concentration in a lump and below) so that the effect on the large-scale result here is negligible. Quantitative results concerning the difference between the two potentials are discussed by Weber (2012); Ayaita et al. (2012b).

While, in the ΛCDM scenario, the large-scale gravitational potentials are constant during matter domination and very slowly decay when dark energy is becoming important, the formation of cosmon-neutrino lumps on large scales in the growing neutrino quintessence model (for the constant β parameter used here) leads to a different behavior. Large-scale gravitational potentials grow significantly at $z \lesssim 2.5$ (corresponding to $a \gtrsim 0.3$). This precedes the nonlinear evolution. The growth of the potential is a result already clear from linear perturbation theory. Nonlinear theory leads to a flattening of this growth once stable cosmon-neutrino lumps have formed. In the case of individually static neutrino lumps, we would still expect a residual growth of the gravitational potential due to two effects. First, the mutual attractive interaction between the lumps and their influence on the surrounding matter perturbations leads to further growth in the perturbations on large scales. Second, if the background cosmon is not yet fully stopped and still rolls down its potential (which happens for the parameters chosen here, cf. Fig. 6.11), this will lead, by virtue of the effective lump coupling, to a (slow) increase of the lump masses again enhancing the potentials. These two points may be regarded as the reason why the potential Ψ is still growing at $z = 1$, cf. Fig. 6.12, despite the fact that a collection of stable cosmon-neutrino lumps has formed. Nonetheless,

the growth has clearly flattened. Although the growth of the potentials is significant, the absolute scale of $\Psi(k)$ is still between 10^{-5} and 10^{-4} on large scales. So, the metric perturbations are still small.

Depending on the scale k, the gravitational potential is enhanced by a substantial factor reaching almost one order of magnitude at very large scales. This is a very strong effect, and if the potentials do not decay after $z = 1$, this would leave a substantial imprint on the CMB spectrum C_ℓ for low multipoles ℓ. Whether it would also be significant in large-scale structure cross-correlation measurements of the ISW effect depends on the correlation between the galaxy density and the distribution of cosmon-neutrino lumps. If the two distributions were statistically independent, the effect of cosmon-neutrino lumps would not be visible in the galaxy-temperature correlation spectrum — it would drop out statistically just as the primordial CMB signal. A full analysis requires to actually measure the cross-correlation between the matter density (which is traced by the galaxies) and the time derivative of the gravitational potential (which corresponds to the ISW-induced CMB temperature fluctuation). Although our simulation contains all the necessary ingredients to actually perform this analysis, we postpone it to future work with higher numerical precision. This is because the estimation of the time derivatives Ψ' and Φ' is very sensitive to numerical noise. Another possibility to directly probe gravitational potentials is gravitational lensing. Since we expect effects on large scales, we will have to wait until gravitational lensing can be used, e. g. via weak lensing tomography or 3d weak lensing, on large scales.

In Sec. 5.5, we have emphasized that the impact of the gravitational potentials induced by cosmon-neutrino lumps on the matter perturbations will be most visible in the large-scale peculiar velocities. Although, for the time being, the observational status is somewhat unclear, and we certainly have to wait for more reliable and precise constraints regarding the large-scale peculiar velocity field, it is an interesting observable to consider from the perspective of the growing neutrino quintessence model. We show the expectations U_λ for matter bulk flows, i. e. averages of peculiar velocities on large scales λ as a function of cosmological redshift z in Fig. 6.13. More precisely, U_λ is the root mean square value of the matter peculiar velocity field $\langle \boldsymbol{v}_m \rangle_{V_i}$ averaged in the $N_\lambda = L^3/\lambda^3$ cubes V_i of comoving volume λ^3,

$$U_\lambda \equiv \sqrt{\frac{1}{N_\lambda} \sum_{i=1}^{N_\lambda} \langle \boldsymbol{v}_m \rangle_{V_i}^2}, \tag{6.44}$$

where $\langle \boldsymbol{v}_m \rangle_{V_i}$ is just the usual spatial average

$$\langle \boldsymbol{v}_m \rangle_{V_i} = \frac{\int_{V_i} d^3x \sqrt{{}^{(3)}g}\, \boldsymbol{v}_m}{\int_{V_i} d^3x \sqrt{{}^{(3)}g}}. \tag{6.45}$$

The root mean square bulk flow is comparable to the value of the dimensionless matter peculiar velocity power spectrum $\Delta_{v,m}(k) = k^3 P_{v,m}(k)/(2\pi^2)$, cf. Sec. 5.5, on scales $k \sim 1/\lambda$.

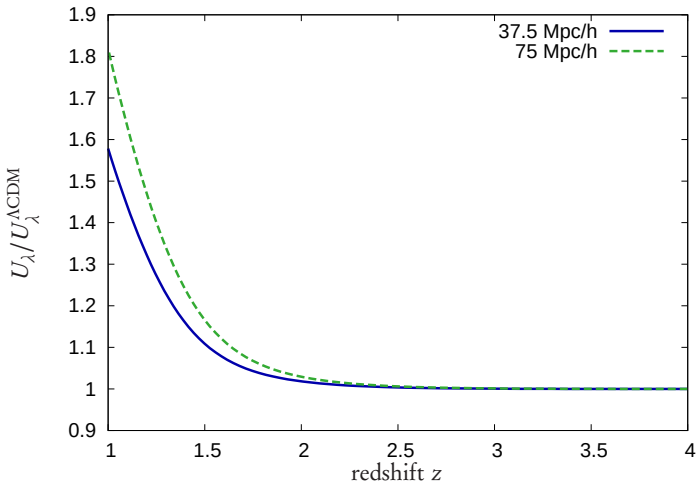

Figure 6.13: Root mean square matter bulk flows U_λ in boxes of side lengths λ, $\lambda = 37.5h^{-1}$Mpc and $\lambda = 75h^{-1}$Mpc, as compared to the 'ΛCDM run'. The figure is taken from Ayaita et al. (2012b).

We see, in Fig. 6.13, a clear delay of the enhancement of the large-scale matter peculiar velocities as compared to the gravitational potentials. Whereas the latter grow, compared to the ΛCDM case, significantly after $z \approx 2.5$, the peculiar velocities follow only after $z \lesssim 2$. This is simply due to (the gradients of) the gravitational potentials being the acceleration of the matter particles. The large-scale peculiar velocities are, subsequently, enhanced by a substantial amount, in particular on very large scales, where the enhancement reaches a factor of about two. This certainly continues for $z < 1$ since the gravitational potentials that have built up until $z = 1$ will exert their influence on the bulk flows with a certain delay. We conclude that the large-scale peculiar velocity field is a very interesting observable to constrain the growing neutrino quintessence model in the case of a cosmon-neutrino lump fluid.

An observable that is accessible with much more precision is the matter power spectrum, for example in its dimensionless form $\Delta_m(k)$. It reacts, however, only slowly to the gravitational potential induced by cosmon-neutrino lumps. Its second time derivative is related to the potential, its first derivative being linked to the peculiar velocity by virtue of the continuity equation. We show the effect of the additional gravitational potentials in growing neutrino quintessence on $\Delta_m(k)$ in Fig. 6.14. Compared to the effect of the cosmon-neutrino lumps on the gravitational potential itself and on the large-scale peculiar velocity field of matter, the effect on the density perturbations is mild. It is at the percent level at $z = 1.5$ where the large-scale potentials have already grown by a factor of more than two and the large-scale peculiar velocities have increased by almost 20%. On large scales, the effect becomes more pronounced at $z = 1$ with a deviation from the ΛCDM case of about 10%. At small scales, the additional gravitational potentials are smaller (due to the large size and distances of the lumps),

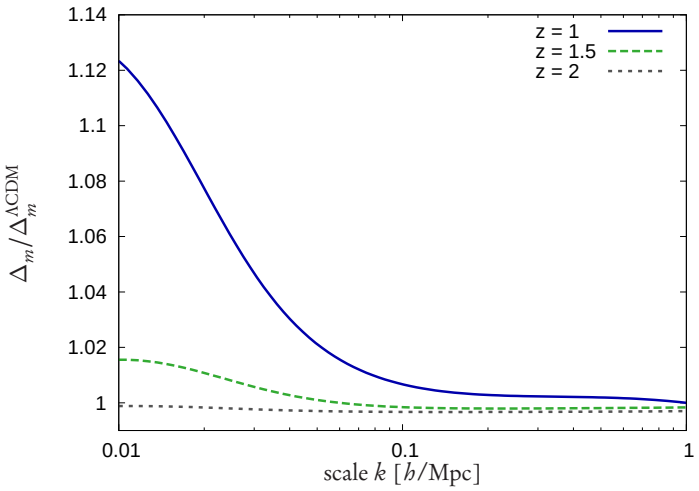

Figure 6.14: Enhancement of the matter density power spectrum for three redshifts $z = 1$, $z = 1.5$, and $z = 2$ as a function of scale. The figure is taken from Ayaita et al. (2012b).

but also the normalization given by the ΛCDM spectrum is large since matter clusters on these scales. In relative terms, the effect is thus weak.

With the growing neutrino model parameters used here, cf. Table 6.1, the enhancement of the matter power spectrum — which will increase until $z = 0$ — would certainly be observable. Yet, for more realistic parameters, the present-day neutrino mass would be much smaller and with it the large-scale gravitational potentials of cosmon-neutrino lumps. In this case, the effect on the matter power spectrum might be too small to be detected in current observations. Although this argument is still imprecise, we emphasize that observations of merely the matter power spectrum are not the ideal tool to constrain growing neutrino quintessence, at least for parameters predicting a small present-day neutrino mass. Direct probes of the gravitational potential possess more constraining power, as do observations of large-scale peculiar velocities. So, the results presented in this section support the general arguments we developed in Sec. 5.5.

6.6 Beyond $a = 0.5$

The crucial limitation of the results presented so far is the boundary $a \approx 0.5$ beyond which the cosmological evolution is not known. Although these results have enabled us to learn a lot about the growing neutrino quintessence model and, in particular, about the physics of cosmon-neutrino lumps, they are insufficient for our final goal of confronting the model quantitatively with observational constraints, for which an evolution until the present cosmic time $a = 1$ is required. Only a simulation scheme that is stable and reliable until $a = 1$ allows to eventually explore the growing neutrino quintessence parameter space in the light of observational constraints.

We have already proposed one possibility to partially achieve this, namely the simplified simulation scheme based on the cosmon-neutrino lump fluid, cf. Sec. 5.4.5. Such a simplified scheme suffers, however, from several drawbacks. First, it only works in the regime where stable cosmon-neutrino lumps form, which constitutes a rather extreme case of the model. This more or less corresponds to a restriction to the constant β model since the assumption of stable lump properties cannot be maintained if β has a strong dependence of φ. Second, even in the constant β model, the assumption of completely virialized lumps with stable, i. e. time-independent, properties may be well motivated, but — in the absence of a full simulation beyond $a = 0.5$ — the error cannot be quantified. Third, although we may expect a qualitatively robust cosmological evolution, the simplified description will not allow to make contact with precision results provided by current and future observational probes.

In this section, we overcome the limitation of $a \leq 0.5$ and thereby provide all the necessary tools to start with a comprehensive study of the parameter space. With several preliminary results, we already sketch two main regimes of this parameter space and thereby set the stage for a detailed exploration. The completion of the simulation scheme also serves as a proof of concept. The simulation method has matured, and it becomes possible to implement everything we have learned in a state-of-the-art N-body code with high spatial resolution and well-established precision. This is a promising task for future work. Quantitatively reliable and accurate results will then be compared with precision data.

At first, we will explain why numerical problems have forced us to stop at $a = 0.5$; they are related to our solution of the field equation for the cosmon perturbation $\delta\varphi$, which becomes severely nonlinear in the case of strong neutrino mass suppressions, Sec. 6.6.1. We will also present a tentative solution based on a locally spherical approximation around individual cosmon-neutrino lumps, allowing to track the cosmological evolution until $a \approx 0.8$. The final solution to the problem lies in an appropriate Newton-Gauß-Seidel relaxation method.

With the help of this method, the simulation with the parameters of Sec. 6.5 can be performed until $a = 1$ and beyond; we present and discuss this in Sec. 6.6.2. As we shall see, the backreaction effect will lead to an unrealistic expansion history, and we will discuss how the expansion history depends on the parameter choice.

In Sec. 6.6.3, we will switch to the varying β model, which has the advantage of enforcing the stop of the background cosmon by a diverging effective potential barrier. We will see that the resulting oscillations of the coupling parameter can be so violent that they do not allow for stable cosmon-neutrino lumps to form. The cosmology will be close to ΛCDM both at the background and at the perturbation level.

6.6.1 Evaluating the cosmon perturbation

Fourier-based fixed-point iteration

The simulation runs investigated in the preceding sections relied on a Fourier-based solution scheme for the field equation of the cosmon perturbation $\delta\varphi$. This solu-

tion method works in the mildly nonlinear regime $|\beta\delta\varphi| \sim 1$. Since the masses $\propto \exp(-\beta(\bar{\varphi}+\delta\varphi))$ approximately freeze within the lumps although the background cosmon $\bar{\varphi}$ continues to roll down its potential towards larger values, cf. Fig. 6.11, the cosmon perturbation $\delta\varphi$ compensates the growth of $\bar{\varphi}$. Consequently, the quantity $|\beta\delta\varphi|$ continuously grows. Once $|\beta\delta\varphi|$ is substantially larger than one, the field equation for $\delta\varphi$ is highly nonlinear and an alternative solution method must be used. In our simulations, this happens at $a \gtrsim 0.5$, why we had to stop. We will explore this now in more detail.

Let us first assume $|\beta\delta\varphi| \ll 1$, in which case the mass function may be linearized,

$$m_\nu(\varphi) = \bar{m}\, e^{-\beta(\bar{\varphi}+\delta\varphi)} \approx m_\nu(\bar{\varphi})\,(1-\beta\delta\varphi) \tag{6.46}$$

in the constant β model. In the nonrelativistic regime, we may write

$$\mathrm{tr}T_{(\nu)} \approx -\rho_\nu \approx -m_\nu(\varphi)\, n_\nu \tag{6.47}$$

with the number density n_ν. As a consequence, the field equation for $\delta\varphi$, Eq. (5.47), becomes linear in $\delta\varphi$; neglecting the metric perturbations for the sake of simplicity, it reads

$$\Delta\delta\varphi - a^2 V_{,\varphi\varphi}(\bar{\varphi})\delta\varphi \approx a^2\beta\delta\,\mathrm{tr}T_{(\nu)} \approx -m_\nu(\bar{\varphi})\delta n_\nu - \beta\delta\varphi\, m_\nu(\bar{\varphi}) n_\nu. \tag{6.48}$$

It is straightforward to solve this linear differential equation in Fourier space. This simple method, completely analogous to the computation of the gravitational potentials, works until $a \approx 0.4$. Thereafter, $|\beta\delta\varphi| \sim 1$ and the linearization is no longer possible. Nonetheless, as long as the nonlinearities are mild, we may still build upon the Fourier scheme. Formally, we may write the nonlinear field equation as

$$\Delta\delta\varphi(\boldsymbol{x}) = f(\delta\varphi(\boldsymbol{x}); \boldsymbol{x}), \tag{6.49}$$

where f is a nonlinear function of $\delta\varphi$ by virtue of the cosmon-dependent mass $\propto \exp(-\beta\delta\varphi)$. If the right-hand side was known, the equation would be solved easily on the reciprocal lattice. If the right-hand side is only known with some uncertainty (e. g., we may take the value of the last time step as a first guess), we may still hope to improve the result by solving for the left-hand side. If this is repeated, it results in the following iterative scheme:

$$\Delta\delta\varphi_{n+1}(\boldsymbol{x}) = f(\delta\varphi_n(\boldsymbol{x}); \boldsymbol{x}). \tag{6.50}$$

If it converges to a fixed point $\delta\varphi_\infty$, this would be the solution for which the field equation is satisfied. In our simulations, we have used this scheme and we observe the convergence until $a \approx 0.5$. Thereafter, the iteration becomes divergent.

We can illustrate this divergence with the help of a very simple, idealized example. We consider a single neutrino overdensity with a size λ, located at position $\boldsymbol{x} = 0$. The iteration $\delta\varphi_n$ corresponds to a mass estimate M_n obtained by evaluating the field $\delta\varphi_n$ at $\boldsymbol{x} = 0$. We further assume nonrelativistic neutrinos so that

$$\mathrm{tr}T_{(\nu)} \approx -\rho_\nu(\boldsymbol{x}) = -\frac{M_n}{a^3} W_\lambda(\boldsymbol{x}) \tag{6.51}$$

with a normalized window W_λ of size λ. In the Fourier description, we may then write approximately (replacing the window by a Dirac delta):

$$k^2 \delta\varphi_{n+1,k} \sim \beta a^2 M_n. \tag{6.52}$$

Transformed back to position space with an ultraviolet cutoff at the scale $k \sim \pi/\lambda$, this yields

$$\delta\varphi_{n+1}(0) \sim \frac{\beta}{2\pi a}\frac{M_n}{\lambda}. \tag{6.53}$$

Assuming that our guess M_n is close to the true value M, $M_n = M(1+\varepsilon_n)$ with $\varepsilon_n \ll 1$, the error of the next iteration would be

$$\varepsilon_{n+1} \approx -\frac{\beta^2}{2\pi a}\frac{M}{\lambda}\varepsilon_n. \tag{6.54}$$

Convergence would require shrinking errors. We observe here that the decisive factor is proportional to $\beta^2 M/\lambda$. In particular, the more concentrated the lumps are, the more likely is the iterative scheme to fail.

Locally spherical approximation

As almost all neutrinos are, at $a \gtrsim 0.5$, bound in lumps, we do not need to know the field values $\delta\varphi(\boldsymbol{x})$ everywhere but just within the lumps. Since the lumps are, to a good approximation, spherical, we may exploit this symmetry. More precisely, the solution of $\delta\varphi$ in a lump is expected to approximately only depend on the radial distance r from the lump's center. The field equation for $\delta\varphi$ becomes a one-dimensional differential equation:

$$\frac{1}{r^2}\frac{\partial}{\partial r}\left[r^2\frac{\partial\delta\varphi}{\partial r}(r)\right] - a^2 V_{,\varphi\varphi}(\bar{\varphi})\delta\varphi(r) \approx a^2\delta\left(\beta \mathrm{tr} T_{(\nu)}\right)(\delta\varphi(r); r). \tag{6.55}$$

This holds as long as the field $\delta\varphi$ is dominated by the considered lump. So, this will be a good approximation for $r \lesssim R_\nu$, where R_ν is the scale of the neutrino concentration of the lump.

The field equation then reduces to a collection of ordinary differential equations, i. e. boundary value problems, that can be solved accurately with well-known numerical techniques if the boundary conditions are known. This motivated the implementation of the method in the full simulation scheme. Once the lumps have formed, they are — in every time step — identified as local maxima in the neutrino number density. Around each lump, the source $\delta \mathrm{tr} T_{(\nu)}$ is measured in spherical shells providing a radial profile. Then, within the lump volume, the radial equation for $\delta\varphi(r)$ is solved (with appropriate boundary values discussed later), and the resulting masses are attributed to the effective neutrino particles.

In the numerical test runs, the method typically worked until $a \approx 0.8$. We show an exemplary result in Fig. 6.15 for the evolution of the average neutrino mass. The plot

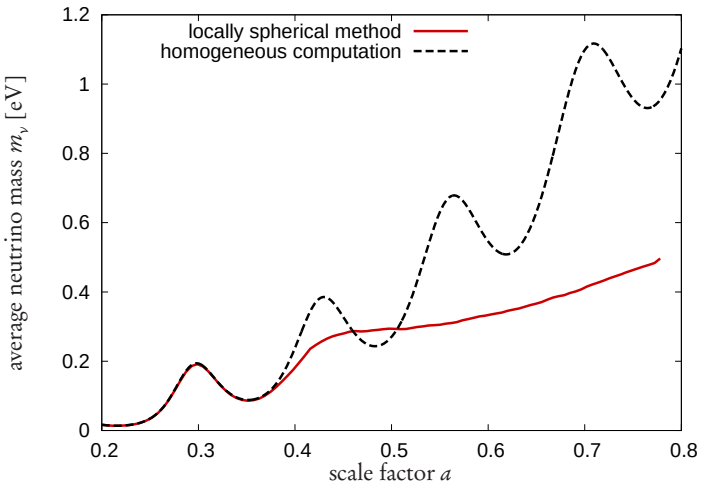

Figure 6.15: The average neutrino mass (particle average) obtained by the locally spherical method compared to the homogeneous estimate based on pure background equations. This plot can be compared approximately with Fig. 5.19.

is in reasonable agreement with the Fourier-based method until $a = 0.5$ but estimates somewhat smaller masses; this expresses the fact that the radial equation is solved without restriction to the lattice resolution. The solution for $\delta\varphi$ can be steeper and lead to a slightly stronger mass suppression.

The plot allows for a remarkable cosmological interpretation. The approximate mass freezing indeed extends to $a > 0.5$; an average mass $m_\nu \sim 1$ eV is, however, needed to effectively stop the evolution of the cosmon in this model with the relatively small coupling parameter $\beta = -52$. Consequently, the onset of the accelerated expansion will be shifted to much later times as compared to the result obtained from a homogeneous computation. We will discuss this in much more detail when we evolve the simulation beyond $a = 1$ in Sec. 6.6.2.

Since we will not use the locally spherical method for further results, we do not present its details. We just mention the most important aspects. One has to decide up to which radius R the spherical solution is obtained; this is, to some extent, related to the allowed minimal distance between two neighboring lumps. Another decision regards the treatment of neutrinos between lumps. Both issues are important in merging processes where the spherical symmetry is violated and the notion of single lumps becomes ill-defined. Once two large lumps merge, the method becomes inherently discontinuous leading to shocks in the background evolution. One would prefer initial conditions that, by chance, do not provoke this complication. The most important drawback is the restriction to $a \lesssim 0.8$.

The instability of the locally spherical method for $a \gtrsim 0.8$ is due to the estimation of boundary values for the spherical equation. The spherical method is incomplete without the boundary values $\delta\varphi_b$. The conditions used in conjunction with the spherical

field equation read

$$\left.\frac{\partial \delta\varphi}{\partial r}\right|_{r=0} = 0 \quad \text{and} \quad \delta\varphi(R) = \delta\varphi_b \tag{6.56}$$

for each lump. The evaluation of $\delta\varphi_b$ still requires the solution of a three-dimensional field equation for $\delta\varphi$. This equation is linear in $\delta\varphi$ if we assume that the right-hand side — i. e. the neutrino masses — are known from the locally spherical method of the previous time step. Yet, in complete analogy to the Fourier-based method, this is not self-consistent. Once the implicit dependence of the right-hand side on $\delta\varphi_b$ becomes strongly nonlinear, the scheme fails due to the same reason as the fixed-point Fourier-based method. In our simulations, we have obtained $\delta\varphi_b$ also by a fixed-point iteration. The relation between $\delta\varphi_b$ and the neutrino masses within the lump are quantified by the lump's effective coupling parameter β_l, cf. Sec. 5.4.3. The reason that the locally spherical method is stable for a longer time than the direct Fourier-based method is related to the fact that the effective coupling β_l is weaker than the fundamental coupling β and that the boundary value $\delta\varphi_b$ (corresponding to the outside value of the cosmon perturbation) is less negative than the local field $\delta\varphi$ within the lump. This means, the moment when $|\beta_l \delta\varphi_b|$ exceeds order one is delayed as compared to $|\beta\delta\varphi|$. However, once this point is reached, the nonlinearities in the three-dimensional field equation cause this method to break down.

Newton-Gauß-Seidel multigrid relaxation

The final solution to the numerical difficulty of solving the field equation for $\delta\varphi$ has been reached with the help of a Newton-Gauß-Seidel multigrid relaxation method originally developed for the simulation of modified gravity models within GADGET (Puchwein, Baldi, Springel, work in progress). As the details of the implementation are, at the time of writing, not yet published by the authors, we will not anticipate them here. Rather, we will content ourselves with explaining the very basic idea and with clarifying the main equations used for our model.

The field equation for $\delta\varphi$ can formally be written as

$$\mathscr{L}[\delta\varphi] \equiv \Delta\delta\varphi - f(\delta\varphi; \boldsymbol{x}) = 0, \tag{6.57}$$

where f is a nonlinear function as in Eq. (6.49), which does not contain derivatives of $\delta\varphi$. A solution for the field equation then corresponds to a root of the nonlinear functional $\mathscr{L}$. Inspired by Newton's method, a root can be found iteratively by linearizing $\mathscr{L}$ and finding, in each step, the zero of the linearly approximated function. If such a linear approximation is done at each point $\boldsymbol{x}$ individually, the resulting scheme can be described as

$$\delta\varphi_{n+1}(\boldsymbol{x}) = \delta\varphi_n(\boldsymbol{x}) - \frac{\mathscr{L}[\delta\varphi_n](\boldsymbol{x})}{\partial\mathscr{L}[\delta\varphi]/\partial\delta\varphi(\boldsymbol{x})}. \tag{6.58}$$

Note that we do not use a functional derivative but rather differentiate, at each point $\boldsymbol{x}$, just with respect to the value $\delta\varphi(\boldsymbol{x})$. In a discretization, the Laplacian will be

a function of $\delta\varphi(\boldsymbol{x})$ and of the values at neighboring points. We use a seven-point stencil

$$\Delta\delta\varphi(\boldsymbol{x}) \approx \frac{\sum_{i=1}^{3}\left[\delta\varphi(\boldsymbol{x}-\Delta x\,\boldsymbol{e}_i)+\delta\varphi(\boldsymbol{x}+\Delta x\,\boldsymbol{e}_i)\right]-6\delta\varphi(\boldsymbol{x})}{\Delta x^2}, \tag{6.59}$$

and thus

$$\frac{\partial(\Delta\delta\varphi(\boldsymbol{x}))}{\partial\delta\varphi(\boldsymbol{x})} = -\frac{6}{\Delta x^2}. \tag{6.60}$$

In the iteration prescription, Eq. (6.58), it remains to find the derivative of f with respect to $\delta\varphi$. Therefore, we have to isolate on the right-hand side of the field equation, cf. Eq. (5.47), the part that depends on $\delta\varphi$. We obtain this by defining a field $\tilde{n}_\nu(\boldsymbol{x})$, which specializes to the neutrino number density in the nonrelativistic limit, by

$$\tilde{n}_\nu(\boldsymbol{x}) \equiv \frac{-\mathrm{tr}T_{(\nu)}(\boldsymbol{x})}{m_\nu(\varphi(\boldsymbol{x}))} = \sum_p \frac{1}{\sqrt{{}^{(3)}g}}\frac{1}{\gamma_p}\delta^3(\boldsymbol{x}-\boldsymbol{x}_p), \tag{6.61}$$

where we have already described how to calculate it with the help of the effective particles p in the N-body simulation. With this quantity, the function f becomes

$$f = a^2 V_{,\varphi\varphi}(\bar{\varphi})\delta\varphi - 2\left[\bar{\varphi}'' + 2\frac{a'}{a}\bar{\varphi}'\right]\Psi - a^2\beta(\bar{\varphi}+\delta\varphi)m_\nu(\bar{\varphi}+\delta\varphi)\tilde{n}_\nu - a^2\overline{\beta\mathrm{tr}T_{(\nu)}}, \tag{6.62}$$

allowing for a cosmon-dependent coupling $\beta = \beta(\varphi)$. Since $\tilde{n}_\nu$ does not depend on $\delta\varphi$, the derivative of f with respect to $\delta\varphi$ only requires

$$\frac{\partial\left[\beta(\bar{\varphi}+\delta\varphi)m_\nu(\bar{\varphi}+\delta\varphi)\right]}{\partial\delta\varphi} = \beta_{,\varphi}(\varphi)m_\nu(\varphi) - \beta(\varphi)^2 m_\nu(\varphi). \tag{6.63}$$

We have now collected all inputs for the numerical method. The method realizes the basic iteration scheme (6.58) in a multigrid approach. This means that the simulation lattice is complemented by a number of coarse grained lattices, and the solver cleverly switches between different levels to obtain a robust and efficient calculation.

6.6.2 The constant coupling model

Equipped with a robust and reliable solver for the field equation for $\delta\varphi$, we can return to the cosmological simulation for which we showed the results until $a = 0.5$ in Sec. 6.5. We have already seen a number of hints leading to the expectation that the onset of dark energy domination will be — as compared to the homogeneous computation reviewed in Sec. 5.1 — substantially delayed due to the backreaction effect.

This expectation is drastically confirmed by a full simulation run using the Newton-Gauß-Seidel multigrid relaxation scheme. We show the most important quantities characterizing the evolution of the dark energy component in Fig. 6.16. Only as late

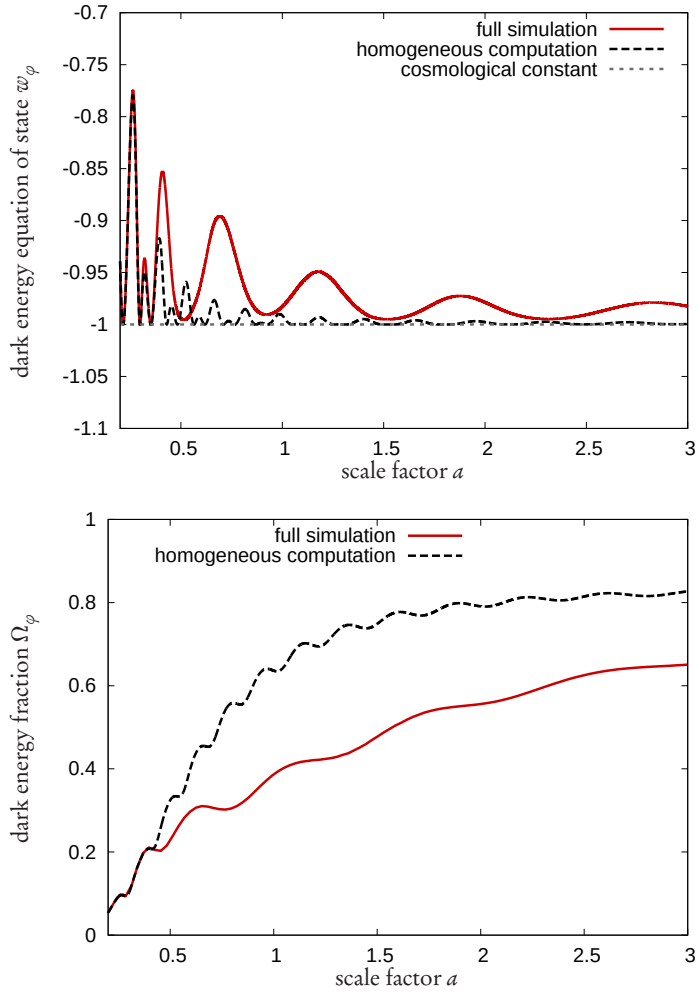

Figure 6.16: The evolution of dark energy in the constant β model until $a = 3$ as compared to the homogeneous computation which leads to an accelerated expansion at $a < 1$ similarly to the ΛCDM scenario. We show the equation of state parameter w_φ and the dark energy fraction Ω_φ. The full simulation shows a substantial delay in the onset of dark energy domination.

as $a \approx 3$, the energy fraction Ω_φ reaches values of about 2/3. The homogeneous computation neglecting the backreaction effect has reached this already at $a \approx 1$. A related quantity is the equation of state w_φ, which deviates more significantly from the cosmological constant value if the backreaction is taken into account. With the parameter choices for the growing neutrino quintessence model used here and summarized in Table 6.1, the expansion dynamics is clearly spoiled. Still, the fact that dark energy eventually dominates tells us that it should be possible to shift this transition to more realistic, i. e. earlier, times, by choosing different parameter values.

The backreaction effect responsible for postponing the onset of dark energy domination has its origin in the neutrino mass suppression within the lumps together with the effect of relativistic neutrinos, as we have explained in Sec. 6.4. Due to the approximate mass freezing within lumps, the effective coupling at the background level,

$$\bar{\beta}(\bar{\varphi}) \equiv -\frac{d \log \bar{m}_\nu}{d\bar{\varphi}} \tag{6.64}$$

quantifying the reaction of some suitably averaged neutrino mass $\bar{m}_\nu$ to the background cosmon, is substantially suppressed, $|\bar{\beta}(\bar{\varphi})| \ll |\beta|$. The mass $\bar{m}_\nu$ used here can be defined to include the relativistic effects and also the contribution of the local cosmon perturbations, similarly to our definition of the mass M_l of the cosmon-neutrino lumps, cf. Sec. 5.4.1. This means, the mass $\bar{m}_\nu$ should properly be defined via the trace of the average energy-momentum tensor

$$\bar{T}^{\mu\lambda} \equiv \bar{T}^{\mu\lambda}_{(\nu)} + \left(\bar{T}^{\mu\lambda}_{(\varphi)} - T^{\mu\lambda}_{(\bar{\varphi})}\right) \tag{6.65}$$

containing both the neutrino and the local cosmon contributions (we subtracted the background cosmon). The suppressed effective background coupling $\bar{\beta}(\bar{\varphi})$ will occur on the right-hand side of the averaged background equation for $\bar{\varphi}$, Eq. (5.11). Its suppression as compared to the fundamental coupling β translates into a corresponding suppression of the effective potential barrier needed to stop the slow roll of the cosmon.

For a qualitative discussion, we may ignore the details of the definition of $\bar{\beta}(\bar{\varphi})$ and just consider the evolution of the neutrino mass averaged over the effective particles in the simulation. It is shown in Fig. 6.17, compared to the homogeneous computation (obtained by evolving the background equations) as well as to the background value $m_\nu(\bar{\varphi})$ (obtained in the full simulation). The actual average nicely connects to the result from the locally spherical method until $a \approx 0.8$, shown in Fig. 6.15, and continues with a slow but stable increase. At $a \approx 3$, it reaches similar values as the homogeneous computation at $a = 1$. We thus have to wait much longer for the average neutrino mass — dominated by the neutrinos bound in lumps — to follow the background cosmon. The reduced stopping power is reflected in the evolution of the background mass $m_\nu(\bar{\varphi}) \propto \exp(-\beta\bar{\varphi})$. Since $\bar{\varphi}$ continues to grow, the background mass also grows drastically. At $a = 1$, it is a factor of about 10^4 above the particle average, thereby being in the 1 keV range, and the factor grows to about 10^7 at $a = 3$. The neutrino

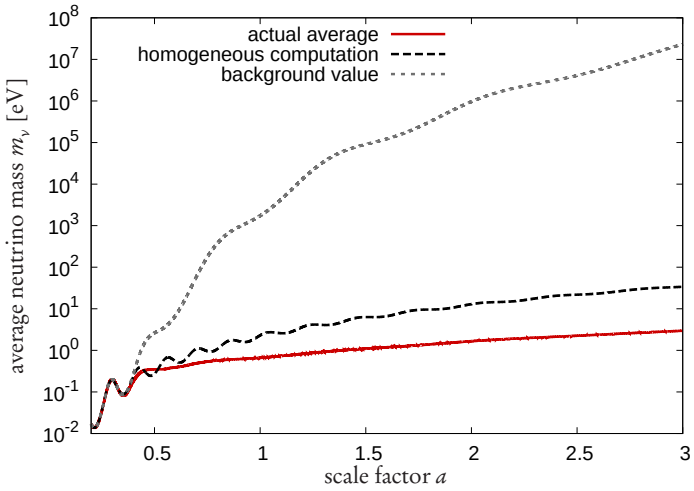

Figure 6.17: The evolution of the average neutrino mass (obtained as a particle average) as compared to the homogeneous computation and to the background value $m_\nu(\bar{\varphi})$, which corresponds to the neutrino mass outside lumps. We show the evolution until $a = 3$. The mass suppression within neutrino lumps corresponds to the comparison between the actual average and the background value. The backreaction effect is quantified by the comparison of the actual average with the homogeneous computation.

mass outside lumps is enhanced by a large amount; we note that laboratory constraints would only be reconciled with this scenario if the Solar System was located within a cosmon-neutrino lump.

The results shown in Fig. 6.17 can also be used to illustrate the nonlinearity of the cosmon field equation; they underline the extraordinary strength of the Newton-Gauß-Seidel solver. In our previous results until $a = 0.5$, the mass suppression within lumps reached one order of magnitude, cf. Fig. 6.6. Since the mass suppression is given by the factor $\exp(-\beta\delta\varphi)$, this implied $|\beta\delta\varphi| \approx \log 10 \approx 2$; this means, the field equation was mildly nonlinear, and the Fourier-based fixed-point iteration still worked. At $a = 3$, we see an average mass suppression (local mass compared to background value) of seven orders of magnitude, whence $|\beta\delta\varphi| \approx 20$. The field equation has become strongly nonlinear, and a fully nonlinear solution method is needed. The Newton-Gauß-Seidel method passes this test. In this extreme case, also the potential $V(\varphi)$ becomes nonlinear in $\delta\varphi$, and the corresponding approximations in the field equations become inaccurate. Since the cosmological evolution remains well-behaved and is in accordance with our qualitative expectations, this is, presumably, not a decisive problem. For a quantitatively reliable analysis, the numerically implemented field equations should be adapted if this strongly nonlinear regime is to be investigated more closely.

The unrealistic expansion history implied by Fig. 6.16 tells us that a quantitative comparison of the constant β model with further observational probes must wait. Before that, a model should be found that reproduces the observed accelerated expan-

sion of the Universe at the right time. Since the exploration of the parameter space is beyond the scope of this thesis, we have to leave this task open for future work.

Still, we can contribute to facilitating the task by clarifying analytically how different parameter choices will, to some approximation, affect the expansion dynamics. For first results, this can be done in the linear regime where the background equations decouple from the perturbations, i. e. where the backreaction is negligible. The idea is to motivate parameter choices where the homogeneous computation predicts a much earlier onset of dark energy domination. This onset will then be delayed due to the suppression of the effective background coupling $\bar{\beta}(\bar{\varphi})$ as compared to the fundamental coupling.

We again turn to the homogeneous equations which we have already discussed in some detail in Sec. 5.1. The onset of dark energy domination in growing neutrino quintessence can be described in two steps. First, the cosmon-neutrino coupling becomes significant once the neutrinos are nonrelativistic. The energy density in the neutrinos grows relative to the other components due to the growing mass. Eventually, the coupling term on the right-hand side of the cosmon background equation (5.11) becomes comparable to the force term $\propto V_{,\varphi}$. This stops the slow roll of the cosmon and approximately fixes the value of the potential. We label this moment of stopping by a_{st}. Second, the energy density ρ_φ is, subsequently, approximately constant and overtakes the other decaying components. A characteristic moment is the onset of dark energy domination after equality a_{eq} where $\rho_\varphi = \rho_m$.

We shall now estimate the time of stopping a_{st} and the cosmon-matter equality a_{eq} in the homogeneous approximation as functions of the model parameters. These model parameters are the (constant) fundamental coupling β, the parameter α in the exponential potential, and the normalization $\bar{m}$ of the neutrino mass $\bar{m} = m_\nu(\varphi = 0)$. According to Eq. (5.14), the effect of the coupling in the equation of the background cosmon overtakes the potential gradient once

$$V_{,\varphi}(\bar{\varphi}) = \beta(\bar{\rho}_\nu - 3\bar{p}_\nu). \tag{6.66}$$

We use this as an estimate for the stopping condition. Hence, the equation will give us a_{st}. Assuming nonrelativistic neutrinos with an average number density $\bar{n}_\nu$ (known from the early Universe), we may rewrite the stopping condition to

$$-\alpha V(\bar{\varphi}) \approx \beta \bar{m} e^{-\beta\bar{\varphi}} \bar{n}_\nu. \tag{6.67}$$

The quantities in this equation have characteristic dependences on the scale factor, e. g. due to the tracker solution of the cosmon. The energy density of the cosmon follows that of matter, $\bar{\rho}_\varphi \propto a^{-3}$ whereby $w_\varphi = 0$ and hence $\bar{\rho}_\varphi = 2V(\bar{\varphi})$. This tells us $V(\bar{\varphi}) \propto a^{-3}$. Moreover, the factor of proportionality is determined by the amount of early dark energy, $\Omega_\varphi = \bar{\rho}_\varphi/(3H^2) \approx 3/\alpha^2$ where the Hubble parameter can be estimated by the amount of matter, $3H^2 \approx \bar{\rho}_{m,0} a^{-3}$. The mass function on the right-hand side of the stopping condition can also be related to the cosmon potential, cf. Eq. (5.16). Finally, the neutrino number density decays as $\bar{n}_\nu = \bar{n}_{\nu,0} a^{-3}$. Plugging

everything together, the stopping condition is equivalent to

$$a_{\mathrm{st}}^{3\frac{\beta}{\alpha}} \approx -\frac{\beta}{\alpha}\bar{m}\bar{n}_{\nu,0}\left(\frac{3\bar{\rho}_{m,0}}{2\alpha^2}\right)^{\frac{\beta}{\alpha}-1} V_0^{-\frac{\beta}{\alpha}}. \tag{6.68}$$

Here, $\bar{\rho}_{m,0}$ and $\bar{n}_{\nu,0}$ are essentially fixed. The constant V_0, i. e. the prefactor of the potential, is not a true model parameter either. A change would simply correspond to a shift in the field value $\bar{\varphi}$ and, therefore, to a change of $\bar{m}$.

Starting at a_{st}, we may approximate $V(\bar{\varphi}) \approx$ const. and neglect the kinetic energy of the cosmon. This constant is determined by

$$\frac{V(\bar{\varphi}_{\mathrm{st}})}{\bar{\rho}_{m,0}a_{\mathrm{st}}^{-3}} \approx \Omega_\varphi \approx \frac{3}{\alpha^2} \tag{6.69}$$

obtained by matching to the tracker solution. The moment of equality where $\bar{\rho}_\varphi \approx V(\bar{\varphi}_{\mathrm{st}}) = \bar{\rho}_m$, is thus simply

$$a_{\mathrm{eq}} = \sqrt[3]{\frac{\alpha^2}{3}}\, a_{\mathrm{st}}. \tag{6.70}$$

These relations will be useful when trying to find regions in the parameter space with a more realistic expansion history. Of course, the equations rely on the homogeneous approximation. One would try to obtain a time a_{eq} substantially earlier than the true onset of dark energy domination in order to compensate the delay due to the backreaction effect. Alternatively, the above derivation can be refined to include a transition from the fundamental coupling β to a later effective background coupling $\bar{\beta}(\bar{\varphi})$ with smaller values. The resulting φ-dependent coupling will complicate the equations to some extent and motivate the switch to a semi-analytical approach.

We conclude that the constant β model shows a very strong backreaction effect delaying the onset of dark energy domination substantially. This might be compensated by adequate modifications of the model parameters. Apart from the expansion history, the constant β model leads to a strong mass suppression within lumps by several orders of magnitude. As a consequence, the neutrino mass outside lumps is large and will be above laboratory constraints. This would be reconciled if our location was assumed to lie within a cosmon-neutrino lump.

6.6.3 The varying coupling

The strong impact of the backreaction effect on the expansion of the FLRW background motivates to consider another class of growing neutrino quintessence models. When introducing the growing neutrino scenario in Sec. 5.1, we have allowed for both the case of a constant coupling parameter and for a general φ dependence $\beta = \beta(\varphi)$. We identified a conceptually attractive feature of this possibility since it allows for a natural explanation of large values for β within the mechanism of neutrino mass generation. Large values of β are a natural consequence of the neutrino mass approaching

a pole when the cosmon becomes close to a critical value $\varphi_{\rm crit}$. The coupling parameter β, which is the (negative) logarithmic derivative of the mass, will also increase in absolute terms. Close to the pole, an approximation $\beta(\varphi) \approx 1/(\varphi - \varphi_{\rm crit})$ may be used.

The conceptual benefit is accompanied by a technical advantage. Since the coupling becomes arbitrarily strong when φ comes very close to $\varphi_{\rm crit}$, the effective potential felt by the background cosmon approaches an infinite potential barrier. The stop of the cosmon's evolution is guaranteed, and the value of φ at which this happens is essentially fixed: it will be close to $\varphi_{\rm crit}$. This means that, in principle, we do not need to worry about the backreaction effect — the varying β model will necessarily enter the stage of accelerated expansion just at the right time.

This comes at a price. When $\bar{\varphi}$ approaches the critical value, the coupling will become very strong and accelerate the neutrinos, which — as a consequence — can become much more relativistic than in the constant β model. The dynamical time scale shrinks, and the numerical precision, in particular regarding the time steps, has to be increased substantially. The field equation for $\delta\varphi$ is not only potentially nonlinear due to the mass suppression; even the function $\beta(\bar{\varphi} + \delta\varphi)$ alone is strongly nonlinear in $\delta\varphi$ when $\bar{\varphi}$ is close to critical. The backreaction effect, although not capable of spoiling the expansion dynamics, adds to the numerical complications. It suppresses the effect of the coupling such that the fundamental coupling has to grow to even larger values in order to compensate the weaker effective coupling. This last effect is the reason why we cannot show conclusive results in this section. The numerical accuracy and the number of time steps have still to be increased. Nonetheless, we show a new physical regime of the growing neutrino quintessence model and results until $a \approx 0.8$ obtained by a simulation that remained largely stable and had to be stopped due to the enormous numerical effort; it will be resumed on larger computational resources. Although clearly preliminary, we will not hold back the intriguing results here.

In Fig. 6.18, we show the evolution of the coupling parameter $\beta(\bar{\varphi})$ in this case, together with the average neutrino mass. Apart from the altered coupling parameter and an accordingly changed mass function,

$$m_\nu(\varphi) = \frac{\bar{m}}{\varphi_{\rm crit} - \varphi}, \quad \text{with} \quad \bar{m} = 5 \times 10^{-4}\,\text{eV}, \tag{6.71}$$

we use the parameters listed in Table 6.1, with reduced resolution $N_c = 128^3$ and number of effective particles, to cope with the increased numerical effort, and with a slightly earlier initial scale factor $a_{\rm ini,\nu} = 0.15$ for the neutrinos. The coupling parameter $\beta(\bar{\varphi})$ shows a violent behavior. Already from the homogeneous computation, we expect very large values indicating that $\bar{\varphi}$ comes very close to the critical value. The average mass exactly mirrors the behavior of β which tells us that there is no mass freezing and no significant mass suppression in this model. The absence of a significant mass suppression is not a general consequence of the varying β model. By increasing the parameter $\bar{m}$, the oscillations in β are less violent (since then, a smaller β suffices for an effective potential barrier), and the model becomes more similar to the constant β case. Still, a mass freezing cannot occur since, even if the effective background coupling

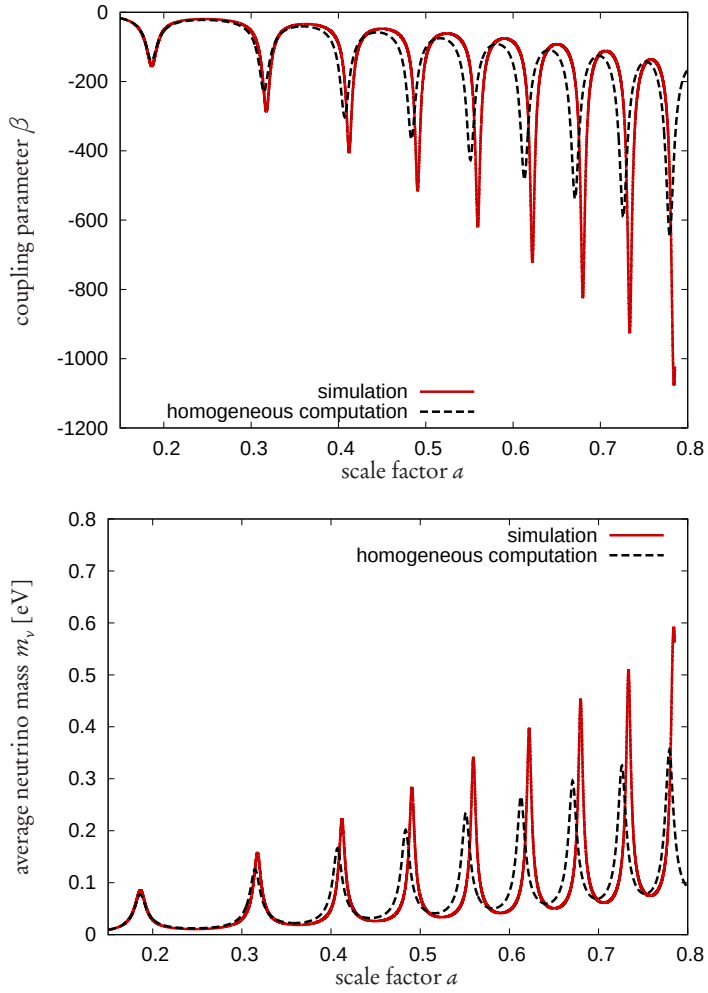

Figure 6.18: The evolution of the coupling parameter $\beta(\bar{\varphi})$ and of the average neutrino mass in the varying β model until $a \approx 0.8$ measured in the full simulation and compared to the homogeneous computation. The oscillations reflect the bouncing of the cosmon against the potential barrier at its critical value. The cosmon comes, accordingly, closer to critical in the nonlinear code than in the background computation.

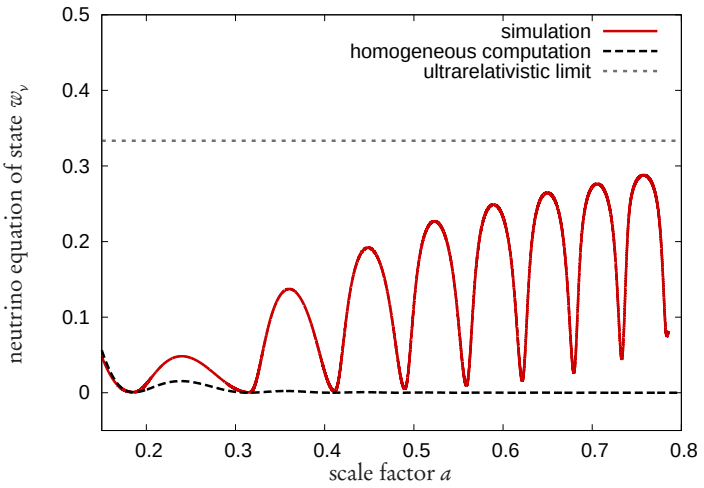

Figure 6.19: The average neutrino equation of state w_ν in the varying β model as compared to the homogeneous estimate in which w_ν quickly approaches the nonrelativistic limit. In the full simulation, the neutrinos are accelerated at the perturbation level.

$\bar{\beta}(\bar{\varphi})$ is suppressed as compared to β, $\bar{\varphi}$ will come so close to the critical value that, eventually, the masses within the lumps will follow.

As a striking feature of the results shown in Fig. 6.18, we observe that the simulation predicts stronger oscillations in β and in the mass than the homogeneous computation. This is equivalent to saying that the background cosmon $\bar{\varphi}$ comes closer to the critical value. We can explain this by the backreaction effect, which — in this case — is dominated by the relativistic contribution. We show the equation of state w_ν of the neutrinos in Fig. 6.19. The large values of β induce strong accelerations in the neutrino perturbations that are not visible in the homogeneous computation. So, this is a nonlinear effect. The neutrinos reach an equation of state $w_\nu \approx 0.3$, close to the ultrarelativistic limit. At the maxima of this curve, the trace $\mathrm{tr}T_{(\nu)} = -\rho_\nu(1 - 3w_\nu)$ is severely suppressed. This exerts a backreaction onto the background cosmon by virtue of Eq. (5.11). The impact of the cosmon-neutrino coupling on the background cosmon $\bar{\varphi}$ is reduced, and the cosmon is accelerated to larger values by the potential gradient $V_{,\varphi}$. As a consequence, it approaches the critical value with a larger 'momentum' $\bar{\varphi}'$ and subsequently comes closer to it, implying even larger values β. This explains the discrepancy between the homogeneous computation and the full simulation in Fig. 6.18.

The violent oscillatory behavior of β has a remarkable effect on the neutrino perturbations. In fact, it does not allow for the formation of stable lumps. Rather, an oscillatory structure formation is seen, visualized in Fig. 6.20. For this figure, we have used a somewhat larger mass parameter $\bar{m} = 10^{-3}$ eV where the oscillations are a bit milder and the short-lived structures can be identified more clearly. We observe that the mildly nonlinear neutrino structures visible at $a = 0.45$ are dissipated away

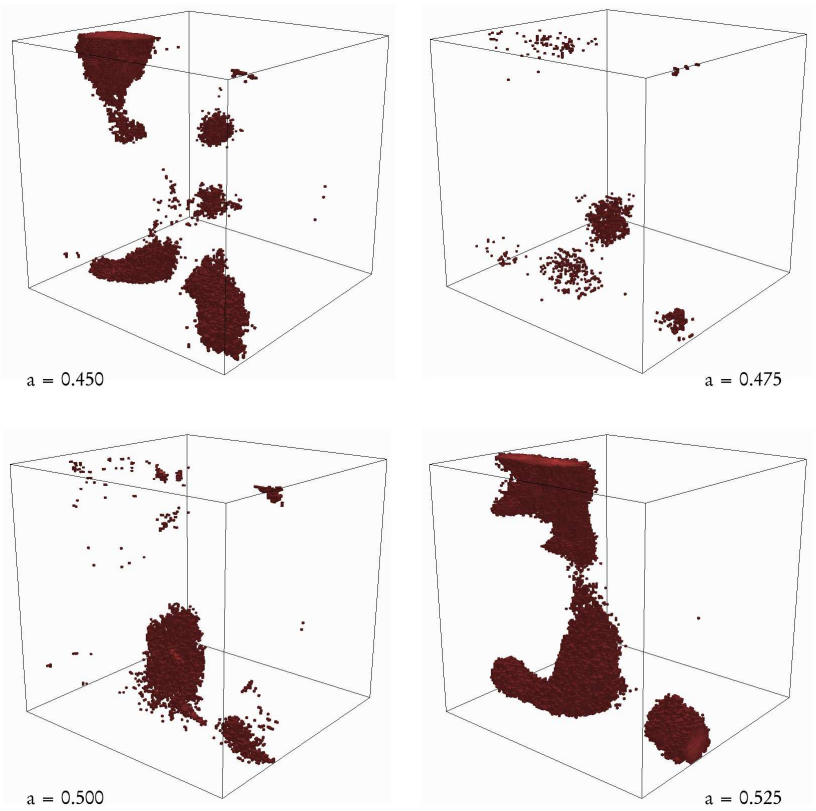

Figure 6.20: Overdensities in the neutrino number density exceeding a threshold of $n_\nu \geq 5\bar{n}_\nu$ in the simulation box around $a = 0.5$. The side length of the box measures $L = 600h^{-1}$Mpc. The structures are only mildly nonlinear with moderate densities. An oscillatory behavior is observed.

at $a = 0.475$ due to the enormous acceleration in the modified Hubble damping term induced by the large values of β. At $a \gtrsim 0.5$, the structures appear again, at roughly the same locations; this last point reveals that the structures do not entirely disappear in the intermediate period but have become mere linear overdensities not visible in the figure. These linear overdensities then grow again quickly once the neutrinos are less relativistic and again feel the attractive cosmon gradient. We recall that the attractive cosmon-mediated force is suppressed by powers of the Lorentz factor in the relativistic regime. As a side remark, we note that the structures in Fig. 6.20 are rather extended as compared to the simulation volume. There will be numerical artefacts of the imposed periodic boundary conditions. A more precise analysis should use an increased box size.

We have found a new physical regime of growing neutrino quintessence where the picture of a cosmon-neutrino lump fluid does not apply. Although the dynamics of the cosmon and the cosmological neutrinos is drastic, the absence of large stable lumps means that the influence on matter perturbations and, in general, on the gravitational potentials will be small. Even during the short periods in which neutrino structures appear, their gravitational potentials are weak. This is due to the overdensities being only at the edge of the nonlinear regime. The density contrasts remain very small compared to the case of cosmon-neutrino lumps. The effect on observables will thus remain small.

One can interpolate between the two extreme cases of growing neutrino quintessence, the formation of stable and very massive cosmon-neutrino lumps on the one side and the violent oscillatory behavior on the other. For example, increasing the mass parameter $\bar{m}$ reduces the amplitude of the oscillations in β; when they are mild enough, stable lumps form again. Alternatively, one can consider less steep functions $\beta(\varphi)$. We leave the quantitative analysis to future work.

We conclude our analysis of the varying β model by verifying that the expansion dynamics is, as expected, realistic. We show the equation of state w_φ and the energy fraction Ω_φ of dark energy in comparison with the cosmological constant in Fig. 6.21. Here, the value of Ω_Λ was chosen in accordance with the WMAP recommended parameters (Bennett et al., 2012). We observe a tight agreement between quintessence and the cosmological constant at the background level.

The varying β model with a small mass parameter $\bar{m}$ and, consequently, violent oscillations in the coupling provides cosmological dynamics very similar to the ΛCDM scenario, both in the metric perturbations (and consequently also in the matter perturbations) and in the FLRW background. Our preliminary results indicate that the growing neutrino quintessence model can lead to a realistic cosmology. Also the constant β model should be analyzed with different parameters, which might yield a realistic expansion as well. The resulting cosmon-neutrino lumps in the constant β model are then expected to provide characteristic observational signatures.

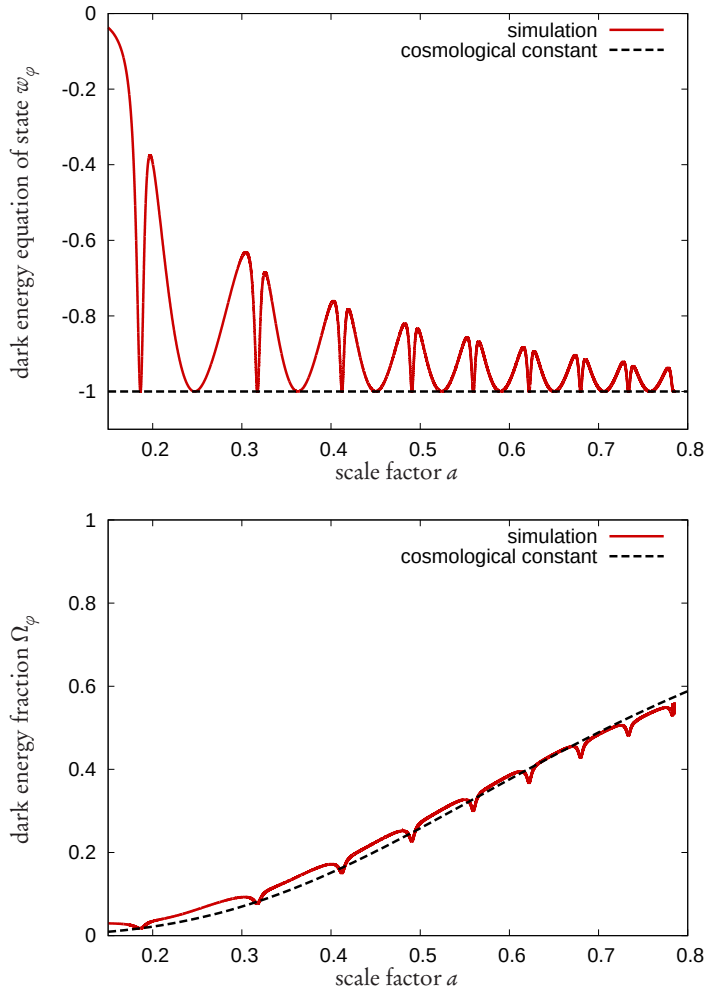

Figure 6.21: The evolution of dark energy, namely its equation of state parameter w_φ and its energy fraction Ω_φ, in the varying β model until $a \approx 0.8$ next to the cosmological constant scenario.

7 Conclusion

At the end of our journey, it is time to recapitulate what we have learned. The direct and heavily traveled road towards a description of the accelerated expansion of the Universe is the cosmological constant. It seems technically remarkably simple, but we have looked behind the scenes. The cosmological constant problem is, indeed, a hard problem, and the most popular tentative explanation, based upon the anthropic principle, is by no means simple. It relies on multiverse scenarios such as eternal inflation; and even then, some open issues remain (Chapter 3). This does not invalidate the cosmological constant as a viable candidate for explaining the onset of an accelerated expansion. It does, however, provide some strong motivation to look around and to seriously consider alternatives.

The alternatives are many, and their number is increasing. In an admirable effort, the variety of models is categorized and a selection is made in review articles and books (Peebles and Ratra, 2003; Copeland et al., 2006; Amendola and Tsujikawa, 2010). Quite understandably, the confusing situation has provoked a gain in popularity of purely phenomenological, generic parametrizations of dark energy like the wCDM parametrization. Although convenient, the usefulness of such parametrizations for learning something about better motivated, dynamical models of dark energy is somewhat doubtful (Sec. 4.1). How can we escape this situation with the cosmological constant as the standard scenario on one side and a vast jungle of models on the other?

As long as observations cannot clearly single out a small number of scenarios, it is up to us theorists to concentrate on the best motivated ideas and to subordinate others. The amount of unnatural fine-tuning required to obtain a realistic expansion history with a recent onset of the accelerated expansion can serve as a clear criterion. Promising solutions with a conceptual advantage over the cosmological constant scenario are those that do not require an enormous tuning of dimensionless quantities, which is often of order $\sim 10^{-120}$ (comparable to the fine-tuning of the energy density of the cosmological constant in natural units). If this is taken seriously, a very large number of models drop out.

From quintessence models for the accelerated expansion, we would then demand a physical mechanism by which the coincidence problem is addressed. We have encountered such a mechanism in the growing neutrino quintessence model (Chapter 5). This model is not only a proof of concept showing that coupled quintessence models can address both the cosmological constant and the coincidence problems. It can be formulated consistently within fundamental theories, in particular within the neutrino mass generation mechanism (Wetterich, 2007). We have taken the point of view, in this thesis, that the model deserves a careful investigation.

This investigation is more involved than early works expected (Sec. 5.2), and a comprehensive approach combining a thorough analysis of highly nonlinear structure formation with the calculation of the expansion of the Universe, linked to one another by a significant backreaction effect, is necessary (Sec. 5.3). We have taken on this task and presented a full simulation method in Chapter 6 accounting for nonlinear structure formation due to gravity and the cosmon-mediated attractive force, relativistic neutrino velocities, local neutrino mass variations, and the backreaction effect. This simulation method, as developed by Ayaita et al. (2012b), is a central achievement of this work. In Sec. 6.6, we have described how to reliably compute the local cosmon perturbations and thereby the local mass variations in the case of strong mass suppressions within very concentrated cosmon-neutrino lumps whose local cosmon fields have approximately decoupled from the background. This improvement has enabled us to show the first quantitative results for growing neutrino quintessence beyond scale factors $a \approx 0.5$ (i. e. for cosmological redshifts below $z \approx 1$).

The most striking feature of the cosmological evolution in the constant coupling model is the formation of large, stable cosmon-neutrino lumps, cf. Fig. 6.4. We have established a detailed physical understanding of the resulting effective fluid of interacting, nonrelativistic lumps. It bases upon several crucial insights. We have collected analytical arguments leading to the expectation that these lumps are, in fact, stabilized due to the local velocity dispersion of the neutrinos. For spherically symmetric lumps, there is an angular momentum conservation in analogy to gravitationally bound structures (Sec. 5.4.4). This replaces earlier ideas of a lump stabilization by virtue of the degeneracy pressure (Brouzakis et al., 2008). A general argument then predicts that the cosmon-neutrino lumps are, at sufficiently large distances, pressureless objects and can be described as effective particles (Sec. 5.4.2). This result is remarkable as the motion of the neutrinos implies a considerable pressure contribution. Yet, a corresponding negative pressure contribution from the local cosmon gradients cancels this pressure. This has led to the notion of *cosmon*-neutrino lumps that cannot be reduced to their neutrino concentrations. The physical situation is similar to a gas of nonrelativistic atoms where the local pressure induced by the electrons is canceled by an exactly opposite pressure due to the electromagnetic field around the atoms (Sec. 5.4.1). The derivation of the equation of motion of cosmon-neutrino lumps motivated the concept of an effective coupling β_l describing how the mass of the lump reacts to the external cosmon field (Sec. 5.4.3). The effective coupling parameters β_l are substantially suppressed as compared to the fundamental coupling parameter β. This is more pronounced for larger lumps. The effective couplings also quantify the influence of the lumps on the external cosmon field. Thereby, both the evolution of the large-scale cosmon perturbations and of the background cosmon can be expressed in terms of cosmon-neutrino lumps. A simplified but complete description of the cosmological dynamics can be given (Sec. 5.4.5). For the exemplary fundamental coupling parameter $\beta = -52$, a total number of 10^3 to 10^4 stable lumps have formed in the Hubble volume at $a \approx 0.5$ reaching 10^{15} to 10^{17} solar masses. The quotient β_l/β quantifying the suppression of the effective coupling amounts to about 1/3 for large lumps and approaches 1 for small

lumps. A more harmless situation is expected for larger couplings where the neutrino masses and also the resulting lump masses will be smaller.

The cosmon-neutrino lumps are expected to leave clear observational signatures. A full quantitative analysis in the light of actual observational constraints has to wait for a systematic exploration of the growing neutrino quintessence parameter space. Nonetheless, we have had a first look at observable consequences (Sec. 5.5). The possibilities to probe growing neutrino quintessence, in addition to the expansion dynamics, fall into two categories. First, there are direct probes related to the neutrino masses and their motion on astrophysical and cosmological distances (Sec. 5.5.1). Second, the cosmon-neutrino lumps are observable via their gravitational potentials. Let us turn to the first point. For example, a strong hint for varying neutrino masses would be given by a laboratory detection of a neutrino mass above the cosmological upper bounds. Currently, the cosmological upper limit for the sum of the neutrino masses is at 0.23 eV (Ade et al., 2013c), while the laboratory constraints, for a relevant combination of the mass eigenvalues, is ten times larger, around 2 eV (Beringer et al., 2012). In the growing neutrino quintessence model, the neutrino masses are small in the early Universe (e. g. around 10^{-3} eV), and the cosmological constraints are easily passed. In the late Universe, however, the neutrino masses grow and typically reach, depending on the model parameters, values of order 0.1 eV or 1 eV today. Moreover, in the constant coupling model, there is a strong discrepancy between the neutrino masses inside cosmon-neutrino lumps and outside. Another possibility to directly probe the cosmon-neutrino coupling is related to its influence on the neutrino motion. The cosmon-mediated force implies a deviation from the geodesic path. This could be interesting, in principle, when high-energy neutrinos are detected from, e. g., supernovae as it was the case for SN1987A. We have estimated the expected delays in the arrival time of neutrinos within growing neutrino quintessence as compared to uncoupled neutrinos and found that the delays are suppressed by powers of the Lorentz factor. For SN1987A and typical values estimated on the grounds of the $\beta = -52$ model, the delay amounts to $\Delta t \sim 10^{-6}$ sec. It will be even smaller for larger couplings.

The gravitational potentials induced by cosmon-neutrino lumps can be detected in three different ways (Sec. 5.5.2). First, their growth leaves an imprint on the cosmic microwave background radiation via the integrated Sachs-Wolfe effect. Second, the potentials can be observed directly by weak gravitational lensing. Third, they lead to an enhanced growth of matter perturbations. This growth is first visible in the large-scale peculiar velocity field and is much less pronounced in the matter density perturbations (cf. also Sec. 6.5). Currently, weak gravitational lensing is restricted to relatively small scales, and reasonably accurate and reliable results on large-scale peculiar velocities have, seemingly, not yet emerged (Sec. 5.5.2). The most favorable way to probe large-scale potentials would be weak gravitational lensing on large scales. We have had a detailed look at the proposed 3d weak lensing method (Heavens, 2003) in Chapter 4, where we have developed appropriate numerical techniques to calculate the 3d weak lensing Fisher matrix. Weak lensing provides an unbiased and direct estimate of the gravitational potentials. We have shown the remarkable sensitivity of 3d weak lensing

to slightly enhanced large-scale potentials when applied to data from the future Euclid survey. In order to allow for a comparison with other studies in the literature, we have considered the standard wCDM parametrization together with a free sound speed parameter c_s^2 (Sec. 4.1). In the case $c_s^2 \lesssim 1 + w$, the perturbations in the parametrized dark energy component lie within the horizon and can be probed by 3d weak lensing to a remarkable accuracy. The question whether stable cosmon-neutrino lumps exist is likely to find an ultimate answer with Euclid data.

In the cosmological simulations of growing neutrino quintessence, we have identified two regimes with qualitatively very different behaviors (Sec. 6.6). First, in the constant coupling model, stable cosmon-neutrino lumps form. The approximate freezing of neutrino masses within the lumps renders the stopping mechanism less effective. This means the background cosmon has to grow by a large amount in order to significantly enhance the masses of the neutrinos, which are — predominantly — located in lumps. As a consequence, the evolution of the cosmon is less effectively stopped, and the onset of dark energy domination and of the accelerated expansion is delayed. In the $\beta = -52$ model, it occurs at a scale factor $a \approx 3$ (Sec. 6.6.2). The same model parameters lead, if only the homogeneous evolution equations are used, to an expansion very similar to the ΛCDM case. Taking account for the backreaction effect is thus a basic requirement for quantitative investigations of the expansion. It will be a task for future work to identify parameters in the constant coupling model with an onset of dark energy domination at the right time.

A second, very different regime of the cosmological evolution has been found for the varying coupling model (Sec. 6.6.3). There, the oscillations in the coupling parameter can be so violent that no stable lumps form. Instead, we have observed mildly nonlinear short-lived structures that are repeatedly formed and disrupted in an oscillatory pattern, cf. Fig. 6.20. In such a case, the large-scale gravitational potentials will remain small and the evolution of matter perturbations will be very similar to the ΛCDM case. Also the expansion is quantitatively very close to the cosmological constant scenario. Although the large values of the coupling, which occur during the oscillations, remain a numerical challenge, the results indicate that the growing neutrino quintessence model allows for a very realistic cosmological evolution with a fair chance of proving compatible with observational constraints. A definite answer, however, requires further studies. In particular, a systematic exploration of the growing neutrino quintessence parameter space is in order.

Let us return to the beginning of this chapter: What have we learned? Undoubtedly a lot about unexpected and remarkable effects that can occur in strongly coupled quintessence models. It has paid off that we have started from a full-fledged theory, which we formulated in terms of action principles. As a result, we could draw a comprehensive, consistent physical picture, and we encountered well-behaved and intriguing physical phenomena, e. g. the cosmon-neutrino lump fluid. The methods we developed, both numerically and analytically, are not necessarily restricted to the growing neutrino quintessence model. And the remarkable effects that we have seen so clearly in this model can be regarded as rather extreme cases of what is, in principle,

also included in less strongly coupled theories of quintessence and in modified gravity theories. As far as observational cosmology is concerned, we are used to shrinking error bars apparently converging towards the ΛCDM predictions. The possibility of cosmon-neutrino lumps is an example showing that surprises — not only small deviations — can occur if the accelerated expansion is, indeed, not due to a cosmological constant. This thesis marks the end of the time when growing neutrino quintessence, a theoretically well-motivated alternative to the cosmological constant, could not be understood quantitatively. In other words, it marks the beginning of a new endeavor that will bring long-awaited answers regarding the compatibility of the model with observational constraints.

Bibliography

Aad, G., Abajyan, T., Abbott, B., Abdallah, J., Abdel Khalek, S., et al. (2012). ATLAS Collaboration. Observation of a new particle in the search for the Standard Model Higgs boson with the ATLAS detector at the LHC. *Phys.Lett.*, B716:1–29, 1207.7214.

Abdo, A., Ackermann, M., Ajello, M., Baldini, L., Ballet, J., et al. (2010). Fermi-LAT Collaboration. Constraints on Cosmological Dark Matter Annihilation from the Fermi-LAT Isotropic Diffuse Gamma-Ray Measurement. *JCAP*, 1004:014, 1002.4415.

Ade, P., Aghanim, N., Arimtage-Caplan, C., Arnaud, M., Ashdown, M., et al. (2013a). Planck Collaboration. Planck 2013 results. I. Overview of products and scientific results. 1303.5062.

Ade, P., Aghanim, N., Arimtage-Caplan, C., Arnaud, M., Ashdown, M., et al. (2013b). Planck Collaboration. Planck 2013 results. XIX. The integrated Sachs-Wolfe effect. 1303.5079.

Ade, P., Aghanim, N., Arimtage-Caplan, C., Arnaud, M., Ashdown, M., et al. (2013c). Planck Collaboration. Planck 2013 results. XVI. Cosmological parameters. 1303.5076.

Ade, P., Aghanim, N., Arimtage-Caplan, C., Arnaud, M., Ashdown, M., et al. (2013d). Planck Collaboration. Planck 2013 Results. XXIV. Constraints on primordial non-Gaussianity. 1303.5084.

Ade, P., Aghanim, N., Arimtage-Caplan, C., Arnaud, M., Ashdown, M., et al. (2013e). Planck Collaboration. Planck 2013 results. XXVI. Background geometry and topology of the Universe. 1303.5086.

Ade, P., Aghanim, N., Arnaud, M., Ashdown, M., Aumont, J., et al. (2011). Planck Collaboration. Planck Early Results. I. The Planck mission. *Astron.Astrophys.*, 536:16464, 1101.2022.

Afshordi, N. (2004). Integrated Sachs-Wolfe effect in cross - correlation: The Observer's manual. *Phys.Rev.*, D70:083536, astro-ph/0401166.

Afshordi, N., Zaldarriaga, M., and Kohri, K. (2005). On the stability of dark energy with mass-varying neutrinos. *Phys.Rev.*, D72:065024, astro-ph/0506663.

Akhmedov, E. K. (1999). Neutrino physics. hep-ph/0001264.

Albrecht, A., Bernstein, G., Cahn, R., Freedman, W. L., Hewitt, J., et al. (2006). Report of the Dark Energy Task Force. astro-ph/0609591.

Albrecht, A. J. and Steinhardt, P. J. (1982). Cosmology for Grand Unified Theories with Radiatively Induced Symmetry Breaking. *Phys. Rev. Lett.*, 48:1220–1223.

Alpher, R., Bethe, H., and Gamow, G. (1948). The origin of chemical elements. *Phys.Rev.*, 73:803–804.

Amara, A. and Refregier, A. (2007). Optimal Surveys for Weak Lensing Tomography. *Mon.Not.Roy.Astron.Soc.*, 381:1018–1026, astro-ph/0610127.

Amendola, L. (2000). Coupled quintessence. *Phys.Rev.*, D62:043511, astro-ph/9908023.

Amendola, L., Appleby, S., Bacon, D., Baker, T., Baldi, M., et al. (2012). Euclid Theory Working Group. Cosmology and fundamental physics with the Euclid satellite. 1206.1225.

Amendola, L., Baldi, M., and Wetterich, C. (2008a). Quintessence cosmologies with a growing matter component. *Phys.Rev.*, D78:023015, 0706.3064.

Amendola, L., Kunz, M., and Sapone, D. (2008b). Measuring the dark side (with weak lensing). *JCAP*, 0804:013, 0704.2421.

Amendola, L. and Tsujikawa, S. (2010). *Dark Energy*. Cambridge University Press, Cambridge.

Amiaux, J., Scaramella, R., Mellier, Y., Altieri, B., Burigana, C., et al. (2012). Euclid Collaboration. Euclid Mission: building of a Reference Survey. 1209.2228.

Ansari, R. U. H. and Unnikrishnan, S. (2011). Perturbations in dark energy models with evolving speed of sound. 1104.4609.

Araki, T., Eguchi, K., Enomoto, S., Furuno, K., Ichimura, K., et al. (2005). KamLAND Collaboration. Measurement of neutrino oscillation with KamLAND: Evidence of spectral distortion. *Phys.Rev.Lett.*, 94:081801, hep-ex/0406035.

Armendariz-Picon, C., Damour, T., and Mukhanov, V. F. (1999). k-Inflation. *Phys. Lett.*, B458:209–218, hep-th/9904075.

Armendariz-Picon, C., Mukhanov, V. F., and Steinhardt, P. J. (2000). A dynamical solution to the problem of a small cosmological constant and late-time cosmic acceleration. *Phys. Rev. Lett.*, 85:4438–4441, astro-ph/0004134.

Armendariz-Picon, C., Mukhanov, V. F., and Steinhardt, P. J. (2001). Essentials of k-essence. *Phys. Rev.*, D63:103510, astro-ph/0006373.

Arnett, W., Bahcall, J. N., Kirshner, R., and Woosley, S. (1989). Supernova SN1987A. *Ann.Rev.Astron.Astrophys.*, 27:629–700.

Astier, P., Guy, J., Regnault, N., Pain, R., Aubourg, E., et al. (2006). SNLS Collaboration. The Supernova Legacy Survey: Measurement of Ω_M, Ω_Λ and w from the First Year Data Set. *Astron. Astrophys.*, 447:31–48, astro-ph/0510447.

Atrio-Barandela, F., Kashlinsky, A., Ebeling, H., and Kocevski, D. (2012). Cosmic Microwave Background filters and the Dark-Flow measurement. 1211.4345.

Atrio-Barandela, F., Kashlinsky, A., Ebeling, H., Kocevski, D., and Edge, A. (2010). The error budget of the Dark Flow measurement. *Astrophys.J.*, 719:77–87, 1001.1261.

Ayaita, Y. (2009). *Challenges for the Cosmological Concordance Model on the Universe's Large Scales*. Diploma thesis, University of Heidelberg.

Ayaita, Y., Schäfer, B. M., and Weber, M. (2012a). Investigating clustering dark energy with 3d weak cosmic shear. *Mon.Not.Roy.Astron.Soc.*, 422:3056–3066, 1110.1985.

Ayaita, Y., Weber, M., and Wetterich, C. (2009). Peculiar Velocity Anomaly from Forces Beyond Gravity? 0908.2903.

Ayaita, Y., Weber, M., and Wetterich, C. (2010). Too few spots in the Cosmic Microwave Background. *Phys.Rev.*, D81:023507, 0905.3324.

Ayaita, Y., Weber, M., and Wetterich, C. (2012b). Structure Formation and Backreaction in Growing Neutrino Quintessence. *Phys.Rev.*, D85:123010, 1112.4762.

Ayaita, Y., Weber, M., and Wetterich, C. (2013). Neutrino Lump Fluid in Growing Neutrino Quintessence. *Phys.Rev.*, D87:043519, 1211.6589.

Babcock, H. W. (1939). The Rotation of the Andromeda Nebula. *Lick Obs. Bull.*, 498:41–51.

Babichev, E., Mukhanov, V., and Vikman, A. (2008). k-Essence, superluminal propagation, causality and emergent geometry. *JHEP*, 02:101, 0708.0561.

Baldi, M. (2011). The nonlinear evolution of large scale structures in Growing Neutrino cosmologies. 1110.2173.

Baldi, M. (2012). Dark Energy Simulations. *Phys.Dark Univ.*, 1:162–193, 1210.6650.

Baldi, M., Pettorino, V., Amendola, L., and Wetterich, C. (2011). Oscillating nonlinear large scale structure in growing neutrino quintessence. 1106.2161.

Baldi, M., Pettorino, V., Robbers, G., and Springel, V. (2010). Hydrodynamical N-body simulations of coupled dark energy cosmologies. *Mon.Not.Roy.Astron.Soc.*, 403:1684–1702, 0812.3901.

Ballesteros, G. and Lesgourgues, J. (2010). Dark energy with non-adiabatic sound speed: initial conditions and detectability. *JCAP*, 1010:014, 1004.5509.

Bardeen, J. M. (1980). Gauge-invariant cosmological perturbations. *Phys. Rev. D*, 22:1882–1905.

Barrow, J. D. and Clifton, T. (2006). Cosmologies with energy exchange. *Phys.Rev.*, D73:103520, gr-qc/0604063.

Bartelmann, M. (2010a). Gravitational Lensing. *Class.Quant.Grav.*, 27:233001, 1010.3829.

Bartelmann, M. (2010b). The Dark Universe. *Rev.Mod.Phys.*, 82:331–382, 0906.5036.

Bartelmann, M., Limousin, M., Meneghetti, M., and Schmidt, R. (2013). Internal Cluster Structure. 1303.3285.

Bartelmann, M. and Schneider, P. (2001). Weak gravitational lensing. *Phys.Rept.*, 340:291–472, astro-ph/9912508.

Bean, R. and Dore, O. (2004). Probing dark energy perturbations: The Dark energy equation of state and speed of sound as measured by WMAP. *Phys.Rev.*, D69:083503, astro-ph/0307100.

Bean, R., Flanagan, E. E., Laszlo, I., and Trodden, M. (2008). Constraining Interactions in Cosmology's Dark Sector. *Phys.Rev.*, D78:123514, 0808.1105.

Behrend, J., Brown, I. A., and Robbers, G. (2008). Cosmological Backreaction from Perturbations. *JCAP*, 0801:013, 0710.4964.

Benitez-Herrera, S., Röpke, F., Hillebrandt, W., Mignone, C., Bartelmann, M., et al. (2011). Model-Independent Reconstruction of the Expansion History of the Universe from Type Ia Supernovae. 1109.0873.

Bennett, C., Halpern, M., Hinshaw, G., Jarosik, N., Kogut, A., et al. (2003). WMAP Collaboration. First year Wilkinson Microwave Anisotropy Probe (WMAP) observations: Preliminary maps and basic results. *Astrophys.J.Suppl.*, 148:1, astro-ph/0302207.

Bennett, C., Larson, D., Weiland, J., Jarosik, N., Hinshaw, G., et al. (2012). Nine-Year Wilkinson Microwave Anisotropy Probe (WMAP) Observations: Final Maps and Results. 1212.5225.

Beringer, J., Arguin, J.-F., Barnett, R., Copic, K., Dahl, O., et al. (2012). Particle Data Group. Review of Particle Physics (RPP). *Phys.Rev.*, D86:010001.

Bernardeau, F., Colombi, S., Gaztanaga, E., and Scoccimarro, R. (2002). Large scale structure of the universe and cosmological perturbation theory. *Phys.Rept.*, 367:1–248, astro-ph/0112551.

Bernstein, G. M. and Jain, B. (2004). Dark energy constraints from weak lensing cross - correlation cosmography. *Astrophys.J.*, 600:17–25, astro-ph/0309332.

Bertone, G., Hooper, D., and Silk, J. (2005). Particle dark matter: Evidence, candidates and constraints. *Phys.Rept.*, 405:279–390, hep-ph/0404175.

Bertschinger, E. (1998). Simulations of structure formation in the universe. *Ann.Rev.Astron.Astrophys.*, 36:599–654.

Bertschinger, E. (2001). Cosmological Perturbation Theory and Structure Formation. astro-ph/0101009.

Bi, X.-J., Feng, B., Li, H., and Zhang, X.-m. (2005). Cosmological evolution of interacting dark energy models with mass varying neutrinos. *Phys.Rev.*, D72:123523, hep-ph/0412002.

Bionta, R., Blewitt, G., Bratton, C., Casper, D., Ciocio, A., et al. (1987). Observation of a Neutrino Burst in Coincidence with Supernova SN 1987a in the Large Magellanic Cloud. *Phys.Rev.Lett.*, 58:1494.

Bond, J. R., Szalay, A. S., Centrella, J., and Wilson, J. R. (1984). Dark matter and shocked pancakes. *In: Formation and evolution of galaxies and large structures in the universe; Proc. of the 3rd Moriond Astrophys. Meeting, La Plagne*, pages 87–99.

Bostrom, N. (2002). *Anthropic Bias. Observation Selection Effects in Science and Philosophy*. Routledge, New York, London.

Brill, D. R. and Wheeler, J. A. (1957). Interaction of neutrinos and gravitational fields. *Rev.Mod.Phys.*, 29:465–479.

Brouzakis, N., Pettorino, V., Tetradis, N., and Wetterich, C. (2011). Nonlinear matter spectra in growing neutrino quintessence. *JCAP*, 1103:049, 1012.5255.

Brouzakis, N., Tetradis, N., and Wetterich, C. (2008). Neutrino Lumps in Quintessence Cosmology. *Phys.Lett.*, B665:131–134, 0711.2226.

Buchdahl, H. A. (1970). Non-linear Lagrangians and cosmological theory. *Mon.Not.Roy.Astr.Soc.*, 150:1.

Buchert, T. (2000). On average properties of inhomogeneous fluids in general relativity. 1. Dust cosmologies. *Gen.Rel.Grav.*, 32:105–125, gr-qc/9906015.

Buchert, T. (2010). Towards physical cosmology: geometrical interpretation of Dark Energy, Dark Matter and Inflation without fundamental sources. 1012.3084.

Buchert, T. and Rasanen, S. (2012). Backreaction in late-time cosmology. *Ann.Rev.Nucl.Part.Sci.*, 62:57–79, 1112.5335.

Cai, Y.-C., Neyrinck, M. C., Szapudi, I., Cole, S., and Frenk, C. S. (2013). A Detection of the Cold Imprint of Voids on the Microwave Background Radiation. 1301.6136.

Caldera-Cabral, G., Maartens, R., and Schäfer, B. M. (2009). The Growth of Structure in Interacting Dark Energy Models. *JCAP*, 0907:027, 0905.0492.

Caldwell, R. R. (2002). A Phantom Menace? *Phys. Lett.*, B545:23–29, astro-ph/9908168.

Camera, S., Kitching, T. D., Heavens, A. F., Bertacca, D., and Diaferio, A. (2010). Measuring Unified Dark Matter with 3D cosmic shear. 1002.4740.

Campo, D. and Parentani, R. (2004). Space-time correlations in inflationary spectra. *Phys. Rev.*, D70:105020, gr-qc/0312055.

Capranico, F., Merkel, P., and Schäfer, B. M. (2012). Parameter likelihood of intrinsic ellipticity correlations. 1207.5939.

Carlson, J., White, M., and Padmanabhan, N. (2009). A critical look at cosmological perturbation theory techniques. *Phys.Rev.*, D80:043531, 0905.0479.

Carroll, S. M. (2001). The Cosmological constant. *Living Rev.Rel.*, 4:1, astro-ph/0004075.

Carroll, S. M., De Felice, A., Duvvuri, V., Easson, D. A., Trodden, M., et al. (2005). The Cosmology of generalized modified gravity models. *Phys.Rev.*, D71:063513, astro-ph/0410031.

Carroll, S. M., Hoffman, M., and Trodden, M. (2003). Can the dark energy equation-of-state parameter w be less than -1? *Phys. Rev.*, D68:023509, astro-ph/0301273.

Carter, B. (1974). Large number coincidences and the anthropic principle in cosmology. *IAU Symp.*, 63:291. reprinted in *Gen.Relativ.Grav.*, 43:3224–3233.

Castagnino, M. and Lombardi, O. (2003). The self-induced approach to decoherence in cosmology. *Int. J. Theor. Phys.*, 42:1281–1299, quant-ph/0211163.

Castro, P. G., Heavens, A., and Kitching, T. (2005). Weak lensing analysis in three dimensions. *Phys.Rev.*, D72:023516, astro-ph/0503479.

Chatrchyan, S., Khachatryan, V., Sirunyan, A. M., Tumasyan, A., Adam, W., et al. (2012). CMS Collaboration. Observation of a new boson at a mass of 125 GeV with the CMS experiment at the LHC. *Phys.Lett.*, B716:30–61, 1207.7235.

Chiba, T., Okabe, T., and Yamaguchi, M. (2000). Kinetically driven quintessence. *Phys. Rev.*, D62:023511, astro-ph/9912463.

Chibisov, G. V. and Mukhanov, V. F. (1982). Galaxy formation and phonons. *Mon.Not.Roy.Astron.Soc.*, 200:535–550.

Chitov, G. Y., August, T., Natarajan, A., and Kahniashvili, T. (2011). Mass Varying Neutrinos, Quintessence, and the Accelerating Expansion of the Universe. *Phys.Rev.*, D83:045033, 0911.1728.

Clifton, T., Ferreira, P. G., Padilla, A., and Skordis, C. (2012). Modified Gravity and Cosmology. *Phys.Rept.*, 513:1–189, 1106.2476.

Cole, S., Percival, W. J., Peacock, J. A., Norberg, P., Baugh, C. M., et al. (2005). 2dFGRS Collaboration. The 2dF Galaxy Redshift Survey: Power-spectrum analysis of the final dataset and cosmological implications. *Mon.Not.Roy.Astron.Soc.*, 362:505–534, astro-ph/0501174.

Colless, M., Dalton, G., Maddox, S., Sutherland, W., Norberg, P., et al. (2001). 2DFGRS Collaboration. The 2dF Galaxy Redshift Survey: Spectra and redshifts. *Mon.Not.Roy.Astron.Soc.*, 328:1039, astro-ph/0106498.

Comelli, D., Pietroni, M., and Riotto, A. (2003). Dark energy and dark matter. *Phys.Lett.*, B571:115–120, hep-ph/0302080.

Copeland, E. J., Sami, M., and Tsujikawa, S. (2006). Dynamics of dark energy. *Int.J.Mod.Phys.*, D15:1753–1936, hep-th/0603057.

Copi, C. J., Huterer, D., Schwarz, D. J., and Starkman, G. D. (2009). No large-angle correlations on the non-Galactic microwave sky. *Mon.Not.Roy.Astron.Soc.*, 399:295–303, 0808.3767.

Crocce, M. and Scoccimarro, R. (2006). Renormalized cosmological perturbation theory. *Phys.Rev.*, D73:063519, astro-ph/0509418.

D'Amico, G., Kamionkowski, M., and Sigurdson, K. (2009). Dark Matter Astrophysics. 0907.1912.

de Putter, R., Huterer, D., and Linder, E. V. (2010). Measuring the Speed of Dark: Detecting Dark Energy Perturbations. *Phys.Rev.*, D81:103513, 1002.1311.

DeDeo, S., Caldwell, R., and Steinhardt, P. J. (2003). Effects of the sound speed of quintessence on the microwave background and large scale structure. *Phys.Rev.*, D67:103509, astro-ph/0301284.

Dent, T., Stern, S., and Wetterich, C. (2009). Time variation of fundamental couplings and dynamical dark energy. *JCAP*, 0901:038, 0809.4628.

Dodelson, S. (2003). *Modern Cosmology*. Academic Press, Amsterdam, Boston and others.

Dolag, K., Borgani, S., Schindler, S., Diaferio, A., and Bykov, A. (2008). Simulation techniques for cosmological simulations. 0801.1023.

Doran, M. (2005). CMBEASY: an object oriented code for the cosmic microwave background. *JCAP*, 0510:011, astro-ph/0302138.

Doran, M. and Jäckel, J. (2002). Loop corrections to scalar quintessence potentials. *Phys.Rev.*, D66:043519, astro-ph/0203018.

Doran, M., Lilley, M. J., Schwindt, J., and Wetterich, C. (2001). Quintessence and the separation of CMB peaks. *Astrophys.J.*, 559:501–506, astro-ph/0012139.

Doran, M. and Müller, C. M. (2004). Analyze This! A Cosmological constraint package for CMBEASY. *JCAP*, 0409:003, astro-ph/0311311.

Doran, M. and Robbers, G. (2006). Early dark energy cosmologies. *JCAP*, 0606:026, astro-ph/0601544.

Doran, M., Robbers, G., and Wetterich, C. (2007). Impact of three years of data from the Wilkinson Microwave Anisotropy Probe on cosmological models with dynamical dark energy. *Phys.Rev.*, D75:023003, astro-ph/0609814.

Doran, M. and Wetterich, C. (2003). Quintessence and the cosmological constant. *Nucl.Phys.Proc.Suppl.*, 124:57–62, astro-ph/0205267.

Duffy, A. R., Schaye, J., Kay, S. T., Dalla Vecchia, C., Battye, R. A., et al. (2010). Impact of baryon physics on dark matter structures: a detailed simulation study of halo density profiles. *Mon.Not.Roy.Astron.Soc.*, 405:2161, 1001.3447.

Durrer, R. (2008). *The Cosmic Microwave Background*. Cambridge University Press, Cambridge.

Efstathiou, G., Davis, M., Frenk, C., and White, S. D. (1985). Numerical Techniques for Large Cosmological N-Body Simulations. *Astrophys.J.Suppl.*, 57:241–260.

Einstein, A. (1915a). Die Feldgleichungen der Gravitation. *Sitzungsber. Preuss. Akad. Wiss. Berlin (Math. Phys.)*, 1915:844–847.

Einstein, A. (1915b). Zur allgemeinen Relativitätstheorie. *Sitzungsber. Preuss. Akad. Wiss. Berlin (Math. Phys.)*, 1915:778–786.

Einstein, A. (1917). Kosmologische Betrachtungen zur allgemeinen Relativitätstheorie. *Sitzungsber. Preuss. Akad. Wiss. Berlin (Math. Phys.)*, 1917:142–152.

Eisenstein, D. J. and Hu, W. (1997). Power spectra for cold dark matter and its variants. *Astrophys.J.*, 511:5, astro-ph/9710252.

Eisenstein, D. J. and Hu, W. (1998). Baryonic features in the matter transfer function. *Astrophys.J.*, 496:605, astro-ph/9709112.

Eisenstein, D. J., Zehavi, I., Hogg, D. W., Scoccimarro, R., Blanton, M. R., et al. (2005). SDSS Collaboration. Detection of the baryon acoustic peak in the large-scale correlation function of SDSS luminous red galaxies. *Astrophys.J.*, 633:560–574, astro-ph/0501171.

Ellis, G. F. (2011). Inhomogeneity effects in Cosmology. 1103.2335.

Enqvist, K. (2008). Lemaitre-Tolman-Bondi model and accelerating expansion. *Gen.Rel.Grav.*, 40:451–466, 0709.2044.

Erickson, J. K., Caldwell, R., Steinhardt, P. J., Armendariz-Picon, C., and Mukhanov, V. F. (2002). Measuring the speed of sound of quintessence. *Phys.Rev.Lett.*, 88:121301, astro-ph/0112438.

Feldman, H. A., Watkins, R., and Hudson, M. J. (2010). Cosmic Flows on 100 Mpc/h Scales: Standardized Minimum Variance Bulk Flow, Shear and Octupole Moments. *Mon.Not.Roy.Astron.Soc.*, 407:2328–2338, 0911.5516.

Feng, J. L. (2010). Dark Matter Candidates from Particle Physics and Methods of Detection. *Ann.Rev.Astron.Astrophys.*, 48:495–545, 1003.0904.

Fixsen, D. J., Cheng, E., Gales, J., Mather, J., Shafer, R., and Wright, E. (1996). The Cosmic Microwave Background Spectrum from the Full COBE/FIRAS Data Set. *Astrophys. J.*, 473:576, astro-ph/9605054.

Fukuda, Y., Hayakawa, T., Ichihara, E., Inoue, K., Ishihara, K., et al. (1998). Super-Kamiokande Collaboration. Measurements of the solar neutrino flux from Super-Kamiokande's first 300 days. *Phys.Rev.Lett.*, 81:1158–1162, hep-ex/9805021.

Gamow, G. (1948). The origin of elements and the separation of galaxies. *Phys. Rev.*, 74:505–506.

Gao, L. and White, S. D. (2007). Assembly bias in the clustering of dark matter haloes. *Mon.Not.Roy.Astron.Soc.*, 377:L5–L9, astro-ph/0611921.

Garriga, J. and Mukhanov, V. F. (1999). Perturbations in k-inflation. *Phys. Lett.*, B458:219–225, hep-th/9904176.

Garriga, J. and Vilenkin, A. (2001). Solutions to the cosmological constant problems. *Phys.Rev.*, D64:023517, hep-th/0011262.

Gelb, J. M. and Bertschinger, E. (1994). Cold dark matter. 1: The Formation of dark halos. *Astrophys.J.*, 436:467, astro-ph/9408028.

Giahi-Saravani, A. and Schäfer, B. M. (2013a). Evolution of intrinsic ellipticity correlations due to peculiar motion. *Mon.Not.Roy.Astron.Soc.*, 428:1312–1320, 1202.1196.

Giahi-Saravani, A. and Schäfer, B. M. (2013b). Weak gravitational lensing of intrinsically aligned galaxies. 1302.2607.

Giannantonio, T., Crittenden, R., Nichol, R., and Ross, A. J. (2012). The significance of the integrated Sachs-Wolfe effect revisited. *Mon.Not.Roy.Astron.Soc.*, 426:2581–2599, 1209.2125.

Giannantonio, T., Scranton, R., Crittenden, R. G., Nichol, R. C., Boughn, S. P., et al. (2008). Combined analysis of the integrated Sachs-Wolfe effect and cosmological implications. *Phys.Rev.*, D77:123520, 0801.4380.

Giuliani, A. and Poves, A. (2012). Neutrinoless Double-Beta Decay. *Adv.High Energy Phys.*, 2012:857016.

Gnedin, O. Y., Kravtsov, A. V., Klypin, A. A., and Nagai, D. (2004). Response of dark matter halos to condensation of baryons: Cosmological simulations and improved adiabatic contraction model. *Astrophys.J.*, 616:16–26, astro-ph/0406247.

Goobar, A., Hannestad, S., Mortsell, E., and Tu, H. (2006). A new bound on the neutrino mass from the sdss baryon acoustic peak. *JCAP*, 0606:019, astro-ph/0602155.

Gordon, C. and Hu, W. (2004). A Low CMB quadrupole from dark energy isocurvature perturbations. *Phys.Rev.*, D70:083003, astro-ph/0406496.

Grishchuk, L., Lipunov, V., Postnov, K., Prokhorov, M., and Sathyaprakash, B. (2001). Gravitational wave astronomy: In Anticipation of first sources to be detected. *Phys.Usp.*, 44:1–51, astro-ph/0008481.

Grossi, M. and Springel, V. (2009). The impact of Early Dark Energy on non-linear structure formation. *Mon.Not.Roy.Astron.Soc.*, 394:1559–1574, 0809.3404.

Gumjudpai, B., Naskar, T., Sami, M., and Tsujikawa, S. (2005). Coupled dark energy: Towards a general description of the dynamics. *JCAP*, 0506:007, hep-th/0502191.

Guo, Z.-K., Ohta, N., and Tsujikawa, S. (2007). Probing the Coupling between Dark Components of the Universe. *Phys.Rev.*, D76:023508, astro-ph/0702015.

Gustafsson, M., Fairbairn, M., and Sommer-Larsen, J. (2006). Baryonic Pinching of Galactic Dark Matter Haloes. *Phys.Rev.*, D74:123522, astro-ph/0608634.

Guth, A. H. (1981). The Inflationary Universe: A Possible Solution to the Horizon and Flatness Problems. *Phys.Rev.*, D23:347–356.

Guth, A. H. (2000). Inflation and eternal inflation. *Phys.Rept.*, 333:555–574, astro-ph/0002156.

Guth, A. H. (2007). Eternal inflation and its implications. *J.Phys.*, A40:6811–6826, hep-th/0702178.

Hannestad, S., Tu, H., and Wong, Y. Y. (2006). Measuring neutrino masses and dark energy with weak lensing tomography. *JCAP*, 0606:025, astro-ph/0603019.

Hansen, F., Banday, A., Gorski, K., Eriksen, H., and Lilje, P. (2009). Power Asymmetry in Cosmic Microwave Background Fluctuations from Full Sky to Sub-degree Scales: Is the Universe Isotropic? *Astrophys.J.*, 704:1448–1458, 0812.3795.

Heavens, A. (2003). 3d weak lensing. *Mon.Not.Roy.Astron.Soc.*, 343:1327, astro-ph/0304151.

Heavens, A., Kitching, T. D., and Taylor, A. (2006). Measuring dark energy properties with 3D cosmic shear. *Mon.Not.Roy.Astron.Soc.*, 373:105–120, astro-ph/0606568.

Heavens, A., Refregier, A., and Heymans, C. (2000). Intrinsic correlation of galaxy shapes: Implications for weak lensing measurements. *Mon.Not.Roy.Astron.Soc.*, 319:649, astro-ph/0005269.

Hebecker, A. and Wetterich, C. (2001). Natural quintessence? *Phys.Lett.*, B497:281–288, hep-ph/0008205.

Hikage, C., Takada, M., Hamana, T., and Spergel, D. (2011). Shear Power Spectrum Reconstruction using Pseudo-Spectrum Method. *Mon.Not.Roy.Astron.Soc.*, 412:65–74, 1004.3542.

Hinshaw, G., Larson, D., Komatsu, E., Spergel, D., Bennett, C., et al. (2012). Nine-Year Wilkinson Microwave Anisotropy Probe (WMAP) Observations: Cosmological Parameter Results. 1212.5226.

Hinshaw, G., Spergel, D., Verde, L., Hill, R., Meyer, S., et al. (2003). WMAP Collaboration. First year Wilkinson Microwave Anisotropy Probe (WMAP) observations: The Angular power spectrum. *Astrophys.J.Suppl.*, 148:135, astro-ph/0302217.

Hirata, K., Kajita, T., Koshiba, M., Nakahata, M., Oyama, Y., et al. (1987). KAMIOKANDE-II Collaboration. Observation of a Neutrino Burst from the Supernova SN 1987a. *Phys.Rev.Lett.*, 58:1490–1493.

Ho, S., Hirata, C., Padmanabhan, N., Seljak, U., and Bahcall, N. (2008). Correlation of CMB with large-scale structure: I. ISW Tomography and Cosmological Implications. *Phys.Rev.*, D78:043519, 0801.0642.

Hobson, M. P., Efstathiou, G., and Lasenby, A. N. (2006). *General Relativity: An Introduction for Physicists*. Cambridge University Press, Cambridge.

Hoftuft, J., Eriksen, H., Banday, A., Gorski, K., Hansen, F., et al. (2009). Increasing evidence for hemispherical power asymmetry in the five-year WMAP data. *Astrophys.J.*, 699:985–989, 0903.1229.

Hollenstein, L., Sapone, D., Crittenden, R., and Schäfer, B. M. (2009). Constraints on early dark energy from CMB lensing and weak lensing tomography. *JCAP*, 0904:012, 0902.1494.

Hu, B. and Ling, Y. (2006). Interacting dark energy, holographic principle and coincidence problem. *Phys.Rev.*, D73:123510, hep-th/0601093.

Hu, W. (1999). Power spectrum tomography with weak lensing. *Astrophys.J.*, 522:L21–L24, astro-ph/9904153.

Hu, W. (2002a). Dark energy and matter evolution from lensing tomography. *Phys.Rev.*, D66:083515, astro-ph/0208093.

Hu, W. (2002b). Dark synergy: Gravitational lensing and the CMB. *Phys.Rev.*, D65:023003, astro-ph/0108090.

Hu, W. and Sawicki, I. (2007). Models of f(R) Cosmic Acceleration that Evade Solar-System Tests. *Phys.Rev.*, D76:064004, 0705.1158.

Hu, W. and Scranton, R. (2004). Measuring dark energy clustering with CMB-galaxy correlations. *Phys.Rev.*, D70:123002, astro-ph/0408456.

Hu, W. and White, M. J. (2001). Power spectra estimation for weak lensing. *Astrophys.J.*, 554:67–73, astro-ph/0010352.

Hubble, E. (1929). A relation between distance and radial velocity among extra–galactic nebulae. *Proc. Nat. Acad. Sci.*, 15:168–173.

Huey, G. and Wandelt, B. D. (2006). Interacting quintessence. The Coincidence problem and cosmic acceleration. *Phys.Rev.*, D74:023519, astro-ph/0407196.

Huterer, D. (2002). Weak lensing and dark energy. *Phys.Rev.*, D65:063001, astro-ph/0106399.

Huterer, D. (2010). Weak lensing, dark matter and dark energy. *Gen.Rel.Grav.*, 42:2177–2195, 1001.1758.

Huterer, D., Takada, M., Bernstein, G., and Jain, B. (2006). Systematic errors in future weak lensing surveys: Requirements and prospects for self-calibration. *Mon.Not.Roy.Astron.Soc.*, 366:101–114, astro-ph/0506030.

Huterer, D. and Turner, M. S. (1999). Prospects for probing the dark energy via supernova distance measurements. *Phys.Rev.*, D60:081301, astro-ph/9808133.

Ilic, S., Langer, M., and Douspis, M. (2013). On the detection of the integrated Sachs-Wolfe effect with stacked voids. 1301.5849.

Jaffe, A. H., Ade, P., Balbi, A., Bock, J., Bond, J., et al. (2001). Boomerang Collaboration. Cosmology from MAXIMA-1, BOOMERANG and COBE / DMR CMB observations. *Phys.Rev.Lett.*, 86:3475–3479, astro-ph/0007333.

Jain, B. and Taylor, A. (2003). Cross-correlation tomography: measuring dark energy evolution with weak lensing. *Phys.Rev.Lett.*, 91:141302, astro-ph/0306046.

Jeong, D. and Komatsu, E. (2006). Perturbation theory reloaded: analytical calculation of non-linearity in baryonic oscillations in the real space matter power spectrum. *Astrophys.J.*, 651:619–626, astro-ph/0604075.

Joachimi, B. and Bridle, S. (2010). Simultaneous measurement of cosmology and intrinsic alignments using joint cosmic shear and galaxy number density correlations. *Astron.Astrophys.*, 523:A1, 0911.2454.

Joachimi, B. and Schneider, P. (2010). Controlling intrinsic alignments in weak lensing statistics: The nulling and boosting techniques. 1009.2024.

Kashlinsky, A., Atrio-Barandela, F., and Ebeling, H. (2011). Measuring the dark flow with public X-ray cluster data. *Astrophys.J.*, 732:1, 1012.3214.

Kashlinsky, A., Atrio-Barandela, F., Kocevski, D., and Ebeling, H. (2009). A measurement of large-scale peculiar velocities of clusters of galaxies: results and cosmological implications. *Astrophys.J.*, 686:L49–L52, 0809.3734.

Kauffmann, G., Nusser, A., and Steinmetz, M. (1997). Galaxy formation and large scale bias. *Mon.Not.Roy.Astron.Soc.*, 286:795–811, astro-ph/9512009.

Kazanas, D. (1980). Dynamics of the Universe and Spontaneous Symmetry Breaking. *Astrophys. J.*, 241:L59–L63.

Keisler, R. (2009). The Statistical Significance of the 'Dark Flow'. *Astrophys.J.*, 707:L42–L44, 0910.4233.

Kiefer, C. (2000). Origin of classical structure from inflation. *Nucl. Phys. Proc. Suppl.*, 88:255–258, astro-ph/0006252.

Kiefer, C. and Polarski, D. (2009). Why do cosmological perturbations look classical to us? *Adv.Sci.Lett.*, 2:164–173, 0810.0087.

Kilbinger, M., Benabed, K., Guy, J., Astier, P., Tereno, I., et al. (2008). Dark energy constraints and correlations with systematics from CFHTLS weak lensing, SNLS supernovae Ia and WMAP5. 0810.5129.

Kirk, D., Bridle, S., and Schneider, M. (2010). The Impact of Intrinsic Alignments: Cosmological Constraints from a Joint Analysis of Cosmic Shear and Galaxy Survey Data. *Mon.Not.Roy.Astron.Soc.*, 408:1502–1515, 1001.3787.

Kitching, T. and Heavens, A. (2010). 3D Photometric Cosmic Shear. 1007.2953.

Kitching, T., Taylor, A., and Heavens, A. (2008). Systematic effects on dark energy from 3D weak shear. *Mon.Not.Roy.Astron.Soc.*, 389:173–190, 0801.3270.

Kitching, T. D., Heavens, A., Taylor, A., Brown, M., Meisenheimer, K., et al. (2007). Cosmological constraints from COMBO-17 using 3D weak lensing. *Mon.Not.Roy.Astron.Soc.*, 376:771–778, astro-ph/0610284.

Klapdor-Kleingrothaus, H., Dietz, A., Harney, H., and Krivosheina, I. (2001). Evidence for neutrinoless double beta decay. *Mod.Phys.Lett.*, A16:2409–2420, hep-ph/0201231.

Klapdor-Kleingrothaus, H., Krivosheina, I., Dietz, A., and Chkvorets, O. (2004). Search for neutrinoless double beta decay with enriched Ge-76 in Gran Sasso 1990-2003. *Phys.Lett.*, B586:198–212, hep-ph/0404088.

Klypin, A. (2000). Numerical simulations in cosmology I: methods. astro-ph/0005502.

Knebe, A. (2004). How to simulate the Universe in a computer. *Publ.Astron.Soc.Austral.*, astro-ph/0412565.

Knox, L. (1995). Determination of inflationary observables by cosmic microwave background anisotropy experiments. *Phys.Rev.*, D52:4307–4318, astro-ph/9504054.

Kodama, H. and Sasaki, M. (1984). Cosmological Perturbation Theory. *Progr. Theor. Phys. Suppl.*, 78:1.

Koivisto, T. (2005). Growth of perturbations in dark matter coupled with quintessence. *Phys.Rev.*, D72:043516, astro-ph/0504571.

Komatsu, E., Smith, K., Dunkley, J., Bennett, C., Gold, B., et al. (2011). WMAP Collaboration. Seven-Year Wilkinson Microwave Anisotropy Probe (WMAP) Observations: Cosmological Interpretation. *Astrophys.J.Suppl.*, 192:18, 1001.4538.

Kowalski, M., Rubin, D., Aldering, G., Agostinho, R., Amadon, A., et al. (2008). Supernova Cosmology Project. Improved Cosmological Constraints from New, Old and Combined Supernova Datasets. *Astrophys. J.*, 686:749–778, 0804.4142.

Kraus, C., Bornschein, B., Bornschein, L., Bonn, J., Flatt, B., et al. (2005). Final results from phase II of the Mainz neutrino mass search in tritium beta decay. *Eur.Phys.J.*, C40:447–468, hep-ex/0412056.

Krauss, L. M. and Chaboyer, B. (2003). Age Estimates of Globular Clusters in the Milky Way: Constraints on Cosmology. *Science*, 299:65–70.

Krauss, L. M. and Tremaine, S. (1988). Test of the weak equivalence principle for neutrinos and photons. *Phys.Rev.Lett.*, 60:176.

Kuhlen, M., Vogelsberger, M., and Angulo, R. (2012). Numerical Simulations of the Dark Universe: State of the Art and the Next Decade. *Phys.Dark Univ.*, 1:50–93, 1209.5745.

Labini, F. S., Vasilyev, N. L., and Baryshev, Y. V. (2009a). Persistent fluctuations in the distribution of galaxies from the Two degree Field Galaxy Redshift Survey. *Europhys. Lett.*, 85:29002, 0812.3260.

Labini, F. S., Vasilyev, N. L., Pietronero, L., and Baryshev, Y. V. (2009b). Absence of self-averaging and of homogeneity in the large scale galaxy distribution. *Europhys. Lett.*, 86:49001, 0805.1132.

Laflamme, R. and Matacz, A. (1993). Decoherence functional inhomogeneities in the early universe. *Int. J. Mod. Phys.*, D2:171–182, gr-qc/9303036.

Laureijs, R., Amiaux, J., Arduini, S., Augueres, J.-L., Brinchmann, J., et al. (2011). Euclid Definition Study Report. 1110.3193.

Lazarides, G., Shafi, Q., and Wetterich, C. (1981). Proton Lifetime and Fermion Masses in an SO(10) Model. *Nucl.Phys.*, B181:287.

Lesgourgues, J. (2011a). The Cosmic Linear Anisotropy Solving System (CLASS) I: Overview. 1104.2932.

Lesgourgues, J. (2011b). The Cosmic Linear Anisotropy Solving System (CLASS) III: Comparision with CAMB for LambdaCDM. 1104.2934.

Lewis, A. and Bridle, S. (2002). Cosmological parameters from CMB and other data: a Monte-Carlo approach. *Phys. Rev.*, D66:103511, astro-ph/0205436.

Lewis, A., Challinor, A., and Lasenby, A. (2000). Efficient computation of CMB anisotropies in closed FRW models. *Astrophys. J.*, 538:473–476, astro-ph/9911177.

Li, B. and Barrow, J. D. (2011). N-Body Simulations for Coupled Scalar Field Cosmology. *Phys.Rev.*, D83:024007, 1005.4231.

Li, H. and Xia, J.-Q. (2010). Constraints on Dark Energy Parameters from Correlations of CMB with LSS. *JCAP*, 1004:026, 1004.2774.

Lifschitz, E. M. (1946). On the gravitational stability of the expanding Universe. *Zh. E. Th. F.*, 16:587–602 (originally in Russian).

Linde, A. D. (1982). Coleman-Weinberg Theory and a New Inflationary Universe Scenario. *Phys. Lett.*, B114:431.

Linder, E. V. (2005). Cosmic growth history and expansion history. *Phys.Rev.*, D72:043529, astro-ph/0507263.

Linder, E. V. and Cahn, R. N. (2007). Parameterized Beyond-Einstein Growth. *Astropart.Phys.*, 28:481–488, astro-ph/0701317.

Longo, M. J. (1988). New precision tests of the Einstein equivalence principle from SN1987A. *Phys.Rev.Lett.*, 60:173.

LoVerde, M. and Afshordi, N. (2008). Extended Limber Approximation. *Phys.Rev.*, D78:123506, 0809.5112.

Lukash, V. N. and Novikov, I. D. (1982). Generation of primordial perturbations in the early Universe. In *Cambridge 1982, Proceedings, The Very Early Universe*, 311-328.

Lyth, D. H. and Liddle, A. R. (2009). *The primordial density perturbation*. Cambridge University Press, Cambridge.

Ma, C.-P. and Bertschinger, E. (1995). Cosmological perturbation theory in the synchronous and conformal Newtonian gauges. *Astrophys. J.*, 455:7–25, astro-ph/9506072.

Ma, Z.-M., Hu, W., and Huterer, D. (2005). Effect of photometric redshift uncertainties on weak lensing tomography. *Astrophys.J.*, 636:21–29, astro-ph/0506614.

Macaulay, E., Feldman, H. A., Ferreira, P. G., Hudson, M. J., and Watkins, R. (2010). A Slight Excess of Large Scale Power from Moments of the Peculiar Velocity Field. 1010.2651.

Macaulay, E., Feldman, H. A., Ferreira, P. G., Jaffe, A. H., Agarwal, S., et al. (2012). Power Spectrum Estimation from Peculiar Velocity Catalogues. *Mon.Not.Roy.Astron.Soc.*, 425:1709–1717, 1111.3338.

Magg, M. and Wetterich, C. (1980). Neutrino mass problem and gauge hierarchy. *Phys.Lett.*, B94:61.

March, M., Trotta, R., Amendola, L., and Huterer, D. (2011). Robustness to systematics for future dark energy probes. *Mon.Not.Roy.Astron.Soc.*, 415:143–152, 1101.1521.

Marcos, B. (2008). Vlasov limit and discreteness effects in cosmological N-body simulations. *Commun.Nonlinear Sci.Numer.Simul.*, 13:119, 0805.1500.

Marra, V. (2008). A back-reaction approach to dark energy. 0803.3152.

Martin, J. (2005). Inflationary cosmological perturbations of quantum-mechanical origin. *Lect. Notes Phys.*, 669:199–244, hep-th/0406011.

Martin, J. (2012). Everything You Always Wanted To Know About The Cosmological Constant Problem (But Were Afraid To Ask). *Comptes Rendus Physique*, 13:566–665, 1205.3365.

Matarrese, S. and Pietroni, M. (2007). Resumming Cosmic Perturbations. *JCAP*, 0706:026, astro-ph/0703563.

McDonald, P. (2007). Dark matter clustering: a simple renormalization group approach. *Phys.Rev.*, D75:043514, astro-ph/0606028.

Mignone, C. and Bartelmann, M. (2007). Model-independent determination of the cosmic expansion rate. 1. Application to type-Ia supernovae. *Astron.Astrophys.*, 0711.0370.

Mody, K. and Hajian, A. (2012). One Thousand and One Clusters: Measuring the Bulk Flow with the Planck ESZ and X-Ray Selected Galaxy Cluster Catalogs. *Astrophys.J.*, 758:4, 1202.1339.

Mota, D., Pettorino, V., Robbers, G., and Wetterich, C. (2008). Neutrino clustering in growing neutrino quintessence. *Phys.Lett.*, B663:160–164, 0802.1515.

Mukhanov, V. (2005). *Physical Foundations of Cosmology*. Cambridge University Press, Cambridge.

Mukhanov, V. F. and Chibisov, G. (1981). Quantum Fluctuation and Nonsingular Universe. (In Russian). *JETP Lett.*, 33:532–535.

Mukhanov, V. F., Feldman, H. A., and Brandenberger, R. H. (1992). Theory of cosmological perturbations. Part 1. Classical perturbations. Part 2. Quantum theory of perturbations. Part 3. Extensions. *Phys. Rept.*, 215:203–333.

Munshi, D., Heavens, A., and Coles, P. (2011). Higher-order Convergence Statistics for Three-dimensional Weak Gravitational Lensing. *Mon.Not.Roy.Astron.Soc.*, 411:2161–2185, 1002.2089.

Munshi, D., Valageas, P., Van Waerbeke, L., and Heavens, A. (2008). Cosmology with Weak Lensing Surveys. *Phys.Rept.*, 462:67–121, astro-ph/0612667.

Navarro, J. F., Frenk, C. S., and White, S. D. (1996). The Structure of cold dark matter halos. *Astrophys.J.*, 462:563–575, astro-ph/9508025.

Netterfield, C., Ade, P., Bock, J., Bond, J., Borrill, J., et al. (2002). Boomerang Collaboration. A measurement by Boomerang of multiple peaks in the angular power spectrum of the cosmic microwave background. *Astrophys.J.*, 571:604–614, astro-ph/0104460.

Nojiri, S. and Odintsov, S. D. (2006a). Introduction to modified gravity and gravitational alternative for dark energy. *eConf*, C0602061:06, hep-th/0601213.

Nojiri, S. and Odintsov, S. D. (2006b). Modified f(R) gravity consistent with realistic cosmology: From matter dominated epoch to dark energy universe. *Phys.Rev.*, D74:086005, hep-th/0608008.

Nunes, N. J., Schrempp, L., and Wetterich, C. (2011). Mass freezing in growing neutrino quintessence. *Phys.Rev.*, D83:083523, 1102.1664.

Oguri, M., Inada, N., Strauss, M. A., Kochanek, C. S., Kayo, I., et al. (2012). SDSS Collaboration. The Sloan Digital Sky Survey Quasar Lens Search. VI. Constraints on Dark Energy and the Evolution of Massive Galaxies. *Astron.J.*, 143:120, 1203.1088.

Olivares, G., Atrio-Barandela, F., and Pavon, D. (2005). Observational constraints on interacting quintessence models. *Phys.Rev.*, D71:063523, astro-ph/0503242.

Osborne, S., Mak, D., Church, S., and Pierpaoli, E. (2011). Measuring the Galaxy Cluster Bulk Flow from WMAP data. *Astrophys.J.*, 737:98, 1011.2781.

Peacock, J. and Smith, R. (2000). Halo occupation numbers and galaxy bias. *Mon.Not.Roy.Astron.Soc.*, 318:1144, astro-ph/0005010.

Peccei, R. (2005). Neutrino models of dark energy. *Phys.Rev.*, D71:023527, hep-ph/0411137.

Peebles, P. and Ratra, B. (2003). The Cosmological constant and dark energy. *Rev.Mod.Phys.*, 75:559–606, astro-ph/0207347.

Peebles, P. J. E. (1980). *The Large-Scale Structure of the Universe*. Princeton University Press, Princeton.

Peebles, P. J. E. (1993). *Principles of Physical Cosmology*. Princeton University Press, Princeton.

Peebles, P. J. E. (1998). The Standard Cosmological Model. astro-ph/9806201.

Penzias, A. A. and Wilson, R. W. (1965). A Measurement of excess antenna temperature at 4080-Mc/s. *Astrophys.J.*, 142:419–421.

Percival, W. J., Reid, B. A., Eisenstein, D. J., Bahcall, N. A., and Budavari, T. o. (2010). SDSS Collaboration. Baryon Acoustic Oscillations in the Sloan Digital Sky Survey Data Release 7 Galaxy Sample. *Mon.Not.Roy.Astron.Soc.*, 401:2148–2168, 0907.1660.

Perlmutter, S., Aldering, G., Goldhaber, G., Knop, R., Nugent, P., et al. (1999). Supernova Cosmology Project. Measurements of Omega and Lambda from 42 High-Redshift Supernovae. *Astrophys. J.*, 517:565–586, astro-ph/9812133.

Perotto, L., Lesgourgues, J., Hannestad, S., Tu, H., and Wong, Y. Y. (2006). Probing cosmological parameters with the CMB: Forecasts from full Monte Carlo simulations. *JCAP*, 0610:013, astro-ph/0606227.

Pettorino, V., Amendola, L., and Wetterich, C. (2013). How early is early dark energy? 1301.5279.

Pettorino, V., Mota, D. F., Robbers, G., and Wetterich, C. (2009). Clustering in growing neutrino cosmologies. *AIP Conf.Proc.*, 1115:291–296, 0901.1239.

Pettorino, V., Wintergerst, N., Amendola, L., and Wetterich, C. (2010). Neutrino lumps and the Cosmic Microwave Background. *Phys.Rev.*, D82:123001, 1009.2461.

Pietroni, M. (2008). Flowing with Time: a New Approach to Nonlinear Cosmological Perturbations. *JCAP*, 0810:036, 0806.0971.

Polarski, D. and Starobinsky, A. A. (1996). Semiclassicality and decoherence of cosmological perturbations. *Class. Quant. Grav.*, 13:377–392, gr-qc/9504030.

Press, W. H. and Schechter, P. (1974). Formation of galaxies and clusters of galaxies by selfsimilar gravitational condensation. *Astrophys.J.*, 187:425–438.

Quartin, M., Calvao, M. O., Joras, S. E., Reis, R. R., and Waga, I. (2008). Dark Interactions and Cosmological Fine-Tuning. *JCAP*, 0805:007, 0802.0546.

Rajaraman, A., Shepherd, W., Tait, T. M., and Wijangco, A. M. (2011). LHC Bounds on Interactions of Dark Matter. *Phys.Rev.*, D84:095013, 1108.1196.

Rasanen, S. (2006). Cosmological acceleration from structure formation. *Int.J.Mod.Phys.*, D15:2141–2146, astro-ph/0605632.

Rasanen, S. (2010). Backreaction as an alternative to dark energy and modified gravity. 1012.0784.

Ratra, B. and Peebles, P. (1988). Cosmological Consequences of a Rolling Homogeneous Scalar Field. *Phys.Rev.*, D37:3406.

Rees, M. and Sciama, D. (1968). Large scale Density Inhomogeneities in the Universe. *Nature*, 217:511–516.

Refregier, A. (2003). Weak gravitational lensing by large scale structure. *Ann.Rev.Astron.Astrophys.*, 41:645–668, astro-ph/0307212.

Refregier, A., Massey, R., Rhodes, J., Ellis, R., Albert, J., et al. (2004). Weak lensing from space. 3. Cosmological parameters. *Astron.J.*, 127:3102, astro-ph/0304419.

Reichardt, C. L., de Putter, R., Zahn, O., and Hou, Z. (2012). New limits on Early Dark Energy from the South Pole Telescope. *Astrophys.J.*, 749:L9, 1110.5328.

Riess, A. G., Filippenko, A. V., Challis, P., Clocchiatti, A., Diercks, A., et al. (1998). Supernova Search Team. Observational Evidence from Supernovae for an Accelerating Universe and a Cosmological Constant. *Astron. J.*, 116:1009–1038, astro-ph/9805201.

Riess, A. G., Strolger, L.-G., Casertano, S., Ferguson, H. C., Mobasher, B., et al. (2007). New Hubble Space Telescope Discoveries of Type Ia Supernovae at $z > 1$: Narrowing Constraints on the Early Behavior of Dark Energy. *Astrophys. J.*, 659:98–121, astro-ph/0611572.

Rindler, W. (1956). Visual horizons in world models. *Mon.Not.Roy.Astr.Soc.*, 116:662.

Rossi-Torres, F., Guzzo, M., de Holanda, P., and Peres, O. (2011). Mass Varying Neutrinos in Supernovae. *Phys.Rev.*, D84:053010, 1012.5304.

Sachs, R. and Wolfe, A. (1967). Perturbations of a cosmological model and angular variations of the microwave background. *Astrophys.J.*, 147:73–90.

Sapone, D. and Kunz, M. (2009). Fingerprinting Dark Energy. *Phys.Rev.*, D80:083519, 0909.0007.

Sapone, D., Kunz, M., and Amendola, L. (2010). Fingerprinting Dark Energy II: weak lensing and galaxy clustering tests. *Phys.Rev.*, D82:103535, 1007.2188.

Sarkar, P., Yadav, J., Pandey, B., and Bharadwaj, S. (2009). The scale of homogeneity of the galaxy distribution in SDSS DR6. 0906.3431.

Schechter, J. and Valle, J. (1980). Neutrino Masses in SU(2) x U(1) Theories. *Phys.Rev.*, D22:2227.

Schrempp, L. and Brown, I. (2010). Do Bound Structures Brake Cosmic Acceleration? *JCAP*, 1005:023, 0912.3157.

Schutz, B. F. (1999). Gravitational wave astronomy. *Class.Quant.Grav.*, 16:A131–A156, gr-qc/9911034.

Schäfer, B. M. (2009). Review: galactic angular momenta and angular momentum correlations in the cosmological large-scale structure. *Int.J.Mod.Phys.*, D18:173–222, 0808.0203.

Schäfer, B. M. and Heisenberg, L. (2012). Weak lensing tomography with orthogonal polynomials. *Mon.Not.Roy.Astron.Soc.*, 423:3445, 1107.2213.

Seljak, U. and Zaldarriaga, M. (1996). A line of sight approach to cosmic microwave background anisotropies. *Astrophys. J.*, 469:437–444, astro-ph/9603033.

Smith, S. (1936). The Mass of the Virgo Cluster. *Astrophs. J.*, 83:23–30.

Spergel, D., Verde, L., Peiris, H., Komatsu, E., Nolta, M., et al. (2003). WMAP Collaboration. First year Wilkinson Microwave Anisotropy Probe (WMAP) observations: Determination of cosmological parameters. *Astrophys.J.Suppl.*, 148:175–194, astro-ph/0302209.

Spitzer, C. (2006). Stability in MaVaN Models. astro-ph/0606034.

Springel, V. (2005). The Cosmological simulation code GADGET-2. *Mon.Not.Roy.Astron.Soc.*, 364:1105–1134, astro-ph/0505010.

Starobinsky, A. A. (1979). Spectrum of relict gravitational radiation and the early state of the universe. *JETP Lett.*, 30:682–685 (orginally in Russian).

Steinhardt, P. J., Wang, L.-M., and Zlatev, I. (1999). Cosmological tracking solutions. *Phys.Rev.*, D59:123504, astro-ph/9812313.

Takada, M. (2006). Can A Galaxy Redshift Survey Measure Dark Energy Clustering? *Phys.Rev.*, D74:043505, astro-ph/0606533.

Takada, M. and Jain, B. (2004). Cosmological parameters from lensing power spectrum and bispectrum tomography. *Mon.Not.Roy.Astron.Soc.*, 348:897, astro-ph/0310125.

Takada, M. and Jain, B. (2009). The Impact of Non-Gaussian Errors on Weak Lensing Surveys. *Mon.Not.Roy.Astron.Soc.*, 395:2065–2086, 0810.4170.

Tegmark, M. (2007). The Multiverse Hierarchy. 0905.1283.

Tegmark, M., Aguirre, A., Rees, M., and Wilczek, F. (2006a). Dimensionless constants, cosmology and other dark matters. *Phys.Rev.*, D73:023505, astro-ph/0511774.

Tegmark, M., Blanton, M. R., Strauss, M. A., Hoyle, F., Schlegel, D., et al. (2004a). SDSS Collaboration. The 3-D power spectrum of galaxies from the SDSS. *Astrophys.J.*, 606:702–740, astro-ph/0310725.

Tegmark, M., Eisenstein, D. J., Strauss, M. A., Weinberg, D. H., Blanton, M. R., et al. (2006b). SDSS Collaboration. Cosmological Constraints from the SDSS Luminous Red Galaxies. *Phys.Rev.*, D74:123507, astro-ph/0608632.

Tegmark, M., Strauss, M. A., Blanton, M. R., Abazajian, K., Dodelson, S., et al. (2004b). SDSS Collaboration. Cosmological parameters from SDSS and WMAP. *Phys.Rev.*, D69:103501, astro-ph/0310723.

Tegmark, M., Taylor, A., and Heavens, A. (1997). Karhunen-Loeve eigenvalue problems in cosmology: How should we tackle large data sets? *Astrophys.J.*, 480:22, astro-ph/9603021.

Torres-Rodriguez, A. and Cress, C. (2007). Constraining the Nature of Dark Energy using the SKA. *Mon.Not.Roy.Astron.Soc.*, 376:1831–1837, astro-ph/0702113.

Torres-Rodriguez, A., Cress, C., and Moodley, K. (2008). Covariance of dark energy parameters and sound speed constraints from large HI surveys. 0804.2344.

Trenti, M. and Hut, P. (2008). Gravitational N-body Simulations. 0806.3950.

Tytler, D., Kirkman, D., O'Meara, J. M., Suzuki, N., Orin, A., et al. (2004). Cosmological parameters sigma(8), the baryon density omega(b), and the UV background intensity from a calibrated measurement of HI Lyman-alpha absorption at z = 1.9. *Astrophys.J.*, 617:1–28, astro-ph/0403688.

van Waerbeke, L., Mellier, Y., Erben, T., Cuillandre, J., Bernardeau, F., et al. (2000). Detection of correlated galaxy ellipticities on CFHT data: First evidence for gravitational lensing by large scale structures. *Astron.Astrophys.*, 358:30–44, astro-ph/0002500.

Viel, M., Lesgourgues, J., Haehnelt, M. G., Matarrese, S., and Riotto, A. (2005). Constraining warm dark matter candidates including sterile neutrinos and light gravitinos with WMAP and the Lyman-alpha forest. *Phys.Rev.*, D71:063534, astro-ph/0501562.

Vilenkin, A. (1983). The Birth of Inflationary Universes. *Phys.Rev.*, D27:2848.

Vilenkin, A. (1995). Predictions from quantum cosmology. *Phys.Rev.Lett.*, 74:846–849, gr-qc/9406010.

Wang, F. (2012). Current constraints on early dark energy and growth index using latest observations. *Astron.Astrophys.*, 543:A91.

Wang, L.-M., Caldwell, R., Ostriker, J., and Steinhardt, P. J. (2000). Cosmic concordance and quintessence. *Astrophys.J.*, 530:17–35, astro-ph/9901388.

Watkins, R., Feldman, H. A., and Hudson, M. J. (2009). Consistently Large Cosmic Flows on Scales of 100 Mpc/h: a Challenge for the Standard LCDM Cosmology. *Mon.Not.Roy.Astron.Soc.*, 392:743–756, 0809.4041.

Weber, M. (2012). *Structure Formation in Growing Neutrino Cosmology*. PhD thesis, University of Heidelberg.

Weinberg, S. (1972). *Gravitation and Cosmology*. Wiley, New York.

Weinberg, S. (1987). Anthropic bound on the cosmological constant. *Phys. Rev. Lett.*, 59:2607–2610.

Weinberg, S. (1989). The cosmological constant problem. *Rev. Mod. Phys.*, 61:1–23.

Weinberg, S. (2008). *Cosmology*. Oxford University Press, Oxford.

Weiner, N. and Zurek, K. M. (2006). New matter effects and BBN constraints for mass varying neutrinos. *Phys.Rev.*, D74:023517, hep-ph/0509201.

Wetterich, C. (1988). Cosmology and the Fate of Dilatation Symmetry. *Nucl.Phys.*, B302:668.

Wetterich, C. (1995). The Cosmon model for an asymptotically vanishing time dependent cosmological 'constant'. *Astron.Astrophys.*, 301:321–328, hep-th/9408025.

Wetterich, C. (2002). Quintessence: The Dark energy in the universe? *Space Sci.Rev.*, 100:195–206, astro-ph/0110211.

Wetterich, C. (2003). Can structure formation influence the cosmological evolution? *Phys.Rev.*, D67:043513, astro-ph/0111166.

Wetterich, C. (2004). Phenomenological parameterization of quintessence. *Phys.Lett.*, B594:17–22, astro-ph/0403289.

Wetterich, C. (2007). Growing neutrinos and cosmological selection. *Phys.Lett.*, B655:201–208, 0706.4427.

Wetterich, C. (2008). Naturalness of exponential cosmon potentials and the cosmological constant problem. *Phys.Rev.*, D77:103505, 0801.3208.

Wetterich, C. (2009). Dilatation symmetry in higher dimensions and the vanishing of the cosmological constant. *Phys.Rev.Lett.*, 102:141303, 0806.0741.

Wetterich, C. (2010). The Cosmological constant and higher dimensional dilatation symmetry. *Phys.Rev.*, D81:103507, 0911.1063.

Wetterich, C. (2013). Cosmon inflation. 1303.4700.

Wetterich, C. and Pettorino, V. (2009). Growing neutrino cosmology. 0905.0715.

White, S. D., Navarro, J. F., Evrard, A. E., and Frenk, C. S. (1993). The Baryon content of galaxy clusters: A Challenge to cosmological orthodoxy. *Nature*, 366:429–433.

Winitzki, S. (2008). Predictions in eternal inflation. *Lect.Notes Phys.*, 738:157–191, gr-qc/0612164.

Winitzki, S. (2009). *Eternal Inflation*. World Scientific Publishing, Singapore, New York, London.

Wintergerst, N. and Pettorino, V. (2010). Clarifying spherical collapse in coupled dark energy cosmologies. *Phys.Rev.*, D82:103516, 1005.1278.

Wintergerst, N., Pettorino, V., Mota, D., and Wetterich, C. (2010). Very large scale structures in growing neutrino quintessence. *Phys.Rev.*, D81:063525, 0910.4985.

Wood-Vasey, W. M., Miknaitis, G., Stubbs, C., Jha, S., Riess, A., Garnavich, P., et al. (2007). ESSENCE Collaboration. Observational Constraints on the Nature of the Dark Energy: First Cosmological Results from the ESSENCE Supernova Survey. *Astrophys. J.*, 666:694–715, astro-ph/0701041.

Zaldarriaga, M., Seljak, U., and Bertschinger, E. (1998). Integral solution for the microwave background anisotropies in nonflat universes. *Astrophys.J.*, 494:491–502, astro-ph/9704265.

Zeh, H. D. (1970). On the Interpretation of Measurement in Quantum Theory. *Foundation of Physics*, 1:69–76.

Zentner, A. R., Semboloni, E., Dodelson, S., Eifler, T., Krause, E., et al. (2012). Accounting for Baryons in Cosmological Constraints from Cosmic Shear. 1212.1177.

Zhang, X. (2005). Statefinder diagnostic for coupled quintessence. *Phys.Lett.*, B611:1–7, astro-ph/0503075.

Zhao, H., Maccio', A., Li, B., Hoekstra, H., and Feix, M. (2010). Structure Formation by Fifth Force: Power Spectrum from N-Body Simulations. *Astrophys.J.*, 712:L179–L183, 0910.3207.

Zlatev, I., Wang, L.-M., and Steinhardt, P. J. (1999). Quintessence, cosmic coincidence, and the cosmological constant. *Phys.Rev.Lett.*, 82:896–899, astro-ph/9807002.

Zwicky, F. (1933). Die Rotverschiebung von extragalaktischen Nebeln. *Helv. Phys. Acta*, 6:110–127.